

# **Unraveling the Structural and Optoelectronic Effects of Rb on Chalcopyrite Solar Cells**

## **Dissertation**

**zur Erlangung des Doktorgrades der Naturwissenschaften  
(Dr. rer. nat.)**

**der**

**Naturwissenschaftlichen Fakultät II  
Chemie, Physik und Mathematik**

**der Martin-Luther-Universität  
Halle-Wittenberg**

**vorgelegt von**

**Herrn Tim Kodalle  
geb. am 17.08.1990 in Troisdorf**

Gutachter:

Prof. Dr. Roland Scheer, Martin-Luther-Universität Halle-Wittenberg

Prof. Dr. Rutger Schlatmann, Hochschule für Technik und Wirtschaft Berlin

Prof. Dr. Susanne Siebentritt, Université du Luxembourg

Datum der wissenschaftlichen Aussprache: 19.02.2020

## Abstract

In this work, the mechanism of Rb-conditioning of Cu(InGa)Se<sub>2</sub> (CIGSe) absorber layers is analyzed starting from the material property level of the absorber layer up to the full device level. In several steps, it is shown how the incorporation of Rb via an RbF post deposition treatment (PDT) is altering the structure, morphology, and optoelectronic properties of the absorber layer in dependence of the amount of Rb incorporated into the layer and of the composition of the CIGSe.

It is demonstrated that the effects of the RbF-PDT are strongly dependent on the interaction of Rb with Na, which is present as a dopant in the CIGSe, and Cu-vacancies in the lattice of the absorber layer. According to the results presented in this thesis, Rb accumulates at grain boundaries and in Cu-depleted regions at the surface of the absorber layer. Its accumulation at the grain boundaries leads to an ion-exchange mechanism with Na and induces either a weakening of the doping effects of Na in very Cu-poor CIGSe or a strengthening of its doping effect in samples with rather high Cu-content. Additionally, and independent of the Cu-content, the Rb-incorporation reduces the non-radiative recombination in the absorber layer presumably by the passivation of deep defects.

With lower Cu-content of the CIGSe, more Cu-vacancies are present at the surface of the absorber layer, which – during a PDT – promotes Rb-incorporation into the surface of the CIGSe. It is shown that the Rb, in turn, pushes the residual Cu and Ga (further) into the absorber layer to then form an amorphous, a few nm thick In<sub>x</sub>Se<sub>y</sub>:(Rb,Na) layer at the surface of the CIGSe. The impact of this newly grown surface phase on the device's efficiency is proposed to be ambivalent: while it is creating an electron barrier for the photo-current reducing the fill factor of the devices, its amorphous character acts as a more homogeneous substrate for the growth of the subsequently deposited buffer layer and therefore improves the lateral homogeneity of the heterojunction.

Combining all of these effects in a complete solar cell device, the RbF-PDT is detrimental to the open-circuit voltage (via weakening of the Na-doping) and the fill factor (due to the In<sub>x</sub>Se<sub>y</sub>:(Rb,Na) layer) of the devices when being applied to rather Cu-poor absorber layers. On the other hand, it improves both parameters and leads to very high efficiencies if applied to devices grown close to stoichiometry.

In order to investigate the structure and composition of the newly formed In<sub>x</sub>Se<sub>y</sub>:(Rb,Na) layer, RbInSe<sub>2</sub>:Na, and In<sub>2</sub>Se<sub>3</sub>:(Rb,Na) reference films are grown and compared to the surface of the RbF-treated CIGSe. Their comparison suggests the formation of a slightly off-stoichiometric RbInSe<sub>2</sub>:Na-layer during the RbF-PDT.

Finally, the proposed effect of the RbInSe<sub>2</sub>:Na on fill factor is tested experimentally by directly depositing RbInSe<sub>2</sub> on CIGSe-layers grown with a composition close to stoichiometry, as well as using device simulations by introducing the RbInSe<sub>2</sub>:Na-layer into a device model and simulating its effects on the device performance. Hereby the optical and electrical properties of the RbInSe<sub>2</sub>:Na reference layer are measured and used as input parameters for the simulations. Both the experimental and theoretical test, support the proposed model.

By comparing the buffer layer growth of chemical bath deposited CdS on samples with and without RbF-PDT, it is furthermore shown that the amorphous nature of the RbInSe<sub>2</sub>:Na leads to a more homogeneous growth of the chemical bath deposited CdS, and therefore enables the growth of a thinner buffer layer without degrading the quality of the heterojunction. The thinner buffer layer reduces the parasitic absorption and therefore leads to an improved current density generated in the solar cell. As a result the formation of a thin layer of RbInSe<sub>2</sub>:Na is advantageous for the efficiency of the solar cell. Additionally, the direct deposition of a thin layer of RbInSe<sub>2</sub>:Na is proposed as a faster alternative to the conventionally used RbF-PDT.

This thesis, for the first time, proposes a comprehensive model of the mechanism of Rb-conditioning in CIGSe solar cells including its dependence on the composition of the absorber layer. This model is well embedded into results published by other groups and enables to solve some of the contradictions in literature regarding the effect of an RbF-PDT.

---

## Zusammenfassung

In der vorliegenden Arbeit wird der Mechanismus einer Rb-Konditionierung von Cu(InGa)Se<sub>2</sub> (CIGSe)-Absorberschichten ausgehend vom Materialeigenschaftsniveau der Absorberschicht bis hin zu ihren Auswirkungen auf die elektrischen Eigenschaften des vollständigen Bauteils analysiert. In mehreren Schritten wird gezeigt, wie der Einbau von Rb ins CIGSe über eine RbF-Nachbehandlung (PDT) die Struktur, Morphologie und die optoelektronischen Eigenschaften der Absorberschicht in Abhängigkeit von der Menge an in die Schicht eingebautem Rb und der Zusammensetzung des CIGSe beeinflusst.

Es wird gezeigt, dass der Mechanismus des RbF-PDT stark von der Wechselwirkung von Rb mit Na, das als Dotant im CIGSe vorhanden ist, und Cu-Leerstellen im Gitter der Absorberschicht abhängt. Nach den in dieser Arbeit vorgestellten Ergebnissen reichert sich Rb an Korngrenzen und in Cu-verarmten Bereichen an der Oberfläche der Absorberschicht an. Die Anreicherung an den Korngrenzen induziert einen Austauschmechanismus mit Na und bewirkt eine Abschwächung des Na-Dotierungseffekts im Falle sehr Cu-armer CIGSe-Schichten beziehungsweise eine Verstärkung des Na-Dotierungseffekts bei Proben mit vergleichsweise hohem Cu-Gehalt. Zusätzlich und unabhängig vom Cu-Gehalt reduziert der Rb-Einbau die nicht strahlende Rekombination in der Absorberschicht; vermutlich durch die Passivierung tiefer Punktdefekte.

In CIGSe-Proben mit geringerem Cu-Gehalt enthält die Absorberschicht eine größere Anzahl von Cu-Fehlstellen, was – während eines PDTs – den Einbau von Rb in die Oberfläche des CIGSe verstärkt. Es wird gezeigt, dass Rb seinerseits das restliche Cu und Ga (weiter) in die Absorberschicht verschiebt, und dadurch eine amorphe, einige nm dünne In<sub>x</sub>Se<sub>y</sub>:(Rb,Na)-Schicht an der Oberfläche des CIGSe bildet. Der Einfluss dieser neu wachsenden Oberflächenphase auf die Effizienz des Bauelements ist ambivalent: Während sie eine Elektronenbarriere für den Photostrom erzeugt, die den Füllfaktor der Solarzelle verringert, bildet sie durch ihren amorphen Charakter ein homogeneres Substrat für das Wachstum der anschließend abgeschiedenen Pufferschicht und führt damit zu einer verbesserten elektrischen Homogenität des Heteroübergangs.

Durch Kombination all dieser Effekte in einer vollständigen Solarzelle wirkt sich das RbF-PDT nachteilig auf die Leerlaufspannung (durch Schwächung der Na-Dotierung) und den Füllfaktor (aufgrund der In<sub>x</sub>Se<sub>y</sub>:(Rb,Na)-Schicht) von auf eher Cu-armen CIGSe-Schichten basierenden Solarzellen aus. Andererseits verbessert es beide Parameter und führt zu sehr hohen Wirkungsgraden, wenn es auf Absorberschichten angewendet wird, die nahe an der Stöchiometrie gewachsen wurden.

Um die Struktur und Komposition der neu gebildeten In<sub>x</sub>Se<sub>y</sub>:(Rb,Na)-Schicht zu untersuchen, werden RbInSe<sub>2</sub>:Na und In<sub>2</sub>Se<sub>3</sub>:(Rb,Na)-Referenzfilme hergestellt und mit der Oberfläche des RbF-behandelten CIGSe verglichen. Die Auswertung dieses Vergleichs legt die Bildung einer RbInSe<sub>2</sub>:Na-Schicht während des RbF-PDTs nahe.

Schließlich werden die der RbInSe<sub>2</sub>:Na-Schicht zugeschriebenen negativen Effekte auf den Füllfaktor experimentell und per Simulationen getestet, indem einerseits RbInSe<sub>2</sub>:Na direkt auf CIGSe-Schichten abgeschieden wird, die mit einer Zusammensetzung nahe der Stöchiometrie gewachsen wurden, und andererseits eine RbInSe<sub>2</sub>:Na-Schicht in den Schichtstapel einer modellierten CIGSe-Solarzelle eingefügt wird. Für Letzteres werden die optischen und elektrischen Eigenschaften der RbInSe<sub>2</sub>:Na-Referenzschicht vermessen und als Eingabeparameter für die Bauteilsimulationen verwendet. Sowohl der experimentelle als auch der theoretische Test untermauern das vorgeschlagene Modell.

Durch den Vergleich des Pufferschichtwachstums von im chemischen Bad abgeschiedenem CdS auf Proben mit und ohne RbF-PDT wird ferner gezeigt, dass die amorphe Natur des RbInSe<sub>2</sub>:Na zu einem homogeneren Wachstum des CdS führt. Dies ermöglicht daher das Wachstum einer dünneren Pufferschicht, ohne die Qualität des Heteroübergangs zu verringern. Eine dünnere Pufferschicht reduziert dabei die parasitäre Absorption und führt daher zu einer erhöhten Kurzschlussstromdichte der Solarzelle. Dies bedeutet, dass die Bildung einer dünnen RbInSe<sub>2</sub>:Na-Schicht vorteilhaft für den

Wirkungsgrad der Solarzelle sein kann. Daher wird die direkte Abscheidung einer dünnen Schicht aus  $\text{RbInSe}_2\text{:Na}$  als schnellere Alternative zum herkömmlich verwendeten RbF-PDT vorgeschlagen.

Diese Dissertation schlägt erstmals ein umfassendes Modell zur Erklärung des Wirkmechanismus einer Rb-Konditionierung von CIGSe-basierten Solarzellen vor, einschließlich dessen Abhängigkeit von der Zusammensetzung der Absorberschicht. Das vorgestellte Modell ist eingebettet in die von anderen Gruppen veröffentlichten Ergebnisse und ermöglicht es, einige der Widersprüche in der Literatur in Bezug auf die Wirkung eines RbF-PDT zu lösen.



# Contents

<b>Nomenclature</b>	<b>IX</b>
<b>List of Publications</b>	<b>XIII</b>
<b>1 Introduction</b>	<b>1</b>
<b>2 Fundamentals</b>	<b>3</b>
2.1 Physics of a (CIGSe) Solar Cell . . . . .	3
2.1.1 Basics of a CIGSe Solar Cell . . . . .	3
2.1.2 Recombination Mechanisms . . . . .	6
2.1.3 Loss Mechanisms: From 100% Energy Conversion to Real Devices . . . . .	8
2.2 Crystal Structure and Defects of CIGSe Absorber Layers . . . . .	15
2.3 Alkali Metals in CIGSe Solar Cells - a Literature Review . . . . .	17
2.3.1 Sodium . . . . .	17
2.3.2 Heavy Alkali Metals . . . . .	20
2.3.3 Secondary Phases . . . . .	25
2.3.4 Summary of the Literature Review . . . . .	26
<b>3 Experimental Methods</b>	<b>27</b>
3.1 Fabrication of CIGSe Solar Cells . . . . .	27
3.1.1 CIGSe-Growth and RbF-PDT . . . . .	27
3.1.2 Buffer Layer Growth . . . . .	31
3.1.3 Growth of RbInSe <sub>2</sub> Thin Films . . . . .	31
3.1.4 Sample Preparation at the IMN . . . . .	32
3.2 Sample Characterization and Numerical Simulation . . . . .	32
3.2.1 Material Characterization . . . . .	32
3.2.2 Device Characterization . . . . .	38
3.2.3 Numerical Device Simulations . . . . .	40
<b>4 Disentangling the Physical Effects of an RbF-PDT</b>	<b>43</b>
4.1 Mechanisms of the RbF-PDT: Effects of the Treatment Time . . . . .	43
4.1.1 Time-Series: CIGSe Bulk and Device Effects . . . . .	44
4.1.2 Time-Series: CIGSe Surface Effects . . . . .	49
4.2 ODC-Induced Transport Barrier Formation: Interplay of the PDT and CGI . . . . .	56
<b>5 On RbInSe<sub>2</sub></b>	<b>67</b>
5.1 Experimental Determination of the Layer Properties of RbInSe <sub>2</sub> -Thin Films . . . . .	67
5.2 Replacing the RbF-PDT with an RbInSe <sub>2</sub> -Deposition . . . . .	72
<b>6 Interaction of an RbF-Conditioned Surface and the Buffer Layer</b>	<b>81</b>
6.1 Analysis of the ODC-Signature . . . . .	82
6.2 Impact of the PDTs on the CdS-Growth . . . . .	83
<b>7 Proposed Model of the Structural Effects of Rb in the Frame of Literature</b>	<b>89</b>
7.1 Interaction of Rb with Na and Point Defects in the CIGSe . . . . .	90
7.1.1 The Case of CGI = 0.90 . . . . .	90
7.1.2 Generalization to a CGI-Dependent Model . . . . .	92

7.2	Passivating Effects of Rb . . . . .	96
7.2.1	Passivation of Deep Defects . . . . .	96
7.2.2	Passivation of Shallow Defects . . . . .	97
7.2.3	Surface-Passivation . . . . .	97
7.3	Summary and Conclusions of Chapter 7 . . . . .	100
<b>8</b>	<b>Modeling the Mechanisms of the Rb-Conditioning by Device Simulations</b>	<b>101</b>
8.1	Setting up the Device Model . . . . .	101
8.1.1	The Reference Case . . . . .	101
8.1.2	Bulk Effects of Rb: Defects and Carrier Density . . . . .	104
8.1.3	Surface Effects of Rb: The RIS-Layer . . . . .	105
8.1.4	Defining the Interface Defects . . . . .	110
8.1.5	Interaction of the RIS-Layer and the Interface Defects . . . . .	112
8.1.6	Interface Effects of the Rb: Roll-Over . . . . .	116
8.2	Modeling the Rb-Conditioned Devices . . . . .	119
8.3	Evaluating the Device Model in Regard to Literature . . . . .	125
<b>9</b>	<b>Summary and Conclusions</b>	<b>127</b>
<b>A</b>	<b>Appendix</b>	<b>131</b>
A.1	Electrostatic Potential Fluctuations - Data taken from Publication [10] . . . . .	131
A.2	Additional XRD-Diffractograms to Section 5.1 . . . . .	132
A.3	Input-Parameter Sets for the Simulations in Chapter 8 . . . . .	132
A.4	Additional Simulations to Chapter 8 . . . . .	136
	<b>Bibliography</b>	<b>140</b>
	<b>Acknowledgments</b>	<b>161</b>
	<b>Curriculum Vitae</b>	<b>163</b>

# Nomenclature

$A_{Dev}$	Area of the Device	$\Delta V_{OC}$	$V_{OC}$ -Deficit
$A_S$	Spot Size of the trPL Laser	$\Delta V_{OC}^{CV}$	$V_{OC}$ -Losses due to Non-Optimal Doping of the Absorber Layer
$\alpha$	Absorption Coefficient		
$\alpha'(x, y)$	Modified Auger Parameter of the Core Level Peak $x$ and the Auger Peak $y$	$\Delta V_{OC}^{el}$	$V_{OC}$ -Losses due to Electrostatic Potential Fluctuations
AM	Air Mass	$\Delta V_{OC}^U$	$V_{OC}$ -Losses due to Tail States in the Bandgap
APT	Atom Probe Tomography	$\Delta V_{OC}^{rem}$	$V_{OC}$ -Losses due to Non-Radiative Recombination that are not Included in $\Delta V_{OC}^{el}$ and $\Delta V_{OC}^{CV}$
ARC	Anti-Reflective Coating		
$B$	Constant of the Radiative Recombination Rate	$\Delta V_{OC}^{nrad}$	$V_{OC}$ -Losses due to Non-Radiative Recombination
$C$	Capacitance	$\Delta V_{OC}^{rad}$	$V_{OC}$ -Losses due to Radiative Recombination
$c$	Speed of the Light in Vacuum		
CBD	Chemical Bath Deposition	$\Delta V_{OC}^{SC}$	$V_{OC}$ -Losses due to Optical Losses via Imperfect Absorption
CBM	Conduction Band Minimum		
$CGI$	Ratio of $\chi_{Cu}$ to $\chi_{Ga} + \chi_{In}$	$\Delta V_{OC}^{SQ}$	$V_{OC}$ -Losses within the Shockley-Queisser-Model
$\chi_i$	Molar Fraction of Element $i$	DFT	Density Functional Theory
CIGSe	$Cu(In,Ga)Se_2$	DOS	Density of States
CIGSSe	$Cu(In,Ga)(S,Se)_2$	$d_{SCR}$	Width of the Space Charge Region
CISE	$CuInSe_2$	$E$	Energy
$d$	Thickness of the Absorber Layer	$E_a$	Activation Energy
$D_{n/p}$	Diffusion Constant of the Electrons/Holes	$E_D$	Energetic Position of a Defect Level
$\Delta E_F$	Quasi Fermi Level Splitting	$E_{Def,B}$	Energetic Position of a Defect in the Bulk of a Layer
$\Delta H$	Formation Energy of a Doping Site	$E_{Def,IF}$	Energetic Position of a Defect at an Interface
$\Delta E_C$	Difference of the CBM of the CdS- and the RIS-Layer	$E_{F,i}$	Quasi Fermi Level of the Electrons ( $i = n$ ) or Holes ( $i = p$ )
$\Delta n$	Density of Generated Charge Carriers	$E_g$	Bandgap Energy

$E_{g,\min}$	Minimum Bandgap Energy	$j_0^{\text{el}}$	Saturation Current Density due to Electrostatic Potential Fluctuations
$E_g^{\text{PV}}$	"Photovoltaic Bandgap"		
$E_{\text{pass}}$	Pass-Energy	$j_0^{\text{nrad}}$	Saturation Current Density Including Radiative and Non-Radiative Recombination
$EA$	Electron Affinity		
EBIC	Electron Beam Induced Current	$j_0^{\text{rad}}$	Saturation Current Density in the Limit of Only Radiative Recombination
$E_g^{\text{SQ}}$	Bandgap Energy within the Shockley-Queisser-Model		
$E_U$	Urbach-Energy	$j_0^{\text{SQ}}$	Saturation Current Density within the Shockley-Queisser-Model
$\epsilon$	Permittivity		
$\epsilon_0$	Vacuum Permittivity	$j_{\text{rad}}$	Current Density of the Radiative Recombination
$EQE$	External Quantum Efficiency	$j_{\text{SC}}$	Short-Circuit Current Density
$FF$	Fill Factor	$A$	Diode Quality Factor
$FF_0$	$FF$ Without Resistive Losses	$j_{\text{SC}}^{\text{rad}}$	Short-Circuit Current Density in the Limit of Only Radiative Recombination
$\nu$	Frequency		
FWHM	Full Width at Half Maximum	$j_{\text{SC}}^{\text{SQ}}$	Short-Current Density in the Shockley-Queisser-Model
GB	Grain Boundary		
GD-OES	Glow Discharge Optical Emission Spectrometry	$j^{\text{SQ}}$	Current Density within the Shockley-Queisser-Model
$G_e$	Generation Rate of the Electrons	$j_{\text{diff}}$	Density of the Diffusion Current
$GGI$	Ratio of $\chi_{\text{Ga}}$ to $\chi_{\text{Ga}} + \chi_{\text{In}}$	$j_{\text{drift}}$	Density of the Drift Current
GI	Grain Interior	$j_e$	Electron-Current
GIXRD	Gracing Incident X-Ray Diffraction	$j_{\text{Ph}}$	Photo Current Density
		$k$	Wavenumber
HAADF	High-Angle Angular Dark Field	$k_B$	$1,38064852(79) \cdot 10^{-23} \frac{\text{J}}{\text{K}}$ (Boltzmann's Constant)
HZB	Helmholtz-Zentrum Berlin	$L_{n/p}$	Diffusion Length of the Electrons/Holes
ILR	Infrared Light Reflectometry		
IMN	Institut des Matériaux Jean Rouxel in Nantes	$L_{\text{eff},n/p}$	Effective Collection Length of the Electrons/Holes
		$\lambda$	Wavelength
$j$	Current Density	LDA	Local Density Approximation
$j_0$	Saturation Current Density	LLS	Laser Light Scattering
$j_{00}$	Temperature-Independent Part of the Saturation Current Density	$\mu_{e,h}$	Mobility of the Electrons/Holes
		$n(x)$	Concentration of the Electrons

$N_{CV}$	Shallow Acceptor Density at the Edge of the Space Charge Region	$h$	$6.62607015 \cdot 10^{-34}$ Js (Planck's Constant)
$n_{CV}$	Minimum of the $N_{CV}$ -Profile, Representing the Intrinsic Carrier Density of the Absorber Layer.	$\Psi_{e,h}$	Chemical Potential of the Electrons/Holes
		PVD	Physical Vapor Deposition
$N_{Def}$	Defect Density	PV	Photovoltaic
		$Q$	Electric Charge
$n_i$	Intrinsic Carrier Density	$q$	$1,6021766208 \cdot 10^{-19}$ C (Elemental Charge)
$n_r$	Refractive Index		
$N_A$	Number of Acceptors	qFL	Quasi Fermi Level
$N_C$	Effective Density of States in the Conduction Band	QNR	Quasi-Neutral Region
		TR	Total Reflectance
$N_D$	Number of Donors	$R_{Auger}$	Recombination Rate of the Auger-Recombination
$\eta$	Power Conversion Efficiency		
$v_{th,e,h}$	Thermal Velocity of the Electrons/Holes	$R_{Def}$	Recombination Rate of the Defect-Related Recombination
		$R_{eff}$	Effective Recombination Rate
$v_{e,h}$	Electro-Chemical Potential of the Electrons/Holes	$R_P$	Parallel Resistance
		$R_{Rad}$	Recombination Rate of the Radiative Recombination
ODC	Ordered Defect Compound		
$P$	Power		
$\phi$	Electrostatic Potential	$R_S$	Series Resistance
		$R_{SRH}$	Rate of the Shockley-Read-Hall Recombination
$p(x)$	Concentration of the Holes		
$p_a$	Absorption-Probability of a Photon Generated by Radiative Recombination in the Solar Cell	$R_e$	Recombination Rate of the Electrons
$p_e$	Emission-Probability of a Photon Generated by Radiative Recombination in the Solar Cell	$\rho$	Charge Density
		RIS	RbInSe <sub>2</sub>
$p_r$	Probability of a Photon Generated by Radiative Recombination in the Solar Cell to be Re-Absorbed in the Cell	$S_{n/h,IF}$	Recombination Velocity at the Heterointerface
		SCAPS	Solar Cell Capacitance Simulator
PDT	Post Deposition Treatment	SCR	Space Charge Region
$\Phi_{bb}$	Photon Flux of a Black Body	SEM-EDX	Energy-Dispersive X-Ray Spectroscopy Using a Scanning Electron Microscope
$\Phi_{BC}$	Energetic Height of a Back-Contact Barrier		
$\Phi_{lum}$	Luminescence Flux	$\sigma_{E_g}$	Standard Deviation of the Distribution of Bandgap Energies
		$\sigma_{e,h}$	Capture Cross Section of the Electrons/Holes
$\Phi_{Sun}$	Photon Flux of the Spectrum of the Sun		

$\sigma_{el}$	Gaussian Energy Width of the Distribution of Electrostatic Potential Fluctuations	trPL	Time-Resolved Photoluminescence
$\sigma_{n,p}$	Capture Cross Section of the Electrons/Holes	$V$	Voltage
SP	Stoichiometry Point	$V_{OC}$	Open-Circuit Voltage
SRH	Shockley-Read-Hall	$V_{OC}^{nrad}$	Open-Circuit Voltage Including Radiative and Non-Radiative Recombination
STEM	Scanning Transmission Electron Microscopy	$V_{OC}^{rad}$	Open-Circuit Voltage Within the Limit of Only Radiative Recombination
$T$	Temperature		
$t$	Time	$V_{OC}^{real}$	Open-Circuit Voltage Measured in a Real Device
$TT$	Total Transmission		
$T_c$	Temperature of the Solar Cell	$V_{OC}^{SQ}$	$V_{OC}$ Within the Shockley-Queisser-Model
$t_{CBD}$	Duration of the CdS-Deposition	$V_i$	Vacancy on an i-Site in the Crystal Lattice
$t_{PDT}$	Duration of the RbF-PDT		
$T_{Sub}$	Substrate Temperature	$V_{bi}$	Diffusion- or Built-In Voltage
$\tau$	Carrier Lifetime	VBM	Valence Band Maximum
$\tau_{Auger}$	Lifetime of the Auger-Recombination	VSCS	Valved Selenium Cracker Source
$\tau_{Def}$	Lifetime of the Defect-Related Recombination	WCT	Wet Chemical Treatment
$\tau_{eff}$	Effective Lifetime	$x$	Position
$\tau_{exp}$	Experimentally Measured Lifetime	$x_{n,p}$	Expansion of the SCR into the $n$ -/ $p$ -side of the Heterojunction
$\tau_{Rad}$	Lifetime of the Radiative Recombination	XPS	X-Ray Photoelectron Spectroscopy
TEM	Transmission Electron Microscopy	XRF	X-Ray Fluorescence Spectroscopy

## List of Publications

- [1] T. Kodalle, M. D. Heinemann, D. Greiner, H. A. Yetkin, M. Klupsch, C. Li, P. A. van Aken, I. Lauermaun, R. Schlatmann, C. A. Kaufmann. Elucidating the Mechanism of an RbF Post Deposition Treatment in CIGSe Thin Film Solar Cells. *Solar RRL*, 2(9): 1800156, 2018.
- [2] T. Kodalle, R. Kormath Madam Ragupathy, T. Bertram, N. Maticiuc, H. A. Yetkin, R. Gunder, R. Schlatmann, T. D. Kühne, C. A. Kaufmann, H. Mirhosseini. Properties of Co-Evaporated RbInSe<sub>2</sub> Thin Films. *physica status solidi (RRL)-Rapid Research Letters*, 13: 1800564, 2019.
- [3] T. Kodalle, L. Choubrac, L. Arzel, R. Schlatmann, N. Barreau, C. A. Kaufmann. Effects of KF and RbF Post Deposition Treatments on the Growth of the CdS Buffer Layer on CIGSe Thin Films - a Comparative Study. *Solar Energy Materials and Solar Cells*, 200: 109997, 2019.
- [4] T. Kodalle, T. Bertram, R. Schlatmann, C. A. Kaufmann. Effectiveness of an RbF Post Deposition Treatment of CIGSe Solar Cells in Dependence on the Cu-Content of the Absorber Layer. *IEEE Journal of Photovoltaics*, 9(6): 1839-1845, 2019.
- [5] T. Kodalle, D. Greiner, V. Brackmann, K. Prietzel, A. Scheu, T. Bertram, P. Reyes- Figueroa, T. Unold, D. Abou-Ras, R. Schlatmann, C. A. Kaufmann, V. Hoffmann. Glow Discharge Optical Emission Spectrometry for Quantitative Depth Profiling of CIGSe Thin-Films. *Journal of Analytical Atomic Spectrometry*, 34: 1233–1241, 2019.
- [6] T. Kodalle, C. A. Hsu, T. Bertram, N. Maticiuc, J. Lauche, I. Kafedjiska, I. Lauermaun, R. Schlatmann, C. S. Ferekides, C. A. Kaufmann. Reducing Air- and Moisture-Induced Degradation of Cu(In,Ga)Se<sub>2</sub> Absorber Layers for Thin Film Solar Cells by RbCl Treatment. *Proceedings of the 46th IEEE Photovoltaic Specialists Conference*, pp. 159-164, 2019.
- [7] M. D. Heinemann, T. Kodalle, C. Hages, M. Klupsch, D. Greiner, L. Korte, S. Levenco, T. Unold, R. Schlatmann, C. A. Kaufmann. Evaluation of Recombination Losses in Thin Film Solar Cells Using an LED Sun Simulator - the Effect of RbF Post-Deposition on CIGSe Solar Cells. *EPJ Photovoltaics*, 9(9): 1-6 2018.
- [8] N. Maticiuc, T. Kodalle, J. Lauche, R. Wenisch, T. Bertram, C. A. Kaufmann, I. Lauermaun. In vacuo XPS Investigation of Cu(In,Ga)Se<sub>2</sub> Surface After RbF Postdeposition Treatment. *Thin Solid Films*, 665: 143–147, 2018.
- [9] T. Bertram, J. Lauche, T. Kodalle, H. A. Yetkin, M. D. Heinemann, R. Schlatmann, C. A. Kaufmann. RbF-PDT Induced Sodium Displacement in Cu(In,Ga)Se<sub>2</sub> Absorbers Grown Under High Substrate Temperatures. *Proceedings of the IEEE 7th World Conference on Photovoltaic Energy Conversion*, pp. 109–113, 2018.
- [10] M. Guc, T. Kodalle, R. Kormath Madam Ragupathy, H. Mirhosseini, T. D. Kühne, I. Becerril-Romero, A. Perez-Rodriguez, C. A. Kaufmann, V. Izquierdo-Roca. Vibrational properties of RbInSe<sub>2</sub>: Raman scattering spectroscopy and first principle calculations, *The Journal of Physical Chemistry C*, 124(2):1285-1291, 2019.
- [11] A. Vilanueva-Tovar, T. Kodalle, C. A. Kaufmann, R. Schlatmann, R. Klenk. Limitation of Current Transport across the Heterojunction in Cu(In,Ga)Se<sub>2</sub> Solar Cells Prepared with Alkali Fluoride Postdeposition Treatment , *Solar RRL*, *Early View* - DOI: 10.1002/solr.201900560, 2020.
- [12] A. Nikolaeva, M. Krause, N. Schäfer, W. Witte, D. Hariskos, T. Kodalle, C. A. Kaufmann, N. Barreau, J. A. Marquez Prieto, S. Levenco, T. Unold, D. Abou-Ras. Electrostatic Potential Fluctuations and Light-Soaking Effects in Cu(In,Ga)Se<sub>2</sub> Solar Cells, *Submitted to Progress in Photovoltaics: Research and Applications*, 2019.



# 1 Introduction

The global need for clean and renewable energy production has finally made its way to the forefront of social and political agendas [13–15]. For decades now, scientists, green parties, environmental activists and NGOs have made significant efforts to raise awareness for the environment's critical state of endangerment that we, as a society, must take responsibility for. The high use of nonrenewable energy sources has clear and direct implications for the environment and the overall health of the human population; effects include air and water pollution, climate change, extinction of species, excessive waste production, and other harmful factors. Not until more recently, the upcoming generation took an active stand to enforce the urgency of these topics upon current media and political power [16]. Although some still ignore or refuse to acknowledge obvious signs of climate change [17–20], there has been a shift in the political direction towards clean energy supply, that will continue to be even more of a crucial aspect in future debates.

As the international debate continues, it is imperative that science and technology actively work to research and find technical solutions for the rising demand for green energy. The scientific community, when cohesively working with the industries invested in energy conservation, now has the opportunity to influence, not only the public discussion [21] but hopefully also the market itself. In technologies that work to provide renewable energies, cost efficiency is the overall decisive factor that can accelerate the willingness of corporations and investors world-wide to invest. By improving the (cost) efficiency of established and emerging technologies, the 'invisible hand of the market' may be pushed in the right direction.

All pertinent models predict that the future energy demand must be met by a variety of different renewable energies which include wind, solar, water power, bio mass, and others [22–28]. And even though the share of solar energy in the total global electricity generation today is just about 2% [29], most simulations predict solar energy as one of the major resources in the future [22–24, 26–28]. Despite the obvious restrictions such as the yield-dependence on region and its span of sunlight exposure, electricity produced by photovoltaic (PV) systems has several advantages. These include its adaptability and compatibility in various locations as well as easy fabrication, installation, and maintenance requirements. These systems can act as reliable energy resources in de-centralized applications, power-plants, and new and existing constructions (e.g. buildings, outdoor and handheld equipment). Furthermore, PV displays a positive trend in cost efficiency [30] and even today shows leveled cost of efficiencies (LCOEs) on the same level as the LCOE of the conventional electricity mix [31]. Already today in many regions solar energy is even the cheapest source of energy [32], and is continuing to steadily decrease in price globally [30]. As a direct result, the overall annual newly installed capacity of solar is constantly increasing and predicted to reach the  $TW_p$ -scale within the next decade [26, 28, 31, 33, 34].

Although the PV market is still dominated by panels based on crystalline silicon, it is imperative to establish diversity in the market in order to be able to adapt to different appliances and react to unpredictable events as e.g. bottlenecks in supply. Therefore, polycrystalline thin film PV is not only a promising candidate for niche products such as flexible modules and space applications but also for mass production.

Within the polycrystalline compound semiconductor thin film techniques, solar cells based on CdTe and Cu(In,Ga)(S,Se)<sub>2</sub> (CIGSSe) are the most promising candidates, possibly accompanied in the future by the emerging technology of the so-called perovskite solar cells [35]. CIGSSe exhibits the highest conversion efficiency ( $\eta$ ) and the lowest amount of toxic material used in the devices based on these three material groups, therefore proving high market

potential [34, 35]. To improve cost-efficiency, and in turn, the market potential, emphasis must be placed on increasing the power conversion efficiency of CIGSSe. The current world record efficiency of 23.4% [36] is still significantly lower than the theoretical limit of approximately 33% for a single junction solar cell, according to Shockley and Queisser [37] (although achieving this goal is improbable, as discussed in Chapter 2). The primary limiting factor for CIGSSe-based devices is the open-circuit voltage,  $V_{OC}$  [38]. By using process optimization, many improvements of the efficiency have been and still can be made. However, it is important to generally understand the mechanisms driving these improvements in order to be able to further adapt the development of the technology to production technologies. Recently, the main driving force for CIGSSe's efficiency improvement is the implementation of heavy alkali-fluoride post deposition treatments (PDTs), which account for significant new record efficiencies, increasing from 20.3% to 23.4% [36, 39], mainly by improving the  $V_{OC}$ . As a result, the highest efficiencies of CIGSSe grown by thermal co-evaporation, are achieved by an RbF-PDT [40], while the highest efficiency of sequentially processed CIGSSe (and the highest overall  $\eta$ ) are achieved by a CsF-PDT [36].

The aim of the present work is to understand the effects of the RbF-PDT on thermally co-evaporated  $\text{Cu}(\text{In,Ga})\text{Se}_2$  (CIGSe) absorber layers, as well as the resulting devices. It is important to not only analyze the optimization of the PDT-procedure but also to understand its mechanism, as not all effects act positively on the efficiency of the solar cell [1, 41]. By understanding the fundamental mechanisms, the PDT-procedure can be further adapted to variations of additional properties due to parallel research in other fields of the CIGSe absorber layer and/or other components of the solar cell such as changes in the buffer and window layer technology. In order to improve the understanding of the mechanisms involved in RbF-conditioning of CIGSe absorber layers, the following aspects will be addressed in the different chapters of this thesis:

In Chapter 2 the fundamental physics of a solar cell, the specific characteristics of a CIGSe solar cell, and the avoidable and un-avoidable loss-mechanisms of solar cells will be presented and discussed. The latter will be useful to understand the mechanisms via which an RbF-treatment can improve the quality of the device, i.e. reduce its losses. Furthermore, a literature review about the history and development of alkali metals in CIGSe absorber layers will be given.

Chapter 3 contains the experimental procedure of the deposition of the analyzed thin films and devices discussed within this thesis, as well as a brief description of the characterization techniques used.

Starting with Chapter 4, the experimental results will be presented and discussed based on literature: firstly, the analysis of the effects of an RbF-PDT on the bulk and the surface properties of the absorber layer as well as their dependence on the composition of the CIGSe.

In Chapter 5 the formation of possible secondary phases will be analyzed and the most likely candidate (based on DFT-calculations and experimental data),  $\text{RbInSe}_2$ , is identified. Subsequently, for the first time  $\text{RbInSe}_2$ -thin films are deposited and their physical properties analyzed. Furthermore,  $\text{RbInSe}_2$  will be directly deposited onto absorber layers in order to compare these samples with those that were RbF-treated.

After identifying and analyzing the effects of the RbF-conditioning on the absorber layer, its impact on the subsequently deposited buffer layer will be studied in Chapter 6.

In Chapter 7, the experimental results of this thesis will be summarized and – together with data from literature – used to propose a model for the structural and optoelectronic effects of the Rb-conditioning on the properties of the absorber layer on a microscopic scale.

In Chapter 8 all these results will be combined and a device model integrating the newly characterized  $\text{RbInSe}_2$ -layer will be presented using one-dimensional device simulations in order to provide a comprehensive device model of the effects of Rb in CIGSe.

In Chapter 9, a summary of the main findings and conclusions will be given.

## 2 Fundamentals

In the first section of this chapter, the basic principles of a CIGSe solar cell are described briefly. The main focus of this chapter lies on an analysis of the loss mechanisms that reduce the main PV-parameters, i.e. the short-circuit current density ( $j_{SC}$ ), the  $V_{OC}$  and the fill factor ( $FF$ ). These thoughts are generally valid but will be adapted to the special case of CIGSe based solar cells. The loss mechanisms are of special interest for this thesis, since – as it is shown in Section 2.3 – conditioning the CIGSe absorber layer with Rb leads to reduced losses. Therefore one has to understand the loss mechanisms first in order to be able to analyze how the RbF-conditioning is improving the quality of the devices. A more detailed study about the general physics of chalcogenide-based solar cell devices can be found in Reference [42].

The second section of this chapter gives a short overview of the crystal structure and the defect physics in CIGSe and in Section 2.3 the state of knowledge about the effects of some alkali metals (Na, K, and Rb) in CIGSe solar cells is presented and discussed.

### 2.1 Physics of a (CIGSe) Solar Cell

#### 2.1.1 Basics of a CIGSe Solar Cell

The heart of a CIGSe solar cell is the name-giving  $\text{Cu}(\text{In,Ga})\text{Se}_2$  absorber layer. This (in most cases) polycrystalline compound semiconductor is intrinsically  $p$ -type (see Section 2.2). Due to its direct bandgap and the correspondingly high absorption coefficient in the order of magnitude of about  $10^5 \text{ cm}^{-1}$  to  $10^6 \text{ cm}^{-1}$  [43], rather thin (order of magnitude of  $1 \mu\text{m}$ ) CIGSe layers can sufficiently absorb the majority of the incident photons with energies above its bandgap energy  $E_g$ . During the absorption process, an incoming photon creates an electron-hole pair in the absorber layer. The electron is excited into the conduction band and then spatially separated from the corresponding hole in the valence band in order to extract a current from the device. The driving force for this charge separation is given by the formation of a  $p$ - $n$ -junction with an  $n$ -type multilayer consisting of the so-called buffer layer and a transparent conductive oxide (see Figure 2.1) on the front side of the absorber layer (facing the incident light) and a metallic contact at the back side of the absorber layer. In the following the working principle of such a  $p$ - $n$ -junction and its use in a solar cell will be explained shortly, starting with the  $p$ - $n$ -junction without illumination, i.e. in dark.

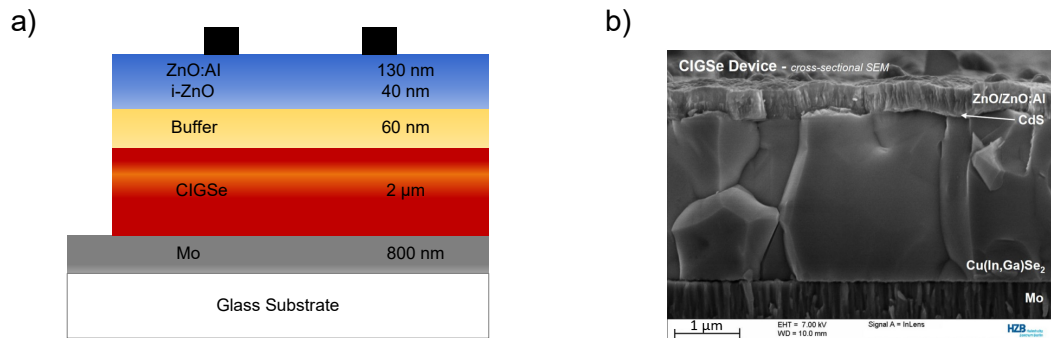


**Figure 2.1:** a) Schematic representation of a CIGSe device as it is used in the present work. b) Scanning electron microscope (SEM) image of a cross section of a CIGSe device fabricated at HZB.

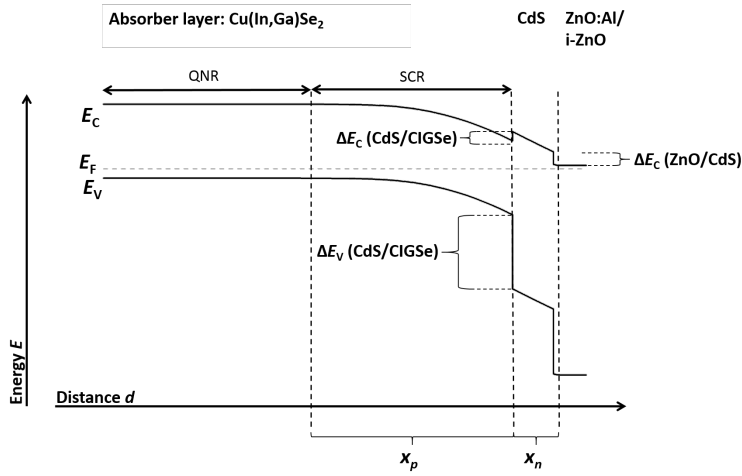


**Abbildung 2.2:** Energy band diagram of the CIGSe/CdS/i-ZnO/ZnO:Al heterostructure without illumination at zero applied bias.

The fact that on the  $p$ -side of the junction there is a high density of free holes, while there is a high density of free electrons on the  $n$ -side, leads to the development of two, opposing currents: the drift current (caused by the different electric potentials in the differently doped sides of the heterojunction) and the diffusion current (caused by the different particle concentrations on both sides) [44]:

$$j_{\text{diff}} = n(x)\mu_e \nabla \psi_e - p(x)\mu_h \nabla \psi_h, \quad (2.1)$$

$$j_{\text{drift}} = n(x)\mu_e \nabla (-q\phi) - p(x)\mu_h \nabla (q\phi), \quad (2.2)$$

$$\Rightarrow j = j_{\text{diff}} - j_{\text{drift}} = n(x)\mu_e \nabla v_e - p(x)\mu_h \nabla v_h. \quad (2.3)$$

Here  $\mu_{e,h}$  are the mobilities and  $n(x)$  and  $p(x)$  the position-dependent concentrations of the electrons and holes,  $q$  is the elementary charge,  $\phi$  the electric potential, and  $\psi_i = \psi_{i,0} + k_B T \ln \frac{n_i}{N_C}$  the chemical potential, with the Boltzmann constant  $k_B$ , the temperature  $T$ , and  $N_C$  as the effective density of states in the conduction band. In Equation 2.3 the electrical and chemical potential are combined via  $v_e = \psi_e - q\phi$  and  $v_h = \psi_h + q\phi$ .

The  $j_{\text{diff}}$  can be interpreted as diffusion of free electrons from the  $n$ -side into the CIGSe layer, where they recombine with holes of the  $p$ -type CIGSe leaving behind positively charged ions on the  $n$ -side and negatively charged ions on the  $p$ -side giving rise to  $j_{\text{drift}}$ . Once an equilibrium of both currents is established, the so called space charge region (SCR) is formed at the heterojunction and the Fermi energy is flat within the heterostructure. This leads to a bending of the conduction band minimum (CBM) and valence band maximum (VBM) on both sides of the heterojunction. This situation is shown in Figure 2.2. With use of the permittivity  $\epsilon_x$  of layer  $x$ , and the vacuum permittivity  $\epsilon_0$ , the variation of the macroscopic potential  $\phi(x)$  within the SCR can be connected with the charge density  $\rho(x)$  caused by  $N_D$  (number of donors) and  $N_A$  (number of acceptors) via the Poisson equation:

$$\frac{\partial^2 \phi(x)}{\partial x^2} = -\frac{\rho(x)}{\epsilon_x \epsilon_0}. \quad (2.4)$$

The width of the SCR is dependent on the doping densities on both sides of the heterojunction and can be expressed as

$$d_{\text{SCR}} = x_n + x_p = \sqrt{\frac{\epsilon_n \epsilon_p \epsilon_0 V_{\text{bi}}}{q} \frac{N_A + N_D}{N_A N_D}} \quad (2.5)$$

with  $x_{n,p}$  as the expansion of the SCR in the  $n$ - and the  $p$ -type part, and  $V_{bi}$  the diffusion voltage or built-in voltage. In particular, it can be shown [44] that

$$\frac{x_n}{x_p} = \frac{N_A}{N_D}. \quad (2.6)$$

These determinations of the width of the SCR are only valid for simple  $n/p$ -heterojunctions, though. The heterojunction in CIGSe devices is more complicated since it consists of three layers – the absorber, the buffer, and the window layer – in a  $p/n/n^+$ -configuration. Considering the rather low doping density and layer thickness of the CdS buffer layer [45], it is assumed that it is completely depleted meaning that the expansion of the SCR into the buffer layer equals the thickness of the buffer layer,  $d_{SCR}^{CdS} = d_{CdS}$ . Assuming the absence of interface charges, the expansion of the SCR into the absorber layer can be described by [42]:

$$d_{SCR}^{CIGSe} = -\frac{\epsilon_{CIGSe} d_{CdS}}{\epsilon_{CdS}} + \sqrt{\left(\frac{\epsilon_{CIGSe} d_{CdS}}{\epsilon_{CdS}}\right)^2 + \frac{2\epsilon_{CIGSe}}{q^2 N_A} \left[ qV_{bi} + \frac{q^2 N_{D,CdS} d_{CdS}^2}{2\epsilon_{CdS}} \right]}. \quad (2.7)$$

If a perturbation is applied to the system (e.g. an external voltage  $V$ , illumination of the device, or both) the current flow is limited by the flow of minority charge carriers (electrons in the absorber layer, holes in the window layer). The (one-dimensional) electron current  $j_e$  in the absorber layer is given by the continuity equation:

$$\frac{\partial n(x)}{\partial t} = G_e - R_e - \frac{1}{q} \frac{dj_e(x)}{dx} = 0, \quad (2.8)$$

in which  $t$  is the time,  $G_e$  is the generation rate, and  $R_e$  the recombination rate of the electrons. The full current is described by the Shockley equation [46]:

$$j = j_e + j_h = j_0 \cdot \left[ \exp\left(\frac{eV}{k_B T}\right) - 1 \right] = j_{00} \cdot \exp\left(-\frac{E_a}{k_B T}\right) \cdot \left[ \exp\left(\frac{eV}{k_B T}\right) - 1 \right] \quad (2.9)$$

or in case of an illuminated device

$$j = j_{00} \cdot \exp\left(-\frac{E_a}{k_B T}\right) \cdot \left[ \exp\left(\frac{eV}{k_B T}\right) - 1 \right] - j_{Ph}. \quad (2.10)$$

Here  $j_0$  is the saturation current density resulting from the (in this case only radiative) recombination of charge carriers,  $j_{00}$  the temperature-independent part of the saturation current density,  $E_a$  the activation energy of the temperature-dependence of  $j_0$ , and  $j_{Ph}$  the photo current density due to the electron-hole pairs that are generated during illumination.

Since during illumination additional carriers are excited, the device is not longer in thermodynamic equilibrium. After thermalization of the excited charge carriers, they fill states in the CB (for electrons, VB for holes) and therefore change the total distribution of both electrons and holes, in the absorber layer. In order to account for the fact that both the electron density and the hole density, increase at the same position and point in time, one has to introduce separate Fermi energies to accurately describe the device, the quasi Fermi levels (qFLs). Using the Boltzmann-approximation, the density of holes in the VB and the density of electrons in the CB can be described by

$$n = N_C \exp\left(-\frac{E_C - E_{F,n}}{k_B T}\right) \quad (2.11)$$

and

$$p = N_V \exp\left(-\frac{E_{F,p} - E_V}{k_B T}\right). \quad (2.12)$$

Here  $E_{F,i}$  are the qFLs of the electrons ( $i = n$ ) and holes ( $i = p$ ). The qFLs are useful instruments to provide descriptive expressions of the mechanisms in a solar cell under illumination. For example, they can be used to rewrite equation 2.3 [44]:

$$j = n(x)\mu_e \nabla E_{F,n} + p(x)\mu_h \nabla E_{F,p}, \quad (2.13)$$

representing the full current in the solar cell as a combination of electron and hole current rather than as drift and diffusion current. Furthermore, the so called qFL-splitting, i.e.  $\frac{1}{q}(E_{F,n} - E_{F,p}) = \Delta E_F/q$ , is an upper limit for the  $V_{OC}$  of the solar cell, as will be discussed in more detail in Section 2.1.3.

### 2.1.2 Recombination Mechanisms

Before the limitations of real (CIGSe) solar cell devices will be discussed in a more general matter in Section 2.1.3, the different ways of charge carrier recombination are briefly discussed in this section.

Electrons, which were promoted to the CB by an incident photon, are in a metastable state and eventually will release their additional energy striving to relax to the lowest possible energetic state. In order to arrive in that state they have to get back to a free state in the VB, i.e. annihilate with a hole – the electron-hole pair recombines. The probability for a charge carrier to recombine depends on the number of generated carriers, i.e. the difference of the charge carrier densities from the respective equilibrium densities. For an electron, therefore, the excess carrier density is introduced (analog for holes):

$$\Delta n = n - n_0, \quad (2.14)$$

with  $n_0$  being the equilibrium electron density. Generally, there are three types of recombination: radiative band to band recombination, defect-assisted recombination, and Auger recombination.

A measure to judge the relevance of each recombination mechanism for a given type of solar cell is the recombination rate of the carriers  $R_i$ , and the corresponding carrier lifetime  $\tau_i$ , which marks the duration after which the amount of generated carriers is decreased to  $\frac{1}{e}$  of the initial value (here  $i$  marks the recombination mechanism). Obviously, all three mechanisms happen at the same time, resulting in an effective recombination rate and carrier lifetime:

$$R_{\text{eff}} = R_{\text{Rad}} + R_{\text{Auger}} + R_{\text{Def}}, \quad (2.15)$$

$$\frac{1}{\tau_{\text{eff}}} = \frac{1}{\tau_{\text{Rad}}} + \frac{1}{\tau_{\text{Auger}}} + \frac{1}{\tau_{\text{Def}}}. \quad (2.16)$$

Hereby the carrier lifetime can be defined by using the continuity equation, from which follows

$$\frac{d}{dt} \Delta n(t) = -\frac{\Delta n}{\tau_{\text{eff}}}, \quad (2.17)$$

if recombination and generation are not in equilibrium and one assumes that  $\tau_{\text{eff}}$  is constant. It furthermore follows

$$\Delta n(t) = \Delta n(t=0) \cdot \exp\left(-\frac{t}{\tau_{\text{eff}}}\right). \quad (2.18)$$

Since Auger-recombination is only relevant in case of very high carrier densities [47–49], which is usually not the case in CIGSe-based devices [42], this process will not be further discussed here and  $1/\tau_{\text{Auger}}$  will be neglected.

Generally, the carrier lifetime can be connected with the diffusion length of the carriers on the respective other side of the  $p$ - $n$ -junction:

$$L_{n/p} = \sqrt{D_{n/p} \tau_{\text{eff},n/p}} \quad (2.19)$$

with  $D_{n/p}$  as the diffusion constant, which is proportional to the mobility of the respective carrier type. Assuming that all carriers that reach the SCR will be collected, the effective collection length can be derived:

$$L_{\text{eff},n/p} = d_{\text{SCR}}^{\text{CIGSe}} + L_{n/p}. \quad (2.20)$$

Although this assumption is generally not valid for CIGSe solar cells, the property  $L_{\text{eff}}$  can still be an interesting measure to compare similar devices.

### Radiative Recombination

Radiative recombination is the inevitable direct recombination of an electron located in the CB and a hole located in the VB. The energy-loss of the electron is emitted in form of a photon. There are three options for this photon once it is generated in the absorber layer [49]: it can be emitted (and then detected, probability  $p_e$ ), it can be parasitically absorbed e.g. by defect states in the buffer layer or the contact (probability  $p_a$ ), or it can be reabsorbed by the absorber layer re-inducing the whole process [50] (probability  $p_r$ ). The recombination rate for radiative recombination is only dependent on the number of electrons in the CB, the number of holes in the VB, the intrinsic carrier density  $n_i$  and a material constant  $B$  [42]:

$$R_{\text{rad}}(x) = B \cdot (n(x) \cdot p(x) - n_i^2). \quad (2.21)$$

Assuming a  $p$ -type semiconductor in low injection (number of generated carriers  $\Delta n$  is smaller than the intrinsic doping density) Equation 2.21 simplifies to [42]:

$$R_{\text{rad}}(x) = B \cdot N_A \cdot \Delta n = \frac{\Delta n}{\tau_{\text{Rad}}}. \quad (2.22)$$

Since the sum of the three photon-probabilities has to be 1, it can be further derived:

- the generation rate of the absorber layer illuminating itself:  $G_e = p_r \cdot R_{\text{rad}}$
- the radiative recombination current density:

$$j_{\text{rad}} = q \int_0^d (1 - p_r) R_{\text{rad}}(x) dx, \quad (2.23)$$

where  $d$  is the thickness of the absorber layer and  $x$  the position.

### Defect-Assisted Recombination

In CIGSe-based solar cells, the main recombination mechanism is non-radiative recombination via defects [42]. The case of recombination via a single defect level in the energy bandgap of the absorber layer is described in the work of Shockley, Read, and Hall [51, 52] (SRH-recombination). This recombination process is a two-step process; before the electron-hole pair is able to annihilate both have to be captured by the defect and have to be present in the defect level at the same point in time, i.e. the second particle has to 'arrive' in the defect level before the first one is re-emitted to the respective band. The latter process could be thermally or illumination-induced. Since the probability of an electron capture is highest for a defect level close to the CB and decreases the further the defect level shifts to the VB (and vice versa for the hole), defect levels close to the middle of the bandgap are most efficient SRH-recombination centers. Using the capture and emission rates for electrons and holes [42] one can derive the SRH-recombination rate:

$$R_{\text{SRH}} = \frac{np - n_i^2}{\left( n + N_C \exp\left(\frac{E_D - E_C}{k_B T}\right) \right) \tau_{\text{Def,h}} + \left( p + N_V \exp\left(\frac{E_V - E_D}{k_B T}\right) \right) \tau_{\text{Def,e}}}. \quad (2.24)$$

Here  $E_D$  is the energetic position of the defect level.

### 2.1.3 Loss Mechanisms: From 100% Energy Conversion to Real Devices

Obviously, the full conversion of the energy provided by the sun into electrical energy via illumination of a solar cell is not achievable. In the following, it will be shown how thermodynamic, optical and electrical factors reduce the theoretically maximum achievable conversion efficiency and which factors are practically hindering real CIGSe devices (single junctions) from reaching this maximum. Special attention will be paid to the losses in  $V_{OC}$  since the main effect of RbF-treatments is to improve exactly this property of the solar cell (cf. literature overview in Section 2.3). Figure 2.3 shows an overview of the unavoidable and avoidable losses reducing  $V_{OC}$  from  $E_g/q$  to the value measured in actual devices  $V_{OC}^{real}$ . This overview is based on the work published in References [38, 49, 53].

A first approach to a theoretical description of an upper limit for the power conversion efficiency of a solar cell based on thermodynamics was given by Shockley and Queisser in 1961 [37]. They provided a model (SQ-model) in which the conversion efficiency is only dependent on one single material parameter of the solar cell: the optical bandgap energy  $E_g$ . The main assumptions of the SQ-model are that the absorption function of an ideal solar cell is a Heaviside-function:  $H(E - E_g)$ , i.e. that every absorbed photon creates exactly 1 electron-hole pair, and that every generated charge carrier will be collected at one of the contacts of the solar cell. Therefore the short-circuit current density in the SQ-model can be written as

$$j_{SC}^{SQ}(E_g) = q \int_{E_g}^{\infty} \Phi_{Sun}(E) dE, \quad (2.25)$$

with  $\Phi_{Sun}$  as the photon flux due to the spectrum of the sun as it arrives at the solar cell (e.g. AM 1.5G). Next to the obvious losses of not absorbed photons with  $h\nu < E_g$  as well as thermalization losses of electrons with  $h\nu > E_g$ , the efficiency in the SQ-model is limited by two further factors. Here  $h$  is Planck's constant and  $\nu$  the frequency of the incident light.

Firstly, non-avoidable radiative recombination of the charge carriers: Following the principle of detailed balance, which states that thermal equilibrium can only be reached if a microscopic process is only permitted if the inverse process is allowed too [49, 54], the solar cell has to be treated as both an absorber and an emitter. Therefore the solar cell is treated

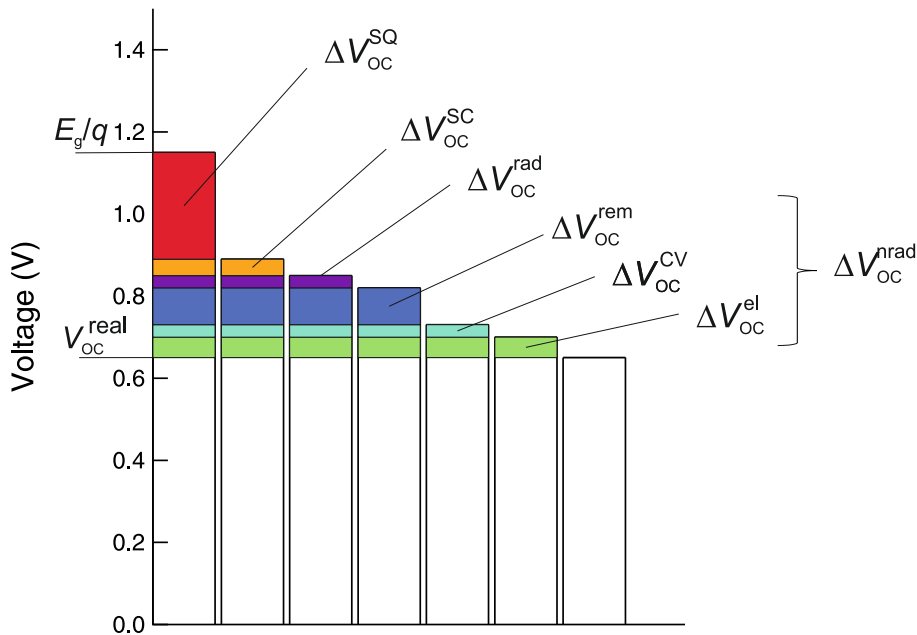


**Figure 2.3:** Unavoidable ( $\Delta V_{OC}^{SQ}$ ,  $\Delta V_{OC}^{SC}$ , and  $\Delta V_{OC}^{rad}$ ) and avoidable losses ( $\Delta V_{OC}^{rem}$ ,  $\Delta V_{OC}^{CV}$ , and  $\Delta V_{OC}^{el}$ ), which occur in all types of solar cells. The severity of each individual loss is estimated for the case of a typical CIGSe solar cell prepared at HZB (free of heavy alkali metals) with a bandgap energy of  $E_g \approx 1.15$  eV.

as black body at the temperature of the solar cell  $T_c$  with a corresponding spectrum of its photon flux  $\Phi_{\text{bb}}$ , and the luminescence flux  $\Phi_{\text{lum}}$  [49]:

$$\Phi_{\text{lum}} = \int_{E_g}^{\infty} (1 - p_r) \Phi_{\text{bb}}(E) dE \left( \exp\left(\frac{qV}{k_B T_c}\right) - 1 \right) \quad (2.26)$$

with [49]:

$$\Phi_{\text{bb}} = \frac{2\pi E^2}{h^3 c^2} \frac{1}{[\exp(E/k_B T) - 1]} \approx \frac{2\pi E^2}{h^3 c^2} \exp\left(\frac{-E}{k_B T}\right). \quad (2.27)$$

Here  $c$  is the speed of the light in vacuum. This radiative loss, which is accounted for by the saturation current density  $j_0^{\text{SQ}}$ , reduces the absolute value of the (negative) extractable current density to

$$\begin{aligned} j^{\text{SQ}}(E_g) &= j_0^{\text{SQ}}(E_g) \left( \exp\left(\frac{qV}{k_B T_c}\right) - 1 \right) - j_{\text{SC}}^{\text{SQ}}(E_g) \\ &= q \int_{E_g}^{\infty} (1 - p_r) \Phi_{\text{bb}}(E) dE \left( \exp\left(\frac{qV}{k_B T_c}\right) - 1 \right) - q \int_{E_g}^{\infty} \Phi_{\text{Sun}}(E) dE. \end{aligned} \quad (2.28)$$

The corresponding value of the  $V_{\text{OC}}$  in the SQ-model can be calculated from  $j^{\text{SQ}}(E_g, V = V_{\text{OC}}) = 0$  as:

$$V_{\text{OC}}^{\text{SQ}}(E_g) = \frac{k_B T_c}{q} \ln \left( \frac{j_{\text{SC}}^{\text{SQ}}(E_g)}{j_0^{\text{SQ}}(E_g)} + 1 \right). \quad (2.29)$$

The last loss mechanism in the SQ-model is the so-called isothermal dissipation [38, 55] that can occur during charge separation. It is referred to as 'isothermal' loss since it is assumed that during charge collection the charge carriers stay in the lowest possible energy state either at the VBM or the CBM [38] meaning that all of them are at the same temperature  $T_c$ . From a thermodynamic point of view, the same loss mechanism can be described as governed by a Boltzmann system that is striving for thermal equilibrium, which due to the finite difference of the temperatures of the device and the sun is furthermore governed by a Carnot efficiency. In other words, the isothermal dissipation accounts for the reduction of the energy of an electron-hole pair from  $E_g$  to  $qV$  (voltage difference between the contacts) due to un-avoidable heat-loss to the surroundings (Carnot-losses) and because of irreversible entropy generation (Boltzmann-loss) [55]. In Figure 2.4 these two losses are combined as 'isothermal' loss. The maximal attainable  $V_{\text{OC}}$  is not further reduced due to the isothermal dissipation loss but is still derived by Equation 2.29 [38]. However, one has to optimize the choice of the voltage the solar cell is operated at, in order to minimize the losses due to absorption and isothermal dissipation [38].

Although it is in principle possible, some of the idealizations of the SQ-model are impossible to achieve in real devices. Therefore restrictions to the optical, electrical, and thermal simplifications of the SQ-model have to be made for an accurate description of real solar cells:

### 1. Optical

For several reasons, such as the fact that layer thickness and absorption coefficient of any real material are finite, even a perfect crystal with a direct energy bandgap cannot fulfill the assumption of a step-like absorption function  $H(E - E_g)$ , i.e. an absorption of 0 below a sharp bandgap energy  $E_g^{\text{SQ}}$  and an

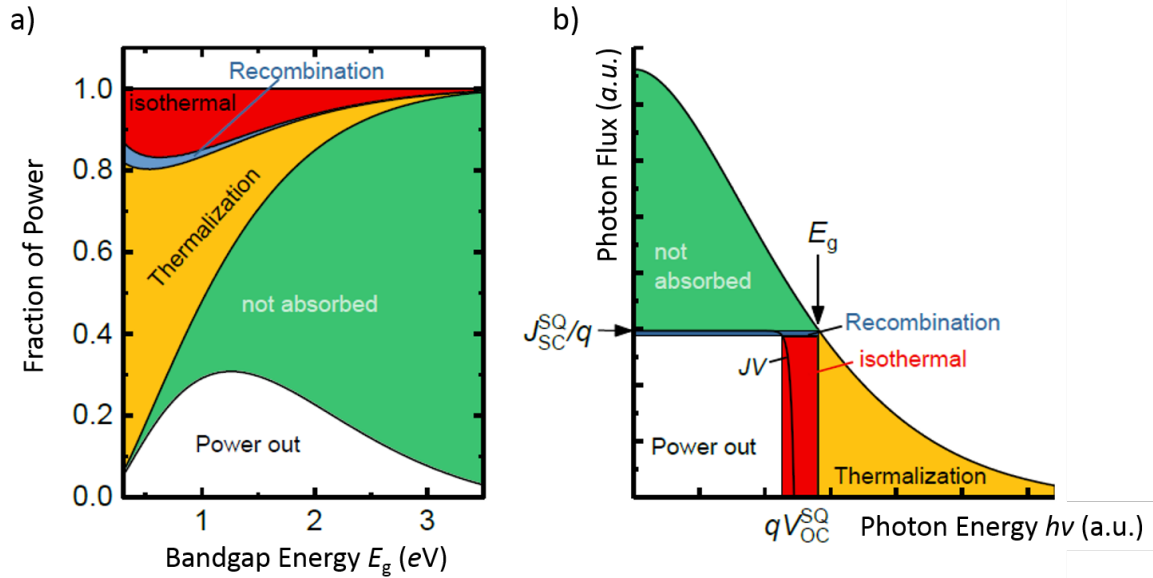


**Figure 2.4:** a) Schematic representation of the maximum output power as well as the different power loss mechanisms in the SQ-model as a function of the bandgap energy (always at the maximum power point, using a 5800 K black body spectrum normalized to  $100 \frac{\text{W}}{\text{cm}^2}$ ). b) Energy losses for a given bandgap energy in a representation of the photon flux versus the photon energy. If multiplying the y-axis with  $1/q$  and the x-axis with  $q$ , it can be read as a plot of current density versus voltage showing the optimal  $j$ - $V$ -curve for this  $E_g$  in the SQ-model. Both graphs are adapted from [38, 55].

absorption of 1 above it. In order to account for the imperfect absorption onset as well as its maximum value  $< 1$  one has to introduce the external quantum efficiency ( $EQE$ ) of the device into the Equations 2.25 to 2.28 [49, 56]:

$$j_{\text{SC}}^{\text{rad}} = q \int_0^{\infty} EQE(E) \cdot \Phi_{\text{Sun}}(E) dE, \quad (2.30)$$

$$j_0^{\text{rad}} = q \int_0^{\infty} (1 - p_r) \cdot EQE(E) \cdot \Phi_{\text{bb}}(E) dE = \frac{qR_{\text{rad}}}{n_r^2} \quad (2.31)$$

with  $n_r$  being the refractive index. Rau et al. [53] recently showed that the onset of the absorption spectrum (or the onset of the  $EQE$ ) of any given absorber material can be described by a Gaussian distribution of Heaviside-type bandgap energies  $P(E_g^{\text{SQ}}, \sigma_{E_g})$ , with  $\sigma_{E_g}$  being the standard deviation of the distribution:

$$EQE(E) = \int_0^{\infty} P(E_g) H(E - E_g) dE_g. \quad (2.32)$$

They further show that the derivative of the  $EQE$  equals  $P(E)$ , which means that the bandgap energy can be directly extracted from the  $EQE$ -measurement. The authors propose the use of a so called “Photovoltaic Bandgap” [53]:

$$E_g^{\text{PV}} = \frac{\int_a^b E_g P(E_g) dE_g}{\int_a^b P(E_g) dE_g}. \quad (2.33)$$

The choice of the integration limits  $a$  and  $b$  determines the width of the  $E_g$ -distribution. Replacing their SQ-counterparts in Equation 2.29 with these new

properties then gives a more accurate description for the open circuit voltage ( $V_{OC}^{\text{rad}}$ ):

$$V_{OC}^{\text{rad}}(E_g) = \frac{k_B T_c}{q} \ln \left( \frac{j_{SC}^{\text{rad}}(E_g)}{j_0^{\text{rad}}(E_g)} + 1 \right) \quad (2.34)$$

## 2. Electrical

The model considering radiative recombination, even though closer to a real device, is still neglecting non-radiative recombination, which is, in fact, the dominant recombination mechanism in CIGSe solar cells and is therefore increasing the recombination current by orders of magnitude compared to the radiative case [38, 49]. The introduction of non-radiative recombination (limited to SRH-recombination, as explained in the section above) further increases the saturation current density and decreases  $V_{OC}$  accordingly:

$$j_0^{\text{nrad}}(E_g, A) = j_{00} \exp \left( -\frac{E_a}{A k_B T} \right), \quad (2.35)$$

$$V_{OC}^{\text{nrad}}(E_g, A) = \frac{A k_B T_c}{q} \ln \left( \frac{j_{SC}(E_g)}{j_0^{\text{nrad}}(E_g)} + 1 \right). \quad (2.36)$$

Here  $j_{SC}$  is the actually measured short-circuit current density. The important change here compared to Equation 2.9 is the diode quality factor  $A$ , which usually lies in the range  $1 \leq A \leq 2$  and is dependent on the region of the non-radiative recombination (see Table 2.1). Note that these values change if one includes tunneling effects and defect distributions instead of single defect levels [42, 57].

In order to be able to account for the separate losses due to realistic absorption/radiative recombination and non-radiative recombination, Equation 2.36 can be rewritten in the following way [49, 53] using the approximation given in 2.27:

$$\begin{aligned} V_{OC}^{\text{nrad}} &\approx \frac{A k_B T_c}{q} \ln \left( \frac{j_{SC}}{j_0} \right) = \frac{A k_B T_c}{q} \ln \left( \frac{j_{SC}^{\text{SQ}}}{j_0^{\text{SQ}}} \cdot \frac{j_{SC}}{j_{SC}^{\text{SQ}}} \cdot \frac{j_0^{\text{SQ}}}{j_0^{\text{rad}}} \cdot \frac{j_0^{\text{rad}}}{j_0} \right) = \\ &= V_{OC}^{\text{SQ}} - \Delta V_{OC}^{\text{SC}} - \Delta V_{OC}^{\text{rad}} - \Delta V_{OC}^{\text{nrad}}. \end{aligned} \quad (2.37)$$

Here  $\Delta V_{OC}^{\text{SC}} \propto \ln(j_{SC}^{\text{SQ}}/j_{SC})$  accounts for the optical losses due to the more realistic description of the absorption,  $\Delta V_{OC}^{\text{rad}} \propto \ln(j_0^{\text{rad}}/j_0^{\text{SQ}})$  for the radiative and  $\Delta V_{OC}^{\text{nrad}} \propto \ln(j_0/j_0^{\text{rad}})$  the non-radiative recombination losses. Including losses within the SQ-model (due to thermalization and isothermal dissipation:  $\Delta V_{OC}^{\text{SQ}}$ ) this can be further generalized to

$$V_{OC}^{\text{nrad}} = V_{OC}^{\text{real}} \approx E_g/q - \Delta V_{OC}^{\text{SQ}} - \Delta V_{OC}^{\text{SC}} - \Delta V_{OC}^{\text{rad}} - \Delta V_{OC}^{\text{nrad}}. \quad (2.38)$$

Table 2.1: Value of the diode quality factor  $A$  in dependence of the region of recombination [42]. Here, it is  $\theta = \epsilon_{\text{CIGS}} N_{A,\text{CIGS}} / (\epsilon_{\text{CIGS}} N_{A,\text{CIGS}} + \epsilon_{\text{Buffer}} N_{D,\text{Buffer}})$ .

Recombination Region	Diode Quality Factor
SCR	$A = 2$
QNR	$A = 1$
Heterointerface	$1/(1 - \theta)$

Due to the fact that the mobility of the charge carriers in the device is not infinite, resistive losses have to be accounted for as well. Introducing a parallel ( $R_P$ ) and a series resistance ( $R_S$ ) to take the resistive losses parallel to the diode current (e.g. shunts) or in series (e.g. resistive losses in the TCO and the metal contacts) into account is mainly affecting the shape of the  $j$ - $V$ -curve (i.e. pronouncing the isothermal loss mechanism) and therefore reducing the  $FF$  of the device:

$$j = j_0 \cdot \left[ \exp \left( \frac{e(V - I \cdot R_S)}{Ak_B T} \right) - 1 \right] + \frac{V - I \cdot R_S}{R_P} - j_{Ph}. \quad (2.39)$$

### 3. Thermal

In real operating solar cells/modules, the operation temperature will not be in equilibrium with the surroundings. Due to the fact that recombination currents are thermally activated (see e.g. Equation 2.10), this deviation from temperature equilibrium will decrease all PV-parameters – and especially the  $V_{OC}$  – during actual operation. However, since all PV-parameters in this work are determined under standard test conditions, i.e.  $T_c = 298 \text{ K} = \text{const.}$ , these additional losses do not have to be considered here.

Although all  $V_{OC}$ -losses are included into the model described above, it is useful to further break down the recombination losses in order to be able to determine how the RbF-PDT is altering them. Therefore three effects contributing to the recombination losses will be discussed in more detail: the effects of a) inhomogeneities, b) sub-bandgap states as well as c) the carrier density in the absorber layer on the carrier recombination. Although all three are affecting radiative and non-radiative recombination, the influence on radiative recombination will be neglected, since in CIGSe solar cells non-radiative recombination is the main recombination path and the most dominant loss mechanism.

#### a) Inhomogeneities

In principle, one can distinguish between two types of spacial inhomogeneities: bandgap energy fluctuations due to fluctuations of the composition or strain, and electrostatic potential fluctuations. The former case can in principle just be included into the definition of the ‘average’ photovoltaic bandgap energy by adjusting the integration limits in Equation 2.33 accordingly and therefore has not to be accounted for separately. Furthermore, it was shown that the variation of the composition and the subsequent bandgap energy fluctuations in state-of-the-art CIGSe devices is small enough to be neglected [58, 59]. However, in case of large-area cells or modules bandgap energy fluctuations due to compositional gradients are likely to become relevant [60].

Electrostatic potential fluctuations can be caused by local variations of the distribution of charge densities e.g. due to dislocations, grain boundaries (GBs) or charged defects, which are inevitable in a polycrystalline and highly compensated semiconductor such as CIGSe [56, 58, 59]. It was discussed by Siebentritt [58] based on References [61–63] that especially random GBs can cause electrostatic potential fluctuations. A schematic illustration of the effect of these potential fluctuations is given in Figure 2.5.

While the bandgap energy is constant at every position in the semiconductor, the qFL-splitting is limited due to the fact that the qFLs can’t move into the bands at any position [58]. In other words, the local splitting of the qFLs is proportional to the local net doping density and the local lifetime [64, 65] ( $\Delta E_F \propto \ln(p, \tau_e)$ ), which means that electrostatic potential fluctuations in  $p$  directly lead to a reduction of  $\Delta E_{F,\text{max}}$  and therefore  $V_{OC}$  (see Figure 2.5). Note that both the probability of radiative recombination as well as of SRH-recombination, increase for a decreased

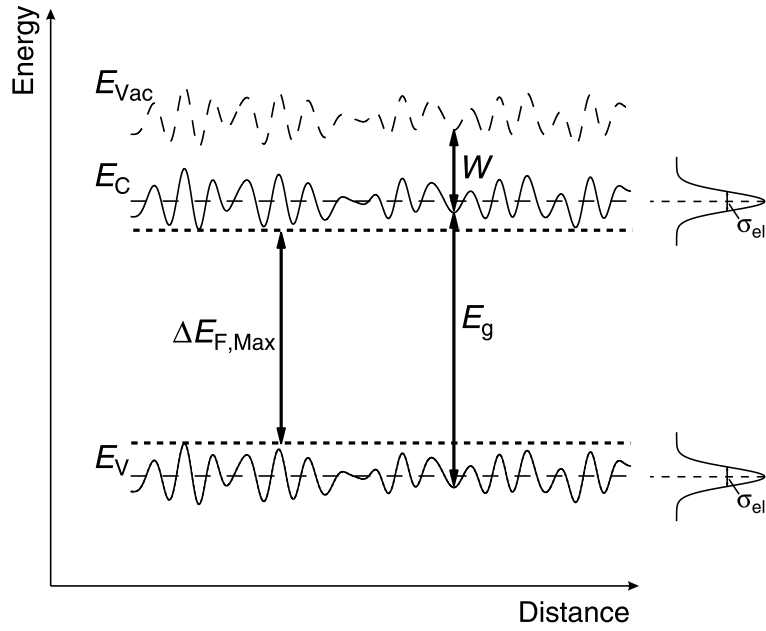


**Figure 2.5:** Schematic representation of electrostatic potential fluctuations in a semiconductor. While the fluctuations are not affecting the local bandgap energy  $E_g$  the positions of both the VBM ( $E_V$ ) and the CBM ( $E_C$ ) are fluctuating. This reduces the maximal possible splitting of the qFLs ( $\Delta E_{F,Max}$ ).

$\Delta E_{F,max}$  [60]. Furthermore, it was shown that electrostatic potential fluctuations lead to an increased  $A$  [56, 58] further reducing  $V_{OC}$  and  $FF$ . However, no analytical model is available yet, accurately quantifying the impact of the electrostatic potential fluctuations on  $A$  [58].

If one describes the distribution of the electrostatic potential fluctuations in each band by a Gaussian distribution function of the energy, the energy width of these distributions  $\sigma_{el}$  can be used as a measure for the amplitude of the fluctuations. Since the fluctuations only limit the  $V_{OC}$  if they are in the order of magnitude of more than  $k_B T$  [56], Equation 2.35 can be extended by a factor considering the influence of the electrostatic potential fluctuations

$$j_0^{el} = j_{00} \cdot \exp\left(-\frac{E_a}{Ak_B T} + \frac{\sigma_{el}}{2A(k_B T)^2}\right). \quad (2.40)$$

And therefore the  $V_{OC}$ -loss due to electrostatic potential fluctuations can be derived to [59]:

$$\Delta V_{OC}^{el} = \frac{\sigma_{el}^2}{2k_B T q}. \quad (2.41)$$

Abou-Ras et al. [59] estimated an average value of up to  $\sigma_{el} = 60 \text{ meV}$  for electrostatic potential fluctuations on a length-scale of 10-100 nm, which could account for a loss in  $V_{OC}$  of up to 70 mV. Werner et al. [56] estimate the fluctuations to be even as high as  $\sigma_{el} \approx 140 \text{ meV}$ .

Another special case of how lateral inhomogeneities can influence the performance of a CIGSe device was described by Rau and Schmidt [66]. The authors argue that the  $V_{OC}$  of the complete devices can be strongly reduced by just a small device volume (e.g. a few grains) or interface area of inferior quality compared to the rest of the device. They show that if the interface quality is deteriorated on as little as 0.1% of the cell area this can lead to a strong reduction of the conversion efficiency of the whole device [66]. Furthermore, it is shown in the same contribution that this effect is more pronounced if no resistive buffer layer (as undoped ZnO) is used and that the effect, on the other hand, can be balanced

and the impact of these small areas reduced if such a highly resistive layer is present. However, since this is an at least two-dimensional effect, it shall not be included in the expression derived for the  $V_{OC}$ -losses here, but should be kept in mind when analyzing the two-dimensional effects of the RbF-conditioning.

b) Sub-bandgap states

Especially in multinary polycrystalline and amorphous materials the rather high level of material disorder, which will be discussed for the case of CIGSe in Section 2.2, leads to the formation of localized energetic states extending into the energy bandgap [67]. On the one hand, these states lead to an absorption below the bandgap energy, which can be described by [42, 68]

$$\alpha = \alpha_0 \exp\left(\frac{h\nu - E_0}{E_U}\right). \quad (2.42)$$

Here  $E_0$  is an energy close to the bandgap energy and  $E_U$  is the Urbach energy, which can be used as a measure of the disorder of the semiconductor. On the other hand, these localized states can increase the recombination due to trapping of charge carriers and therefore reduce the energy barrier of these carriers to the respective other band and to defect levels closer to mid-gap, finally leading to an additional loss in  $V_{OC}$  [69, 70]. Although there is no analytical expression available describing the relation between  $E_U$  and  $V_{OC}$  (to the best of the author's knowledge) it was empirically shown that the  $V_{OC}$ -loss depends linearly on  $E_U$  [71–73]:

$$\Delta V_{OC}^U = aE_U + b, \quad (2.43)$$

where  $a$  and  $b$  are empirical constants. Therefore  $E_U$  can be used as a measure for the comparison of two devices, while the explicit integration of  $\Delta V_{OC}^U$  into Equation 2.38 does not appear useful. As a rule of thumb, it was empirically shown that Urbach energies below the thermal energy ( $E_U < k_B T$ ) have negligible influence on  $V_{OC}$  [71, 74].

Note that Urbach energies lower than  $k_B T$  are not unusual since the absorption into tail states is not thermally activated but just dependent on the energetic position of the defect. Thermally activated absorption below the bandgap energy, e.g. by a three particle interaction via a virtual state (photon, electron, phonon), is much more unlikely and therefore hardly detectable in the absorption spectra of CIGSe.

c) Absorber doping

Since the SRH-recombination is most effective at the position where  $\tau_{Def,h}n = \tau_{Def,e}p$  [42], the absorber doping is one crucial parameter when determining the severity of the defect-related recombination. It also affects the collection probability, tunneling probability, and – as already stated above – the Auger recombination rate. It can be shown, that the difference in  $V_{OC}$  of two devices (x and y) with different absorber doping densities  $N_{A,x}$  and  $N_{A,y}$  can be deduced as [42]:

$$\Delta V_{OC}^{CV} = \frac{Ak_B T}{q} \ln \sqrt{\frac{N_{A,x}}{N_{A,y}}} = \frac{Ak_B T}{2q} \ln \frac{N_{A,x}}{N_{A,y}}. \quad (2.44)$$

Note that this relation is only valid for  $N_A \lesssim 1 \cdot 10^{17} \text{ cm}^{-3}$  (because Auger-recombination becomes relevant at higher  $N_A$ ) and not extreme  $\tau_{Def,e}$  [42].

The total losses due to SRH-recombination in CIGSe devices can therefore be broken down to:

$$\Delta V_{OC}^{\text{nrad}} = \Delta V_{OC}^{\text{el}} + \Delta V_{OC}^{\text{CV}} + \Delta V_{OC}^{\text{rem}}. \quad (2.45)$$

Here  $\Delta V_{OC}^{\text{rem}}$  denotes the remaining loss in  $V_{OC}$  due to SRH-recombination, which occurs even in an absorber layer free of electrostatic potential fluctuations and with an optimum doping, and is therefore proportional to the defect-related lifetime of the electrons  $\tau_{\text{Def},e}$ . Furthermore,  $\Delta V_{OC}^{\text{U}}$  is included into  $\Delta V_{OC}^{\text{rem}}$  due to the lack of an analytical expression describing it. Therefore Equation 2.38 can be rewritten as

$$V_{OC}^{\text{real}} \approx E_g/q - \Delta V_{OC}^{\text{SQ}} - \Delta V_{OC}^{\text{SC}} - \Delta V_{OC}^{\text{rad}} - \Delta V_{OC}^{\text{CV}} - \Delta V_{OC}^{\text{el}} - \Delta V_{OC}^{\text{rem}}. \quad (2.46)$$

Since  $\Delta V_{OC}^{\text{SQ}}$  and  $\Delta V_{OC}^{\text{rad}}$  will hardly be affected by the RbF-conditioning, one major topic of this thesis will be to find the mechanisms of the RbF-conditioning, which lead to an (indirect) reduction of absorption losses and therefore  $\Delta V_{OC}^{\text{SC}}$ , or a direct reduction of  $\Delta V_{OC}^{\text{CV}}$ ,  $\Delta V_{OC}^{\text{el}}$  and/or  $\Delta V_{OC}^{\text{rem}}$ .

Furthermore, it will be important to evaluate the impact of the RbF-conditioning on  $FF$ . In contrast to the effect of the microscopic properties of the solar cell on  $j_{SC}$  and  $V_{OC}$ , there is no analytical expression accurately describing  $FF$  yet, even in the most ideal cases. However, an approximate equation for the relation of  $FF_0$  (the fill factor without resistive losses) and  $V_{OC}$  can be derived and will be useful in the further course of this work [38, 75]:

$$FF_0 = \frac{\frac{qV_{OC}}{Ak_B T_c} - \ln\left(\frac{qV_{OC}}{Ak_B T_c} + 0.72\right)}{\frac{qV_{OC}}{Ak_B T} + 1}. \quad (2.47)$$

## 2.2 Crystal Structure and Defects of CIGSe Absorber Layers

### Crystal Structure

Depending on the growth conditions of the absorber layer, there are different phases of the CIGSe compound, each resulting in different crystal structures. The most suitable phase for thin film photovoltaics is the  $\alpha$ -phase  $\text{CuInSe}_2$  (see phase diagram in Figure 2.6 b), a ternary I-III-VI compound semiconductor assigned to the class of chalcopyrites because of its crystal structure (see Figure 2.6 a). The tetragonal unit cell of a CIGSe-crystal of this phase (see Figure 2.6 a) can be derived from the zincblende structure, but contains eight instead of four Se atoms and is therefore twice as large. It has a body centered tetragonal order in which each two Cu and boron-group atoms are tetragonally ordered around a Se-atom, while in turn four Se atoms are arranged tetragonally around each Cu or boron-group atom. The zincblende structure is based on the diamond structure in which tetragonal structures of five carbon atoms are present in  $sp^3$ -hybridization. However, the covalent bond in the chalcopyrite crystal is based on a  $pd$ -hybridization of the  $p$ -states of the Se and  $d$ -states of the Cu, to which each atom contributes four valence electrons according to the Grimm-Sommerfeld rule [77, 78]. Due to the higher electronegativity of the Se atoms in comparison with the Cu and boron-group atoms, the Se atoms are designated as anions and the Cu and boron-group atoms as cations and the covalent bond becomes overlaid by an ionic bond. Due to the different electronegativities of each of the anions and cations, the charge density distribution along a bond is not independent of the type of anion or cation of the corresponding bond, whereby the bonds between Cu and Se atoms exhibit a higher covalent and the bonds between boron-group and Se atoms a higher ionic bond fraction [79]. Therefore, the corresponding bond lengths are different, which is the reason for the tetragonal distortion of the unit cell:  $\delta = c/2a \neq 1$ , where  $a$  and  $c$  are the lattice constants of the unit cell (see Figure 2.6 a).

According to density functional theory (DFT) calculations, the  $pd$ -hybridized orbitals of the Cu and Se atoms define the VBM of the chalcopyrite crystal, while the CBM is predom-

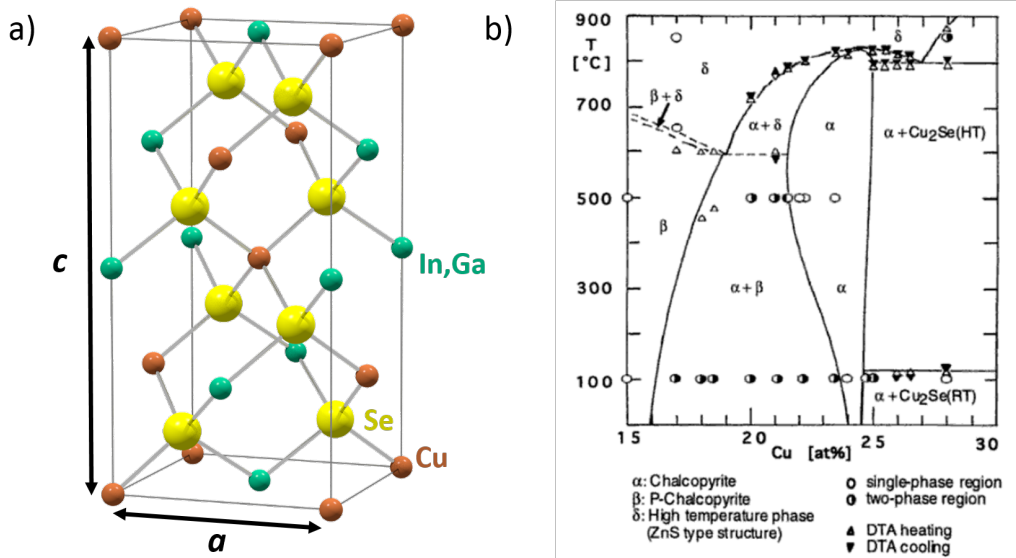


**Figure 2.6:** a) Schematic of the CIGSe crystal in chalcopyrite structure ( $\alpha$ -phase). The size of the unit cell is determined by the lattice constants  $a$  and  $c$ , which are dependent on the composition of the CIGSe. b) Quasi-binary phase diagram  $\text{Cu}_2\text{Se} - \text{In}_2\text{Se}_3$  in the range of  $0.15 < \chi_{\text{Cu}} < 0.30$  and  $20^\circ\text{C} < T < 900^\circ\text{C}$  [76].

inantly determined by the s-orbitals of the boron-group atoms and the p-orbitals of the Cu atoms [79]. For this reason, the ratios

$$GGI = \frac{\chi_{\text{Ga}}}{\chi_{\text{Ga}} + \chi_{\text{In}}}, \quad (2.48)$$

and

$$CGI = \frac{\chi_{\text{Cu}}}{\chi_{\text{Ga}} + \chi_{\text{In}}}, \quad (2.49)$$

where  $\chi_i$  is the molar fraction of the element  $i$ , determine the bandgap energy. The impact of  $GGI$  can be derived directly based on empirical equations, such as [80]:

$$E_g^{\text{CIGSe}}(GGI) = (1 + 0564 \cdot GGI + 0.116 \cdot GGI^2) \text{ eV}. \quad (2.50)$$

In order to account for the dependency of  $E_g$  on the Cu-content an additional term can be added [81]:

$$E_g^{\text{CIGSe}}(GGI, \chi_{\text{Cu}}) = (1 + 0564 \cdot GGI + 0.116 \cdot GGI^2) + 0.017(25 + \chi_{\text{Cu}}) \text{ eV}. \quad (2.51)$$

Note, that since all absorber layers investigated in this thesis were grown Cu-poor ( $CGI < 1$ ), the following discussions will always consider the Cu-poor case, if not explicitly stated otherwise.

## Defects

The electrical properties, for example the doping, of the CIGSe are strongly influenced by its point defects. Unlike many other semiconductors, such as silicon or GaAs, which need to be selectively doped by impurities, CIGSe has its  $p$ -type character due to intrinsic defects. In the crystal lattice of the chalcopyrite a total of twelve point defects can occur:

- 3 vacancies:  $V_{\text{Cu}}$ ,  $V_{\text{In,Ga}}$  and  $V_{\text{Se}}$ ,
- 3 interstitials:  $\text{Cu}_i$ ,  $(\text{In, Ga})_i$  and  $\text{Se}_i$ ,
- 6 antisites:  $\text{Cu}_{\text{In,Ga}}$ ,  $\text{Cu}_{\text{Se}}$ ,  $(\text{In, Ga})_{\text{Cu}}$ ,  $(\text{In, Ga})_{\text{Se}}$ ,  $\text{Se}_{\text{Cu}}$  and  $\text{Se}_{\text{In,Ga}}$ .

Generally, CIGSe is considered a highly compensated semiconductor. Theoretical calculations show that the donor-like defects  $(\text{Ga, In})_{\text{Cu}}$  and  $V_{\text{Se}}$  as well as the acceptor-like  $V_{\text{Cu}}$  are most likely to form [82]. In most models, it is assumed that the net  $p$ -type character of the CIGSe is mainly determined by the Cu-vacancies  $V_{\text{Cu}}$  [83, 84] due to their low formation enthalpy, which can be even negative depending on the exact composition [82]. This self-doping can be further enhanced by reducing the  $CGI$  during growth of the crystal. However, if growing the CIGSe very Cu-poor, one exceeds the limits of the  $\alpha$ -phase and the presence of the  $\beta$ -phase  $\text{Cu}(\text{In, Ga})_3\text{Se}_5$  (see Figure 2.6 b) becomes likely.

Furthermore, it was shown that defect complexes such as  $(2V_{\text{Cu}}^- + \text{In}_{\text{Cu}}^{2+})$  have particularly low formation enthalpies as well [82]. Zhang et al. [82] state that the neutralization of the  $\text{In}_{\text{Cu}}^{2+}$  by the formation of this defect complex is the reason why (especially Cu-poor) CIGSe exhibits an “electrically benign character” despite its high defect density. Furthermore, this defect pair is proposed to be responsible for the formation of the so called ordered defect compounds (ODCs), which describe Cu-deficient phases such as  $\text{CuIn}_3\text{Se}_5$  ( $\beta$ -phase) or  $\text{CuIn}_5\text{Se}_8$ , which especially form in the surface region of Cu-poor CIGSe [85]. Depending on the exact growth conditions, the ODC can be  $n$ - [85] or  $p$ -type [86]. It was proposed that due to the lower position of the VBM in the ODC [81] the interface recombination rate could be reduced if an ODC is present at the surface of CIGSe. In case of an  $n$ -type ODC this effect would be enhanced, because the  $p$ - $n$ -junction would be shifted into the absorber layer (interface ODC/CIGSe) [85, 87]. Furthermore, this effect might be supported by the easier in-diffusion of Cd in Cu-poor material [88] and the following formation of  $\text{Cd}_{\text{Cu}}$ -donors [89, 90].

The presence of an ODC at the surface of Cu-poor CIGSe will be part of the mechanism described in Chapter 4.2.

## 2.3 Alkali Metals in CIGSe Solar Cells - a Literature Review

The history of alkali metal doping of CIGSe absorber layers for thin film solar cells started with the unintentional incorporation of Na into the CIGSe by diffusion from soda-lime glass, which was used as substrate for the first time in the early 1990s by Hedström et al. [91], Bodegard et al. [92], and Schock et al. [93]. From there on, Na is used as the main dopant in most laboratories working on CIGSe absorber layers.

Although heavier alkali elements such as K were occasionally used in experimental studies [94], it was not before 2013 that the CIGSe-community intensified research regarding heavy alkali post deposition treatments [95]. In the following section a literature review about the most commonly accepted models regarding the effect mechanisms of Na (Section 2.3.1) as well as the heavier alkali metals K and Rb (Section 2.3.2) in CIGSe absorber layers is given.

### 2.3.1 Sodium

While some general effects of Na-incorporation in CIGSe are widely observed in samples from different laboratories and are therefore considered to be independent of the nature of the Na-supply as well as the growth parameters of the CIGSe layer, other effects seem to be strongly dependent on these factors. Therefore there is no generally accepted model for the role of Na in CIGSe thin film solar cells yet. However, there are models available, which are able to explain most of the published results.

In the following, the main effects of Na-incorporation are discussed in dependence of the growth parameters of the CIGSe. Moreover, the most common models, namely the model based on Wei et al. [96] as well as the model based on Yuan et al. [97] will be presented. Please note that this overview will be focused on the effects in sulfur-free  $\text{Cu}(\text{In, Ga})\text{Se}_2$  and  $\text{CuInSe}_2$  (CIGSe) absorber layers grown by 3-stage co-evaporation (cf. Chapter 3.1.1). For a more general review, the reader is referred to Reference [98].

### Commonly observed effects of Na in CIGSe absorber layers

The three most commonly used ways to incorporate Na into the CIGSe layer are via diffusion from soda-lime glass substrates through the Mo back contact during the deposition of the absorber layer [92, 93, 99, 100], via deposition of a NaF-precursor layer on top of the Mo back contact [94, 101], or via a PDT of Na-compounds such as e.g. NaF [98], Na<sub>2</sub>S [99], or Na<sub>2</sub>Se [99] after finishing the absorber layer growth. Independent of the nature of the Na-supply devices fabricated with absorber layers containing moderate amounts of Na show higher conversion efficiencies than Na-free devices – mainly due to improved  $FF$  and  $V_{OC}$  of the cells [91–94, 99, 101–104]. The incorporation of ‘high’ amounts of Na on the other hand can lead to delamination of the absorber layers or deterioration of the device performance [99, 105]. Typically a molar fraction of Na in the order of magnitude of 100 ppm leads to an optimal device performance [92, 99, 105, 106]. The positive effects of Na are mainly attributed to an increased hole concentration in the absorber layer and film conductivity [94, 99, 101, 102, 104], which are widely observed independently of the Na-supply. While it was reported that Na – if present during the growth of the CIGSe layer – can lead to both bigger [103] and smaller grain size [107] as well as a more pronounced formation of (112)-oriented CIGSe-grains [91, 100, 103], which could be part of the mechanism enhancing the electrical parameters, these effects are not observed in case of a NaF-PDT [98]. However, devices prepared by the latter method still show improved carrier concentration and PV-parameters [104]. Therefore it is assumed that the beneficial effects of Na on the electrical parameters are mostly decoupled from its impact on the CIGSe-growth [108]. This interpretation is supported by the fact that the main part of Na in the absorber layers is not incorporated into the CIGSe lattice but can be found at surfaces and grain boundaries [105, 109, 110]. In fact only in Cu-poor absorber layers ( $CGI < 1$ ) Na could be detected within the grain interior (GI) so far [111–114], while for example the introduction of Na into the bulk of stoichiometric CuInSe<sub>2</sub> single crystals was not successful [115]. Couzinie-Devy et al. [112] for example performed atom probe tomography (APT) measurements on samples from interrupted 3-stage processes during the Cu-poor and Cu-rich phases of otherwise identical samples and found Na at the GBs in all of them, while they could only detect it in the GI in the Cu-poor ones but not in the Cu-rich ones. Consequently, most models connect the mechanism of Na in CIGSe absorber layers either with its presence at the GBs or its interaction with structural and point defects as e.g. Cu-vacancies ( $V_{Cu}$ ), which are naturally present in Cu-poor CIGSe.

#### Model by Wei et al.

Wei et al. [96] utilized calculations based on the local density approximation (LDA) using a supercell containing 8 CIGSe molecules as well as the respective defect level in the center of the supercell to model the effects of Na in CIGSe. Discussing models that were already proposed by other authors, Wei et al. sum up three effects related to the incorporation of Na into the CIGSe.

Firstly, they propose the formation of a NaInSe<sub>2</sub> secondary phase if Na is “present in stoichiometric quantities” [96], i.e. in the order of magnitude of 1%. Alkali-In-Se-phases will be discussed in more detail in Section 2.3.3.

Secondly, in agreement with work done by Contreras et al. [94] as well as Niles et al. [106], they propose the formation of point defects, if Na is present as a dopant. They find that the formation of Na<sub>Cu</sub> as well as Na<sub>In</sub> are energetically favorable. While – according to their calculations – Na<sub>Cu</sub> is electrically inactive, Na<sub>In</sub> is considered to increase the hole density. This increase of the hole density occurs either by the direct formation of the shallow acceptor level Na<sub>In</sub> [106] or by reducing the amount of In<sub>Cu</sub> by transforming it to Na<sub>Cu</sub> [94] (see Figures 2.7 a-c). Wei et al. [96] claim that the latter effect is the main mechanism via which Na is increasing the hole density in Cu-poor CIGSe since a Cu-poor absorber naturally exhibits high numbers of In<sub>Cu</sub>.

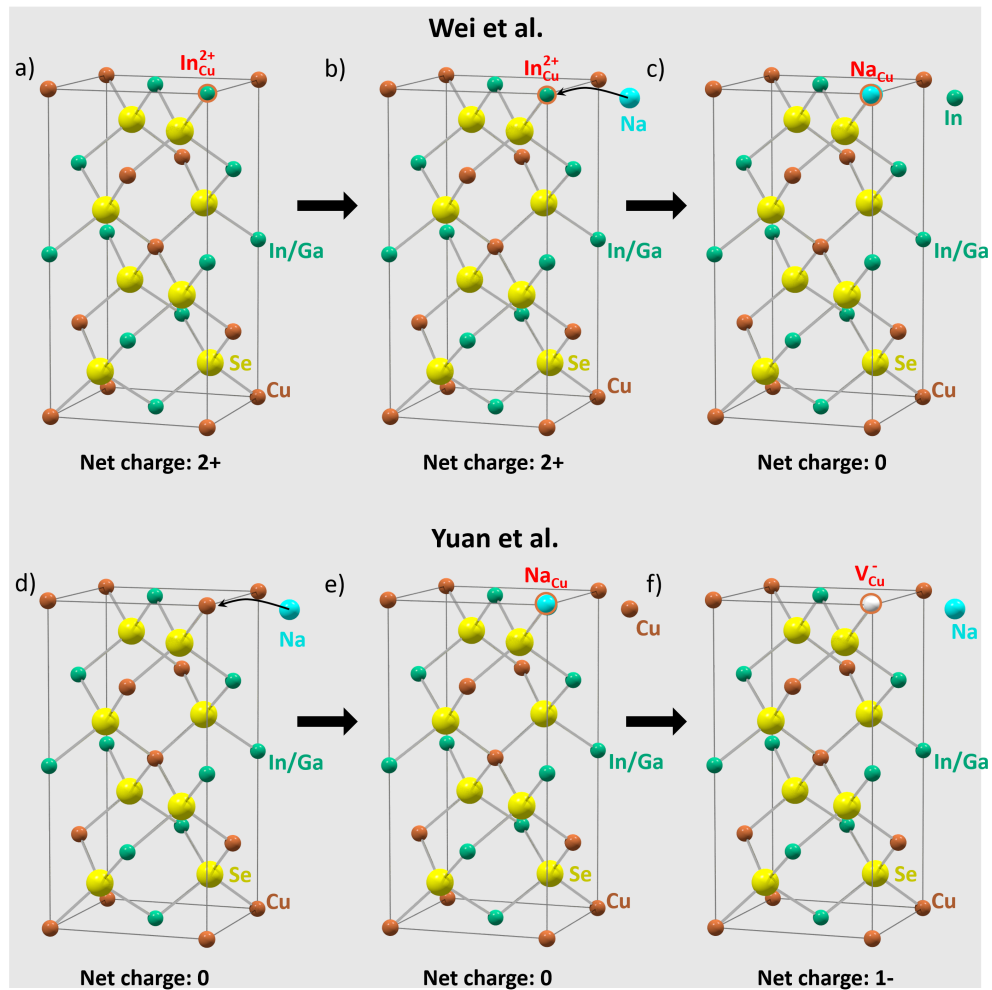


**Figure 2.7:** Main Na-doping mechanisms as proposed by Wei et al. [96] (a-c) as well as Yuan et al. [97] (d-f). a)  $\text{In}_{\text{Cu}}^{2+}$  antisite formed during the growth process due to the high availability of  $\text{V}_{\text{Cu}}$  in the Cu-poor material. b) Still during growth, a sodium atom is replacing the indium atom on the Cu site. c) Finally, the Na-atom neutralizes the  $\text{In}_{\text{Cu}}$  by forming an electrically inactive  $\text{Na}_{\text{Cu}}$  antisite. The 'free' In-atom either creates an interstitial or diffuses to an In-site. Net charge difference in the latter case: 2-. d) During growth Na replaces a Cu-atom forming an electrically inactive  $\text{Na}_{\text{Cu}}$  anti-site. e) The 'free' Cu-atom diffuses either to the surface or to a GB. f) During cool-down and the subsequent WCT of the absorber layer, the  $\text{Na}_{\text{Cu}}$  gets less stable. Some of the Na-atoms diffuse to the surface/GBs leaving behind  $\text{V}_{\text{Cu}}$ . Net charge difference: 1-.

As mentioned above, Cu-poor CIGSe naturally also exhibits a significant number of the shallow acceptor  $\text{V}_{\text{Cu}}$  and accordingly Wei et al. note that Na can also simultaneously passivate  $\text{V}_{\text{Cu}}$ , decreasing the hole concentration. However, they consider the latter effect to be less favorable than the passivation of  $\text{In}_{\text{Cu}}$  leading to an overall increased effective hole concentration [96]. Both effects contribute to the suppression of the formation of the  $(2\text{V}_{\text{Cu}}^- + \text{In}_{\text{Cu}}^{2+})$ -complex though, which is part of the formation mechanism of the ODC (see Section 2.2 above). Therefore it is also proposed that Na can suppress the formation of the ODC [96, 116, 117].

Thirdly, Wei et al. suggest – based on Reference [102] – that Na indirectly leads to an increase of the hole density by reducing the amount of  $\text{V}_{\text{Se}}$  in the CIGSe by oxidation. Based on the fact that Na weakens the O-O bond of  $\text{O}_2$  [118] it forms atomic oxygen, which Kronik et al. [118] claim can penetrate the CIGSe-lattice in contrast to  $\text{O}_2$ . Therefore the incorporation of Na into the absorber layer (not even necessarily into the GI) could directly lead to the incorporation of O into the CIGSe lattice. Due to the highly favorable formation of  $\text{O}_{\text{Se}}$ , the donor-like  $\text{V}_{\text{Se}}$  are passivated and the effective hole density increased due to the Na-incorporation.

**Model by Yuan et al.**

Contrary to the results of Wei et al., Yuan et al. [97] state in their contribution that the formation of  $\text{Na}_{\text{In}}$  antisite defects is in fact unfavorable. The authors base this hypothesis on first principle calculations performed by Oikkonen et al. [119] as well as Ghorbani et al. [120]. Furthermore, they review corresponding experimental results: Using temperature dependent Hall effect measurements performed on epitaxially grown CIGSe, Schroeder and Rockett [121] observe a gain in the effective hole concentration after incorporating Na into epitaxially grown CIGSe but do not observe any hints for the formation of  $\text{Na}_{\text{In}}$ .

Based on first principle calculations Yuan et al. therefore suggest to look for a possible Na-induced doping mechanism aside from equilibrium doping theory. In agreement with Wei et al. [96] they show that the electrically inactive  $\text{Na}_{\text{Cu}}$  is generally the most favorable point defect in Cu-poor CIGSe. Along with the transformation of  $V_{\text{Cu}}$  to  $\text{Na}_{\text{Cu}}$ , this should lead to a decreased effective hole density. To explain the contrary experimental observations they propose the following model [97], which is illustrated in Figures 2.7 d-f.

Since the equilibrium concentration of dopants in a semiconductor is proportional to  $\exp\left(-\frac{\Delta H}{k_{\text{B}}T}\right)$ , where  $\Delta H$  is the formation energy of the respective doping site, the solubility of Na during growth or a PDT at elevated temperatures is significantly higher than after cooling down the sample. Therefore the high number of  $\text{Na}_{\text{Cu}}$  forming at these elevated temperatures is thermodynamically unstable after cool-down. Due to the high diffusivity of Na in Cu-poor CIGSe [113, 119], Na is prone to out-diffuse from the GI leading to the formation of  $V_{\text{Cu}}$ . Yuan et al. further propose that this effect is enhanced by the usually following wet chemical treatment (WCT) in water or ammonia based solutions, which dissolves Na at the surface of the CIGSe leading to a lower chemical potential of Na and therefore a stronger out-diffusion of Na from the GI [97]. This mechanism would result in a higher number of  $V_{\text{Cu}}$  (about  $10^{16} \text{ cm}^{-3}$  to  $10^{18} \text{ cm}^{-3}$  for a NaF-PDT performed at  $400^\circ\text{C}$ ), which could explain the observed increased effective hole density.

**2.3.2 Heavy Alkali Metals**

Although – as mentioned above – the introduction of alkali metals heavier than Na was already tested in the 1990's [94], it was not before the year 2013 that the introduction of heavy alkali elements into the CIGSe absorber layer *additionally* to Na gathered the interest of the community by initiating a series of new record efficiencies [95]. In particular, the incorporation of first K and later also Rb or Cs was the main driving force for the boost in record efficiencies from 20.3% to 23.4% from 2011 till 2019 [36, 39]. Until it was shown by Jackson et al. in 2016 that one can obtain even higher  $\eta$  by RbF- or CsF-PDTs [40], the main focus of the community was on the introduction of K. Therefore, at the beginning of the present work in October 2016, no other published work regarding RbF- or CsF-PDTs was yet available than the study by Jackson et al. [40]. But due to that study by Jackson et al. many groups shifted their efforts to RbF- and CsF-PDTs after 2016. Therefore this literature review is divided into two parts. The first part discusses the effects of KF-PDTs and will contain mostly work published before the beginning of this thesis. The second part of this section is discussing the effects of an RbF-PDT, and therefore contains the literature, that was published during the development of this thesis.

One should keep in mind while reading this literature review that in a lot of publications the exact experimental details of the PDTs are not given, e.g. whether there was a vacuum break in between the deposition of the absorber layer and the PDT or if and how the absorber layers were rinsed by ammonia solution or other chemicals before or after the PDT is unclear in a lot of studies. This might be a reason for some of the contradictory results that will be mentioned below.

**KF-PDT**

Although K-supply via different techniques was tested [81, 94, 95, 122–125], the introduction of K via a KF-PDT (co-evaporation of KF in Se-atmosphere at temperatures below the growth temperature of the CIGSe layer and subsequent annealing) is commonly used in most laboratories in order to rule out influences of K on the growth of the CIGSe. The main effects of the KF-PDT are similar to those of the incorporation of Na. Although K does not seem to work comparably efficient as Na as a sole dopant [94, 126], both a further increase [127–130] or a decrease [126] of the effective hole concentration of CIGSe devices in combination with Na-introduction are reported. In all these cases the effect on  $V_{OC}$  was beneficial [40, 95, 122, 126–131].

However, the influence of K on the  $FF$  is not consistent: Both lower  $FF$  [132] as well as higher  $FF$  [40, 127, 129] as compared to the K-free reference, are reported. Since one would generally expect a gain in  $V_{OC}$  to induce a beneficial effect on  $FF$  (following Equation 2.47), the reason for the  $FF$ -loss remains unclear.

In order to be able to provide a systematic overview of the effects of K on  $V_{OC}$  as well as of the models, which were proposed consequently, possible reasons for a general gain in  $V_{OC}$  have to be evaluated step by step. In accordance with the considerations of Section 2.1.3 the commonly reported gain in  $V_{OC}$  is generally assumed to be a combination of increased hole concentration, the reduction of microscopic fluctuations of the electrostatic potential or a more direct reduction of the SRH-recombination e.g. via defect-passivation.

## a) Effects of the KF-PDT on the hole concentration in CIGSe

Similar to the case of Na, the widely reported beneficial effect of K on the hole concentration was discussed in regard to the interaction of K with defects in (Cu-poor) CIGSe – at GBs [127, 133–136] and/or in the GI [129, 137]. However, first principle calculations found  $K_{Cu}$  to be less stable than  $Na_{Cu}$  [97, 120, 136], which is in agreement with the experimental results that its (additional) doping effect appeared less pronounced (see above).

Analogue to their hypothesis regarding the doping mechanism of Na, Yuan et al. [97] propose that K is further improving the hole density by the formation of additional  $V_{Cu}$  during cool-down/WCT of the absorber layer after the KF-PDT. Please note, that the stability of  $K_{Cu}$  increases with lower Cu-content [120], which means that more K can be incorporated in Cu-poorer material.

Another widely reported effect of the KF-PDT is related to the interaction of Na and K. It was shown that the overall Na-concentration after a KF-PDT is lower than in K-free samples [95, 127, 129, 137, 138]. Similar effects were reported for CsF-PDTs [40] and later on for RbF-PDTs as well [1].

Furthermore, it was shown that a heat-light-soaking procedure of devices based on KF-treated absorber layers can further increase the carrier concentration of the absorber layer [139, 140]. The authors of these publications show that this additional improvement of the carrier density is due to the interaction of Na and K as well: they observe a redistribution of both alkali metals due to the heat-light-soaking. However, no conclusive model for this so-called ion-exchange mechanism was presented in case of K.

## b) Effects of the KF-PDT on recombination

It is widely assumed that the KF-PDT passivates defects at the GBs [127, 133, 135, 136], at which K is observed to aggregate [141, 142], and in the GI [129, 137] resulting in improved minority carrier lifetimes [130, 131, 143]. However, in a recent publication of Abou-Ras et al. [144], the authors did not observe a significant reduction of the average recombination velocity at GBs as measured by cathodoluminescence.

Several groups found that the surface of the CIGSe absorber layer is Cu- and Ga-depleted after a KF-PDT [95, 138, 145]. It was shown that the VBM at the surface of the CIGSe is lowered [132, 145] and the surface-CBM raised by the KF-PDT [145] leading to a widening of the energy bandgap at the surface of the absorber layer. Based on work by Handick et al. [145] as

well as Lepetit [138], it was proposed that these phenomena occur due to the fact that a high-bandgap secondary phase forms at the very surface of the absorber layer during the PDT. Considering the Cu- and Ga-depletion, it was suggested that this phase is a K-containing  $\text{In}_x\text{Se}_y$  compound [146] such as e.g.  $\text{KInSe}_2$  [138, 145].

Lepetit proposed the following mechanism [138]: During the KF-PDT, K is diffusing into the near-surface region of the Cu-depleted ODC-region at the surface of Cu-poor CIGSe and is forming  $\text{K}_{\text{Cu}}$  by occupying  $V_{\text{Cu}}$  as well as Cu-sites. Residual Cu is 'pushed' into the underlying part of the ODC occupying available  $V_{\text{Cu}}$  leading to a further Cu-depletion of the surface. At the same time, Ga diffuses to the surface forming  $\text{GaF}_3$  and Ga oxides. The remaining K, In, and Se form  $\text{KInSe}_2$ . It was further argued that the lower VBM of this surface layer would reduce the SRH-recombination at the heterointerface and therefore improve  $V_{\text{OC}}$  [128, 146, 147].

Please note that Lepetit's model is in good agreement with the fact, that  $\text{K}_{\text{Cu}}$  was theoretically found to be more stable in Cu-poor material [120]. Furthermore, Lepetit et al. argued that the presence of the ODC is mandatory for the KF-PDT to act beneficially on the device performance and also supported this claim by data. Performing their PDT-procedure on absorbers with  $CGI$  close to 1 leads to a drastic drop of all PV-parameters. They argued that without an ODC K is still occupying Cu-sites in the CIGSe-lattice forcing the Cu-atoms to diffuse to the surface where they react with the Se-vapor and form metallic  $\text{Cu}_{2-x}\text{Se}$  and therefore strongly reduce the performance of the devices [128].

However, there are other examples in literature where a KF-PDT was successfully applied to Cu-rich grown CIGSe after etching the surface with KCN [148, 149]. In this case, the authors still observed a Cu-depleted surface phase after the KF-PDT and therefore concluded that they successfully grew an additional layer on top of the stoichiometric CIGSe – independent of its composition. The key difference here, apart from obvious differences in the growth and PDT-procedure, is that Lepetit et al. did not etch the absorber layers with KCN [128], while the group of the University of Luxembourg did [148, 149].

Moreover, it was reported that a KF-PDT modifies the morphology of the surface of the CIGSe layer. Several groups reported the growth of about 50-100 nm wide islands growing at the surface of the CIGSe during the PDT [130, 150, 151]. These islands are soluble in water, and rinsing the samples leaves holes of the same size in the surface of the remaining absorber layer. Reinhard et al. [150] proposed that this nanopatterning of the surface leads to a point contact passivation of the heterointerface and therefore to a reduced recombination velocity at the interface. While this effect was not excluded by further experiments and similar mechanisms are actually used in silicon PERL cells [152], there are no further hints reported supporting this hypothesis for CIGSe devices.

### c) Effects of the KF-PDT on potential fluctuations

Nicoara et al. [153] as well as Aguiar et al. [154] report more homogeneous electronic properties of the GBs in the near-surface region of the absorber layer after KF-PDT (measured by Kelvin probe force microscopy). In combination with the already mentioned publication of Abou-Ras et al. [144], this leads to the assumption that a possible GB-mechanism via which the KF-PDT causes improved  $V_{\text{OC}}$ , works rather by reducing the variation of the potential fluctuations at the GBs than by passivating point defects. An actual mechanism of the reduced potential fluctuations due to the incorporation of K is not proposed.

Additionally, it is reported that the KF-PDT also directly affects the formation of the CdS/CIGSe heterointerface. While both a more pronounced Cd-indiffusion into KF-treated CIGSe layers [95, 126, 138, 155] as well as a more distinct CdS/CIGSe-interface, were reported [154], it is general consensus that one can grow thinner CdS absorber layers on KF-treated CIGSe and therefore improve  $j_{\text{SC}}$  of the devices by reducing the parasitic absorption in the CdS [95, 138, 156]. As a possible reason, it was proposed by Friedlmeier et al. [156] that the KF-treated surface increases the number of nucleation sites for the CdS leading to a more homogeneous growth and an improved coverage of the CIGSe. Note that it was reported by Rau et al. that the presence of a highly resistive layer in between the CIGSe and

the ZnO:Al is necessary to reduce the impact of electrostatic potential fluctuations (independent of KF-PDTs) [66]. Although it was not investigated yet, it might be possible that a highly resistive character of the KInSe<sub>2</sub> surface-phase enhances this effect, even though this was not argued by Friedlmeier et al. [156].

The latter observations and thoughts will be picked up and discussed in more detail in Chapter 6 of the present work.

## RbF-PDT

### a) Theoretical work

Over the last three years, several groups intensified their efforts to elucidate the mechanisms of RbF- and CsF-PDTs in comparison to the KF-PDT. Similar to the case of KF-PDT, the RbF-PDT mainly improves the  $V_{OC}$  of the solar cells [1, 40, 157–160]. In 2017 Malitckaya et al. [161] theoretically investigated the effects of alkali metal impurities in CIGSe using DFT calculations. They provided a comprehensive overview of the formation energies of possible defect states, alkali migration mechanisms, and formation of secondary phases. Some of their main findings were:

- All alkali metals are likely to replace Cu in Cu-poor CIGSe creating  $A_{Cu}$  ( $A = Li, Na, K, Rb, Cs$ ). However, the formation energy of this defect steadily increases with the size of the alkali metal from Na to Cs.
- The formation energy of the  $A_{In}$  antisite can be almost as low as that of  $A_{Cu}$  but also increases with increasing size of the alkali metal used.
- The barriers for migration via interstitial sites are steadily increasing with the size of the alkali metal from Na to Cs. While the migration barriers are low enough to expect considerable migration at PDT-temperatures for Li, Na, and K, Rb, and Cs are less likely to migrate via interstitials. However, all alkali metals can migrate via Cu-vacancies in Cu-poor CIGSe. This mechanism becomes more likely if more  $V_{Cu}$  are present.
- While the formation of mixed secondary phases like  $(Cu, A)InSe_2$  is more likely for  $A = Li, Na$ ,  $AInSe_2$  phases are more stable for  $A = K, Rb, Cs$  and might therefore form at GBs and surfaces/interfaces.

Based on these results, Malitckaya et al. concluded that while Li and Na can be expected to diffuse easily in stoichiometric and Cu-poor CIGSe, Rb and Cs can only diffuse in Cu-poor material. Therefore, for PDTs, the concentration of Rb and Cs in the GI is expected to be neglectable and they are more likely to stay at the GBs and form secondary phases, while Li and Na are expected to form point defects at GBs and also within the grains. Due to its intermediate size, K is expected to participate in both mechanisms: it is considered to be able to diffuse into the GI in a considerable amount but also to form secondary phases at GBs and surfaces.

These observations are compatible with both models for the effect of Na in CIGSe presented in the section above and are supported by other theoretical works as well [119, 136, 162]. However, the evaluation of the formation energy of  $A_{In}$  is different in the calculations of Oikkonen et al., Wei et al., and Malitckaya et al. leading to slightly different interpretations of the role of this point defect – similar to what was discussed above in case of Na.

Chugh et al. [134] investigated the effect of Li, Na, and Rb close to symmetrical GBs in CuInSe<sub>2</sub> using the DFT-based Vienna ab initio simulation package [163]. Similar to the results of Malitckaya et al. [161] they found that Rb in contrast to Na is unlikely to diffuse into the GI but rather segregates at Cu-poor regions close to the GBs. Furthermore, they calculated the density of states at the GBs in three different cases: alkali-free CIGSe, CIGSe with  $Na_{Cu}$  defects at the GB, and CIGSe with  $Rb_{Cu}$  defects at the GBs. They found that the density

of states within the energy bandgap is reduced by the presence of alkali metals at the GBs in general. In particular, the passivation at some GBs is more effective by Rb than by Na: Rb is more effectively compensating Se-dangling bonds than Na due to the fact that it is bigger in size and more electropositive [134]. This could be a hint that Rb – in contrast to K – more effectively reduces the recombination at GBs. However, no experimental study similar to that Abou-Ras et al. carried out in case of K [144], is available for the case of Rb yet.

## b) Experimental results

Other than the last point mentioned above, the theoretical observations are in good agreement with recently published experimental work regarding RbF-PDTs. In several studies it was shown that the RbF-PDT leads to an increase in the hole concentration of the absorber layer [1, 158, 159, 164] and hints for a reduction of the recombination rate in the bulk and at the heterointerface were given [7, 159, 160, 164]. Schöppe et al. [165, 166] found that Rb indeed accumulates at surfaces, interfaces, and random GBs, and that its concentration in the GI is below the detection limit of their measurements (nano-X-ray fluorescence spectroscopy). Vilalta-Clemente et al. [167] and other groups [168, 169] also confirmed that Rb stays mostly at the GBs and cannot be found within the grains using APT or transmission electron microscopy (TEM).

Furthermore, Vilalta-Clemente et al. [167] showed that the presence of Na at the GBs is less likely in samples with RbF, while the concentration of Na in the GI is strongly increased. Wuerz et al. [170] on the other hand could experimentally confirm that Rb diffuses within the grains of rather Cu-poor CIGSe, which supports the proposed Cu-vacancy assisted alkali-migration mechanism described by Malitckaya et al. [161]. Furthermore, they showed a strong dependence of the Rb- and Na- diffusion on whether or not the respective other alkali is already present in the film [170]. This already mentioned exchange mechanism of Na and heavy alkali metals was also observed in Publication [1] and by other groups for the case of RbF-PDTs [1, 157, 158, 169].

*Therefore one of the goals of the work presented in this thesis (and partially published in Publications [1] and [4]) was to analyze the Rb-Na exchange mechanism in dependence of the Cu-content of the CIGSe and to model its consequences in regard to the device properties, as e.g. its impact on  $V_{OC}$ . This work will be presented and discussed in more detail in Chapters 4, 5, and 7.*

Moreover, it was experimentally proven that the amount of Rb-incorporation, the extend of the Rb-Na interaction as well as the effect of the RbF-PDT on the electrical parameters in general is not only strongly dependent on the availability of Cu-vacancies [4, 171] as proposed by Malickaya et al., but also on the Ga-content of the absorber layer [158, 172]. While it was shown that the RbF-PDT (as well as a KF- and CsF-PDTs) increase all device parameters in samples with  $GGI = 0.75$  [172], no performance improvements were achieved on samples with  $GGI = 1$  [158]. Furthermore, it was experimentally proven in Publications [1, 8] and References [157, 158, 168, 169] that the RbF-PDT does indeed lead to the formation of a secondary phase at the surface of CIGSe absorber layers, while it does not on In-free  $CuGaSe_2$  [158].

*To investigate the formation and the nature of this surface phase was the motivation for the work presented in Publication [2] as well as Chapters 4 and 5, in which it will be shown that  $RbInSe_2$  is indeed the most likely candidate for that secondary phase.*

Note that the role of these secondary surface phases is discussed controversially in literature. While some studies assume that  $RbInSe_2$  (as well as  $KInSe_2$  in case of the KF) contributes to the improved  $V_{OC}$  by reducing the interface recombination velocity [128, 146, 147, 157, 168], other studies identify the  $RbInSe_2$  as possible electron barrier with a detrimental effect on  $FF$  [4, 41]. However, since the effect of the RbF-PDT on  $FF$  is ambivalent in different studies (lower  $FF$  after RbF-PDT [1, 41, 159] versus higher  $FF$  after RbF-PDT [4, 40, 157, 158, 164]), this effect seems to be strongly dependent on the exact growth conditions (e.g.  $CGI$  and  $GGI$  of the absorber layers) as well as the WCTs performed after the PDT. However, these parameters are not mentioned in most publications prohibiting a more sophisticated comparison.

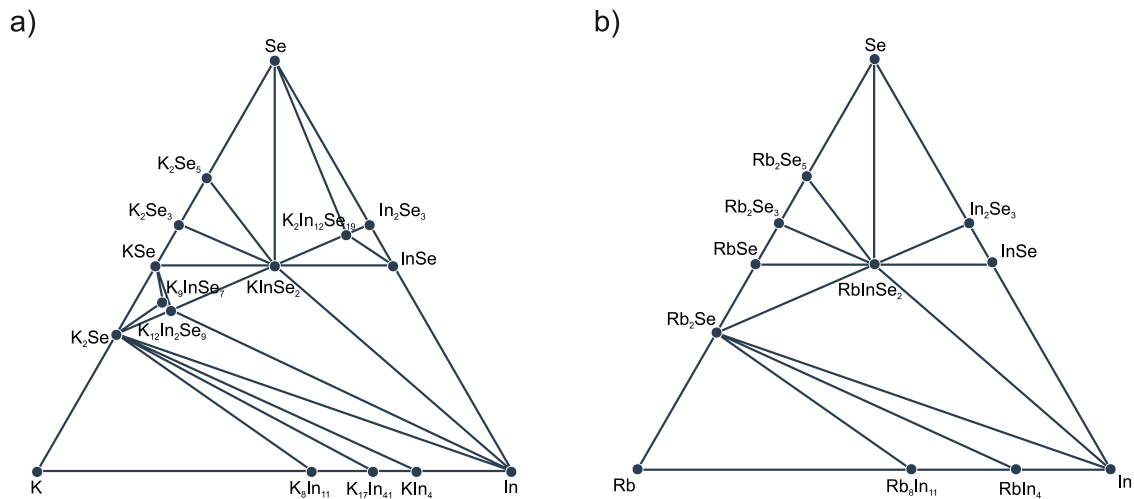


**Figure 2.8:** a) Phase diagram of the K-In-Se system; b) Phase-diagram of the Rb-In-Se. Both adapted from the Materials Project Database [173].

To clarify these contradictory results from literature as well as the role of the secondary phases was therefore the motivation for the work shown in Publication [4] and Chapters 4.2, 5.2, and 8.

Even though the formation of a  $RbInSe_2$  surface layer might not be part of the enhanced  $V_{OC}$  after an RbF-PDT, it was shown in Publication [3] as well as in References [156, 160] that both KF- and RbF-PDT, lead to an improved quality of the heterojunction. This was attributed to a more homogeneous coverage of the absorber layer during the subsequent buffer layer deposition [3, 156], which is also explaining the fact that one can grow the buffer layer thinner on RbF-treated CIGSe samples as well [3, 157, 171]. Note that several groups found a similar nanopatterning of the surface of the CIGSe after RbF-PDT as in case of a KF-PDT [1, 157, 158, 168], which might influence the growth of the subsequently following buffer layer and could therefore be part of the mechanism improving the coverage of the CdS.

The interplay of the secondary surface phase and the subsequent buffer layer deposition will be analyzed and discussed in Chapter 6 and was presented in Publication [3].

### 2.3.3 Secondary Phases

While it was shown by Wei et al. that Na has to be present in high concentrations in CIGSe in order to form secondary phases (e.g.  $NaInSe_2$ ) [96], the presence of K- and Rb-containing secondary phases was shown experimentally even after the respective PDTs [1, 124, 128, 146, 158, 168], which lead to an alkali incorporation in the order of magnitude of 100 ppm only. In Figure 2.8 the phase diagrams for the A-In-Se systems ( $A = K, Rb$ ) as adapted from the Materials Project Database are shown [173]. Cu and Ga are not considered in these systems, because in both cases, the KF- and the RbF-PDT, it was found that the surface of the CIGSe is strongly Cu- and Ga- depleted after the PDT [1, 138, 146, 157].

Based on calculations regarding the formation energies and the stability diagrams of the K- [161], and Rb-containing phases [2, 161] one can identify the most likely candidates to form under the experimental conditions given during the A-PDTs. Malickaya et al. [161] found that for  $A = Na, K, Rb,$  and  $Cs$  the respective  $AInSe_2$  phase has the lowest formation enthalpy of all possible secondary phases and are therefore more likely to form than e.g.  $A_2Se$ . Furthermore, it was shown that the stability region of the  $AInSe_2$  is increasing with increasing size of the A-atom [161] reducing the stability region of the corresponding  $A_xSe_y$ -phases respectively.

In the theoretical part of Publication [2], which was conducted in a collaboration with the University of Paderborn, it was shown for the case of the Rb-In-Se system that the lowest formation energies occur for  $RbInSe_2$ ,  $Rb_2Se_3$  and  $Rb_2Se_5$ . Since no experimental ev-

idence of  $A_x\text{Se}_y$ -phases was found in co-evaporated A-In-Se layers [2, 124, 125], it was proposed (for the case  $A = \text{Rb}$ ) that these phases, if they form, further react to  $\text{RbInSe}_2$ , which is proposed to be an  $n$ -type semiconductor. The formation energy of the reaction  $\text{In}_2\text{Se}_3 + \text{Rb}_2\text{Se} \rightarrow 2\text{RbInSe}_2$  was calculated to be negative ( $-1.41 \text{ eV}$ ) indicating that this is likely to happen [2].

*Based on these theoretical findings, it will be shown in more detail in Chapter 5.1 that stable  $\text{RbInSe}_2$  is forming when co-evaporating  $\text{RbF}$ ,  $\text{In}$  and  $\text{Se}$  at the corresponding evaporation rates, which supports these theoretical considerations. Furthermore, some fundamental properties of  $\text{RbInSe}_2$  will be examined experimentally, as they were already presented in the experimental part of Publication [2].*

### 2.3.4 Summary of the Literature Review

The following aspects of the literature review given above should be kept in mind when reading this thesis:

- The hole density in CIGSe absorber layers is strongly improved by the incorporation of Na. This is most likely either due to the passivation of  $\text{In}_{\text{Cu}}$  sites by the formation of  $\text{Na}_{\text{Cu}}$ , the suppression of  $V_{\text{Se}}$  during the growth of the absorber layer and/or by the indirect formation of additional  $V_{\text{Cu}}$  during the subsequent WCT. Furthermore, a combination of these mechanisms is possible. E.g. Na could eliminate  $\text{In}_{\text{Cu}}$  creating  $\text{Na}_{\text{Cu}}$  during the growth and then subsequently be released during the WCT creating an additional Cu-vacancy.
- K and Rb are not as effective in increasing the hole density, because of their bigger size and consequently higher energy barrier for the diffusion into the GI. While K can still diffuse even in stoichiometric material (occupying Cu-sites), Rb can only diffuse into Cu-poor material. Generally, the solubility of all alkali metals in CIGSe is improved with lower Cu-content.
- With increasing size of the alkali metal, the formation of secondary phases, as e.g.  $\text{AInSe}_2$  ( $A = \text{alkali metal}$ ) becomes more favorable compared to the formation of point defects. Therefore  $\text{NaInSe}_2$  will only form if Na is present in high concentrations, while there are hints that  $\text{KInSe}_2$  and  $\text{RbInSe}_2$  are forming already under the conditions of the commonly used respective PDTs.
- Both K and Rb, are reducing the recombination rate in the CIGSe-based devices. However, it is unclear whether they reduce the recombination only in the bulk (SCR or QNR) or also at the heterointerface. Furthermore, it is unclear if the bulk recombination is reduced due to passivating effects on the GBs (where the alkali metals accumulate) or in the GI.
- Heavy alkali PDTs improve the quality of the heterojunction. Whether this is due to the formation of the secondary phases, due to the formation of a nanopatterned surface, or due to other effects is not finally clarified.

## 3 Experimental Methods

This chapter gives an overview of the experimental methods used for the fabrication and characterization, as well as the device-modeling of the samples that will be analyzed in the following chapters. In Section 3.1 the experimental details of the sample preparation are explained and in Section 3.2 the utilized characterization and simulation tools are described. Please note that, while the majority of the experiments described in this thesis were performed at Helmholtz-Zentrum Berlin (HZB), some of them (including device fabrication and/or measurements) were carried out by the author but not at HZB or were performed by third parties, e.g. as part of a collaborative work or within a project. In all cases, in which (a part of) an experiment was not performed at HZB, this will be noted in the respective section. The respective experimental details will be described separately in this chapter.

### 3.1 Fabrication of CIGSe Solar Cells

In the following the process steps of the deposition of CIGSe- and RbInSe<sub>2</sub>-samples, the RbF-PDT, as well as the buffer layer deposition are explained as they were performed at HZB (Sections 3.1.1 through 3.1.3). In Section 3.1.4 the respective experimental details of experiments carried out at the Institut des Materiaux Jean Rouxel in Nantes (IMN) are discussed.

All absorber layers discussed in this thesis were deposited by thermal co-evaporation of the respective elements/compounds (Cu, In, Ga, Se, and RbF) onto heated substrates in a face-down setup. This physical vapor deposition (PVD) approach allows for a good controllability of the elemental composition and depth gradients. To complete solar cell devices after the CIGSe/buffer layer deposition, a bi-layer of undoped ZnO (about 40 nm thick) and ZnO:Al (about 130 nm thick) was deposited by RF-sputtering as the window layer on top of the glass/Mo/CIGSe/buffer-stack. If not explicitly mentioned differently, additionally a Ni-Al-Ni front contact grid was deposited by electron beam evaporation via a shadow-mask, and no anti-reflective coating (ARC) was applied.

#### 3.1.1 CIGSe-Growth and RbF-PDT

##### CIGSe-Growth

At HZB rigid float-glass slides with a thickness of 2 mm and a size of 5x5 cm<sup>2</sup> were used as substrates. Before the CIGSe-deposition, the substrates were cleaned in an aqueous washing process and then covered with an 800 nm thick Mo back contact, which was deposited by DC-sputtering. Figure 3.1 shows a schematic representation of the machine, which is used for the CIGSe-deposition, generally referred to as 'PVD-B'. The vacuum-based tool is equipped with a valved selenium cracker source (VSCS) allowing for a fast regulation of the Se-flux, which is adapted to the fluxes of the other sources during the different depositions stages, i.e. to establish a ratio of Se/metal of 3 to 5. Furthermore, the chamber is equipped with shuttered Cu-, In-, Ga-, NaF-, and RbF-sources, which can be heated and opened/closed individually. The background pressure of the system is below 10<sup>-7</sup> mbar. Seven substrates can be placed on the rotating substrate holder facing the crucibles, which evaporation cones 'aim' towards the middle of the substrate holder. Six of the substrates are ordered symmetrically on a circle around the seventh substrate, which is placed in the middle. The lateral inhomogeneity of the composition from the outer point of the outer substrates to the middle of the centered substrate were derived to be lower than ±4% and

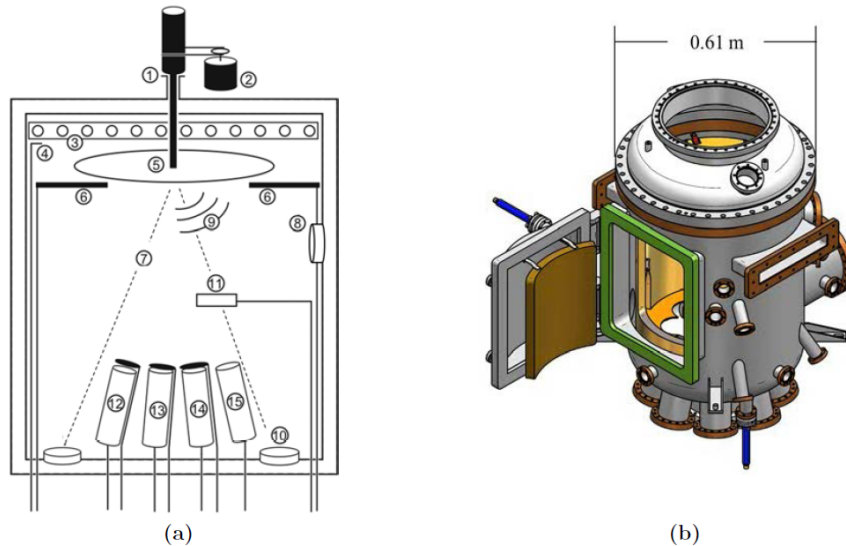


**Figure 3.1:** a) Schematic representation of the PVD-B system: 1) Manipulator, 2) Motor for substrate rotation, 3) Substrate heater, 4) Thermoelement, 5) Rotating substrate holder, 6) Substrate shutter, 7) ILR and LLS signals, 8) LLS-detector, 9) IR-radiation to be detected by the pyrometer, 10) ILR-detector, 11) Quartz crystal microbalance, 12-14) Representation for the effusion cells of Cu, In, Ga, NaF, RbF, 15) VSCS. b) Technical drawing of the PVD-B system, showing the liquid N<sub>2</sub> cooling shroud in yellow and the in and outlets in blue. Images taken from [174].

the deviation of the sample thickness to be lower than  $\pm 10\%$ . The substrate temperature is measured using a thermocouple that is placed a few mm above the centered substrates and below the substrate heater. In order to be able to accurately control the composition and the elemental depth gradients, the chamber is equipped with various process controls: rate measurements via quartz crystal microbalance, logging of the substrate heater's output power, which can be used for 'end-point' detection [175], laser light scattering (LLS) [176, 177], infrared-light reflectometry (ILR), and a pyrometer. The latter three are measured on the centered substrate. The chamber walls are cooled using a cooling-shroud filled with liquid nitrogen in order to avoid re-deposition from the walls.

A scheme of a typical three stage process, as adapted from the work published in References [178, 179], is given in Figure 3.2. Additionally, the data of the (optical) process control of Stage 2 and 3 of an example process are shown in Figure 3.3. In the first stage, the substrates are kept at a temperature of 300°C and two alternating layers of Ga<sub>2</sub>Se<sub>3</sub> and In<sub>2</sub>Se<sub>3</sub> are deposited. The thickness of each layer is controlled by ILR: monochromatic infrared light ( $\lambda = 1040$  nm) is shone on the substrates and penetrates the film during growth. Approximately knowing the refractive index of the films, the film thickness can be estimated from the interference extrema of the specular reflected light.

During the second stage, the substrate temperature is ramped up to 530 °C, while Cu-Se is evaporated. Therefore the *CGI* steadily increases during the second stage until the first point of stoichiometry (SP1, see Figure 3.3) is reached at  $CGI = 1$ . SP1 shows signatures in different process controls: due to the segregation of Cu<sub>2-x</sub>Se<sub>x</sub>, the optical properties at the surface of the growing film are altered, which can be detected by LLS. At the same time the radiative heat-loss of the film increases, which can be detected by the pyrometer and the substrate heater's output power, which increases in order to balance the heat-loss (cf. Figure 3.3). At the end of Stage II, the film is kept in the Cu-rich regime at  $CGI = 1.03$  ( $CGI = 1.05$  in case of the samples discussed in Section 5.2) for 3 minutes in order to profit from the increased diffusion velocities that are established under Cu-rich conditions, which improve the crystal quality of the film [180–183]. With the beginning of Stage III, In<sub>2</sub>Se<sub>3</sub> and Ga<sub>2</sub>Se<sub>3</sub> are evaporated simultaneously in order to reach the final Cu-poor composition. During the third stage, *CGI* steadily decreases, passing the second point of stoichiometry (SP2), which is again visible via pyrometer, substrate output power, and LLS. Extrapolating the slope of

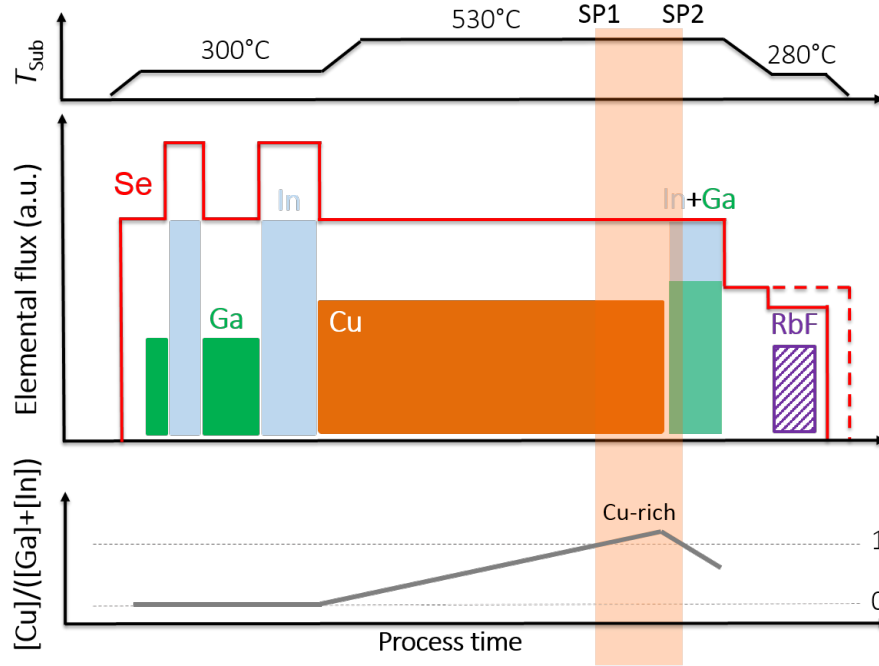


**Figure 3.2:** Schematic representation of the substrate temperature  $T_{\text{Sub}}$ , the elemental fluxes and the corresponding evolution of the CGI during a 3-stage process. The dashed red lines show the evaporation rate profile in case no RbF-PDT is performed.

the decrease of CGI one can adjust the final CGI of the film by adjusting the duration of the third stage accordingly. Since the variation of the CGI is achieved via the duration of the third stage, this also alters the elemental in-depth distribution within the thin film and therefore the depth profile of the energy bandgap. Figure 3.4 shows the energy bandgap-profile of a sample with  $\text{CGI} = 0.9$  and one with  $\text{CGI} = 0.7$  as calculated via Equation 2.50 using elemental depth gradients measured by glow discharge optical emission spectrometry (GD-OES). It can be seen that the position of the minimum bandgap energy ( $E_{g,\text{min}}$ ) as well as its value are changed by the variation of the duration of Stage III. This has to be kept in mind and will be further accounted for in the respective chapters.

### RbF-PDT

After finishing the growth of the CIGSe, the Se-rate is reduced and the substrate is cooled down. In case of samples without RbF-PDT, the VSCS is completely closed at a substrate temperature of  $T_{\text{Sub}} = 250^\circ\text{C}$  and the substrates are transferred to the load-lock of the system. In case an RbF-PDT is performed, the cool-down is interrupted and the substrate temperature kept constant at  $T_{\text{Sub}} = 280^\circ\text{C}$ . The RbF is then evaporated with a deposition rate of approximately  $0.2 \frac{\text{\AA}}{\text{s}}$  (as measured by quartz crystal microbalance). If not stated otherwise (e.g. in Section 4.1), the duration of the PDT is set to 10 min. During the RbF-PDT the Se-rate is reduced to less than  $0.1 \frac{\text{\AA}}{\text{s}}$ . After finishing the PDT, the Se-supply is cut off completely and the substrates are cooled down to room temperature.

On the samples, which are discussed in Section 5.2, RbInSe<sub>2</sub> was deposited instead of performing an RbF-PDT. This was achieved by keeping the samples at CIGSe growth temperature ( $T_{\text{Sub}} = 530^\circ\text{C}$ ) after finishing Stage III. The subsequent RbInSe<sub>2</sub>-layer was then deposited according to the procedure described in Section 3.1.3 before the Se-supply was cut off and the samples were cooled down to room temperature.

Please note that although all CIGSe- deposition processes as well as the RbF-PDTs and RbInSe<sub>2</sub>-depositions were nominally performed identically (apart from intended variations), unintentional parameter variations cannot be ruled out completely. For example, changes in the humidity over the different seasons as well as chamber conditioning due to different

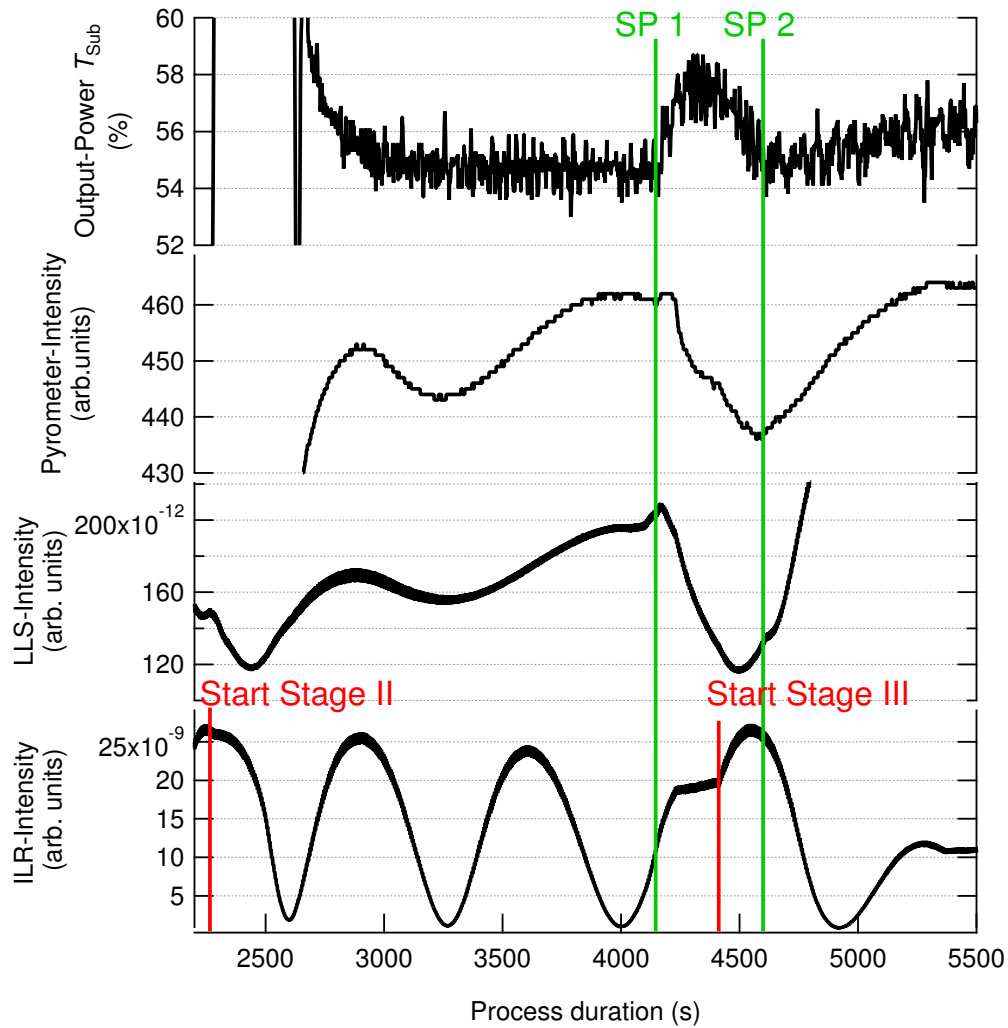


**Figure 3.3:** Data of the output power of the substrate heater, the pyrometer, the LLS and the ILR (from top to bottom) of the second and third stage of a typical three-stage deposition process.

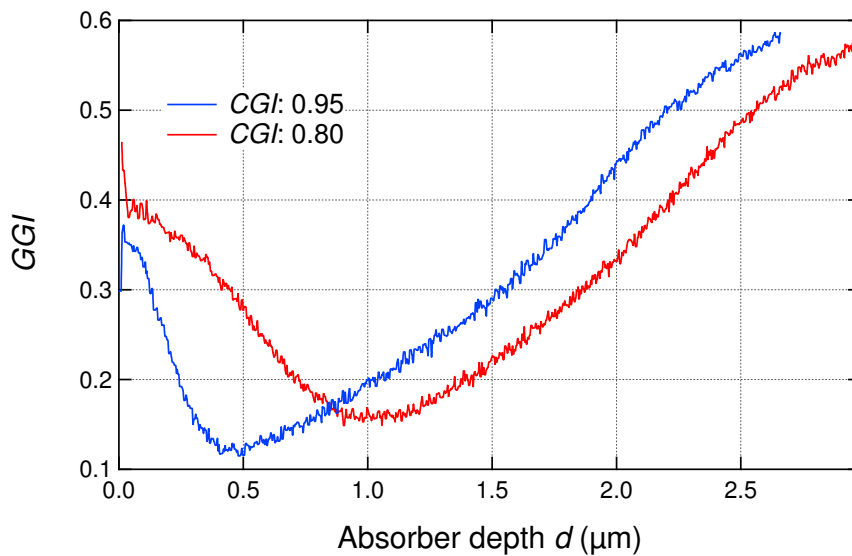


**Figure 3.4:** Example of how a change of the CGI via a prolongation of the third deposition stage alters the profile of the GGI as well.

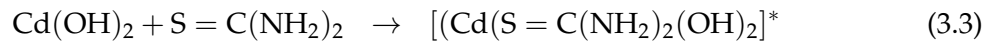
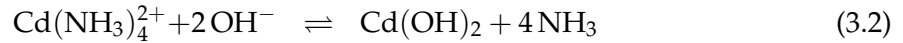
deposition processes and maintenance routines might affect the reproducibility of the processes. However, all samples of each experiment presented in this thesis were performed as fast after each other as possible in order to minimize such effects.

### 3.1.2 Buffer Layer Growth

After finishing the growth of the absorber layer, the samples are rinsed in diluted ammonia before a CdS buffer layer is deposited by chemical bath deposition (CBD). If not mentioned otherwise, the buffer layers were deposited as described in the following.

#### CBD-CdS

In order to deposit a homogeneous CdS-film on top of the absorber layer, the samples are dipped in a reactor at room temperature containing the following solutions: Cd-acetate ([2.5 mM]), thiourea ([0.05 M]), and ammonia ([1 M]) (chemical purity of all used chemicals:  $\geq 0.99$ ) dissolved in deionized water. Subsequently, the bath is heated up to a setpoint of 60°C. During heat-up several reactions are triggered, finally leading to the growth of the CdS-layer (the asterisk marks adsorbed species):



It is generally assumed that the CdS-growth can be divided into three growth stages [184–186]. After an initial ‘induction/coalescence’ phase, which means the adsorption of  $\text{Cd}(\text{OH})_2$  on the substrate and a subsequent nucleation mechanism of the layer, the CdS is growing via an ‘ion-by-ion’-deposition mechanism resulting in a compact and dense CdS-layer. While ion-by-ion-growth happens on the surface of the CIGSe, CdS-colloids start to form in the solution, which after a critical time leads to a reduced substrate-colloid repulsion and results in colloid-adsorption to the CdS-layer (third growth stage: ‘cluster-by-cluster’ deposition). The adsorption of the CdS-clusters leads to the growth of a second, less dense sub-layer of the CdS. In order to minimize the deposition of this porous CdS layer, the CBD is terminated once the solution reaches a certain turbidity, which typically results in a layer thickness of about 60-80 nm. However, as it will be discussed in Chapter 6, details of the growth process are dependent on the substrate used, e.g. CIGSe or RbF-conditioned CIGSe. After finishing the CdS-growth, samples are rinsed again in diluted ammonia in order to wash residual colloids off of the surface.

### 3.1.3 Growth of RbInSe<sub>2</sub> Thin Films

The RbInSe<sub>2</sub> thin films, which will be discussed in Chapter 5, were deposited using a one-stage thermal co-evaporation process using the PVD-B. If not specified otherwise, the glass/Mo/RbInSe<sub>2</sub>-samples have been prepared under Na-free conditions on soda lime glass that was covered with a SiO<sub>x</sub>N<sub>y</sub> diffusion barrier. In cases where the RbInSe<sub>2</sub> was deposited onto CIGSe, no diffusion barrier was used.

During the deposition processes In, Se, and RbF were deposited on the substrates at a temperature of  $T_{\text{Sub}} = 550^\circ\text{C}$  in case of the glass/Mo/RbInSe<sub>2</sub>- and at  $T_{\text{Sub}} = 530^\circ\text{C}$  in case of the glass/Mo/CIGSe/RbInSe<sub>2</sub>-samples. The temperatures of the crucibles were adjusted to reach evaporation rates of  $0.4 \frac{\text{\AA}}{\text{s}}$  for RbF and for In each, ensuring excess Se-supply (Se-Rate approx.  $1.0 \frac{\text{\AA}}{\text{s}}$ ). These rates lead to a growth of RbInSe<sub>2</sub> with a rate of about  $5 \frac{\text{nm}}{\text{min}}$ . After finishing the deposition processes all samples were rinsed in diluted ammonia to wash off residual fluorine and excess Rb.

### 3.1.4 Sample Preparation at the IMN

The samples that are investigated in Chapter 6 are fabricated at the IMN using a three stage co-evaporation process [179] on 1 mm thick glass substrates coated with 400 nm thick DC-sputtered molybdenum. All samples are prepared without diffusion barriers, so that Na can diffuse from the glass substrates into the films during growth. The three stage process is performed similarly to that at HZB. However, due to the absence of optical process control tools the stoichiometry points are determined using the output power of the substrate heater only ('End-point detection'). The maximum substrate temperature during the second and third stage of the process is 580°C, the final integral composition as measured by X-Ray Fluorescence spectroscopy (XRF) exhibits  $CGI \approx 0.8$  and  $GGI \approx 0.35$ . For additional details of the CIGSe deposition system, the reader is referred to Reference [180]. After the CIGSe deposition, samples are taken out of the system, i.e. are exposed to air, before additional PDTs and/or depositions of the subsequent layers are performed.

The RbF-PDT is performed in a separate, self-assembled chamber at a substrate temperature of 280°C with an RbF-deposition rate of around  $0.2 \frac{\text{Å}}{\text{s}}$  in Se atmosphere. The Se-atmosphere during the RbF-PDT is provided using two Se-sources aiming towards the substrate from a distance of about 50 cm. The evaporation rates of the Se-sources are set to values lower than  $0.1 \frac{\text{Å}}{\text{s}}$ . The base pressure of the system in stand-by is  $\sim 10^{-6}$  mbar. After depositing an approximately 10 nm thick (as measured by quartz crystal microbalance) RbF film, both the RbF and the Se-fluxes are switched off and the substrates are annealed for another 5 minutes before cooling them down.

Sample-deposition at IMN was performed by the author in order to investigate the growth of the CBD-CdS buffer layer. Hence, no standard CBD is performed on them. The experimental details of the CBD-variation are described in Section 6.1.

## 3.2 Sample Characterization and Numerical Simulation

In order to be able to analyze and model the effects of the RbF-treatments on the material properties of the CIGSe absorber layer as well as on a complete device level, various characterization techniques were employed. This section briefly introduces the measurement setups, which were used in order to measure the properties of the absorber layers and of the complete solar cell devices. For a detailed and thoroughly researched overview of most characterization techniques for thin film solar cells, the reader is referred to Reference [187].

### 3.2.1 Material Characterization

#### Determination of the Composition and Morphology

In order to measure the composition of the CIGSe absorber layers, XRF and energy-dispersive X-ray spectroscopy using a scanning electron microscope (SEM-EDX) are used. XRF measurements were carried out using a wavelength dispersive XRF type ZSX Primus II from Rigaku. For X-ray generation electrons with energies of up to 4 kW are accelerated onto a rhodium target, which then, in addition to the continuous bremsstrahlung, emits characteristic X-rays. Exposure of the samples to be investigated to the X-rays results in the emission of element-specific fluorescence-radiation from the samples [188], which is detected by a wavelength-dispersive detector.

SEM-EDX was measured using a Zeiss LEO Gemini 1530 SEM with a Thermo Noran X-ray detector. The acceleration voltage was set to 20 kV in order to be able to measure the integral composition of the whole film. The same SEM was used to take the images of the CIGSe samples presented in Chapters 4, and 5, while the SEM-images shown in Chapter 6 were taken at the IMN with a Jeol JSM-7600F microscope. In both cases, images were taken with an acceleration voltage of 5 kV at different magnifications as indicated in the respective images.

TEM-images were taken by Dr. Chen Li at the Max Planck Institute for Solid State Research in Stuttgart. Samples for the Scanning TEM (STEM) measurements were prepared with a Thermo Scientific FEI Scios DualBeam FIB-SEM instrument. A C-Gas and a Pt-Gas injection system were used to deposit C and Pt layers on the sample surface for protection from Ga ion beam damage. From rough cut towards finer thinning of the specimens, a Ga-ion beam with progressively lower voltages from 30 kV to 1 kV and progressively lower ion beam currents from 65 nA to 16 pA has been used. Then a Fischione Nanomill 1040 with a low- $V$  (0.5 kV - 1 kV) Ar beam was used for final thinning and cleaning of the specimens to  $\sim 50$  nm thickness. STEM investigations were performed using a JEOL JEM-ARM 200CF electron microscope equipped with a cold FEG, a CEOS DCOR probe corrector, and a 100 mm<sup>2</sup> JEOL Centurio EDX detector. The operating voltage is 200 kV, with a semi-convergence angle of 20.4 mrad and a probe size of  $\sim 1$  Å. For STEM high-angle angular dark field (HAADF) imaging, a collection semi-angle of 115 mrad - 276 mrad was used.

### Depth Profiling

Depth profiling via GD-OES was performed using a GDA650 by the company Spectruma GmbH. The water cooled sample is placed onto the glow lamp and an RF argon plasma is used to sputter the samples in a pulsed mode. The shape of the sputtering crater, which has a diameter of about 2.5 mm, was optimized by variation of the sputtering parameters [5]. The depth resolution of the measurement is up to 5% of the sample depth (depending on the sample properties), while the detection limits, depending on the element and the corresponding emission yield, lie between 0.1 ppm and 50 ppm [189]. By using eight CCDs, the optics of the GD-OES-system can detect the spectral range between 120 nm and 670 nm with a resolution of  $\Delta\lambda < 20$  pm [189]. In order to assure the linearity between the measured intensities and the product of the sputtering rate and the molar fraction of the respective element for all used emission lines, calibration curves were measured and evaluated in Publication [5].

After making sure that the used emission lines fulfill this criterion, the measured depth profiles of intensity versus sputtering time were quantified using reference samples of known composition and homogeneous distribution of the elements. The quantification is performed using an algorithm based on the assumption of constant emission yield [190] and implemented in a self-written software. The procedure of the quantification as well as the choice of the reference samples are discussed in Publication [5] as well.

Since no reference samples with a homogeneous distribution of Rb (laterally as well as over the sample depth) is available, quantification of the depth profiles of Rb is not possible. However, because Rb is only present as a dopant in the CIGSe layers, the quantification of the thickness of the respective samples was performed neglecting the influence of Rb on the sputtering rate. Therefore all elemental depth profiles of Rb will be given as profiles of the measured intensity of the Rb emission line at  $\lambda_{\text{Rb}} = 780$  nm versus the sample depth.

### Analysis of the Surface Chemistry

In order to analyze the composition as well as the chemical environment of the respective elements at the very surface of the absorber layer X-ray photoelectron spectroscopy (XPS) was performed at the CISSY-setup, which is described in detail by Lauermann et al. in Reference [191]. For all measurements performed in this thesis, the Mg- $K_{\alpha}$  line with a transition energy of  $E = (1253.6 \pm 0.2)$  eV was used as excitation source. The pass energy was set to  $E_{\text{pass}} = 10$  eV for the Ga spectra and to  $E_{\text{pass}} = 20$  eV for all other spectra. The measurements were performed on bare absorber layers (with and without PDT), which were kept in vacuum after the deposition. Some of the samples (indicated in the respective sections) were etched in diluted ammonia solution, in order to reduce the amount of surface oxides and Na-containing compounds without affecting the contributions of Cu, In, Ga and Se [192]. Although the subsequent air exposure during the transfer into the XPS-system was kept to

a minimum, there are still 'fresh' oxides and hydroxides forming at the surface of the samples as will be seen in Chapter 4.

In order to be able to identify the compounds at the surface, the measured spectra were fitted using the commercially available software PeakFit, Version 4. In a first step, a linear background, which is not shown in the respective figures, was subtracted from the measured data before the actual fitting was performed using Voigt profiles. The full width at half maximum (FWHM), of both the Gaussian and the Lorentzian part of the profiles, as well as the energetic position, were kept constant for all signal contributions to one spectrum for the different samples (if present). The relative intensity of all presented spectra was not re-scaled.

### Structural Analysis

The Raman spectra that are shown in Section 5.1 were recorded at HZB using a setup based on S&I components equipped with a laser emitting light at a wavelength of  $\lambda = 532$  nm and an Andor iDus InGaAs detector (if not stated otherwise). Other than the removal of the background, no further data treatment was performed on these spectra. All Raman spectra shown in Section 5.2 on the other hand were measured by Dr. Maxim Guc at the Institut de Recerca en Energia de Catalunya (IREC) in Barcelona using a Horiba Jobin-Yvon FHR640 spectrometer coupled with a CCD detector. These measurements were performed using a laser emitting at a wavelength of  $\lambda = 442$  nm in order to establish resonant conditions with the RbInSe<sub>2</sub> [10]. The background was removed and all spectra normalized to the CIGSe A<sub>1</sub>-mode.

Finally, the Raman spectra that are shown in Section 6.1 were recorded in back-scattering configuration on a Jobin-Yvon T64000 spectrometer coupled to a microscope (spot surface  $5 \mu\text{m}^2$ ) at 514.5 nm excitation wavelength at the IMN. For each sample, five spectra on different spots of the investigated sample were measured in order to take lateral inhomogeneities into account. Subsequently, the background was removed from the recorded spectra using the software fityk [193] and all spectra were fitted with a combination of 6 peaks (samples with no CdS signature visible) or 8 peaks respectively (samples with visible CdS contributions). In Figure 3.5 representative examples of a spectrum with (Figure 3.5 a) and without CdS-contributions (Figure 3.5 b) including the respective fits are shown. One peak each is attributed to the CIGSe A<sub>1</sub> (CIGS-1) [194, 195], and the B- and E- contributions (CIGS-2, -3), three to the respective contributions of the ODC (ODC-1, -2, -3) [196] as well as two peaks to the longitudinal optical (LO) phonon scattering in the CdS (CdS-1, -2) [197]. Being aware that more Raman active modes are reported for each of these materials [194, 196, 197], this fitting routine was chosen in order to be able to maintain stable fitting conditions. All CIGSe spectra are normalized to the maximum of the CIGSe A<sub>1</sub> mode. Due to this normalization, it is ensured that all reported effects are directly relatable to the amount of the respective phases in the probed volume of the samples. The origin of the most prominent modes of both the ODC and the  $\alpha$ -phase CIGSe (ODC-1 and CIGS-1), is the motion of the Se-atoms with the cations being at rest [195]. Rincon et al. [195, 196] show that the frequency of the respective A<sub>1</sub>-mode can be derived to

$$\nu \approx \sqrt{\frac{s}{M_{\text{Se}}}}, \quad (3.5)$$

assuming that the vibrational frequencies mainly depend on the interaction of nearest neighbor atoms. Here,  $s$  is a force constant related to the stretching forces between the cations and anions, and  $M_{\text{Se}}$  is the atomic mass of Se. Taking into account that in the ODC-phase there is one  $V_{\text{Cu}}$  for every five Se-atoms, the authors further assume that the force constant in the ODC is about 20% lower than in the  $\alpha$ -phase CIGSe, which is in excellent agreement with the experimentally observed shift of the respective mode [196]. Since factors like stress and strain in the different phases would always influence the lattice parameters and therefore

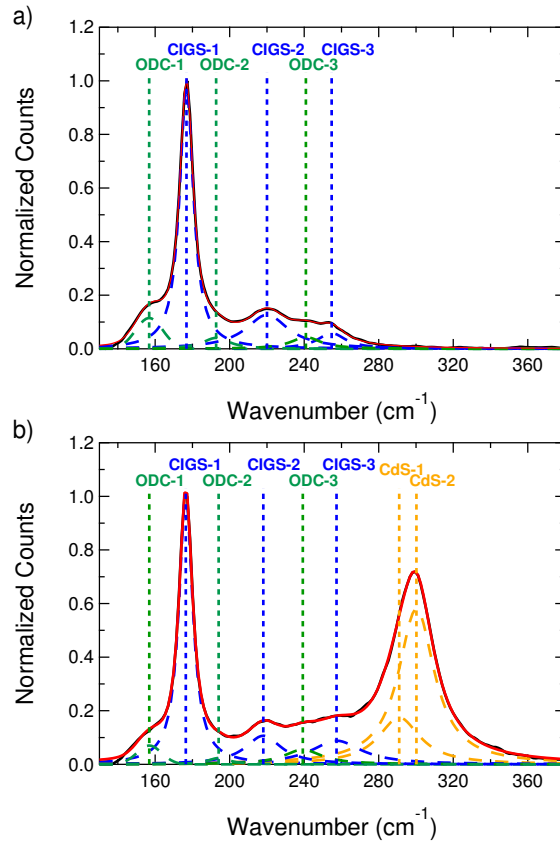


**Figure 3.5:** Examples for the fitting routine used to analyze the recorded Raman spectra. a) Spectrum after 0 min CBD showing no CdS contributions. b) Spectrum after 5 min CBD showing contributions of CIGSe, ODC, and CdS.

lead to a change of  $s$  and consequently to a shift of the measured peaks [198, 199], the relative intensity of ODC-1 to CIGS-1 at a fixed position is a good indicator for a variation of the amount of ODC in the probed sample volume.

The grazing incidence X-ray diffraction (GI-XRD) patterns shown in Section 5.1 were recorded by René Gunder using a PANalytical X'Pert Pro MPD diffractometer employing Cu-K $_{\alpha}$  ( $\lambda = 1.54187 \text{ \AA}$ ) radiation. The measured diffraction patterns were fitted using the LeBail method [200], which describes a theoretical fit that is based on an iterative algorithm to reproduce the measured intensities by refining the structure factors and lattice parameters. All other GI-XRD patterns were measured with a Bruker D8 using Cu-K $_{\alpha}$  radiation as well.

### Optical Analysis

Total reflectance and total transmission measurements were done in a commercial UV-Vis setup, the Lambda 1050 by Perkin Elmer. The absorption coefficient  $\alpha$ , which is shown in Section 5.1 was calculated from the total reflectance  $TR$  and total transmission  $TT$  based on [201] via

$$\alpha = -\frac{1}{d} \cdot \ln \left( \frac{\sqrt{(1 - TR)^4 + 4 \cdot TT^2 \cdot TR^2} - (1 - TR)^2}{2 \cdot TT \cdot TR^2} \right). \quad (3.6)$$

### Time Resolved Photoluminescence

As it was shown in Section 2.1.2 the density of photo-generated electrons, which are generated e.g. by a light pulse, decays exponentially with the lifetime  $\tau_{\text{eff}}$  of the recombination mechanisms (cf. Equation 2.18). However, the actually measured lifetime  $\tau_{\text{exp}}$  (e.g. via time

resolved photoluminescence measurements, trPL) does not necessarily equal  $\tau_{\text{eff}}$  due to several effects of the absorber properties and measurement conditions [202–204]. The actual decay times  $\tau_i$  of the individual recombination mechanisms are overlapped by [202–204]:

- An initial redistribution by diffusion of the generated carriers due to the inhomogeneous generation profile following Lambert-Beer’s law. This effect might be enhanced by energetic relaxation of the carriers due to the grading of the bandgap energy within the absorber layer and potential fluctuations.
- Separation of charge carriers in the electric field due to band bending at the surface of the absorber layer.
- Surface recombination.
- Trapping and de-trapping of charge carriers in shallow defect states in the bulk of the absorber layer.
- Saturation of deep bulk defects due to the photo-generated carriers.

When measuring trPL on bare absorber layers in low injection ( $\Delta n(t = 0) < p_0$ ), the decay of the PL-intensity is dominated by recombination at the surface and in the bulk, drift due to band bending, and the influence of traps. If significant recombination at the surface occurs, a very fast initial decay appears, before the transient is dominated by the effect of bulk recombination [202]. Additionally, the decay can be influenced by the presence of trap states. If trap states with a rather low capture lifetime and high emission lifetime (compared to  $\tau_{\text{eff}}$ ) are present, the initial decay appears shorter than the actual lifetime, because additionally to the recombination of the carriers, some of them are captured by the shallow defect states. Later on, these carriers get emitted back into the respective band and might recombine from there. Therefore the slow component of the decay is prolonged by the time the carriers were captured and is higher than the actual lifetime due to recombination [203].

In high injection ( $\Delta n(t = 0) > p_0$ ) on the other hand, the initial decay of the PL-intensity is additionally influenced by the diffusion of the carriers and bi-molecular recombination [204], but the drift of the carriers can be reduced due to partial screening of the band bending [202].

Depending on the ratio of  $\Delta n$  and the density of trap states, the longer component of the decay can be less influenced by trap states, if these are saturated by the high number of photo-generated carriers. However, the decay is prolonged again by the saturation of deep defects [203].

In order to take these influences into account when trying to quantitatively access the carrier lifetime, one therefore has to measure the excitation not only intensity- but also temperature-dependent [202–205]. However, just measuring the trPL at different excitation intensities and comparing the results of samples from one experiment series can give a good approximation of the qualitative trend of the carrier lifetime. This is done by fitting the background corrected data with a bi-exponential decay defined as

$$I(t) = A_1 \cdot \exp\left(\frac{-t}{\tau_1}\right) + A_2 \cdot \exp\left(\frac{-t}{\tau_2}\right). \quad (3.7)$$

Here  $A_{1,2}$  are the amplitudes and  $\tau_{1,2}$  the lifetimes of the respective decay. Then an effective, experimental lifetime is calculated using the weighted average of both lifetimes:

$$\tau_{\text{exp}} = \frac{\tau_1 A_1 + \tau_2 A_2}{A_1 + A_2}. \quad (3.8)$$

In this work, the measurements of the carrier lifetime by trPL are performed in a custom-built setup using a pulsed 660 nm laser as excitation source and time-correlated single photon counting with an InGaAs photomultiplier with a time resolution of about 400 ps. The

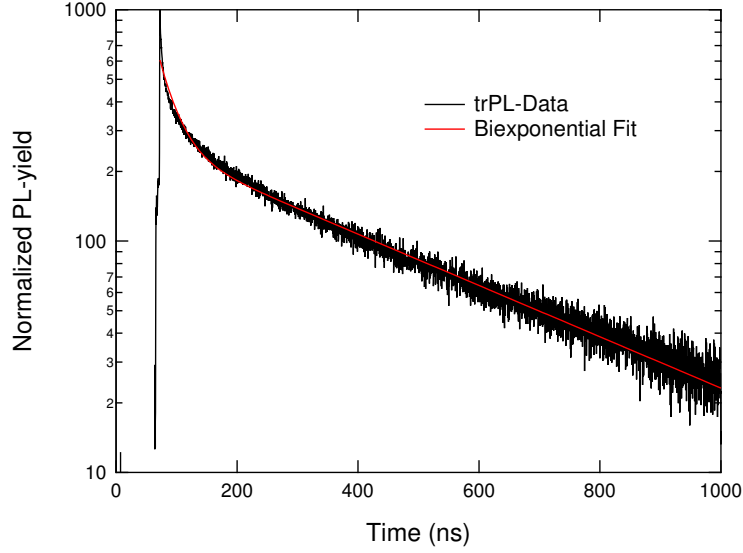


**Figure 3.6:** Example of a measured trPL-transient (back curve) and the bi-exponential fit of the data using Equation 3.7. Due to the very fast initial decay, the first  $\sim 150$  ns of the transient are not properly fitted by the used function.

excitation spot size is  $A_S \approx 490 \mu\text{m}^2$ . The laser power is set to  $P_1 = 50 \text{ nW}$ ,  $P_2 = 150 \text{ nW}$ , and  $P_3 = 500 \text{ nW}$ , which translates to a photon density per pulse between  $5.5 \cdot 10^{10} \text{ photons/cm}^2$  and  $5.5 \cdot 10^{11} \text{ photons/cm}^2$ , and to a generated carrier density of  $\Delta n = 1.55 \cdot 10^{15} \text{ cm}^{-3}$  to  $\Delta n = 1.55 \cdot 10^{16} \text{ cm}^{-3}$  using an absorption coefficient of  $\alpha = 2.8 \cdot 10^4 \text{ cm}^{-1}$  at the wavelength of the laser  $\lambda = 660 \text{ nm}$  (estimated from UV-Vis measurements of CIGSe on glass) as well as assuming that all carriers are generated within a cylindrical volume with a diameter of the spot size of the laser:

$$\Delta n = \frac{P \cdot \lambda \cdot \alpha}{h \cdot c \cdot \nu \cdot A_S}. \quad (3.9)$$

The samples are prepared from complete solar cells: the window and buffer layer were etched off using HCl after which the samples were immediately transferred into a glove box. Within the glove box, each sample is placed on a Cu-plate, of which the temperature can be controlled by a Peltier element. The Cu-plate/Peltier-setup is placed in a small metal box with a quartz window and is sealed in the glove box ensuring that the sample stays in a  $\text{N}_2$ -atmosphere avoiding oxygen-induced degradation of the carrier lifetime [203, 205]. During the measurements of the carrier lifetime at room temperature, the sample temperature is logged by a small Pt100 temperature sensor placed on top of the Cu-plate and controlled to be stable within the range of  $1^\circ\text{C}$  via the Peltier element.

Note that due to the fact that the window layers were etched off of the absorber layers before the measurements, the transients show at least one additional feature to the bi-exponential decay due to HCl-induced surface modifications of the absorber layer, which presumably induce an increased surface recombination. A typical fit of a data set is shown in Figure 3.6. Due to the very fast initial decay, the fit does not accurately describe the first 50 ns after excitation. As it was stated above, this effect has a stronger influence on the measurements under low injection, which therefore tend to underestimate the lifetime due to bulk recombination. The lifetime obtained from the measurements under high injection are overestimating the actual lifetime, due to trapping and the saturation of deep defects. Therefore in this work, only the qualitative trend of the measured lifetimes of each experiment series will be analyzed.

### 3.2.2 Device Characterization

#### Optoelectronic Measurements

The  $j$ - $V$ -measurements were performed under standard test conditions (AM 1.5 spectrum,  $1000 \text{ W} \cdot \text{m}^{-2}$ ,  $25^\circ\text{C}$ ) using a WACOM A+ dual source solar simulator equipped with a combination of a xenon and a halogen lamp and a water cooled sample stage. The lateral inhomogeneity of the system is given to be lower than 2% on a  $10 \cdot 10 \text{ cm}^2$  area, the instability over time lower than 1%. The intensities of the lamps were calibrated using certified silicon reference samples. Measurements were performed with a Keithley SMU using an integration time of 2 ms per measurement point and a waiting time of 20 ms. The voltage sweep of the measurement was set from negative to positive voltages. No light soaking was performed prior to the measurements.

Next to the analysis of the actual  $j$ - $V$ -curves of selected cells, so-called boxplots are used in order to represent the PV-parameters of groups of solar cells and to get an overview of the spread of the measured data (see for example Figure 4.1). Hereby one box contains data of at least one substrate (15 cells). The centered line of a box marks the median of the measured values, the boxes below and above contain 25% of the measured values each, and the outer whiskers include the next 15% each.

To determine the  $EQE$ , the cell to be measured is contacted without applying a bias voltage. Then it is illuminated with monochromatized light of a combination of a halogen and a xenon lamp through a grid monochromator. To ensure realistic conditions during the measurements (i.e. the behavior of the cell under illuminated short-circuit conditions), the solar cell is additionally irradiated with white light bias. In order to be able to distinguish the current due to the white light and due to the monochromized light, a chopper wheel is used to periodically interrupt the white light. As a result, the white light current can be calculated from the measured signal and removed before the cleaned signal is passed to a Stanford Research lock-in amplifier to be further processed [206]. To determine the quantum efficiency from the current measurement, it is compared to the current measurement of a reference sample with known quantum efficiency. The spectra were taken with 10 nm steps over the wavelength range  $300 \text{ nm} < \lambda_{\text{Measured}} < 1400 \text{ nm}$ . The optical bandgap energy of the solar cell can be derived using the maximum of the derivative of the  $EQE$ , i.e. using the definition of the photovoltaic bandgap energy as described by Equation 2.33, setting  $a = b$ .

In order to obtain the internal quantum efficiency ( $IQE$ ), the total reflectance  $TR$  of the same sample was measured using the UV-Vis setup described above. The  $IQE$  is then calculated using  $IQE = EQE \cdot (1 - TR)^{-1}$ .

Furthermore, the Urbach energy is calculated from the  $IQE$  using the procedure established by Troviano and Taretto [207] for double-graded energy bandgap profiles with  $E_{g,\text{front}} < E_{g,\text{back}}$ , which is the case for all devices analyzed in this thesis. The authors show that the sub-bandgap absorption can be described by the Equation

$$\ln[-\ln(1 - IQE_{\text{Sub}}(h\nu))] = \ln(A_1) + \frac{h\nu}{E_U}. \quad (3.10)$$

Here  $IQE_{\text{Sub}}$  is the  $IQE$  in the photon energy-range in which only sub-gap absorption takes place ( $h\nu < E_{g,\text{min}} + \frac{E_U}{2}$ ) and  $A_1$  is a positive scalar being independent of  $h\nu$ . Plotting the left hand side of Equation 3.10 versus the photon energy  $h\nu$ , enables to extract  $E_U$  from a linear fit in the region below the estimated minimum bandgap energy.

Furthermore, the  $IQE$  can be used to extract the effective collection length  $L_{\text{eff}}$  (cf. Equation 2.20). Since photons with lower energy are – in average – penetrating deeper into the absorber layer than photons with higher energies, recombination in the bulk (and therefore a rather small  $L_{\text{eff}}$ ) leads to a lowered red-response in the  $IQE$ . The following connection of  $IQE$  and  $L_{\text{eff}}$  was shown [208]:

$$IQE = K(1 - \exp(-L_{\text{eff}} \cdot \alpha(\lambda))). \quad (3.11)$$

Here  $K$  is a dimensionless prefactor modulating the maximum of the  $IQE$ . For the present work it was chosen to set  $K = 1$  and linearize Equation 3.11:

$$L_{\text{eff}} \cdot \alpha(\lambda) = -\ln(1 - IQE). \quad (3.12)$$

Using this Equation the effective collection length can be extracted as the slope from plots of  $-\ln(1 - IQE)$  versus  $\alpha(\lambda)$ .

### Capacitance Profiling

Capacitance-voltage-measurements were used to determine the charge carrier density of the absorber layer. Assuming that every acceptor defect releases one hole into the absorber layer, it is  $p = N_{\text{CV}}$  with  $N_{\text{CV}}$  being the shallow acceptor density at the edge of the SCR. In order to determine  $N_{\text{CV}}$  one uses the fact that in CIGSe solar cells the doping density on the  $n$ -side of the heterojunction is usually much higher than the doping density on the  $p$ -side of the junction, which – according to Equation 2.6 – enables to assume that the SCR is mostly located in the absorber layer. Further assuming that the SCR is completely depleted from free charge carriers, it can be shown [209] that the SCR can be described similar to a plate capacitor with an inserted dielectric and the capacitance

$$C = A_{\text{Dev}} \epsilon_0 \frac{1}{\frac{d_{\text{SCR}}^{\text{CIGSe}}}{\epsilon_{\text{CIGSe}}} + \frac{d_{\text{SCR}}^{\text{CdS}}}{\epsilon_{\text{CdS}}} + \frac{d_{\text{SCR}}^{\text{ZnO}}}{\epsilon_{\text{ZnO}}}}, \quad (3.13)$$

where  $A_{\text{Dev}}$  is the area of the device. Assuming  $d_{\text{SCR}}^{\text{ZnO}} \approx 0$  due to the high doping of the ZnO, Equation 2.7 can be used to rewrite Equation 3.13:

$$\frac{1}{C} = \frac{1}{A_{\text{Dev}} \epsilon_0} \sqrt{\left(\frac{d_{\text{CdS}}}{\epsilon_{\text{CdS}}}\right)^2 + \frac{2\epsilon_0(V_{\text{bi}} - V)}{qN_{\text{CV}}\epsilon_{\text{CIGSe}}} + \frac{N_{\text{D}}d_{\text{CdS}}^2}{N_{\text{CV}}\epsilon_{\text{CdS}}\epsilon_{\text{CIGSe}}}}, \quad (3.14)$$

where  $V$  is a DC voltage applied to the device. This can be used to derive the well-known Mott-Schottky representation of the capacitance:

$$\frac{1}{C^2} = \frac{1}{A_{\text{Dev}}^2 \epsilon_0^2} \left( \left(\frac{d_{\text{CdS}}}{\epsilon_{\text{CdS}}}\right)^2 + \frac{2\epsilon_0(V_{\text{bi}} - V)}{qN_{\text{CV}}\epsilon_{\text{CIGSe}}} + \frac{N_{\text{D}}d_{\text{CdS}}^2}{N_{\text{CV}}\epsilon_{\text{CdS}}\epsilon_{\text{CIGSe}}} \right), \quad (3.15)$$

which e.g. can be used in order to determine the built-in voltage of the device. However, in most publications [209, 210] and also in this work, the influence of the geometrical capacitance of the buffer layer is neglected due to the assumptions stated above, simplifying the Mott-Schottky expression to

$$\frac{1}{C^2} = \frac{2(V_{\text{bi}} - V)}{q\epsilon_{\text{CIGSe}}\epsilon_0 A_{\text{Dev}}^2 N_{\text{CV}}}. \quad (3.16)$$

Using this equation for the determination of  $N_{\text{CV}}$  is only possible for simple  $p/n$ -heterojunctions consisting of homogeneously doped semiconductors without any deep defects [209]. When applying a small AC-voltage  $V_{\text{AC}}$  to the device additionally to  $V$ ,  $d_{\text{SCR}}$  gets modulated by this voltage and the shallow defects at the edge of the SCR get charged and discharged with the frequency of  $V_{\text{AC}}$ . This leads by definition of the capacitance via the electric charge  $Q$ ,

$$C = A \frac{dQ}{dV}, \quad (3.17)$$

to a variation of the capacitance in dependence of the local doping density  $N_{\text{CV}}(x)$ , since  $N_{\text{CV}}$  at the edge of the SCR determines the change in charge. It can be shown [211, 212] that the change in capacitance follows

$$\frac{dC}{dV} = -\frac{A_{\text{Dev}}\epsilon_{\text{CIGSe}}\epsilon_0}{d_{\text{SCR}}^2} \cdot \frac{dd_{\text{SCR}}}{dV}. \quad (3.18)$$

Furthermore, the combination of Equations 3.13, 3.14, and 3.18 leads to [211, 212]:

$$N_{CV}(d_{SCR}) = \frac{-C^3}{q\epsilon_{\text{CIGSe}}\epsilon_0 A^2 dC/dV}. \quad (3.19)$$

For small changes of  $dV$ , the change of the capacitance can be assumed to be linear with the change in voltage and one can replace  $dC/dV$  by  $\Delta C/\Delta V$ , which is more practical for the evaluation of measurement data.

Please note that this expression is still only valid in cases where no deep defects are present, which is not necessarily true for CIGSe devices. However, in this thesis, the property  $N_{CV}$  is mainly used as a relative measure for the comparison of different devices and in order to find an estimate for  $\Delta V_{OC}^{CV}$  as described in Section 2.1.3 justifying the neglect of the impact of deep defects. For a more detailed analysis of this influence of deep defects, the reader is referred to the work of T. Eisenbarth [209].

In order to determine the  $N_{CV}$ -profile of a solar cell, it was contacted and stored in dark for 5 minutes before a DC voltage ranging from -0.5 V to +0.5 V as well as an AC-voltage of  $V_{AC} = 20$  mV at a frequency of  $\nu = 100$  kHz were applied using a self-built setup based on an Agilent 4284A LCR meter. The influence of the connecting probes was corrected before every measurement. Furthermore, the parallel resistance of the contacted cell was measured prior to each  $C$ - $V$ -measurement and only cells showing resistances of at least several hundred Ohm were analyzed. It was also ruled out that the current flowing in the devices exceeds the limit of the LCR meter.

Throughout this thesis, the minimum of the  $N_{CV}$ -profiles, which will be called  $n_{CV}$ , will be used as a measure of the intrinsic  $p$ -type doping of the absorber layer. Although it is known that this way of the determination of the carrier density slightly underestimates the real value of  $p_0$  [210], it is widely accepted in the community, because it gives easily comparable results and qualitatively correct trends.

#### 3.2.3 Numerical Device Simulations

In order to model the measurement results obtained by various analytical methods, the effects of parameters, such as energy bandgap gradients, band line-up, doping densities, carrier lifetimes, etc. on the measurement results can be simulated. In the present work, the program SCAPS-1D, which was developed at the University of Gent [213], is used. With SCAPS, a one-dimensional stack of up to seven semiconducting layers and their interfaces can be modeled between two contacts, with numerous parameters selectable in each component. As a result of the underlying one-dimensional model, multi-dimensional structures such as GBs, surface roughness or patterning, and lateral potential fluctuations can not be considered with SCAPS.

SCAPS determines the properties of the designed components by deriving the charge distribution as well as the drift and diffusion currents by the Poisson equation (cf. Equation 2.4) and the continuity equation (cf. Equation 2.8). The current densities  $j_{n,p}$  are composed of the respective drift and diffusion current densities (Equations 2.1 and 2.2). Since the layer stack is divided into  $N$  discrete simulation points, a total of  $5N$  non-linear equations are solved in order to simulate the potential and current density profiles over the entire device. SCAPS chooses tighter intervals between the simulation points near interfaces and further distances deep within the individual layers to give more weight to the influence of the interfaces. SCAPS starts with a first guess of the potential  $\phi(x)$  and carrier densities, whereupon the potential is calculated and corrected via the Poisson equation and the carrier densities are calculated via the continuity equations. This procedure is continued iteratively until a convergence criterion is reached and the final values for potential and carrier densities can be determined.

Table 3.1 lists the input parameter set for the CIGSe, CdS, RbInSe<sub>2</sub>, and ZnO layers as used as starting point for the simulations performed within this work, if not mentioned otherwise; they are based on the parameters from Reference [45]. Additionally, to the data

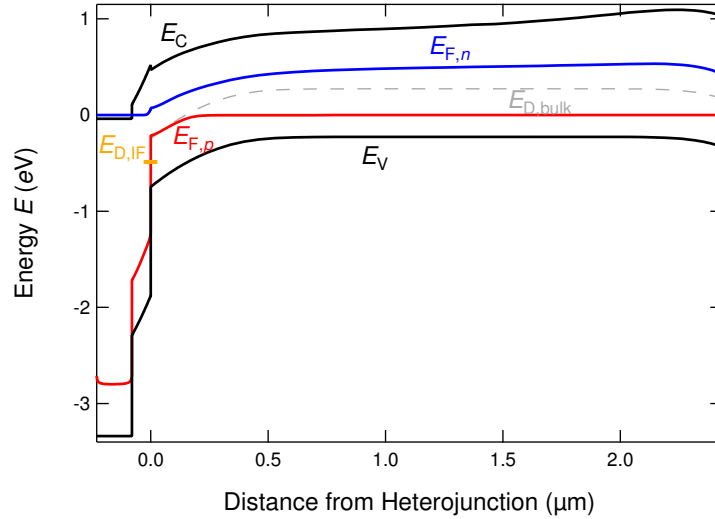


**Figure 3.7:** Energy band diagram of the reference device used for SCAPS modeling. The parameters are given in Table 3.1 and in the text.

shown in the table, a back contact barrier was added to the modeled device. The reference barrier height, which was estimated using the  $j$ - $V$ -curves of some Rb-free baseline devices, was set to  $\Phi_{BC} = 150$  meV below the CBM of the absorber layer. The total reflectance of the front contact, which was implemented without any barrier to the i-ZnO, was measured by UV-Vis. In addition to the bulk defects mentioned in Table 3.1, an acceptor-like interface defect was introduced to the heterointerface CdS/CIGSe at the energetic position of  $E_{Def,IF} = 0.3$  eV above the VBM of the absorber layer.

Figure 3.7 shows the energy band diagram of this reference model (without RbF) with the defect levels of the bulk-defects ( $E_{Def,B}$ ), the interface-defect as well as the back-contact barrier (under illumination without applied bias). In Chapter 8 this reference device is modified using experimental results for GD-OES depth profiles, measurements of the carrier density via  $C$ - $V$ -profiling, and absorption spectra via UV-Vis measurements to simulate the effects of the Rb-conditioning of the absorber layer in accordance with the experimentally derived results presented in Chapters 4 to 6. Thereby it is possible to not only model the general effects of a variation of these parameters on e.g. the modeled  $j$ - $V$ -curve, but also to actually fit experimental data using SCAPS. In order to do so, SCAPS allows up to nine interdependent fit parameters, which are then iteratively varied within a range of values the user can choose. After each iteration, SCAPS is calculating the desired properties (e.g. a  $j$ - $V$ - or a  $C$ - $V$ -curve) and the deviation of the simulated curve to a measured curve. By minimizing this deviation the accuracy of the fit is optimized.

Table 3.1: Input parameters for the four modeled layers of a chalcopyrite solar cell, as utilized in the present work for the simulation with SCAPS (unless stated otherwise). The data for the effective densities of states (DOS), the thermal velocities, mobilities, and dielectric permittivity were taken from Reference [45]

Note that the interface defect at the CdS/CIGSe-interface in the devices without RIS-layer and the interface defect at the CdS/RIS-interface in the devices with RIS-layer are at the same energetic position with regard to the CBM and VBM of the CdS-layer at the respective interface. Furthermore, it should be noted that for the parameter variations in Chapter 8 not always both defects are present in order to be able to analyze their effects independently. It is indicated in the caption of each figure, which defects are present in the respective device model.

Symbol	Parameter	Unit	CIGSe	CdS	RbInSe <sub>2</sub>	ZnO
$E_g$	Bandgap Energy	eV	from GD-OES	2.4	2.8	3.3
$EA$	Electron Affinity	eV	from GD-OES	4.3	varied	4.45
$N_C$	Eff. DOS in the CB	cm <sup>-3</sup>	$2.2 \cdot 10^{18}$	$2.2 \cdot 10^{18}$	$2.2 \cdot 10^{18}$	$2.2 \cdot 10^{18}$
$N_V$	Eff. DOS in the VB	cm <sup>-3</sup>	$1.8 \cdot 10^{19}$	$1.8 \cdot 10^{19}$	$1.8 \cdot 10^{19}$	$1.8 \cdot 10^{19}$
$v_{th,e}$	Th. Electron-Velocity	cm s <sup>-1</sup>	$1 \cdot 10^7$	$1 \cdot 10^7$	$1 \cdot 10^7$	$1 \cdot 10^7$
$v_{th,h}$	Th. Hole-Velocity	cm s <sup>-1</sup>	$1 \cdot 10^7$	$1 \cdot 10^7$	$1 \cdot 10^7$	$1 \cdot 10^7$
$\mu_e$	Electron-Mobility	cm <sup>-2</sup> V <sup>-1</sup> s <sup>-1</sup>	100	100	100	40
$\mu_h$	Hole-Mobility	cm <sup>-2</sup> V <sup>-1</sup> s <sup>-1</sup>	25	25	25	25
$\epsilon_r$	Rel. Dielectric Permittivity		13.6	10	13.6	9
$d$	Thickness	nm	from GD-OES	60	varied	150
$N_D/N_A$	Min. Carrier Concentr.	cm <sup>-3</sup>	$p = 2.9 \cdot 10^{15}$	$n = 1 \cdot 10^{16}$	varied	$n = 1 \cdot 10^{19}$
$\alpha$	Absorption Coefficient	cm <sup>-1</sup>	from UV-Vis	$\sqrt{h\nu - E_g}$	from UV-Vis	from UV-Vis
Neutral (Gaussian) Defect States						
$N_{Def,B}$	Defect Density	cm <sup>-3</sup>	$1.1 \cdot 10^{14}$	$1.8 \cdot 10^{18}$	-	$1.8 \cdot 10^{16}$
$\sigma_D$	Distribution Width	eV	Single Defect	0.1	-	0.1
$E_{Def,B}$	Energetic Position	eV	0.5 above VB	Mid-gap	-	Mid-gap
$\sigma_n$	Capture Cross Section	cm <sup>2</sup>	$1.8 \cdot 10^{-14}$	$1 \cdot 10^{-13}$	-	$1 \cdot 10^{-12}$
$\sigma_p$	Capture Cross Section	cm <sup>2</sup>	$1 \cdot 10^{-15}$	$1 \cdot 10^{-13}$	-	$1 \cdot 10^{-12}$
Single Acceptor Interface Defect States						
	Interface without RIS		CdS/CIGSe			
	Interfaces with RIS				RIS/CIGSe	CdS/RIS
$N_{Def,IF}$	Defect Density	cm <sup>-3</sup>	$2.26 \cdot 10^{11}$		varied	$1.8 \cdot 10^{11}$
$\sigma_D$	Distribution Width	eV	Single Defect		Single Defect	Single Defect
$E_{Def,IF}$	Energetic Position	eV	0.3 eV above $E_V^{CIGSe}$		0.3 eV above $E_V^{CIGSe}$	0.96 eV below $E_C^{CdS}$
$\sigma_n$	Capture Cross Section	cm <sup>2</sup>	$1.8 \cdot 10^{-16}$		$1.8 \cdot 10^{-16}$	$1.8 \cdot 10^{-16}$
$\sigma_p$	Capture Cross Section	cm <sup>2</sup>	$1.2 \cdot 10^{-14}$		$1.2 \cdot 10^{-14}$	$1.2 \cdot 10^{-14}$

## 4 Disentangling the Physical Effects of an RbF-PDT

In this chapter, the general effect of an RbF-PDT on the material and device properties of CIGSe thin film solar cells is investigated. Thereby the morphological and compositional changes induced by the RbF-PDT as well as its impact on the device parameters are compared with reference samples free of heavy alkali elements. In order to be able to elucidate the different effects of the RbF-PDT and decipher its mechanisms, a two-dimensional approach is chosen.

In Section 4.1, which is based on Publication [1], the effectiveness of the PDT on absorber layers with  $CGI = 0.9$  is analyzed in dependence on the amount of RbF deposited, in order to be able to identify its general effects. Since the variation of the RbF-amount is realized by a variation of the process time of the PDT, it will be referred to as the 'Time-series'.

In Section 4.2, on the other hand, the effectiveness of the PDT is analyzed in dependence on the integral  $CGI$  of the CIGSe absorber layers in order to examine the interplay of the fraction of  $\alpha$ -phase CIGSe and the ODC with the RbF-PDT in more detail. This second experimental series will be referred to as the 'CGI-series' and the respective section is based on Publication [4].

### 4.1 Mechanisms of the RbF-PDT: Effects of the Treatment Time

One handle in understanding the RbF-PDT is to carefully vary all involved parameters (such as the RbF- and Se-evaporation rates, the PDT-duration, the substrate temperature, and the subsequent annealing and cool-down procedures) and to analyze and model the resulting trends. Based on initial optimization work [214], in a first step, the PDT-procedure described in Section 3.1.1 was developed with respect to all aforementioned parameters. During the final optimization steps, it became clear that the best way to understand the mechanism of the RbF-PDT is to analyze the trend observed when varying the amount of RbF deposited on the CIGSe absorber layers. In the following the results of an experiment are described in which the duration of the PDT of otherwise identically processed absorber layers ( $CGI = 0.9$ ) was varied from 0 min up to 20 min at a constant deposition rate. The resulting PV-parameters are represented as boxplots in Figure 4.1.

While there is no visible correlation between  $j_{SC}$  and the duration of the PDT, a clear trade-off between increasing  $V_{OC}$  and decreasing  $FF$  is observed as the duration of the RbF-deposition increases. This trade-off leads to an optimum efficiency at a duration of 10 min with an efficiency enhanced by about 0.8% (absolute) compared to the Rb-free reference device.

The sample that was treated with RbF for only one minute does not follow this overall trend but shows strongly deteriorated  $V_{OC}$  and  $FF$ . Furthermore,  $V_{OC}$  of the sample which underwent the longest PDT (20 min) drops compared to the samples with slightly shorter PDT duration. In the following the general trends, as well as these two exceptions, are analyzed in more detail.

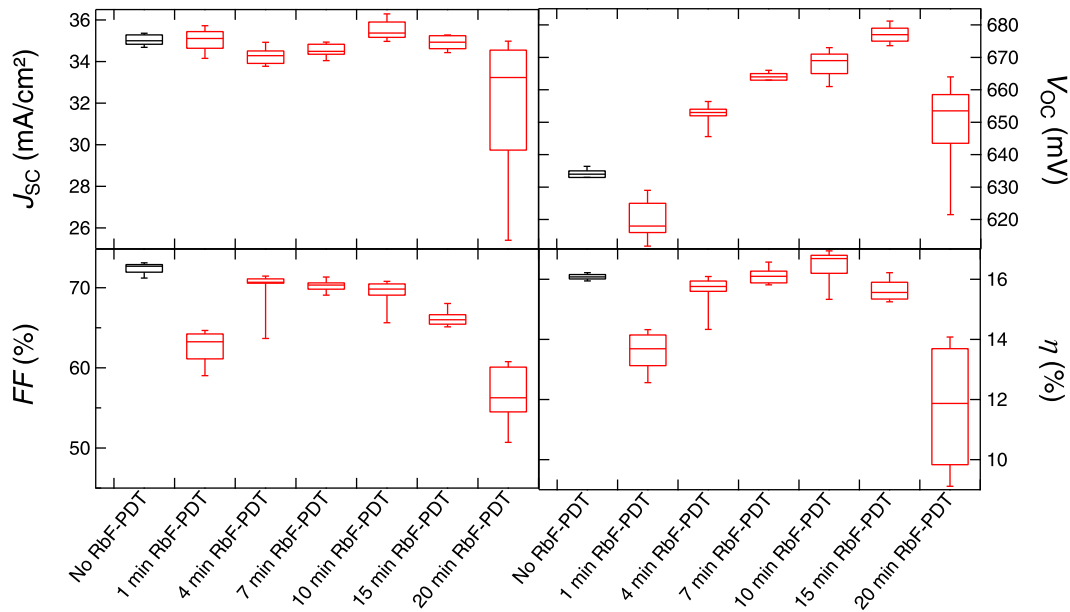


**Figure 4.1:** Boxplots of the electrical parameters of CIGSe solar cells ( $CGI = 0.9$ ) determined by  $j$ - $V$ -analysis. Each box represents the values measured on 15 cells of the corresponding substrate.

#### 4.1.1 Time-Series: CIGSe Bulk and Device Effects

##### Beneficial Effect of the RbF-PDT: $V_{oc}$ -gain

###### Part I: Results

In Figure 4.2 depth profiles of the Na and Rb content in these samples are shown as measured by GD-OES. All measurements were carried out after etching off the window from the complete solar cells using HCl. The profiles are corrected for their slightly different thicknesses by aligning the onset of the molybdenum signals. The measured profiles reveal that with prolonged Rb-deposition Na is steadily driven from the absorber layers, leading to an overall lower Na-content within the CIGSe and especially a flatter Na-distribution near the back contact (see Figure 4.2 a). Accordingly, the strong increase of the Na-signal in the untreated sample (and in that after  $t_{PDT} = 1$  min) between about  $2.5 \mu\text{m}$  and  $2.8 \mu\text{m}$  is reduced in the other RbF-treated samples.

The correlation of the Rb-distribution in the CIGSe with  $t_{PDT}$  is less obvious. A clear trend of increasing Rb-content with  $t_{PDT}$  can be seen at the CIGSe/Mo-interface and a higher amount of Rb is located at the surface of the absorber layer after longer PDTs, although the latter trend is not completely steady: The Rb-intensity at the surface of the samples with  $t_{PDT} < 15$  min shows only a slight trend of increasing Rb with  $t_{PDT}$ , which is indistinguishable within the error of the measurement. The two samples with  $t_{PDT} \geq 15$  min on the other hand show a significantly increased amount of Rb accumulating at the surface of the CIGSe. The amount of Rb detected in the bulk of the absorber layers, however, shows only a weak trend of increasing  $I_{Rb}$  with  $t_{PDT}$ , which is indistinguishable within the error. Especially since the Rb-signal is not quantified (cf. Section 3.2), no direct conclusions about the amount of Rb incorporated into the bulk of the CIGSe can be drawn.

In order to gain more insights into the distribution of Rb within the absorber layer, STEM imaging of the near-surface region was performed. Figure 4.3 a shows a HAADF image of a cross section of a CIGSe absorber layer after 10 min RbF-PDT. Figures 4.3 b to h show elemental maps measured by STEM-EDX on the same area. Next to surface effects, which will be discussed in the next section, a GB is visible in the displayed view (ellipses in Figure 4.3). STEM-EDX shows that this GB is enriched in Rb, Cu, and O, while it shows slightly lower count-rates for Se. This result suggests that most of the Rb, detected within the bulk of the absorber layer by GD-OES, is actually located at GBs.

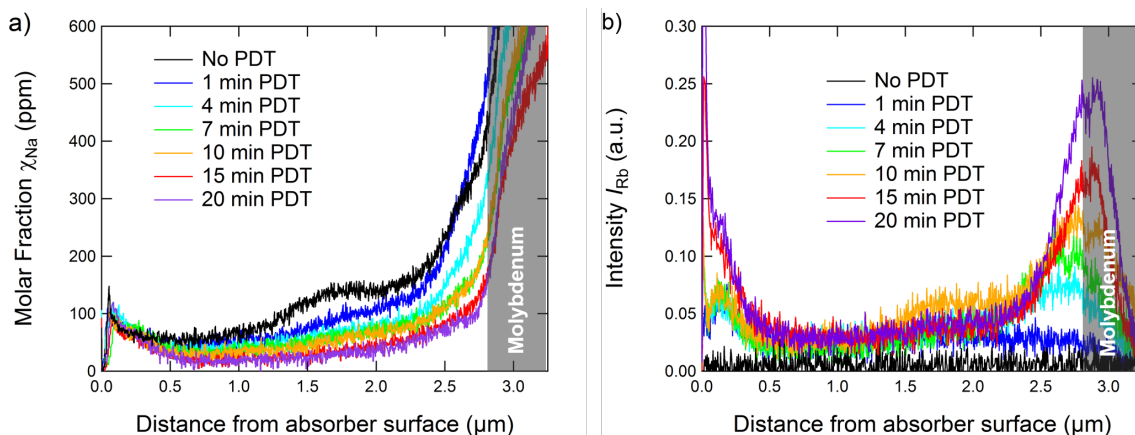


**Figure 4.2:** a) GD-OES depth profiles of Na measured on seven CIGSe samples with varied RbF-amount deposited after etching the window off of the solar cells using HCl. b) Depth profiles of the Rb-signal (unquantified, cf. Section 3.2) of the same samples. Note that the information value of the Rb-profiles is limited since they were measured about 1 year later than the rest of the measurements shown in this section due to an upgrade of the GD-OES system, which only then enabled to detect the Rb-emission.

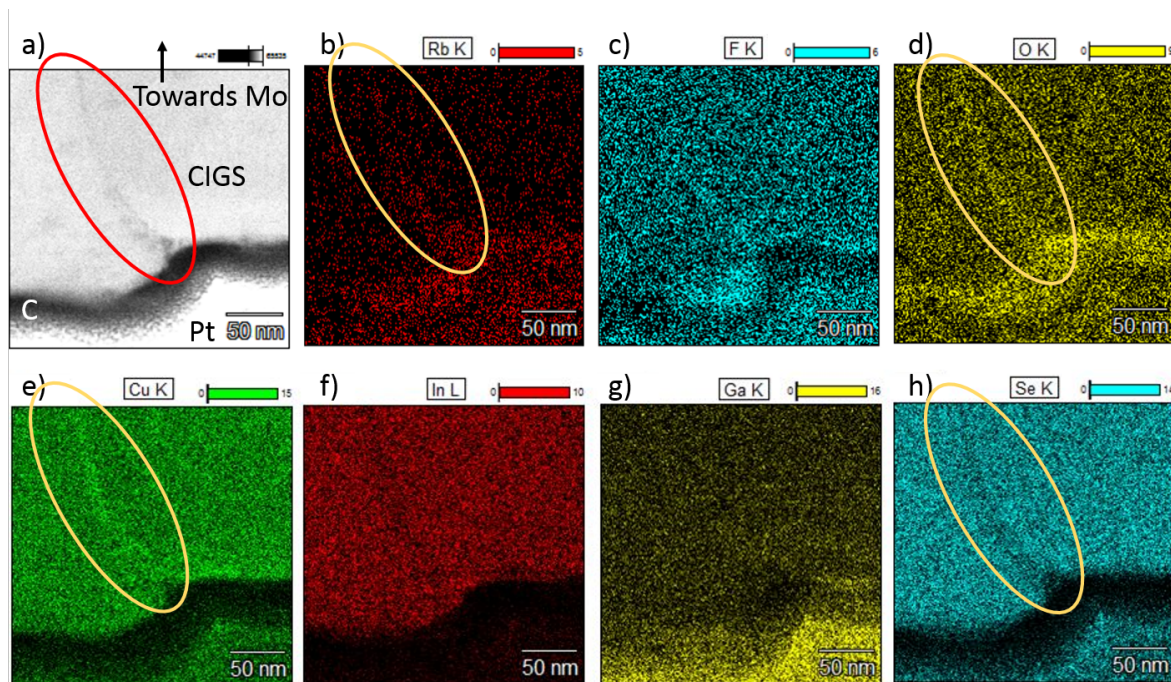


**Figure 4.3:** a) STEM-ADF image of the surface of a CIGSe absorber layer ( $CGI = 0.9$ , after an RbF-PDT with  $t_{PDT} = 10$  min) covered with carbon and platinum to protect the surface from damage during the focused ion beam preparation. b) to h): STEM-EDX maps of Rb (b), F (c), O (d), Cu (e), In (f), Ga (g) and Se (h). The area marked by the ellipses shows a GB, which is enriched in Rb, O, and Cu as well as depleted of Se.

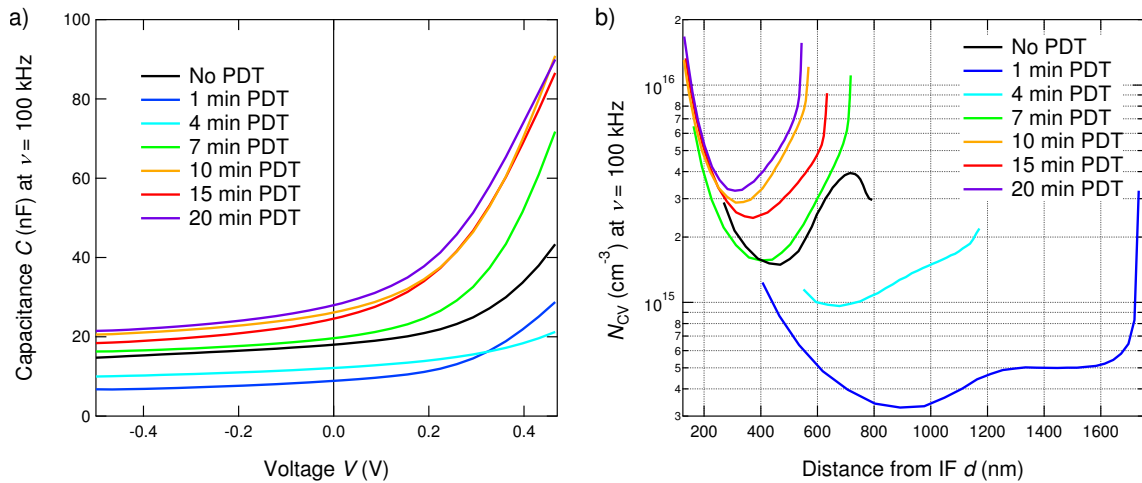


**Figure 4.4:** a)  $C$ - $V$ -curves of the solar cells based on absorber layers with varied RbF-amount deposited. b)  $N_{CV}$ -profiles extracted from the  $C$ - $V$ -curves of the corresponding solar cells.

Figure 4.4 a shows the  $C$ - $V$ -profiles of the corresponding devices, Figure 4.4 b the respectively determined profiles of the carrier concentration  $N_{CV}$ . As can be seen, a very short RbF-PDT leads to a severe reduction of the minimum of these profiles,  $n_{CV}$ , of almost one order of magnitude. Furthermore, electron beam induced current measurements show that the electrostatic potential fluctuations  $\sigma_{el}$  on this sample are about a factor 4 higher than on the reference sample or samples with longer RbF-PDT (see Appendix A.1 and Publication [12]). These two effects can, following Equations 2.41 and 2.44, explain the observed drop in  $V_{OC}$  for this sample.

When deploying longer RbF-PDTs,  $n_{CV}$  is recovered leading to even higher values as measured on the Rb-free reference device for  $t_{PDT} \geq 7$  min. While the initial reduction of  $n_{CV}$  can be directly explained by the lower Na-concentration, the following increase of the carrier concentration with  $t_{PDT}$  cannot be explained by the Na-depth profiles. This shows that there is an additional doping effect due to the incorporation of Rb – either directly or indirectly, e.g. via its interaction with Na. Furthermore, the level of the potential fluctuations  $\sigma_{el}$  is reduced to the same level as that of the reference sample (see Appendix A.1 and Publication [12]). The intermediate increase in  $\sigma_{el}$  is most likely due to the incomplete covering of the surface of the CIGSe by RbF after the very short PDT.

Additionally, to the effect of Rb on the carrier density, the samples with  $t_{PDT} \geq 7$  min show a strongly increasing capacitance at high positive bias voltages (see Figure 4.4 a). An additional contribution to the capacitance at these voltages might be attributed to an additional or more pronounced defect. This is surprising since it would mean that the  $V_{OC}$  of these devices increases after the RbF-PDT, despite the fact that there is an additional defect contribution present. However, other origins for this increased capacitance are possible as well, such as the influence of a back contact barrier.

Figure 4.5 a shows the results of trPL measurements performed on this set of samples and Figure 4.5 b shows the results of the respective fits following the procedure described in Section 3.2. As it was already discussed in Section 3.2, the sample preparation and measurement conditions do not allow for a quantitative evaluation of the actual effective carrier lifetime  $\tau_{eff}$  but only for a qualitative analysis of the trend of the experimentally derived carrier lifetime  $\tau_{exp}$ . The discussion in Section 3.2 furthermore revealed that  $\tau_{exp}$  is overestimating  $\tau_{eff}$  in measurements at high injection. This becomes apparent e.g. from the sample with  $t_{PDT} = 15$  min, of which  $\tau_{exp}^{high} = 400$  ns seems to be too high for a device with  $V_{OC} \approx 680$  mV.

However, a qualitative analysis of the trend of the measured effective lifetime  $\tau_{exp}$  is possible. Independent of  $\Delta n$ ,  $\tau_{exp}$  shows the very same trend as one can observe in  $V_{OC}$ : Starting from the reference sample,  $\tau_{exp}$  slightly drops after 1 min of RbF-PDT before it steadily rises

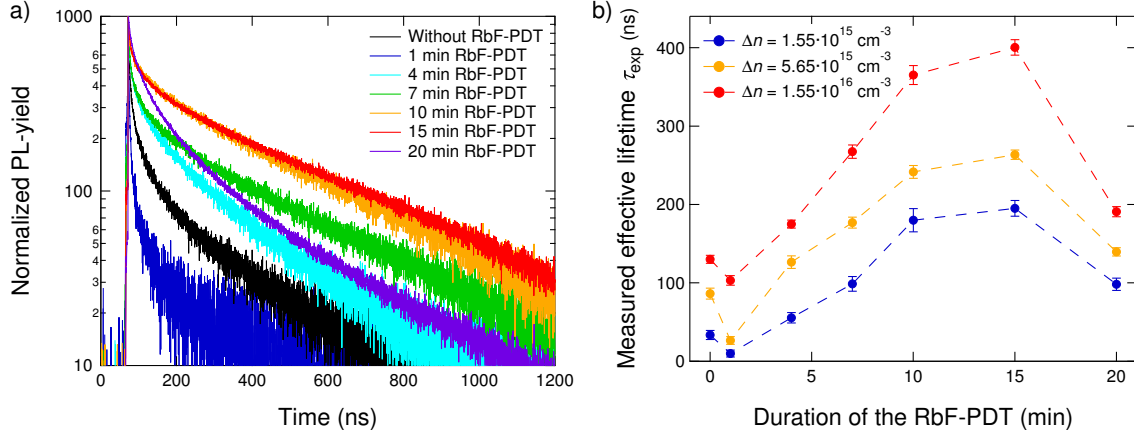


**Figure 4.5:** a) Example of the trPL results measured at  $\Delta n = 5.65 \cdot 10^{15} \text{ cm}^{-3}$ . A constant background was subtracted from each transient before they were normalized to a maximum PL yield of 1000 counts. b) Results of the fit-procedure described in Equations 3.7 and 3.8 for all samples at all three excitation conditions. The error bars show the error of the numerical fit.

with longer  $t_{\text{PDT}}$ , reaches a maximum after 15 min, and drops back down to the level of about  $t_{\text{PDT}} = 4 \text{ min}$  to  $t_{\text{PDT}} = 7 \text{ min}$ .

This higher lifetime after moderate  $t_{\text{PDT}}$  is a strong indicator for a reduced SRH-recombination rate compared to Rb-free samples. Therefore one would expect the RbF-PDT to also reduce the diode quality factor  $A$  (cf. Table 2.1) and subsequently the saturation current density  $j_0$  via a reduction of  $j_0^{\text{nrad}}$ . Indeed a general trend of decreasing  $A$  and  $j_0$  is obtained from fits of the  $j$ - $V$ -curves measured without illumination of samples with and without RbF-PDT (not shown in this work). However, due to the strong anomalies of the  $j$ - $V$ -curves after RbF-PDT (see effects on  $FF$  below), the  $j$ - $V$ -curves cannot accurately be fitted using the standard one-diode or two-diode model. Therefore a more detailed analysis of the transport mechanism in samples with and without RbF-PDT is under current investigation in a separate thesis [215].

However, the presented results indicate that the lowering of the  $V_{\text{OC}}$ -losses due to an RbF-PDT works at least via two mechanisms: the reduction of  $\Delta V_{\text{OC}}^{\text{CV}}$  and  $\Delta V_{\text{OC}}^{\text{rem}}$ . In order to be able to isolate the mechanism that leads to the reduction of  $\Delta V_{\text{OC}}^{\text{rem}}$ , the Urbach energy  $E_U$  was extracted from measurements of the  $IQE$  following Equation 3.10. The fits and the respective results are shown in Figures 4.6 a and b respectively. As can be seen from the results of the fits, the determination of  $E_U$  is rather strongly dependent on the choice of the fitting range. However, the general trend shows a slight reduction of  $E_U$  after short PDTs and a subsequently increasing trend for very long PDTs. Therefore the optimum  $E_U$  is reached after moderate PDTs (7 to 10 min). All obtained values for  $E_U$  are lower than the thermal energy  $k_B T \approx 26 \text{ meV}$  at room temperature indicating that in all cases the structural disorder, which is the origin of these tail states (cf. Section 2.1.3), and its effect on  $V_{\text{OC}}$  are rather low [71, 74].

## Part II: Combined Discussion

In total there are at least three different, accumulating effects of the RbF-PDT, which could be part of the mechanism leading to the observed gain in  $V_{\text{OC}}$ : the increased  $n_{\text{CV}}$  (lower  $\Delta V_{\text{OC}}^{\text{CV}}$ ) as well as the increased  $\tau_{\text{exp}}$  and the slightly reduced  $E_U$  (combined to a lower  $\Delta V_{\text{OC}}^{\text{rem}}$ ), while the magnitude of the electrostatic potential fluctuations is not altered for a moderately long RbF-PDT (no change in  $\Delta V_{\text{OC}}^{\text{el}}$  for  $t_{\text{PDT}} = 10 \text{ min}$ ). Furthermore, there is an additional contribution to the capacitance of the solar cells emerging with longer PDTs.

The increased carrier concentration measured on samples after long RbF-PDTs suggests that a combined incorporation of Na and Rb enhances the existing or gives rise to an additional doping mechanism compared to the incorporation of Na alone, although the mechanism

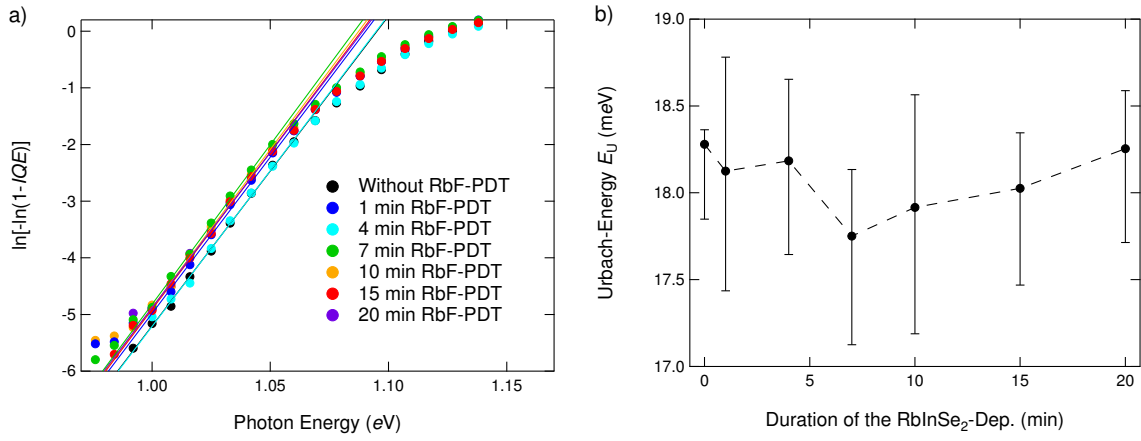


**Figure 4.6:** a) Sub-bandgap data calculated from the IQE via Equation 3.10 plotted versus the photon energy of the incident light. By fitting the linear part of the data (as indicated by the straight lines)  $E_U$  can be extracted. The results of the displayed linear fits are shown as data-points in b). The error bars result from the extension of the range of the linear fit in a), including one data-point more (leading to a higher  $E_U$ ) and one data-point less (leading to a lower  $E_U$ ).

enhancing  $n_{CV}$  is not conclusive by the data shown in this section. A direct link of the  $n_{CV}$ -profiles and the GD-OES-profile of Na seems possible only for very short RbF-PDTs: here, Rb drives out Na from the GBs and therefore the carrier concentration is reduced. The results for longer PDTs on the other hand seem to contradict each other: although more Rb is steadily decreasing the measurable amount of Na throughout the bulk of the absorber,  $n_{CV}$  is recovering constantly and – after very long treatments – reaches higher values than the Rb-free reference. A more complete model that is able to explain the observed effects taking into account results of DFT-calculations from literature will be given in Chapter 7.1. Independent of its origin, the observed gain in  $n_{CV}$  is only a partial explanation for the measured  $V_{OC}$ -boost. According to Equation 2.44 an increase in  $n_{CV}$  after the PDT can be connected to a maximum difference in  $\Delta V_{OC}^{CV}$  of

$$\Delta V_{OC}^{CV} \leq \frac{k_B T}{q} \ln \frac{n_{CV,10min}}{n_{CV,NoPDT}} \approx 17 \text{ mV} \quad (4.1)$$

for the sample with  $t_{PDT} = 10$  min. The observed gain in  $V_{OC}$  for this Subsequently, cell is about 37 mV.

Since the RbF-PDT does not reduce the magnitude of the electrostatic potential fluctuations for this sample ( $t_{PDT} = 10$  min), one has to assume that the remaining reduction of  $\Delta V_{OC}$  due to the RbF-PDT is via the reduction of  $\Delta V_{OC}^{rem}$  (cf. Equation 2.46).

This assumption is in correspondence with the observed gain in carrier lifetime and the slightly reduced  $E_U$ . Although  $E_U$  is not always free of influences of deep defects [216, 217], in general, it can be separated from the absorption due to deep defects [217] and even strong variations of the density of such deep defects were reported to not impact the value of  $E_U$  determined from the quantum efficiency [218]. Since  $E_U$  of all samples is lower than the thermal energy  $k_B T$  at room temperature, it can be assumed to not be a limiting factor for  $V_{OC}$  in any of the cells [74]. Additionally, there is hardly any trend of  $E_U$  observable with  $t_{PDT}$  taking into account the error of the measurements. Subsequently, it can be concluded that the main effect of the PDT on  $\Delta V_{OC}^{rem}$  is a reduction of the SRH-recombination rate, which gives rise to the observed increase in carrier lifetime.

The accumulations of Rb at the surface, the CIGSe/Mo-interface (as seen in GD-OES) and at the GBs (as seen by STEM-EDX) suggest that the recombination rate is reduced at either of these locations. Although the accumulation of Rb at GBs could only be shown for one example in this work, this example is in good agreement with similar measurements in literature. Several groups observed similar accumulations of Rb at the GBs as well as at the front and back interfaces [165–167, 169, 219]. However, no direct link of these accumulations

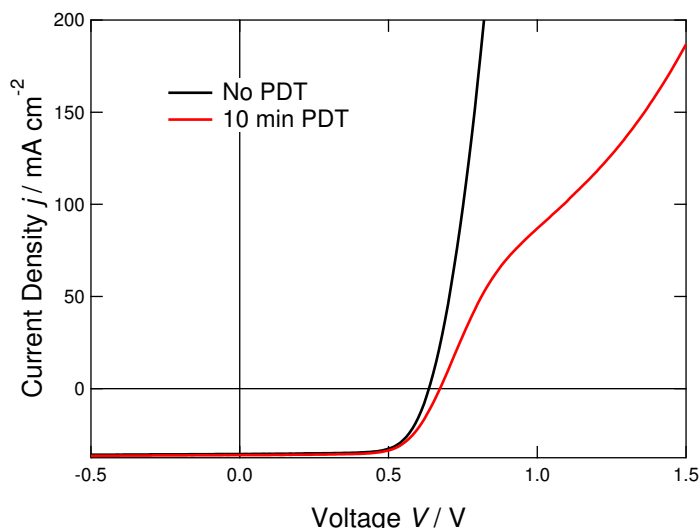


**Figure 4.7:** Measured  $j$ - $V$ -curves of the best reference cell (black,  $\eta = 16.2\%$ ) and the best RbF-treated cell (red,  $\eta = 17.0\%$ ) of the investigated sample set. The roll-over of the  $j$ - $V$ -curve after RbF-PDT appears for all  $t_{\text{PDT}}$  (not shown).

and the effects on  $n_{\text{CV}}$ ,  $\tau_{\text{exp}}$ , and  $E_{\text{U}}$  can be drawn from the presented data and therefore these correlations will also be discussed in more detail taking into account APT-data and DFT calculations from literature in Chapter 7.1.

The fact that there is an additional contribution emerging at high positive bias voltages in the C- $V$ -profiles, after the RbF-PDT compared to the untreated case, seems to be contradictory to the improved carrier lifetime. Usually one would expect lower defect contributions to the capacitance in samples with a higher lifetime and higher  $V_{\text{OC}}$ . This phenomenon will be discussed in more detail using numerical device simulations in Chapter 8.

#### Detrimental Effect of the RbF-PDT: $FF$ -loss

In contrast to the beneficial effects of the RbF-PDT on the  $V_{\text{OC}}$ , a steady decrease in  $FF$  is observed even after short PDT-durations. This  $FF$ -loss is surprising, since one would generally expect  $FF$  to follow the trend of  $V_{\text{OC}}$  (cf. Equation 2.47). The loss in  $FF$  is accompanied by a pronounced roll-over effect (reduction of the uprising slope at higher bias voltages) developing in the measured  $j$ - $V$ -curves after the RbF-PDT. This is exemplarily shown with the comparison of the  $j$ - $V$ -curves of the cells with the highest  $\eta$  (untreated and RbF-treated respectively) in Figure 4.7.

Both detrimental effects will be analyzed in more detail in Section 4.2, in which the correlation between absorber layer composition and PDT effectiveness is discussed.

### 4.1.2 Time-Series: CIGSe Surface Effects

#### Part I: Results

In Figure 4.8 SEM top view images of a CIGSe absorber layer treated with RbF ( $CGI = 0.9$ ,  $t_{\text{PDT}} = 10$  min) are shown. Directly after the PDT (left image in Figure 4.8), the surface of the CIGSe is covered with islands of a size of around 50 nm to 100 nm in diameter. Since these islands are not present on the untreated absorber layers (not shown), one can conclude that they form during the RbF-PDT and therefore very likely consist of Rb, F and/or Se. Indeed, STEM-EDX measurements indicate that the islands contain Rb, F and O. Figure 4.9 a again shows the HAADF image of a cross section of the surface area of a CIGSe absorber layer after 10 min RbF-PDT that was already presented in Figure 4.3. Figures 4.9 b to h show elemental maps measured by STEM-EDX on the same area. In the investigated region, there is a dark region visible in between the absorber layer and the covering C and Pt protection

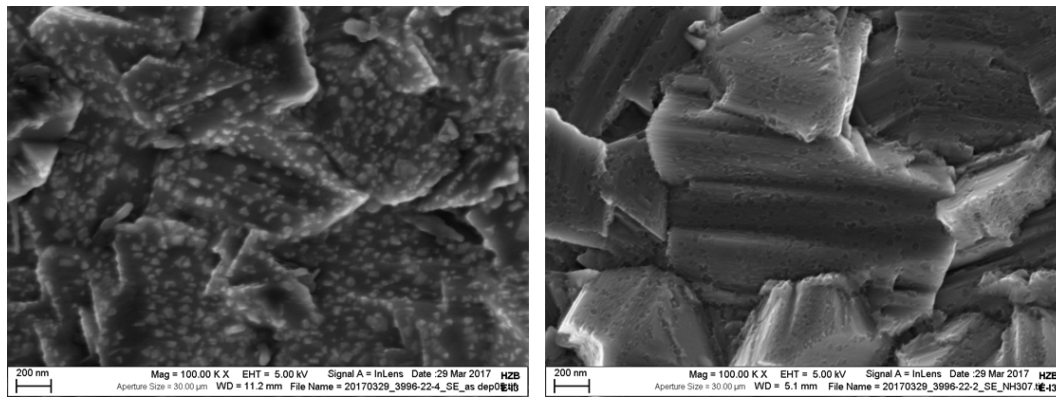


**Figure 4.8:** Left: SEM top view image of a CIGSe absorber layer's surface directly after the RbF-PDT. Right: SEM top view image of the same absorber after etching with  $\text{NH}_3(\text{aq})$ .

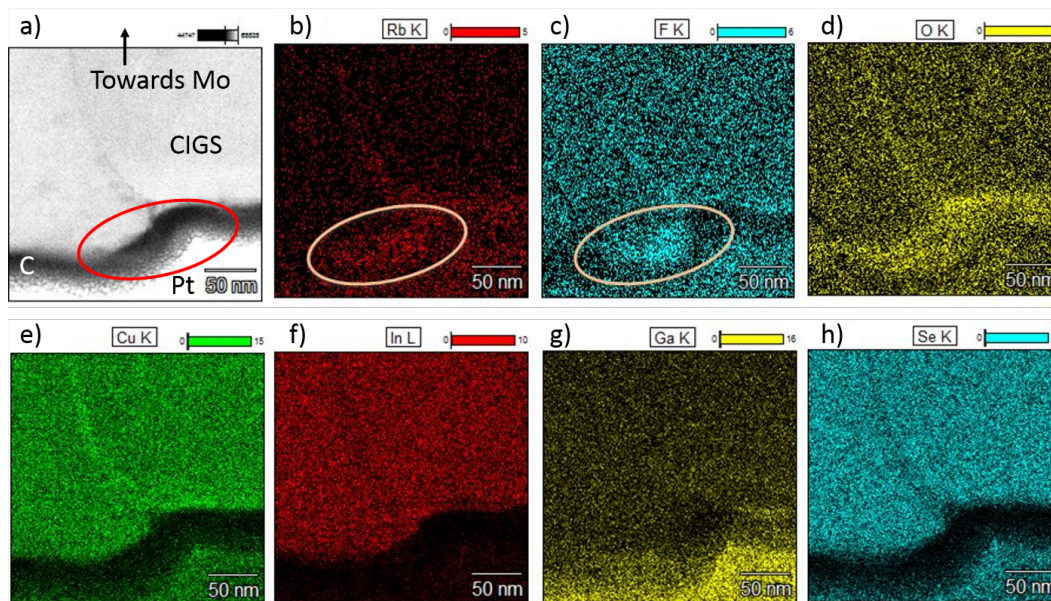


**Figure 4.9:** a) The same STEM-ADF image of the surface of a CIGSe absorber layer ( $\text{CGI} = 0.9$ , after an RbF-PDT with  $t_{\text{PDT}} = 10$  min) that was shown in Figure 4.9.

b) to h): STEM-EDX maps of Rb (b), F (c), O (d), Cu (e), In (f), Ga (g) and Se (h). The surface of the CIGSe layer is sharply visible on the Cu-, In- and Se-maps. On the STEM-ADF image, there is a dark region in between the CIGSe layer and the covering C and Pt layers. This region contains Rb, F, and O.

layers (highlighted by ellipses in Figures 4.9 a to c). Within this region, an agglomerate can be identified, of which the size fits to one of the islands observed in SEM. At the position of this agglomerate higher count rates for Rb, F and O were measured, while there is no Cu, In, Ga or Se detected.

After etching the absorber with  $\text{NH}_3(\text{aq})$  the islands are removed, leaving behind a nanostructured surface layer (Figure 4.8 b). This behavior indicates that there are at least two additional components forming at the surface of the CIGSe during the RbF-PDT – of which one is soluble in  $\text{NH}_3(\text{aq})$ .

To gain more insights into the compositional evolution of the absorber layer's surface during the RbF-deposition and the subsequent WCT with  $\text{NH}_3(\text{aq})$ , an XPS study was carried out. A bare CIGSe absorber layer without RbF-PDT was analyzed in comparison with two pieces of the same absorber layer of an RbF-treated sample ( $t_{\text{PDT}} = 10$  min). One of the latter samples as well as the reference sample were rinsed in  $\text{NH}_3(\text{aq})$  prior to the measurements, while the other Rb-treated sample was not. In the following, it will be referred to them as 'CIGSe +  $\text{NH}_3$ ' for the rinsed but untreated reference sample, 'CIGSe/RbF' for the treated

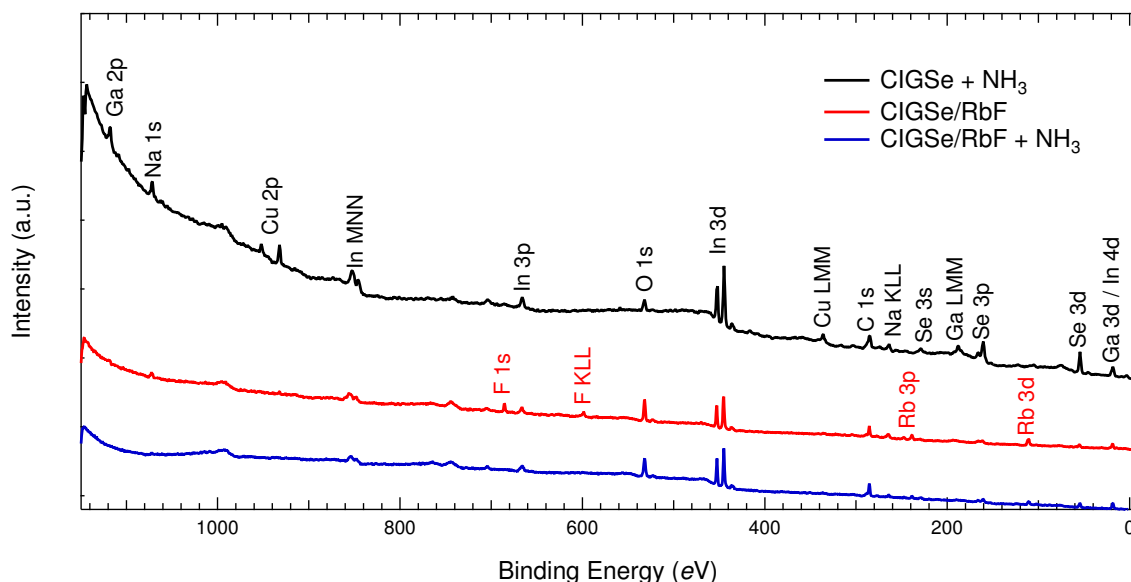


Figure 4.10: XPS survey spectra measured on the 'CIGSe + NH<sub>3</sub>', 'CIGSe/RbF', and 'CIGSe/RbF + NH<sub>3</sub>' sample.

but unrinsed sample, and 'CIGSe/RbF + NH<sub>3</sub>' for the treated and rinsed sample.

The XPS survey spectra of all three samples are shown in Figure 4.10. Please note that the transfer to the XPS system after the etching took about 5-10 min in air and that there are therefore still oxide-contributions measurable on their surfaces, which can be clearly seen in the survey spectra. However, since the transfer of the samples from the rinsing step to the buffer layer deposition takes place in air as well (cf. Section 3.1.2), these 'contaminated' surfaces describe the condition of the surface of the absorber layer in the completed device. An analysis of a vacuum-transferred sample set is shown in Section 5.1.

In Figure 4.11, the measured data of the key core level peaks as well as the Na KLL Auger electron spectrum are presented together with the corresponding data fits (for fitting details see Section 3.2.1). Additionally, an overview of all contributions measured in the different spectra is shown in Table 4.1. The results of the fits are discussed in the following.

**Impact on the metals (Cu, In, Ga).** In comparison to the untreated reference, there is a strong reduction of the Cu-1, Ga-1 and In-1 contributions after the RbF-PDT. These contributions are attributed to the respective metal bound to Se [106]. While Cu-1 and Ga-1 remain below the detection limit on the rinsed sample, the In-Se contribution (In-1) reappears after rinsing. Additionally, there is a contribution at higher binding energies in both the Ga 2p<sub>3/2</sub> and In 3d<sub>5/2</sub> spectra (Ga-2 and In-2 respectively). These can be attributed to their corresponding oxides [220, 221], which formed at the sample surfaces during transfer in air. Ga-2, however, can also be attributed to the formation of GaF<sub>3</sub> [138]. Due to the low signal to noise ratio and the broad appearance of the Ga-2 contribution in case of the 'CIGSe/RbF'-sample, Ga-oxides and GaF<sub>3</sub> are hardly distinguishable. However, in another experiment, in which a nominally identical sample set was transferred from the deposition to the XPS system without air exposure, the presence of GaF<sub>3</sub> could be shown [8]. Therefore it is assumed that Ga-2 represents both Ga-oxides and GaF<sub>3</sub>.

While Ga-2 is completely removed by the rinsing step, In-2, which does appear after RbF-PDT, partly remains after rinsing. In Figure 4.12 the In MNN Auger spectra of the three investigated samples are shown. Using the position of the In MNN contributions (MNN-1 through MNN-3) and the In-1 and In-2 contribution, the following modified Auger-parameters can be calculated:  $\alpha'_1(\text{In-1, MNN-1}) = (852.5 \pm 0.3) \text{ eV}$ ,  $\alpha'_2(\text{In-2, MNN-2}) = (850.8 \pm 0.3) \text{ eV}$  and  $\alpha'_3(\text{In-2, MNN-3}) = (849.8 \pm 0.3) \text{ eV}$ . While  $\alpha'_1$  can be attributed to the In-Se bond in CIGSe ( $\alpha'_{\text{Lit}} = 852.5 \text{ eV}$ , [146]),  $\alpha'_2$  fits to literature

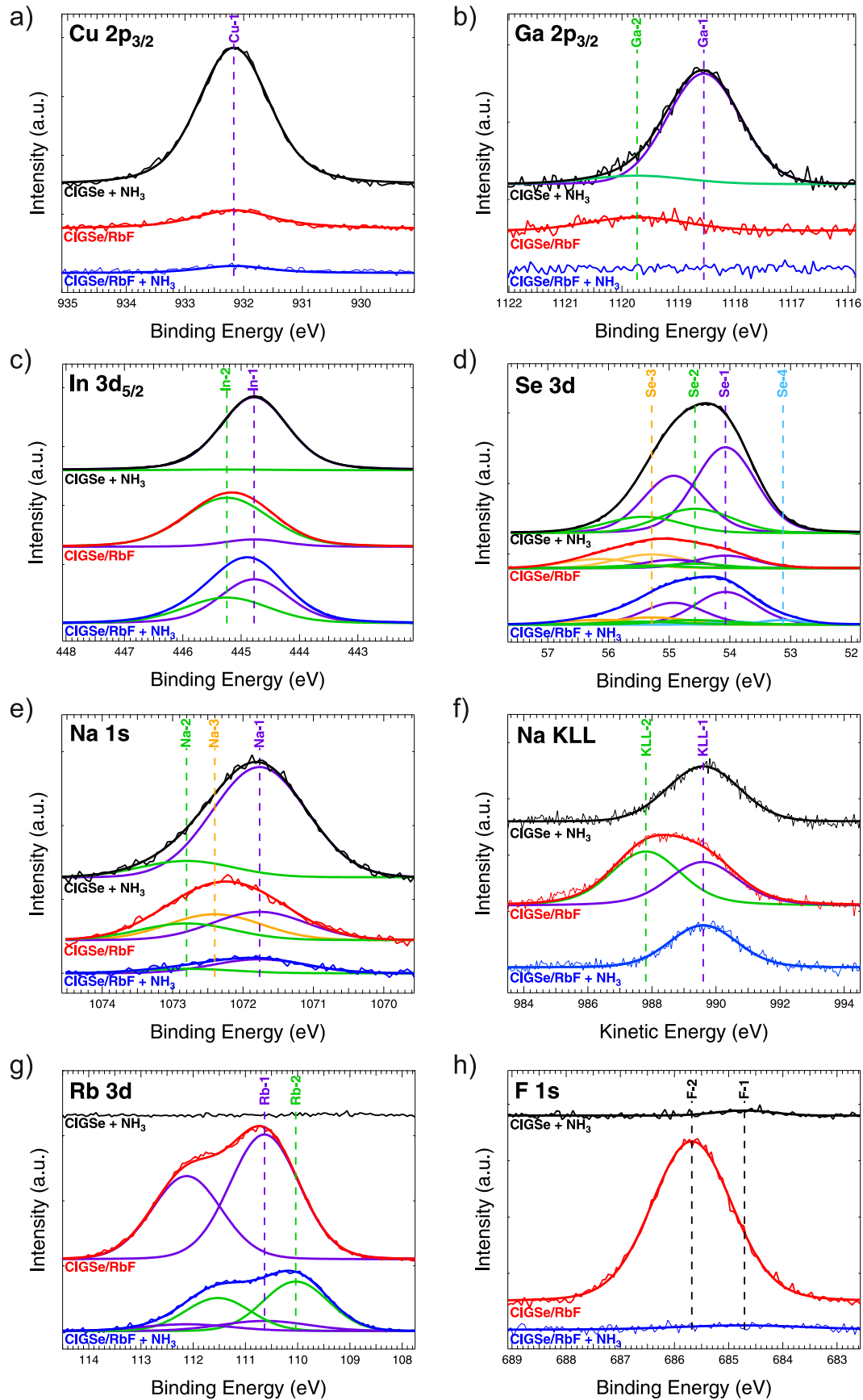


**Figure 4.11:** XPS-spectra and corresponding peaks-fits of the Cu 2p<sub>3/2</sub> (a), Ga 2p<sub>3/2</sub> (b), In 3d<sub>5/2</sub> (c), Se 3d (d), Na 1s (e), Rb 3d (g) and F 1s (h) core levels as well as the Na KLL Auger (f) measured on the surfaces of an RbF-free CIGSe absorber layer as well as an absorber layer after 10 min RbF-PDT. In case of the Rb and Se 3d peaks, only the corresponding 3d<sub>5/2</sub> sub-levels of each contribution were indicated for the sake of clarity.

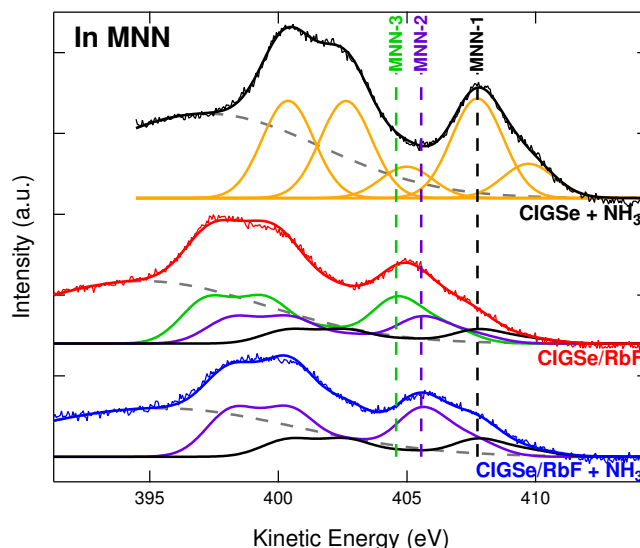


**Figure 4.12:** In MNN Auger electron spectra of the three investigated samples. The spectrum of 'CIGSe + NH<sub>3</sub>' was fitted with the lowest possible number of peaks (orange lines) and a decoupled peak representing the background in the analyzed energy range (dashed gray line). The other two spectra were then fitted with combinations of the fitted spectrum of the 'CIGSe + NH<sub>3</sub>'-fit (maintaining all energetic distances, area ratios and FWHM within each set of five peaks). The position of each set of five peaks is set to the position of the peak at the second highest kinetic energy since it is usually used in the literature to calculate  $\alpha'$ .

values of In<sub>2</sub>O<sub>3</sub> ( $\alpha'_{\text{Lit}} = 850.8 \text{ eV}$ , [220]), and  $\alpha'_3$  to In(OH)<sub>3</sub> ( $\alpha'_{\text{Lit}} \approx 850.0 \text{ eV}$ , [222]). While the In(OH)<sub>3</sub> is removed by the rinsing step and is no longer observed in the In-MNN spectrum of 'CIGSe/RbF+NH<sub>3</sub>', the contribution attributed to In<sub>2</sub>O<sub>3</sub> stays in part. The fact that the energetic position of the In 3d line is almost the same for both compounds [220, 222], explains why there is only one additional contribution to the In 3d spectrum.

**Sodium.** Two contributions (Na-1 and Na-2) are visible in the Na 1s spectrum of 'CIGSe+NH<sub>3</sub>' as well as in that of 'CIGSe/RbF+NH<sub>3</sub>'. The presence of two Na-species on the surface of CIGSe was already reported by Heske et al. [223]. On 'CIGSe/RbF' on the other hand an additional contribution – Na-3 – was detected, which lays energetically between the other two.

In combination with the Na KLL Auger electron spectrum (Figure 4.11 f), the modified Auger parameter can be calculated for each species. Combining Na-1 with KLL-1  $\alpha'_{\text{Na-1}} = (2061.4 \pm 0.2) \text{ eV}$  is found, Na-2 combined with KLL-1 leads to  $\alpha'_{\text{Na-2}} = (2062.4 \pm 0.2) \text{ eV}$  and Na-3 and KLL-2 combine to  $\alpha'_{\text{Na-3}} = (2060.2 \pm 0.2) \text{ eV}$ . According to the literature, Na-1 can be attributed to Na<sub>2</sub>SeO<sub>3</sub> ( $\alpha'_{\text{Lit}} = 2061.3 \text{ eV}$ , [106]), Na-2 to Na<sub>2</sub>O ( $\alpha'_{\text{Lit}} = 2062.5 \text{ eV}$ , [106, 224]), and Na-3 to NaF ( $\alpha'_{\text{Lit}} = 2060.1 \text{ eV}$ , [225]). However, due to the overlap in binding energies of different compounds and since the formation of pure Na<sub>2</sub>O on the surface of CIGSe does not seem likely, Na-2 may also be attributed to other sodium-oxides or -hydroxides.

**Rubidium.** After the PDT, the Rb-1 signal is detected (see Figure 4.11 g), which is strongly reduced by the rinsing step, giving rise to a second contribution at lower binding energies (Rb-2). Rb-1 can be attributed to RbF [226], while no literature data could be found for Rb-2. Given the fact that the chemical shift between Rb-1 and Rb-2 is exactly the same as between Na-1 and Na-2 ( $\Delta_{\text{Rb}} = \Delta_{\text{Na}} = (0.6 \pm 0.2) \text{ eV}$ ), Rb-2 could be attributed to an Rb-Se-O-compound as e.g. Rb<sub>2</sub>SeO<sub>3</sub>. However, in the already mentioned study on a similar sample set transferred to the XPS-system without air exposure [8], it was shown that this contribution can be attributed to a Rb-In-Se-compound. The mentioned data will be shown and discussed in more detail in Section 5.1. The attribution of Rb-2 to such a compound therefore appears more straightforward, although the additional formation of a Rb-Se-O-compound after air exposure cannot be ruled out.

**Fluorine.** The fluorine, which is deposited during the RbF-PDT (F-2 in Figure 4.11 f) and is apparently attributed to GaF<sub>3</sub>, RbF, and NaF at the CIGSe's surface, is completely removed by rinsing the surface with NH<sub>3</sub>(aq). The additional peak at lower binding energies, which is already present in the bare 'CIGSe+NH<sub>3</sub>'-sample and still present on 'CIGSe/RbF+NH<sub>3</sub>', can be attributed to a 'ghost peak' of the In 3d<sub>3/2</sub>-contribution. The energetic distance between F-1 and In 3d<sub>3/2</sub> is  $(232.5 \pm 0.5) eV$  and therefore fits to the difference of the energies of the Mg-K<sub>α</sub> and the Al-K<sub>α</sub> line ( $(233.0 \pm 0.4) eV$  [222]). Possible origins for the appearance of such 'ghost peaks' are accidental Al-deposition from the Al-anode onto the Mg-anode or slight misadjustments of the cathode's filament of the CISSY setup, which is equipped with a twin anode containing both an Mg- and an Al-excitation source.

**Selenium.** The Se 3d spectrum of the 'CIGSe+NH<sub>3</sub>'-sample could be fitted by the two doublets that are generally attributed to the chalcopyrite phase [227]. After the RbF-PDT Se-1 and Se-2 are strongly reduced, but there is an additional contribution emerging at higher binding energies (Se-3). This contribution can be attributed to the formation of selenium oxides [228]. Taking into account that this species is reduced by rinsing with ammonia solution in a similar manner as the In-2 contribution, it is assumed that an In-Se-O compound is present at the surface after the RbF-PDT. The presence of such a layer has also previously been reported in case of KF-PDT [151]. Additionally, there is a fourth component – Se-4 – appearing in the Se core level peak after rinsing. This contribution can either belong to the In-Se bond, as it may be attributed to different In<sub>x</sub>Se<sub>y</sub>-phases, or it may be attributed to the Rb-Se-O-compound [227, 229]. But since there is no contribution visible in the Se 3d spectra being attributed to Na<sub>2</sub>SeO<sub>3</sub>, the allocation to an In<sub>x</sub>Se<sub>y</sub>-phase, as e.g. the Rb-In-Se-compound, seems more likely.

Note that the spectrum of the 'CIGSe/RbF + NH<sub>3</sub>'-sample could generally be fitted without the contribution Se-2. However, as stated above, in literature the Se 3d peak is usually fitted with both the Se-1 and Se-2 contribution [227]. As it is described in the fitting procedure in Section 3.2, all contributions which are present in the reference sample were propagated to the spectra of the RbF-treated samples.

Furthermore, the contribution Se-4 is rather weak, which might raise the question whether it is needed for an accurate fit. Generally, all positions as well as the share of the Gaussian and the Lorentzian part of all peaks and the respective FWHM were kept constant, and therefore the spectrum of the sample 'CIGSe/RbF + NH<sub>3</sub>' cannot be fitted without Se-4. A fit of this spectrum without the Se-4 contribution could only be compensated if the position of the Se-1 contribution was allowed to differ at least  $\Delta E_B \approx 0.3 eV$  from the other samples. Since no such shift is observed in spectra consisting of only one peak, such as the Cu 2p or the Na KLL spectrum, the appearance of the contribution Se-4 seems validated.

## Part II: Combined Discussion

Summarizing the results of the SEM-, TEM- and XPS-studies, a reaction model for the surface development during the PDT and the consecutive rinsing step is proposed (cf. Figure 4.13). Starting from the surface of the bare CIGSe absorber layer, which is covered by GaO<sub>x</sub> (indicated by Ga-2), the present study indicates that at least three different layers form at the surface of the CIGSe. The deposited RbF forms islands (Volmer-Weber-growth [231]) on top of the CIGSe (Rb-1, F-2, SEM, TEM) from which the Rb diffuses into the surface area of the CIGSe. The residual fluorine stays at the surface and forms NaF (Na-3, F-2) as well as GaF<sub>3</sub> (Ga-2, F-2). Furthermore, the hydrophilic character of these alkali-fluorides [138] leads to a stronger formation of oxides and hydroxides at the surface (In-2, Se-3).

Underneath these fluorides and oxides, the in-diffusing Rb leads to a redistribution of Cu and Ga: Even after etching with NH<sub>3</sub>(aq) the surface of the absorber layer is strongly Cu- and Ga-depleted (Cu-1, Ga-1) indicating the formation of a In<sub>x</sub>Se<sub>y</sub>-layer (In-1, Se-4) at the surface during the RbF-PDT. The fact that alkali-oxides are found at the surface after rinsing and short contact to air (Rb-2, Na-1, Na-2), indicates that Na and Rb are incorporated in this

Table 4.1: Peak positions and the attributed compounds of the fits shown in Figures 4.11 and 4.12.

Core level peak	Binding energy (eV)	Auger peak	Kinetic energy (eV)	$\alpha'$ (eV)	Compound	Reference
Cu-1	932.2	-	-	-	CIGSe	[106]
Ga-1	1118.6	-	-	-	CIGSe	[220]
Ga-2	1119.7	-	-	-	GaO <sub>x</sub> , GaF <sub>3</sub>	[8, 138]
In-1	444.8	MNN-1	407.7	852.5±0.3	CIGSe	[106, 146]
In-2	445.2	MNN-2	405.6	850.8±0.3	In <sub>2</sub> O <sub>3</sub>	[220]
In-2	445.2	MNN-3	404.6	849.8±0.3	In(OH) <sub>3</sub>	[222]
Se-1	54.1	-	-	-	CIGSe	[227]
Se-2	54.6	-	-	-	CIGSe	[227]
Se-3	55.3	-	-	-	In-Se-O/Se <sup>0</sup>	[151] / [138, 227]
Se-4	53.1	-	-	-	In <sub>x</sub> Se <sub>y</sub>	[227, 229]
Na-1	1071.8	KLL-1	989.6	2061.4±0.3	Na <sub>2</sub> SeO <sub>3</sub>	[106]
Na-2	1072.8	KLL-1	989.6	2062.4±0.3	Na <sub>2</sub> O	[106, 224]
Na-3	1072.4	KLL-2	987.8	2060.2±0.3	NaF	[225]
Rb-1	110.6	-	-	-	RbF	[8, 226]
Rb-2	110.0	-	-	-	RbInSe <sub>2</sub> , Rb <sub>2</sub> SeO <sub>3</sub>	[8] / -
F-1	684.7	-	-	-	In-Ghost	[222]
F-2	685.7	-	-	-	RbF, NaF, GaF <sub>3</sub>	[230], [103], [138]

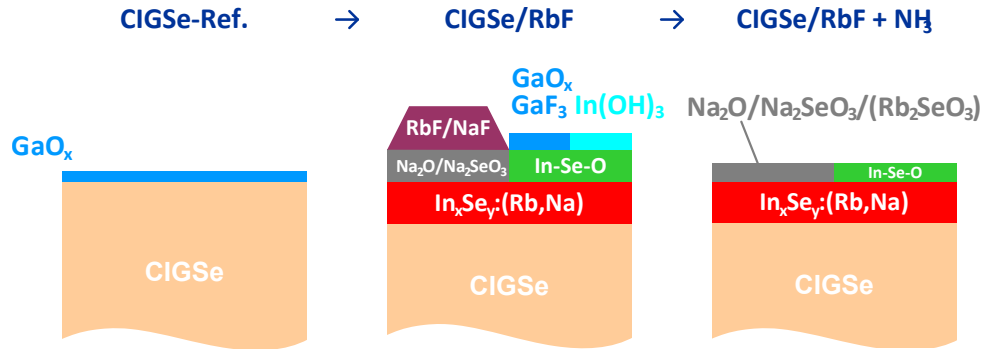


**Figure 4.13:** Proposed model of a surface layer formation during the RbF-PDT. Please note that in the final layer model ('CIGSe/RbF + NH<sub>3</sub>') there is no nanopatterning indicated since from the presented data it is not conclusive which layer shows the nanopatterning.

In<sub>x</sub>Se<sub>y</sub>-layer. In particular, a significant amount of Rb seems to be incorporated into this surface layer since the Rb-2 contribution is also visible in nominally similarly processed CIGSe layers after rinsing with NH<sub>3</sub>(aq) and no subsequent air-exposure [8]. Possible candidates for this In<sub>x</sub>Se<sub>y</sub>:(Rb,Na)-layer are discussed in Chapter 5.

A similar behavior of the shallow core levels (Cu 2p<sub>3/2</sub>, Ga 2p<sub>3/2</sub>, Se 3d) as it was described here for the first time in case of an RbF-PDT, has been reported by other groups for a KF-PDT [128, 146]. In agreement with the interpretation above, both groups attributed the additional Se-species at lower binding energies (here Se-4) to the formation of a K-In-Se surface layer. While Handick et al. [146] could support this hypothesis with an additional In-species at lower binding energies, Lepetit et al. [128] did not observe this contribution. The latter is similar to the study presented here, in which an additional species (Se-4) is observed at lower binding energies in the Se-spectrum of the sample 'CIGS/RbF + NH<sub>3</sub>' (Se-4), while there is none in the spectrum of In 3d<sub>5/2</sub>. However, the presence and intensity of these additional contributions seems to be attributed to the respective growth parameters of the CIGSe and the PDT, which are different in all three cases discussed here.

Also similar to the presented results, a nanopatterning of the CIGSe's surface after an alkali-PDT has already been reported in case of KF-PDT and RbF-PDT [150, 157]. The role of this nanopatterning as a possible passivating layer will be further discussed in Section 7.2.3.

Summarizing the discussion, in this section it was shown that the RbF-PDT leads – additionally to the bulk effects described in the section above – to the formation of a nanopatterned  $\text{In}_x\text{Se}_y:(\text{Rb},\text{Na})$ -layer at the surface of CIGSe absorber layers with  $\text{CGI} = 0.9$ . In the following section, it will be investigated how a change of the properties of the underlying substrate, e.g. of the  $\text{CGI}$  of the absorber layer, alters this formation mechanism. The nature of this surface layer will be investigated in more detail in Chapter 5 and its role in the finished, Rb-conditioned device will be modeled and discussed independently of the nanopatterning in Chapter 8.

## 4.2 ODC-Induced Transport Barrier Formation: Interplay of the PDT and CGI

The effect of the RbF-PDT is not only dependent on the process parameters of the PDT itself (see section above), but on the properties of the underlying CIGSe absorber layer as well. While manifold process parameters can influence the effectiveness of the PDT, as it was shown in Section 2.3.2 of the literature review, the interaction of the RbF-PDT with absorber layers featuring different Cu-contents is of special interest for the present work.

As it was already stated in the aforementioned literature review and in the previous section, the interaction of heavy alkali and Cu atoms at the surface and at the GBs of the CIGSe absorber layer is an important part of the mechanism of the PDT.

In order to clarify the role of the Cu-content at the surface of the absorber layers, 10 deposition processes resulting in samples with five different  $\text{CGI}$  (without and with 10 min RbF-PDT each) were performed. The analysis of the properties of the resulting samples and devices is presented and discussed in the following.

### Part I: Results

Table 4.2 shows the length of Stage III as well as the targeted and measured  $\text{CGI}$  of the whole sample set as measured by SEM-EDX. Despite an offset between the targeted and the actually measured  $\text{CGI}$  in case of  $\text{CGI} = 0.3$ , the achieved values fulfill the purpose of the study. In all cases, the measured  $\text{CGI}$  of the samples with and without PDT are in good agreement and therefore enable an evaluation of the effectiveness of the PDT in dependence of the  $\text{CGI}$ .

Table 4.2: Duration of stage III of the deposition process as well as  $\chi_{\text{Cu}}$  the  $\text{CGI}$  as measured by SEM-EDX and the thickness measured by SEM. The thickness of the absorber layer was only measured on the sample set with RbF-PDT. However, the GD-OES profiles as well as  $t_{\text{III}}$  show a very good agreement between the respective samples of each set.

Target-CGI	RbF	$t_{\text{III}}$ (s)	$\chi_{\text{Cu}}$ (at%)	$\text{CGI}_{\text{EDX}}$	$d_{\text{CIGSe}}^{\text{SEM}}$ ( $\mu\text{m}$ )
0.30	no	5300	14.6	$0.46 \pm 0.02$	-
0.30	yes	5300	14.4	$0.45 \pm 0.02$	4.0
0.60	no	2275	18.3	$0.61 \pm 0.02$	-
0.60	yes	2260	18.9	$0.63 \pm 0.02$	2.9
0.80	no	1228	22.3	$0.81 \pm 0.02$	-
0.80	yes	1241	21.8	$0.79 \pm 0.02$	2.6
0.90	no	685	23.0	$0.90 \pm 0.02$	-
0.90	yes	669	23.4	$0.87 \pm 0.02$	2.3
0.95	no	365	24.7	$0.94 \pm 0.02$	-
0.95	yes	411	24.7	$0.95 \pm 0.02$	2.2

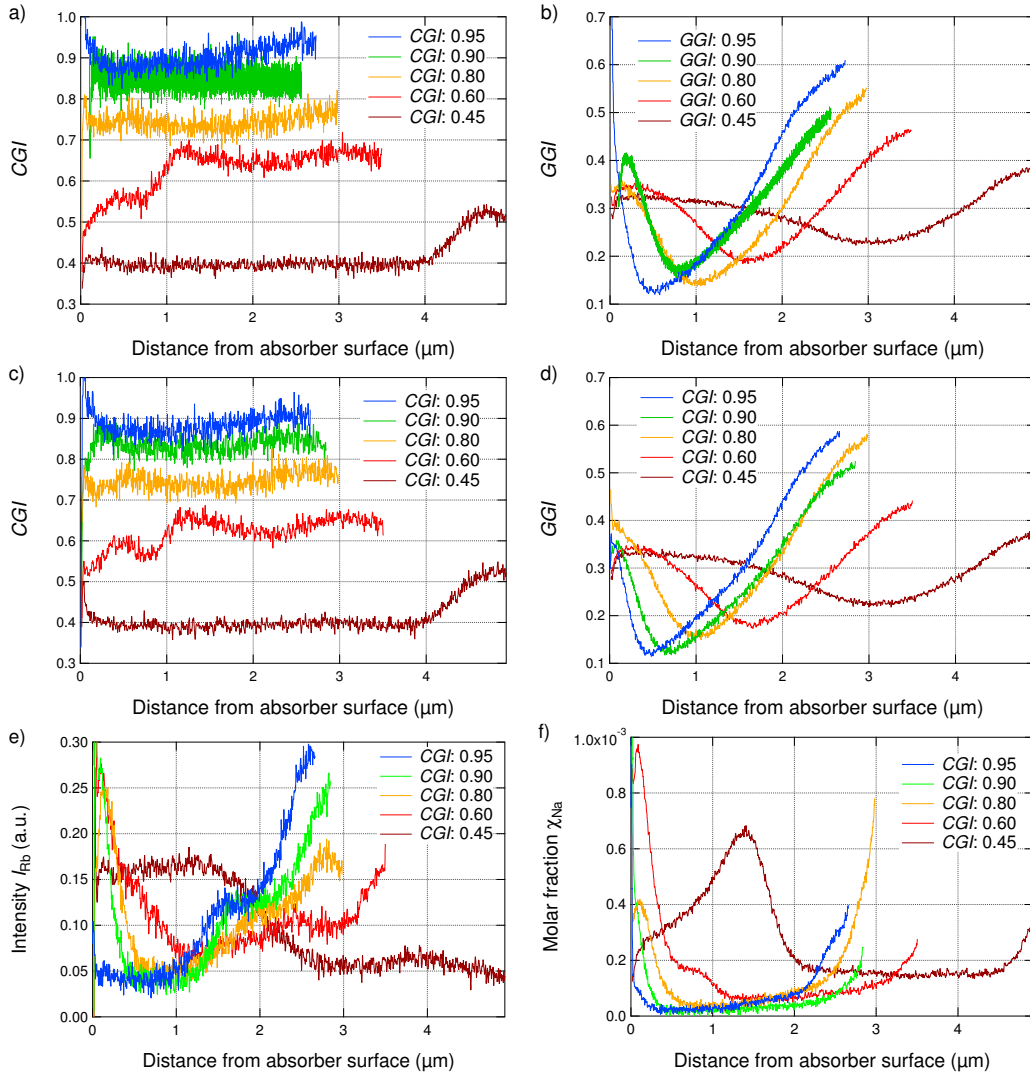


**Figure 4.14:** Depth profiles of the CGI (a,c) and the GGI (b,d) of the sample set without (a,b) and with RbF-PDT (c,d) as measured by GD-OES. It can be clearly seen how the variation of the duration of stage three of the deposition process alters not only the Cu-content but also the thickness and GGI-profile of the absorber layers. However, both the CGI and the GGI profiles for each CGI are the same in case with and without RbF ensuring the direct comparability. Figures e) and f) show the distribution of Rb (e, unquantified) and Na (f) in the absorber layers with different CGI as measured by GD-OES.

Due to the fact that the variation of the CGI was achieved by varying the duration of Stage III, the absorber layers are not only different in CGI and thickness, but also the  $E_g$ -grading as well as the position and value of the minimum bandgap energy are affected (see CGI and GGI depth profiles of the RbF-treated samples in Figure 4.14). However, the purpose of the experiment – judging the effectiveness of the RbF-PDT – is not affected by these deviations, since they are identical for samples with and without RbF-PDT.

Furthermore, it is interesting to note that there is a step in the CGI depth profile for the samples with  $CGI = 0.45$  and  $CGI = 0.60$ , but not for samples with higher CGI. As it was discussed in Section 3.2 and shown in Publication [5], the CGI determined by GD-OES is not accurate for  $CGI \lesssim 0.9$  due to phase segregation and the influence of  $V_{Cu}$ . This is confirmed by the depth profiles of the samples with  $CGI_{EDX} \approx 0.90$ , which show substantially lower CGI in GD-OES. Therefore the absolute value of the plateaus in the profiles of the samples with  $CGI_{EDX} = 0.45$  and  $CGI_{EDX} = 0.60$  are not reliable.

Figure 4.15 shows SEM images on cross sectional specimen prepared from these samples. All samples show the typical threefold grain structure due to the Ga-gradient in the absorber layer: Close to the back contact there is a thin 'layer' with a very fine-grained structure, followed by large columnar grains that in some areas extend until the surface, while in other

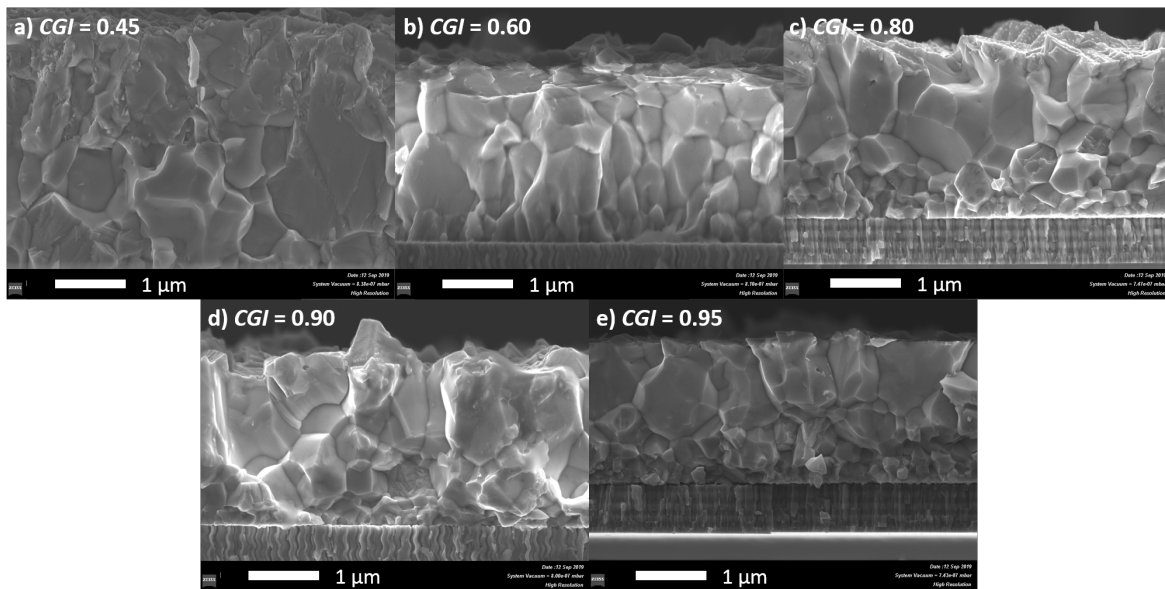


**Figure 4.15:** Cross sectional SEM images of the sample set with RbF-PDT. No differences in grain size and morphology were seen in individual comparisons to samples without RbF-PDT.

areas there are additional, smaller grains on top of these columnar grains. There is no general trend in grain size with  $CGI$  visible and also no correlation to the steps in the GD-OES depth profiles of the samples with  $CGI = 0.45$  and  $CGI = 0.60$  is found.

In order to investigate the structure of the samples in more detail, Raman spectra of this sample set are shown in Figure 4.16 a. All spectra are normalized to the CIGSe  $A_1$ -mode at wavenumbers of about  $174 \text{ cm}^{-1} < k < 184 \text{ cm}^{-1}$  depending on the surface- $GGI$  [194–196]. On samples with  $CGI \leq 0.8$ , there is a clear contribution of the ODC  $A_1$  mode visible at a wavenumber of  $k_{A_1}^{\text{ODC}} = (158 \pm 5) \text{ cm}^{-1}$  in the spectra [196], which is not detected anymore on samples with higher  $CGI$ . However, Raman spectra of the samples with  $CGI = 0.95$  recorded with a more advanced system and therefore higher resolution reveal that even in these samples the ODC  $A_1$  mode is visible, indicating that this is true for all used  $CGI$  (see Figure 4.16 b).

As it can be seen from the phase diagram (cf. Figure 2.6 and Reference [76]), both the  $\alpha$ - and the  $\beta$ -phase of the CIGSe, coexist for a wide range of Cu-content (roughly 16% to 24%) at room temperature. Comparison with the Cu-content determined by EDX (see Table 4.2) indicates that the samples with the lowest and highest  $CGI$  of the series should consist solely of the  $\beta$ - or  $\alpha$ -phase CIGSe respectively, while the other samples are proposed to contain regions of both phases. If both phases are present in the same sample, the fraction of the  $\beta$ -phase would obviously increase with lower Cu-content, which is in agreement with the Raman results.

However, also the samples with  $\chi_{\text{Cu}} \approx 14.5\%$  and  $\chi_{\text{Cu}} = 24.7\%$  show contributions of both phases in the Raman spectra. These deviations from the rules set by the phase diagram are explainable by the deposition procedure. During the growth of all samples, the common starting point for the  $CGI$ -variation is the second stoichiometric point during the third growth stage (cf. Section 3.1.1), i.e. a complete layer of  $\alpha$ -phase CIGSe. The further reduction of the  $CGI$  is achieved by evaporating Cu-free material on top of this layer, which then inter-diffuses with the CIGSe leading to the overall lower  $CGI$  via successive phase transitions during the growth [232]. Therefore it seems possible that the  $\alpha$ - and  $\beta$ -phase CIGSe are not completely intermixing during this dynamic growth process and that especially after long durations of Stage III, regions with a higher fraction of the  $\alpha$ -phase segregate near to the back contact, which could explain the steps in the measured profiles.

However, taking into account the penetration depth of the Raman measurements of about 100 nm to 150 nm, it can be assumed that the observed steps in the GD-OES depth profiles

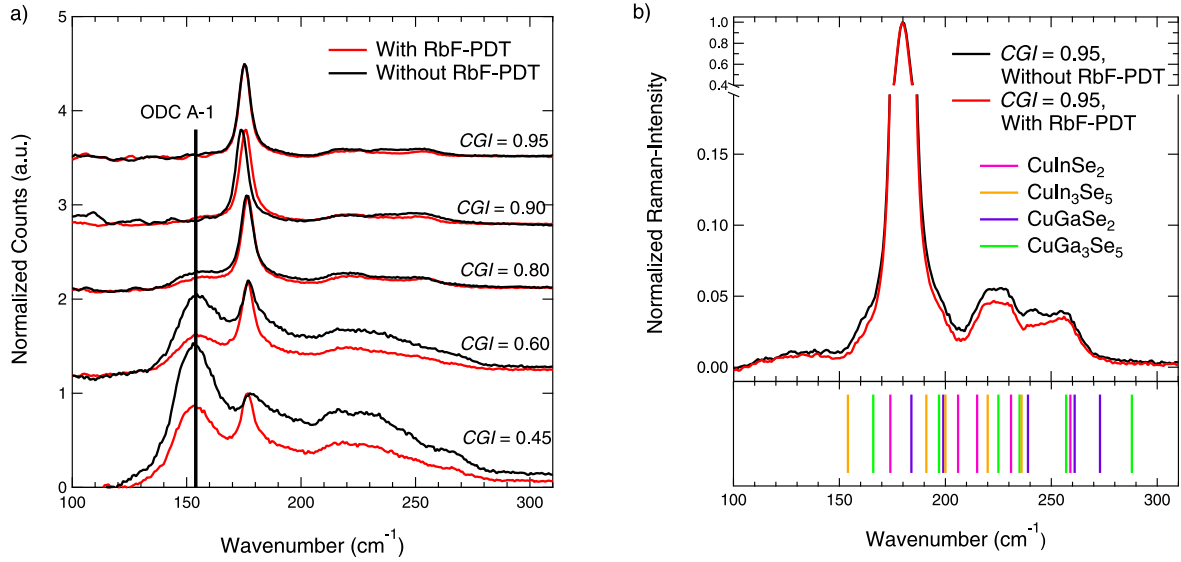


**Figure 4.16:** a) Comparison of the Raman spectra of the samples with and without RbF-PDT in dependence on the CGI. All spectra were normalized to the CIGSe A1 mode. b) High resolution Raman spectrum of the samples with  $CGI = 0.95$  with and without RbF-PDT, recorded by Dr. Maxim Guc. The bottom part of the graphs indicates the positions of the known modes of  $\text{CuInSe}_2$ ,  $\text{CuIn}_3\text{Se}_5$ ,  $\text{CuGaSe}_2$ , and  $\text{CuGa}_3\text{Se}_5$  taken from References [195, 196]. Note that due to the high number and overlap of the different peak positions as well as the fact that the used material is a mixture of the In- and Ga-compounds, the exact determination of the positions of the peaks related to CIGSe and the ODC is difficult. However, the position of the  $A_1$ -mode of CIGSe and the ODC at wavenumbers of around  $k_{A_1}^{\text{CIGSe}} = (180 \pm 0.5) \text{ cm}^{-1}$  and  $k_{A_1}^{\text{ODC}} = (158 \pm 5) \text{ cm}^{-1}$ , can be isolated.

do not originate from a complete phase segregation (i.e.  $\beta$ -phase at the front, mixed phase at the back of the absorber layer). Therefore it is assumed that these steps are due to the formation of regimes with different, fixed ratios of  $\alpha$ - to  $\beta$ -phase. Note that similar behavior, i.e. the evolution of such steps in GD-OES depth profiles, was observed in a previous study [86]. However, this phenomenon needs more investigation, which does not directly lie in the scope of this work and is not feasible with the utilized techniques. In the following it is assumed that the surface area of all absorber layers contains homogeneously intermixed  $\alpha$ - and  $\beta$ - (or ODC-)phase CIGSe and that the fraction of the ODC steadily increases with decreasing CGI.

Figure 4.17 shows the measured  $j$ - $V$ -parameters of this sample set. Several observations can be made:

1. Independent of the PDT, high-efficient devices can only be fabricated in the range of  $0.8 \lesssim CGI < 0.95$ , which is already known from literature [39].
2. For  $CGI < 0.8$  the RbF-PDT does not in- but decrease the  $V_{OC}$ .
3. The RbF-PDT leads to an improved  $FF$  only on samples grown at  $CGI = 0.95$ .

Contrary to these results, Lepetit et al. [128] observed an increase of all PV-parameters after a KF-PDT for samples with rather low CGI, while the KF-PDT lead to strong deterioration of all parameters on absorbers grown close to stoichiometry. Although the RbF-PDT leads to similar alterations of the properties of an absorber layer with  $CGI = 0.9$  as the KF-PDT does (see literature review in Section 2.3 and discussion in Section 4.1), the CGI-dependence is contrary, which indicates that the mechanism during the RbF-PDT is different from that during a KF-PDT. In order to be able to analyze this discrepancy, Observations 2 and 3 will be analyzed in more detail in the following.

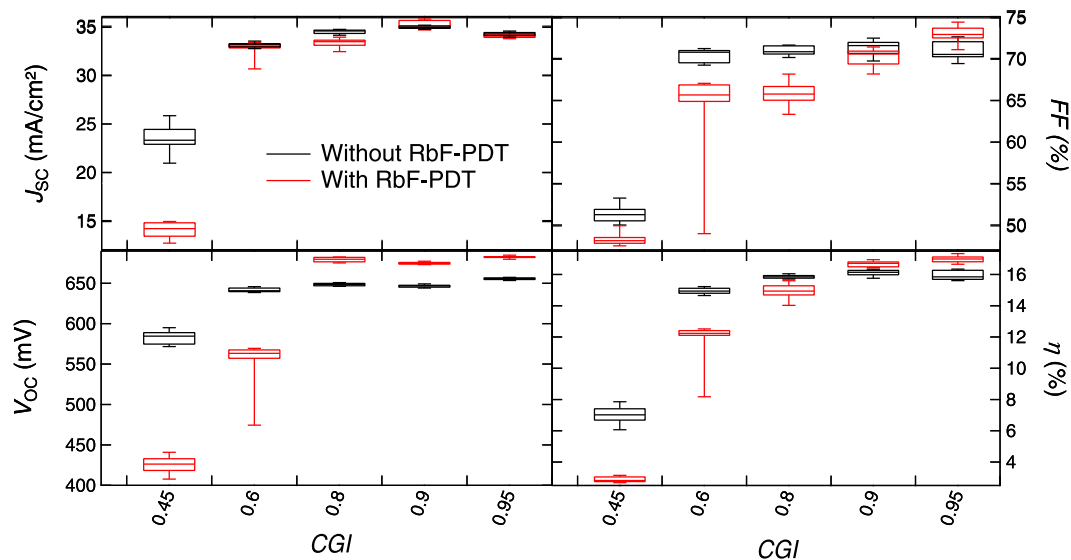


**Figure 4.17:** Boxplots of the PV-parameters of samples with and without RbF-PDT in dependence on the CGI of the absorber layer.

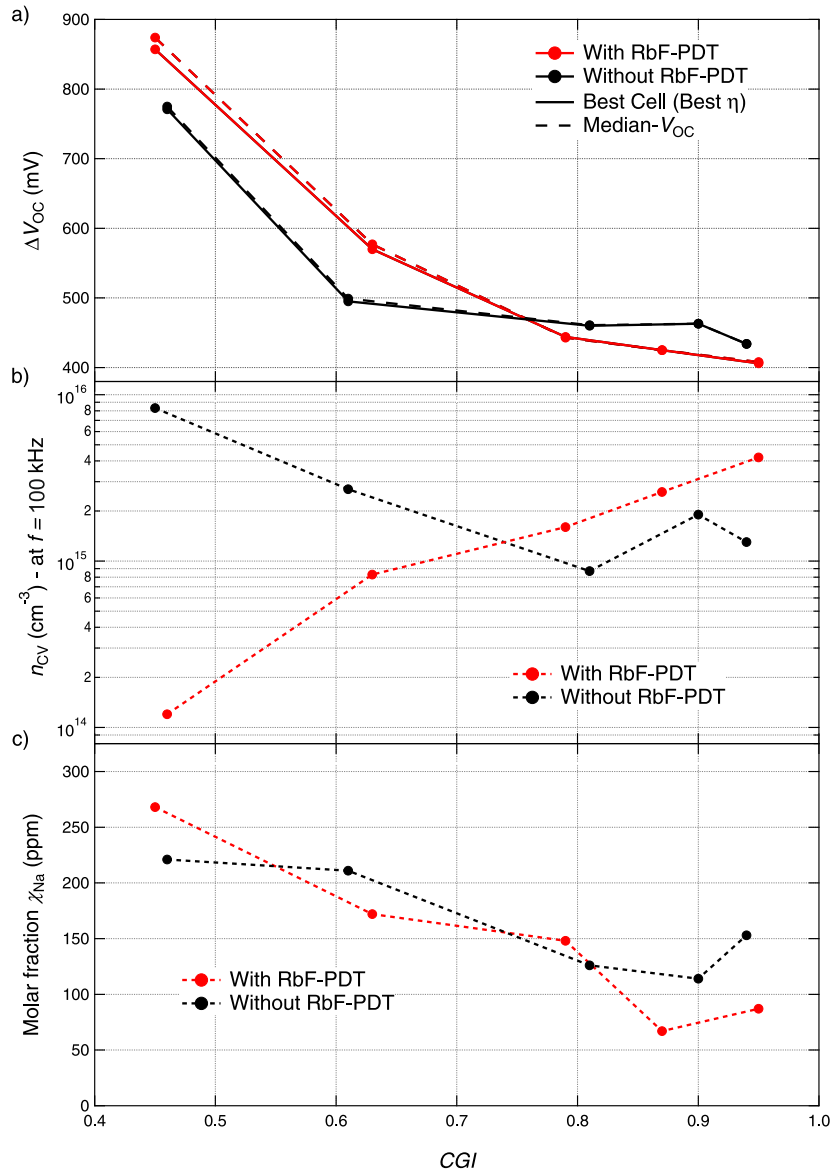
### Observation 2: CGI-Series – Impact of the PDT on $V_{OC}$

In order to take the deviations of  $E_{g,min}$  into account when judging the effectiveness of the RbF-PDT, the  $V_{OC}$ -deficit ( $\Delta V_{OC} = E_g/q - V_{OC}$ ) of all samples is shown in Figure 4.18 a. For  $CGI < 0.8$ ,  $\Delta V_{OC}$  of RbF-treated samples is about 100 mV higher than that of samples without the PDT. At a CGI of 0.8, there is a change of this trend and the RbF-PDT leads to  $\Delta V_{OC}$  of about 30 mV to 50 mV lower compared to the untreated references.

This behavior of  $\Delta V_{OC}$  correlates with the carrier concentration as measured by C-V-profiling (cf. Figure 4.18 b). While  $n_{CV}$  of the untreated devices shows a slightly decreasing trend with higher CGI, the carrier concentration of RbF-treated devices is rising steadily. Therefore the RbF-PDT leads to lower  $n_{CV}$  in samples with  $CGI < 0.8$  and to higher  $n_{CV}$  in samples with  $CGI > 0.8$ . This is the same trend as observed for  $\Delta V_{OC}$ .

In Figure 4.18 c the molar fraction of Na ( $\chi_{Na}$ ) as derived from integrating the respective GD-OES depth profiles is displayed versus the CGI. The exchange mechanism between Rb and Na, which was described in Section 4.1.1 for the case of  $CGI = 0.9$ , is apparently only valid in samples with rather high CGI ( $CGI > 0.8$ ). On samples with lower CGI, the integral  $\chi_{Na}$  of treated and untreated samples is comparable indicating that the RbF-PDT does not lead to an out-diffusion of Na in these samples. Given the fact that in Section 4.1.1 it was shown that the out-diffusion of Na correlates with the improved  $n_{CV}$  for RbF-treated samples, this could explain the rather low carrier concentrations measured on RbF-treated devices with low CGI and therefore also the observed trend in  $\Delta V_{OC}$ . However, this behavior will be discussed in a broader context taking into account theoretical results from DFT-calculations in Chapter 7.1.

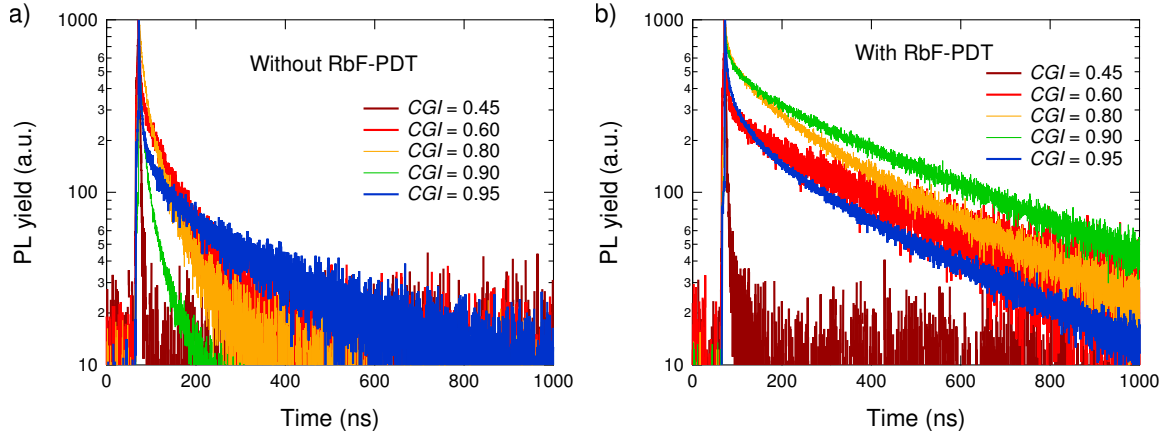
Figure 4.19 shows the results of the trPL measurements performed at a photo-generated carrier density of  $\Delta n = 5.65 \cdot 10^{15} \text{ cm}^{-3}$ . As described in Section 3.2 the HCl-etching leads to a strong curvature of the transients, which hinders a quantified analysis of the results. Based on the discussion in Section 3.2 the real carrier lifetime  $\tau_{eff}$ , which is mostly determined by SRH-recombination, is assumed to lie in between the derived values for  $\tau_{exp}^{low}$  and  $\tau_{exp}^{high}$ . It can be seen that the values measured at the highest  $\Delta n$ , show a slightly different trend with CGI compared to those measured at lower  $\Delta n$ . This could be due to slightly different densities of shallow traps and/or deep defects, which both influence the decay time at high injection (cf. Section 3.2) and therefore hinder a detailed analysis of the dependence of the lifetime on CGI.



**Figure 4.18:** a)  $V_{OC}$ -deficit of the most efficient cell as well as the cell with the median  $V_{OC}$  of each sample plotted versus the CGI. b) Evolution of the carrier concentration layer with CGI as measured by C-V-profiling. c) Molar fraction of Na in dependence of the CGI of the absorber layer (as measured by GD-OES).

However, a qualitative trend of the effect of the RbF-PDT on the lifetime at different CGI can be deduced: for all CGI the effective lifetime  $\tau_{exp}$  is – independently of the carrier generation rate – significantly higher after the RbF-PDT than before (compare also the summary of the results of the fits in Figure 4.21 b and Table 4.3). This indicates that the SRH-recombination is reduced due to the RbF-PDT – independently of the CGI. Furthermore, the overview in Figure 4.21 b qualitatively suggests that the improvement of  $\tau_{exp}$  might be stronger at higher CGI ( $CGI \geq 0.8$ ).

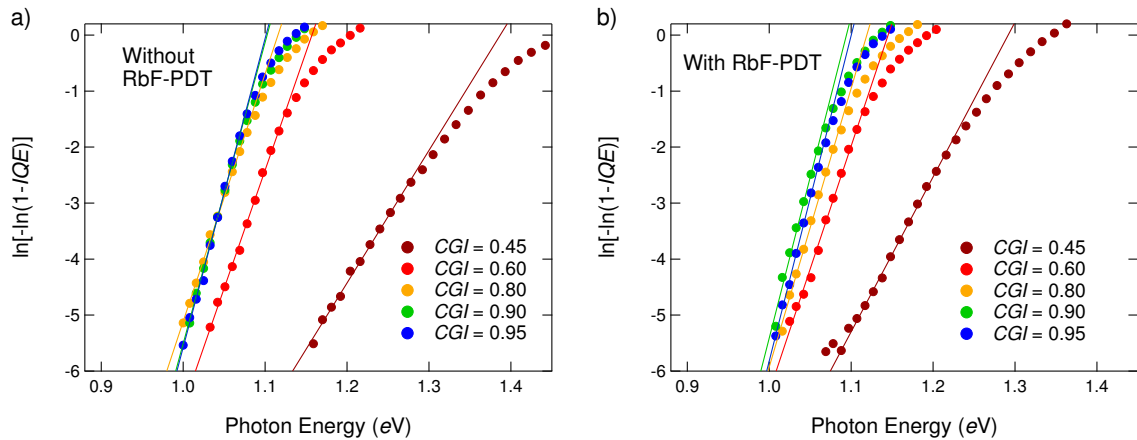
Figure 4.20 shows the extraction of  $E_U$  from the IQE-data of the complete sample set. The respective fit results are displayed in Figure 4.21 a. The extracted  $E_U$  is slightly lower after RbF-PDT compared to the Rb-free samples for all CGI. Just as in the case of the samples with a varied amount of RbF (cf. Figure 4.6) this decrease is rather small and in some cases the error bars of the measurements even overlap. However, combining these results with those shown in the previous section justifies the statement that the RbF-PDT generally leads to a slightly reduced  $E_U$  and therefore to a reduced amount of sub-bandgap states. It is worth mentioning that for all cases  $CGI > 0.45$ ,  $E_U$  of RbF-treated and untreated samples is lower than  $k_B T$  and is therefore not supposed to have a strong influence on  $V_{OC}$  [74].



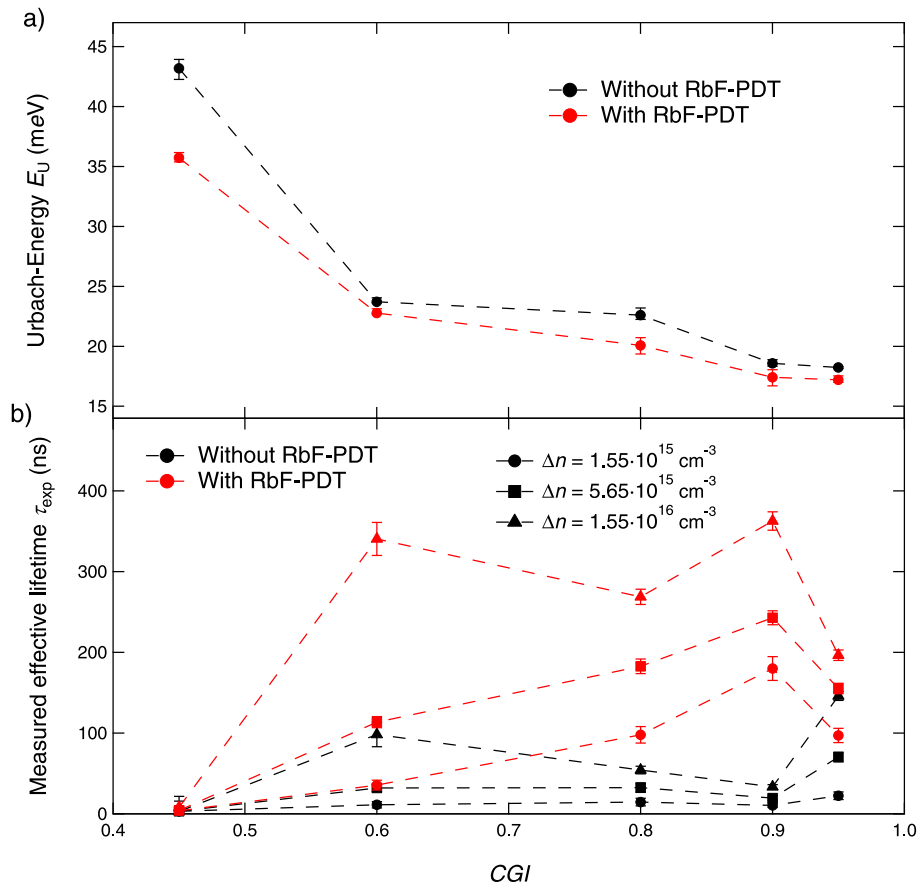
**Figure 4.19:** Time resolved measurements of the PL yield of the samples without (a) and with (b) RbF-PDT measured at a photo-generated carrier density of  $5.65 \cdot 10^{15} \text{ cm}^{-3}$ . The lifetimes extracted from the fits of these curves are shown in Table 4.3. Note that due to the fact that an InGaAs photomultiplier was used for the detection of the photons, the quantum efficiency of the detector drops by several orders of magnitude at  $\lambda \approx 940 \text{ nm}$ , which is close to the minimum bandgap energy of the samples with  $\text{CGI} = 0.45$ . Therefore the absolute PL yield of these samples might not be measured correctly.

Table 4.3: Lifetimes  $\tau_2$  as derived from the double exponential fit according to Equation 3.7.

	$\Delta n \text{ (cm}^{-3}\text{)}$	$\text{CGI} = 0.45$	$\text{CGI} = 0.60$	$\text{CGI} = 0.80$	$\text{CGI} = 0.90$	$\text{CGI} = 0.95$
		$\tau_{\text{exp}} \text{ (ns)}$				
Without RbF-PDT	$1.55 \cdot 10^{15}$	3	11	15	10	22
	$5.65 \cdot 10^{15}$	3	32	32	19	70
	$1.55 \cdot 10^{16}$	3	98	54	33	146
With RbF-PDT	$1.55 \cdot 10^{15}$	4	36	98	180	97
	$5.65 \cdot 10^{15}$	4	114	183	243	155
	$1.55 \cdot 10^{16}$	8	340	269	362	197



**Figure 4.20:** Sub-bandgap data calculated from the IQE via Equation 3.10 plotted versus the photon energy of the incident light with the respective linear fits (straight lines) to extract  $E_U$ . a) shows the data and fits for the samples without, b) for those with RbF-PDT. The fit-results are shown in Figure 4.21 a).



**Figure 4.21:** Results of the fits of a) the extraction of  $E_U$  from the sub-bandgap data of the IQE and b) the extraction of  $\tau_{\text{exp}}$  from the trPL measurements at three different generation rates.

### Observation 3: CGI-Series – Impact of the PDT on FF

The steady  $FF$ -loss that was observed in the time-series, which was described in Section 4.1.1, is not valid for absorber layers grown close to stoichiometry (cf. Figure 4.17). In fact, the RbF-PDT leads to an improved  $FF$  on samples grown at  $CGI = 0.95$ , while the  $FF$ -loss due to the PDT on samples with lower  $CGI$  gets larger with decreasing  $CGI$ .

In Figure 4.14 elemental depth profiles of Rb (Figure 4.14 e) and Na (Figure 4.14 f), both measured on the RbF-treated sample set, are shown. Please note again that the profiles of Rb are unquantified and therefore do not show the molar fraction of Rb in the samples but the intensity of the Rb-signal (cf. Section 3.2.1).

One can see that the distributions of Rb and Na correlate and that both accumulate near the surface of the absorber layer. Furthermore, this accumulation steadily extends deeper into the absorber layer the lower the  $CGI$  is. In the previous section, it was shown that Rb accumulates at the GBs meaning that the trend of a higher amount of Rb being incorporated into the CIGSe with decreasing  $CGI$  could be attributed to an increased number of GBs. However, in the cross sectional SEM images that are shown in Figure 4.15 no difference in grain size depending on the  $CGI$  can be found. It can therefore be excluded that this enhanced in-diffusion into the surface of the CIGSe is attributed to a grain size effect. Moreover, all profiles were measured on absorbers, which have been rinsed in  $\text{NH}_3(\text{aq})$ , showing that the observed accumulations represent either Rb incorporated into the lattice of the CIGSe or into a secondary phase growing on top of the CIGSe during the PDT. Considering the fact that such a secondary, Rb- and Na-containing phase was found on top of the surface of the RbF-treated sample with  $CGI = 0.9$  (cf. XPS-study in Section 4.1.2) these depth profiles suggest that the thickness of this surface phase increases with decreasing  $CGI$ .

Going back to the Raman spectra shown in Figure 4.16, one can see that for all  $CGI$  the ratio of the ODC  $A_1$  to the CIGSe  $A_1$  mode is reduced by the RbF-PDT indicating an interaction

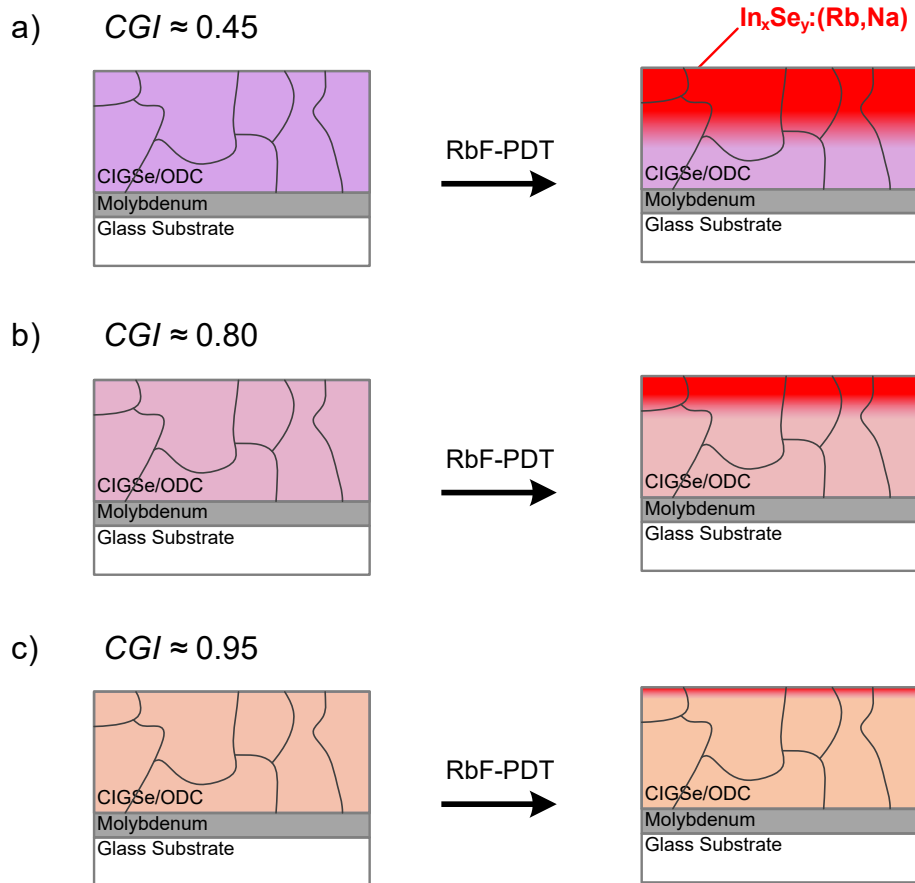


**Figure 4.22:** Schematic representation of the proposed mechanism of the surface modification happening during the RbF-PDT in dependence of the  $CGI$  of the absorber layer. Please note that this representation is simplified and neglects the details of the surface composition prior and after the PDT, which are shown for the case  $CGI = 0.9$  in Figure 4.13.

During the RbF-PDT Rb is diffusing into the bulk of the absorber and furthermore occupying available  $V_{Cu}$  in the ODC-phase at the surface of the absorber. The higher the  $CGI$  of the CIGSe is (a to c), the thinner the ODC phase and consequently the  $In_xSe_y:(Rb,Na)$ -layer in the end. Note that in all three cases the relation of the thickness of each layer (ODC, CIGSe, and  $In_xSe_y:(Rb,Na)$ ) is not depicted true to scale.

of Rb with Cu in the lattice of the CIGSe leading to a lower amount of the ODC, i.e. the incorporation of Rb reduces the number of  $V_{Cu}$  in the surface region of the absorber layer. Furthermore, there is a qualitative trend in the Raman spectra that the amount of the ODC, which is consumed during the PDT, is lower for increasing  $CGI$ .

Combining this result with the observation that the amount of Rb, which is incorporated into the surface of the absorber layer increases with lower  $CGI$ , it can be concluded that the presence of a higher fraction of the ODC-phase at the surface of the CIGSe promotes the accumulation of more Rb there. Since it was furthermore shown that this Rb is incorporated into the lattice, and that the incorporation of Rb into the surface of the CIGSe leads to the formation of an  $In_xSe_y:(Rb,Na)$ -layer, it is proposed that the thickness of this layer increases with decreasing  $CGI$  of the CIGSe (cf. schematic representation of the proposed model in Figure 4.22). Therefore not only  $CGI$  but also the thickness of the  $In_xSe_y:(Rb,Na)$ -layer correlates with the effect of the RbF-PDT on  $FF$ .

## Part II: Combined Discussion

Combining the results described by the Observations 2 and 3, it can be concluded that the effect of the RbF-PDT on  $V_{OC}$  and  $FF$  is strongly related to the interaction of Rb and Na with the CGI, i.e. the ratio of  $\alpha$ -phase CIGSe to ODC or the number of  $V_{Cu}$  in the absorber layer. As it was shown for samples grown with  $CGI = 0.90$  in Section 4.1, the positive effect of Rb on  $V_{OC}$  is – among possible interface-mechanisms, which will be discussed in Chapter 6 – generally attributable to the following effects: an Rb-Na exchange mechanism, which correlates with  $n_{CV}$ , a reduction of the SRH-recombination rate leading to improved carrier lifetimes, and a reduced  $E_U$ , i.e. to a reduction of the losses attributed to  $\Delta V_{OC}^{CV}$  and  $\Delta V_{OC}^{rem}$ . The experimental results shown in this section suggest that the reduction of the SRH-recombination rate due to the RbF-PDT takes place for all CGI-values, even though a dependence of the significance of these effects on CGI cannot be ruled out due to the qualitative nature of the trPL results. The Rb-Na exchange mechanism on the other hand is strongly dependent on CGI and correlates with  $n_{CV}$  and  $\Delta V_{OC}$ . Therefore the interaction of Rb and Na seems to be the driving force for the dependence of  $V_{OC}$  on CGI and at least for the reduction of the  $V_{OC}$  on samples with  $CGI < 0.80$ , since the PDT leads to a lowered  $V_{OC}$  in these samples despite the reduced  $\Delta V_{OC}^{rem}$  via  $\tau_{exp}$  and  $E_U$ . On samples with  $CGI \geq 0.80$ , however, the positive effects of all three mechanisms combined lead to the improved  $V_{OC}$ . Furthermore, it was suggested that the effect of the RbF-PDT on  $FF$  is directly related to the amount of Rb that is incorporated into the surface of the CIGSe, i.e. the thickness of the  $In_xSe_y:(Rb,Na)$ -layer. Since no direct evidence of an increasing thickness of this layer was given, the increased amount of Rb incorporated into the surface of the CIGSe and the subsequently stronger reduction of the amount of ODC at the surface of the absorber layer could also be explained by the formation of a mixed  $(Rb,Cu)(In,Ga)Se_2$  layer. However, taking into account the fact that almost no Ga and Cu were found at the surface of samples after RbF-PDT and rinsing in  $NH_3(aq)$  in the XPS study in Section 4.1.2, an increasingly thick  $In_xSe_y:(Rb,Na)$ -layer seems more likely. Following that interpretation and including the fact that the detrimental effect by the RbF-PDT on  $FF$  gets smaller with increasing CGI until the RbF-PDT actually improves  $FF$  at  $CGI = 0.95$ , indicates that the  $In_xSe_y:(Rb,Na)$ -layer might have a negative impact on  $FF$ . This will be analyzed in more detail in the next chapters.

Figure 4.23 shows the  $j$ - $V$ -curve of a device prepared with  $CGI = 0.95$  and an RbF-PDT, which according to the results presented in this chapter, is the best way to profit from the beneficial effects of the RbF-PDT while minimizing the impact of the detrimental effects. The device was completed using the 'high-efficiency'-line at HZB, which means that the grid-deposition as well as the cell separation were performed photolithographically. Furthermore, an  $MgF_2$  anti-reflective coating (ARC) was deposited on top of the finished device. The high efficiency of  $\eta = 20.0\%$  demonstrates the relevance of the samples prepared in the frame of this thesis. Furthermore, it shows that the  $FF$  can be further improved by using the photolithographic steps, meaning that part of the general  $FF$ -loss can be ascribed to two-dimensional effects.

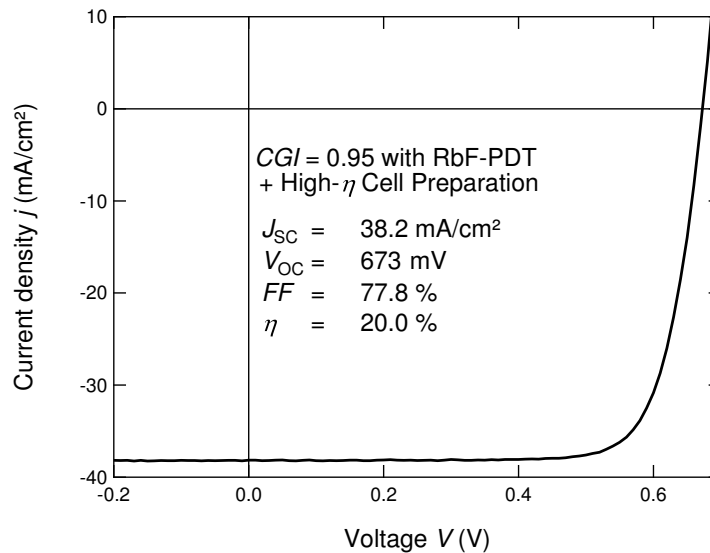


**Figure 4.23:** PV-parameters as well as the  $j$ - $V$ -curve of a device, which was fabricated with  $CGI = 0.95$  and RbF-PDT. The device was finished using HZB's 'high- $\eta$ '-line, which consists of a photolithographic cell preparation and the deposition of an ARC (see text).

Note for the reader of Chapter 8: Other than the 'high- $\eta$ ' cell-finish, this sample was prepared in the same way as the samples with  $CGI = 0.95$  and RbF-PDT, that are shown in Figure 4.17. Therefore the gain in  $FF$  ( $FF = 77.8\%$  for this cell versus  $FF \approx 75\%$  for the best cell with the standard cell completion) can be attributed to the cell-finishing.

## Summary and Conclusions of Chapter 4

Judging from the results presented in this chapter, the RbF-PDT leads to several effects on the bulk and surface properties of the CIGSe absorber layer. However, the quality of some of these effects (beneficial or detrimental to cell performance) depends strongly on the overall  $CGI$  of the absorber layers. While the PDTs' effect on the carrier lifetime and Urbach-energy qualitatively is beneficial regardless of the  $CGI$ , its effect on the carrier concentration, which is linked to the Rb-Na exchange mechanism, is only beneficial on samples with  $CGI \geq 0.8$  – leading to improved  $V_{oc}$  on these samples – but is detrimental on samples with lower  $CGI$ . The fact that the latter samples show a decreased  $V_{oc}$  after the RbF-PDT suggests that the effect of the RbF-PDT on  $\Delta V_{oc}^{CV}$  is the dominant one. However, a slight trend of increasingly effective defect passivation with increasing  $CGI$  can be seen from the trPL-measurements, which might therefore contribute to the overall trend of  $V_{oc}$  with  $CGI$  as well.

The process window for the optimization of  $FF$  is even narrower: only on samples with  $CGI \approx 0.95$ , the RbF-PDT leads to an increased  $FF$ . While a complete model for these effects will be proposed in Chapter 8, one can already draw conclusions from the measurements presented in this chapter. The ratio of ODC and  $\alpha$ -phase CIGSe seems to be a key factor deciding the effectiveness of the PDT. In samples with very low  $CGI$  more Rb is incorporated into the surface region of the absorber layer leading to a more pronounced growth of the secondary  $\text{In}_x\text{Se}_y:(\text{Rb},\text{Na})$ -layer at the surface, which correlates with the lowered  $FF$ . In samples with high  $CGI$ , however, the amount of the ODC is lower, leading to a thinner secondary phase at the absorber surface and therefore better  $FF$ .

In the following chapter, the nature of the secondary surface phase will be analyzed in more detail before its interplay with the subsequently deposited buffer layer will be discussed in more detail in Chapter 6.

## 5 On RbInSe<sub>2</sub>

In the previous chapter, indications were given for the formation of an Rb- and Na-containing In<sub>x</sub>Se<sub>y</sub> compound at the surface of CIGSe with  $CGI \lesssim 0.9$  during an RbF-PDT. As shown by DFT-calculations in literature [161] and in a collaborative work with the University of Paderborn (cf. Chapter 2.3.3), the most likely candidate for this compound is RbInSe<sub>2</sub> (RIS) [2, 161], which is predicted to be *n*-type [2]. In the first section of this chapter, which is based on the experimental part of the study presented in Publication [2], the properties of a thermally co-evaporated RIS thin film will be analyzed experimentally and compared to those of In<sub>2</sub>Se<sub>3</sub>:Rb thin films. In the second section of this chapter, it will be investigated how a direct deposition of RIS onto CIGSe absorber layers grown with  $CGI = 0.95$  affects the distribution of alkali metals in the layer stack as well as the resulting device parameters.

### 5.1 Experimental Determination of the Layer Properties of RbInSe<sub>2</sub>-Thin Films

Four different samples were deposited on Mo-coated glass substrates: two In-Se:Rb samples (deposition of In-Se and a subsequently performed RbF-PDT) and two Rb-In-Se samples, one with and one without Na incorporated from the glass substrate each. The deposition procedures are described in detail in Section 3.1.3. All samples were rinsed in NH<sub>3</sub>(aq) before characterization in order to remove F-compounds and excess-alkali species from their surfaces. The fact that this etch did not dissolve the actual thin films shows that all samples are stable in NH<sub>3</sub>(aq), which is important to note, since the presence of the In<sub>x</sub>Se<sub>y</sub>:(Rb,Na)-layer that forms at the surface of Cu-poor CIGSe during an RbF-PDT was concluded from measurements which were done after an NH<sub>3</sub>(aq)-etch.

To identify the phase content of these samples, GI-XRD diffractograms of all four samples as well as the results of the respective fits via LeBail analysis [200] are displayed in Figure 5.1. While the measured pattern of the Na-free In-Se:Rb sample shows contributions of two different phases (In<sub>2</sub>Se<sub>3</sub> and In<sub>4</sub>Se<sub>3</sub>, see Figure 5.1 a), the pattern of the Na-containing In-Se:Rb sample can be fitted using only In<sub>2</sub>Se<sub>3</sub>-contributions (Figure 5.1 c). However, taking into account the composition of the films as measured by XRF, which fits to almost stoichiometric In<sub>2</sub>Se<sub>3</sub> in both cases (see Table 5.1), it can be assumed that the amount of In<sub>4</sub>Se<sub>3</sub> in the former sample is rather small compared to the amount of In<sub>2</sub>Se<sub>3</sub>.

Furthermore, it seems likely that the traces of In<sub>4</sub>Se<sub>3</sub> segregate close to the surface, because the GI-XRD measurements are surface sensitive. Since both In<sub>2</sub>Se<sub>3</sub>- and In<sub>4</sub>Se<sub>3</sub>, show many overlaying reflexes, the individual peaks are not marked in Figure 5.1 a. Instead of an evaluation of the fits with only In<sub>2</sub>Se<sub>3</sub>-, and with both In<sub>2</sub>Se<sub>3</sub>- and In<sub>4</sub>Se<sub>3</sub>-contributions is shown in Figure A.2 in the appendix of this work. Table 5.1 shows the results of the LeBail analyses [200] assuming there is only In<sub>2</sub>Se<sub>3</sub> present in both samples in order to be able to compare the derived lattice parameters. The derived lattice parameters for both In-Se samples fit very well to literature values of  $\gamma$ -In<sub>2</sub>Se<sub>3</sub> [233].

Both the RIS and the RIS:Na sample, on the other hand, show only contributions associated with monoclinic RbInSe<sub>2</sub> (cf. Figs. 5.1 b and d), which also is in good agreement with the composition as measured by XRF (see Table 5.1). The lattice parameters derived by LeBail analysis agree very well with those reported for a RIS single crystalline sample [235], confirming that both samples consist of single phase RIS or RIS:Na respectively. In all cases, the incorporation of Na does not have a relevant impact on the lattice parameters nor on the composition as measured by XRF.

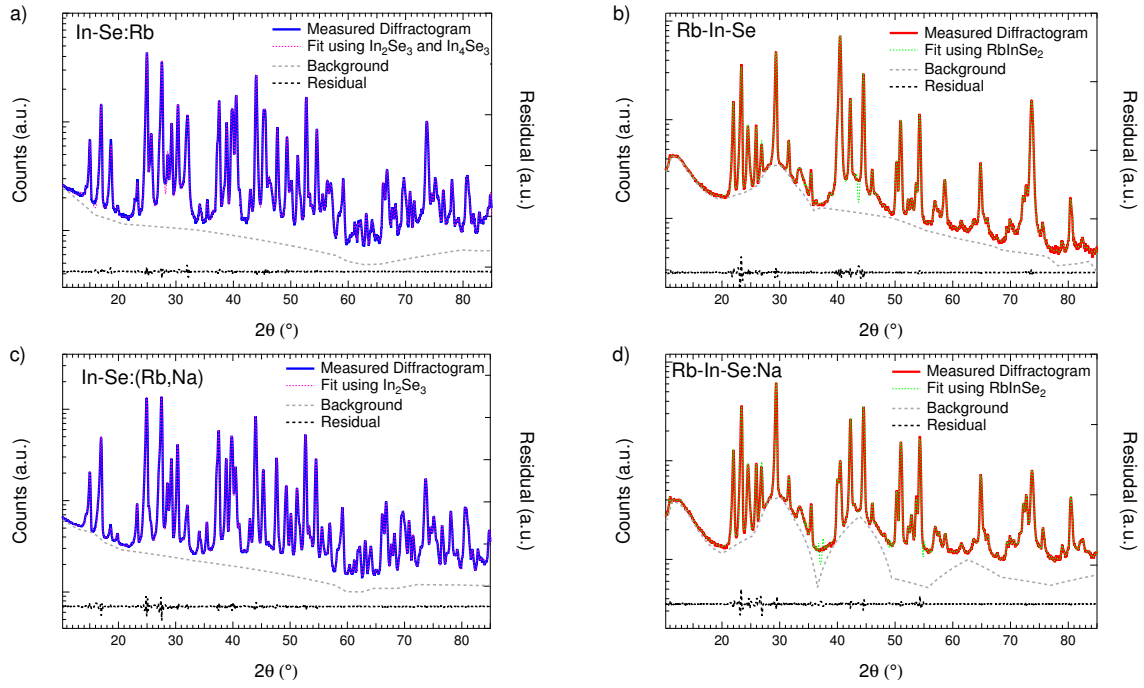


**Figure 5.1:** XRD-diffractograms as well as the results of the corresponding Le Bail analyses [200] of a) the In-Se:Rb-sample b) the Rb-In-Se-sample, c) the In-Se:(Rb,Na) sample, and d) the Rb-In-Se:Na-sample. The fits were performed using the following data from literature: Reference [233] for  $\text{In}_2\text{Se}_3$ , Reference [234] for  $\text{In}_4\text{Se}_3$ , Reference [235] for  $\text{RbInSe}_2$ , and Reference [236] for Mo. Note that the counts are shown on a logarithmic scale, while the residuals are shown on a linear one.

**Table 5.1:** Results of the LeBail analyses of the GI-XRD-diffractograms shown in Figure 5.1 as well as the results of the composition of the In-Se and Rb-In-Se samples measured by XRF and the derived bandgap energy of the main leading edge of the absorption spectra shown in Figure 5.3.

Sample	$a$ (Å)	$b$ (Å)	$c$ (Å)	$\beta$ (°)	$\chi_{\text{Rb}}$ (%)	$\chi_{\text{In}}$ (%)	$\chi_{\text{Se}}$ (%)	Thickness (nm)	$E_g$ (eV)	
									Direct	Indirect
Mo/ $\text{In}_2\text{Se}_3$ : Rb	7.127	-	19.398	90	$0.1 \pm 0.1$	$39.9 \pm 0.1$	$59.9 \pm 0.1$	$\approx 580$	-	-
Mo/ $\text{In}_2\text{Se}_3$ :(Rb,Na)	7.128	-	19.409	90	$0.2 \pm 0.1$	$39.9 \pm 0.1$	$59.9 \pm 0.1$	$\approx 550$	-	-
$\text{In}_2\text{Se}_3$ :(Rb,Na)	-	-	-	-	$0.1 \pm 0.1$	$39.6 \pm 0.1$	$60.2 \pm 0.1$	$\approx 670$	$2.0 \pm 0.1$	$1.9 \pm 0.1$
Mo/RIS	11.502	11.496	16.469	100.781	$24.1 \pm 0.1$	$24.9 \pm 0.1$	$51.0 \pm 0.1$	$\approx 800$	-	-
Mo/RIS:Na	11.499	11.500	16.482	100.787	$24.5 \pm 0.1$	$24.4 \pm 0.1$	$51.0 \pm 0.1$	$\approx 800$	-	-
RIS:Na	-	-	-	-	$23.6 \pm 0.1$	$25.1 \pm 0.1$	$51.2 \pm 0.1$	$\approx 810$	$2.8 \pm 0.1$	$2.6 \pm 0.1$

The incorporation of Na does, however, impact the morphology of the films as can be seen in the SEM cross sectional images shown in Figure 5.2. While Na-free  $\text{In}_2\text{Se}_3$ :Rb shows a porous morphology consisting of small grains, Na-containing  $\text{In}_2\text{Se}_3$ :Rb shows a more compact morphology. The FWHM of the main peaks of both samples is indistinguishable though, indicating similar average grain size. The presence of Rb does not strongly alter the morphology of either  $\text{In}_2\text{Se}_3$  samples compared to Rb-free  $\text{In}_2\text{Se}_3$  (not shown, [2]), most likely because it is not present during film growth. The impact of Na-incorporation on the morphology of the RIS samples is less pronounced. Both the RIS and the RIS:Na sample, show a rather smooth, compact, and large-grained morphology. The incorporation of Na leads to the growth of overall bigger grains though.

Additional to the aforementioned samples, an  $\text{In}_2\text{Se}_3$ :(Rb,Na) and a RIS:Na-sample have been deposited on glass substrates in order to be able to measure their optical properties. Total transmission and reflectance were measured by UV-Vis in order to calculate the absorption spectra using Equation 3.6. The composition of the films is hardly affected by the lack of the Mo-layer (see Table 5.1). Therefore it is assumed that the differences between the optical properties of the film grown on glass and those grown on Mo are negligible.

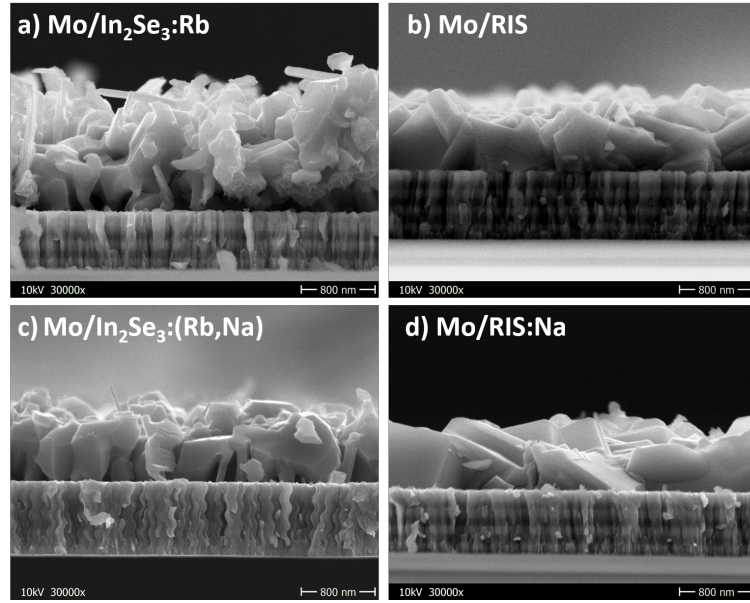


**Figure 5.2:** Cross sectional SEM-images of the Mo/In<sub>2</sub>Se<sub>3</sub>:Rb (a), the Mo/RIS (b), the Mo/In<sub>2</sub>Se<sub>3</sub>:(Rb,Na) (c), and the Mo/RIS:Na samples (d).

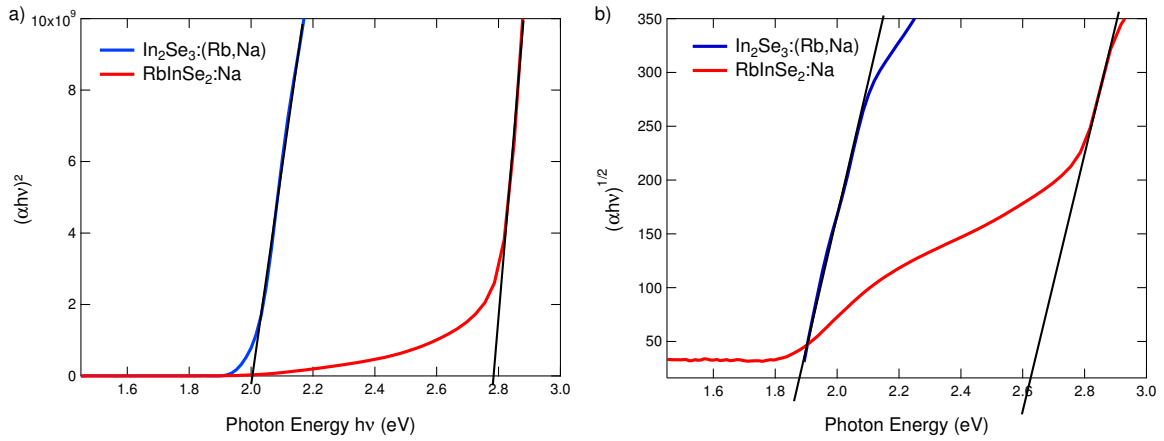


**Figure 5.3:** Absorption spectra of the In<sub>2</sub>Se<sub>3</sub>:(Rb,Na) (blue) and RIS:Na sample (red) grown on glass. The bandgap energy is determined by linearly fitting the leading edge of the spectra (solid black lines). a) shows the case of direct transitions, b) the case of indirect transitions.

The energy bandgap of both semiconductors was reported to be direct [235, 237], but since the band structure can depend on the crystallinity of the films, Figure 5.3 a shows the  $(\alpha h\nu)^2$ - and Figure 5.3 b the  $(\alpha h\nu)^{1/2}$ -spectra of both samples. The comparison of the spectra shows a more linear behavior of the leading edge for the  $(\alpha h\nu)^2$ -spectra, indicating a direct transition in both cases. Therefore in the following, the case of a direct transition is discussed. All statements are valid for the indirect case, using the respective values of the linear fit, as well. By linearly fitting the slope of the leading edge of the spectra, the optical bandgap energy  $E_g$  of the main transition of both thin films was derived (see Table 5.1). The full incorporation of Rb into the crystal increases the bandgap energy by about 0.8 eV in case of RIS:Na compared to that of In<sub>2</sub>Se<sub>3</sub>:(Rb,Na). This value for  $E_g$  fits well with results of recently published theoretical work, in which the authors derived it to  $E_g^{\text{RIS}} = 2.57 \text{ eV}$  [161] and  $E_g^{\text{RIS}} = 2.7 \text{ eV}$  respectively [2] using DFT calculations within the hybrid functional scheme.

However, all these values for  $E_g^{\text{RIS}}$  do not agree with the bandgap energy that was obtained in aforementioned study for a RIS single crystal [235], which was determined to  $E_g = (2.0 \pm 0.1) \text{ eV}$  (direct transition). The authors of that study used the results of their XRD-measurements to calculate  $E_g^{\text{RIS}}$  using the LDA functional, which is known to underestimate the bandgap energy [238]. Since the lattice parameters derived by Huang et al. match

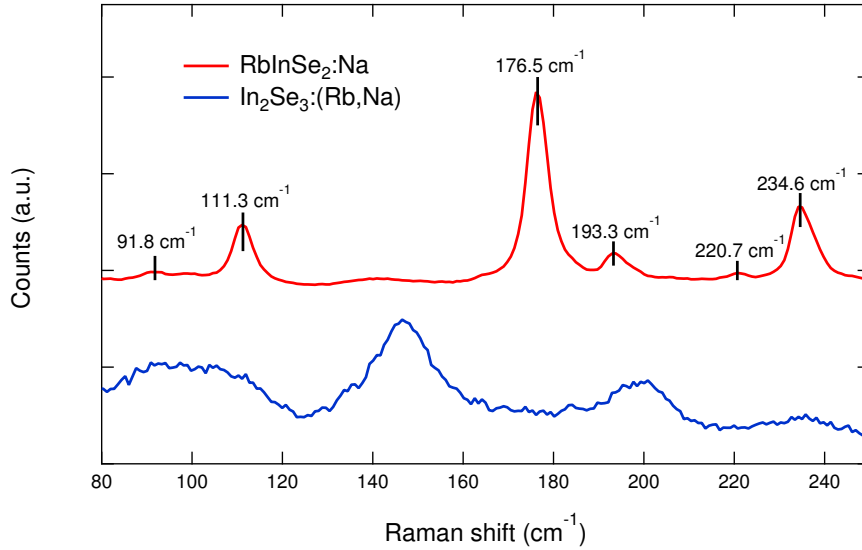


**Figure 5.4:** Raman spectra of the  $\text{In}_2\text{Se}_3\text{:}(\text{Rb,Na})$  (blue) and the  $\text{RIS:Na}$  sample (red). While there are different results for the positions of the peaks around  $k = 200 \text{ cm}^{-1}$  reported in literature, the main peak of  $\gamma\text{-In}_2\text{Se}_3$  is consistently found at  $k = 150 \text{ cm}^{-1}$  [124, 240, 241], which is in good agreement with the spectrum shown in this Figure.

the results shown in Table 5.1, it must be assumed that the reason for the different results for  $E_g^{\text{RIS}}$  are to be found in the method utilized to derive  $E_g$  in that study [235].

The derived value for the optical bandgap of  $\text{In}_2\text{Se}_3$ , however, is in good agreement with experimental data from the literature [239]. Bindu et al. [239] determined the optical bandgap of  $\text{In}_2\text{Se}_3$  in dependence of the annealing temperature of the films and obtained values between  $E_g = 1.84 \text{ eV}$  (annealed at  $150^\circ\text{C}$ ) and  $E_g = 2.09 \text{ eV}$  (annealed at  $450^\circ\text{C}$ ). The samples discussed in this work were deposited at a substrate temperature of  $550^\circ\text{C}$  and therefore fit this range ( $E_g = (2.0 \pm 0.1) \text{ eV}$ ).

In order to provide reference values, Raman spectra of the  $\text{In}_2\text{Se}_3\text{:}(\text{Rb,Na})$  as well as the  $\text{RIS:Na}$  sample are shown in Figure 5.4. The spectra of the respective samples without Na (not shown) do not show considerable deviations. Just as the respective GI-XRD pattern the Raman spectrum of the  $\text{In}_2\text{Se}_3\text{:Rb}$  sample fits very well to literature values for pure  $\gamma\text{-In}_2\text{Se}_3$  [124] supporting the statement that other phases are present in these layers only to a very limited amount.

No other Raman spectrum of a RIS structure has been reported in literature so far. The positions of the main peaks, for which the respective errors are estimated to be lower than  $\pm 0.5 \text{ cm}^{-1}$ , are indicated by markers in Figure 5.4.

The most intense Raman mode of the  $\text{RIS}$ -sample at  $k = 176.5 \pm 0.5 \text{ cm}^{-1}$  overlaps with the  $\text{CIGSe A}_1$ -mode (cf. Figure 4.16), while the most intense mode of the Raman spectrum of  $\text{In}_2\text{Se}_3\text{:Rb}$  overlaps with the  $\text{ODC A}_1$ -mode. Therefore it is hard to judge by the Raman spectra of  $\text{RbF}$ -treated  $\text{CIGSe}$  layers whether one of these phases,  $\text{RIS}$  or  $\text{In}_2\text{Se}_3\text{:Rb}$ , is growing during the PDT as suggested by the XPS-study presented in Section 4.1.2. However, also none of the less intense peaks, as e.g. the mode at  $k = (111.3 \pm 0.5) \text{ cm}^{-1}$  in the Raman spectrum of the  $\text{RIS:Na}$ -sample, are visible in the Raman spectra of the  $\text{RbF}$ -treated  $\text{CIGSe}$ -samples. Due to the low intensity of this peak and the fact that the layer that forms during the  $\text{RbF}$ -PDT is predicted to be only a few nm thin, no final conclusions can be drawn from this comparison and accordingly the comparison of the Raman spectra and GI-XRD-diffractograms taken on the samples discussed in Chapter 4 with those of the reference samples discussed here is inconclusive (the GI-XRD-data are shown in Figure 5.10 in Section 5.2). Hence, it cannot be judged based on these data whether or not a polycrystalline  $\text{RIS}$  or  $\text{In}_2\text{Se}_3\text{:Rb}$  forms during the  $\text{RbF}$ -PDT.

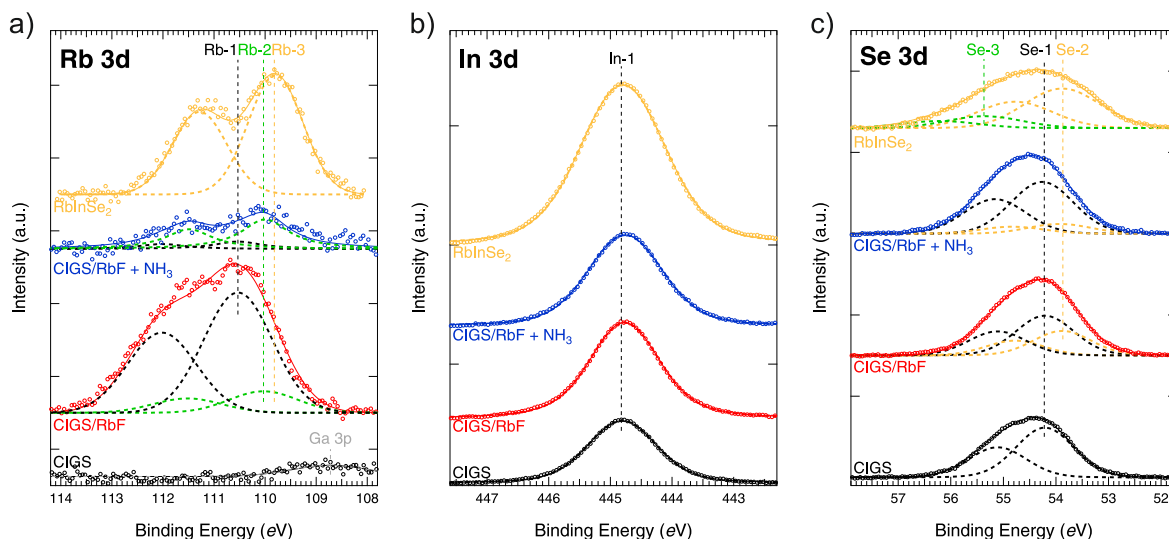


**Figure 5.5:** Comparison of the Rb 3d (a), the In 3d (b) and the Se 3d (c) XPS spectra of an untreated CIGSe sample, a CIGSe sample after RbF-PDT, a CIGSe sample after RbF-PDT and subsequent etching in  $\text{NH}_3(\text{aq})$  and the RIS:Na-sample. The graphs were adapted from Reference [8].

However, comparing the surface composition of the RIS:Na-sample with that of an RbF-treated CIGSe sample via XPS, shows a very good agreement of the chemical environment of Se and Rb (see Publication [8] and Figure 5.5). The data shown in Figure 5.5 was measured on samples with  $\text{CGI} = 0.90$  and is therefore comparable to those discussed in Section 4.1. Note that there was no air-exposure between the layer deposition and the XPS measurement [8], which explains the absence of oxide-contributions in these spectra. The contribution at lower binding energies in the Rb 3d spectrum of the RbF-treated sample (Rb-2) agrees with the Rb-2 contribution, which was found on the air-exposed sample in Section 4.1 (cf. Figure 4.11 g) and is very close to the position of the Rb-signal in the spectrum measured at the RIS:Na sample (Rb-3). The slight shift of the binding energy that is still detected indicates that the chemical environment of the Rb-atoms in RIS and at the surface of the RbF-treated CIGSe are slightly different. However, both the In-position (In-1) as well as the additional Se-species in the spectrum of RbF-treated CIGSe (Se-2), are at the very same positions as the respective main peak in the spectra of the RIS:Na-sample. Note that the Se 3d spectrum cannot accurately be fitted without the presence of the additional Se-contribution at lower binding energies compared to the CIGSe-contributions (here Se-2). Therefore the slightly controversial appearance of the Se-4-contribution, which was discussed in context with the XPS-study in Section 4.1.2, is supported.

Due to the good agreement of the chemical environment of Rb, In, and Se at the surface of the CIGSe after the RbF-PDT and the RIS:Na-sample, it can be concluded that the  $\text{In}_x\text{Se}_y:(\text{Rb},\text{Na})$  layer growing during the PDT (cf. Figure 4.13) is either RIS:Na or a slightly similar (e.g. Rb-deficient) compound. In the following sections, it will therefore be referred to the  $\text{In}_x\text{Se}_y:(\text{Rb},\text{Na})$  as RIS-layer. Taking furthermore into account that the RIS-layer on RbF-treated absorber layers was only detected by XPS but not by Raman scattering or GI-XRD, it is assumed that it grows in an amorphous phase hindering its detection with these structure-sensitive methods. Furthermore, it can be assumed that the bandgap energy of the surface layer lies in between  $2.0 \text{ eV}$  ( $\text{In}_2\text{Se}_3:(\text{Na},\text{Rb})$ ) and  $2.8 \text{ eV}$  (RIS:Na).

## 5.2 Replacing the RbF-PDT with an RbInSe<sub>2</sub>-Deposition

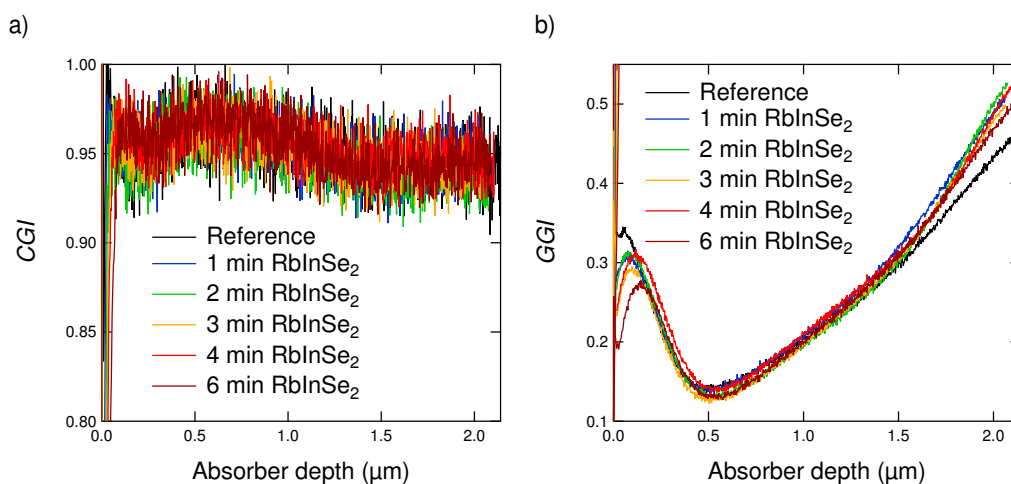
To test the influence of a RIS:Na-layer on  $FF$ , RIS-layers are intentionally grown on top of CIGSe thin films with  $CGI = 0.95$ . Following the argumentation presented in Section 4.2,  $FF$ -loss due to the RbF-PDT does not occur on cells prepared with these absorber layers, because at this composition the share of the ODC in the CIGSe is rather low and only little Rb is incorporated into the surface of the absorber layer. Following the interpretation of that section, only a very thin RIS-layer forms, which is proposed to be the reason why no  $FF$ -loss occurs. If this model is correct, a RIS-layer that is grown on top of such a CIGSe layer independently of the ratio of ODC and  $\alpha$ -CIGSe should reduce the  $FF$ . Furthermore,  $FF$  should steadily decrease with an increasingly thick RIS-layer.

In order to test this prediction, a sample set consisting of six CIGSe deposition processes with  $CGI = 0.95$  was produced. While the absorber layers of one deposition process were kept free of Rb, different thicknesses of RIS were deposited on top of the absorber layers of the other 5 deposition runs.

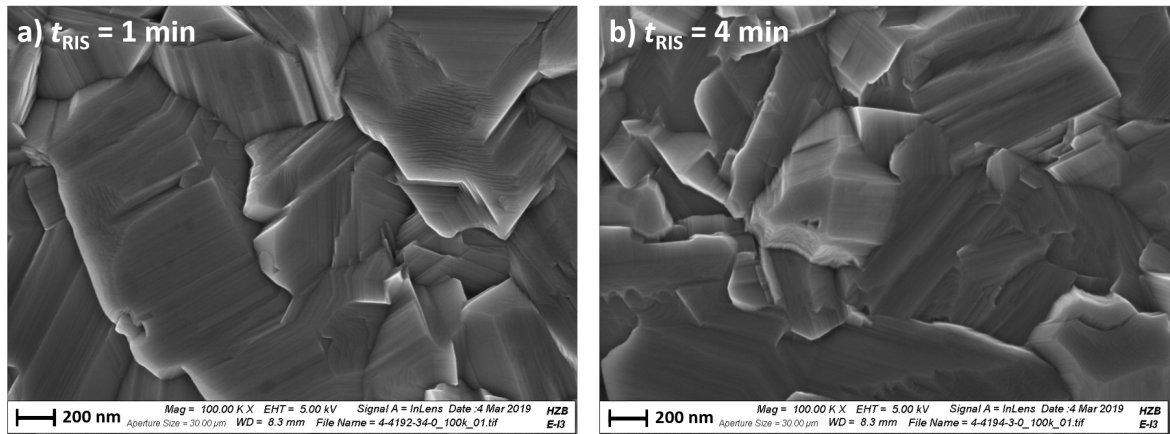
### Part I - Results

The thickness of the deposited RIS was varied from nominally 5 nm (1 min RIS) up to 30 nm (6 min RIS). Figure 5.6 shows the  $CGI$  and  $GGI$  depth profiles of all samples as measured by GD-OES. The sample set shows a high reproducibility in terms of the  $CGI$ -profiles. On the other hand, one can clearly see the impact of the additional In that is deposited during the RIS-deposition on the  $GGI$ -profiles at the surface of the absorber layers. Longer RIS-depositions generally lead to lower surface  $GGI$ . The position of the notch as well as  $E_{g,min}$  and the further profile of the  $GGI$  are not altered by the RIS depositions.

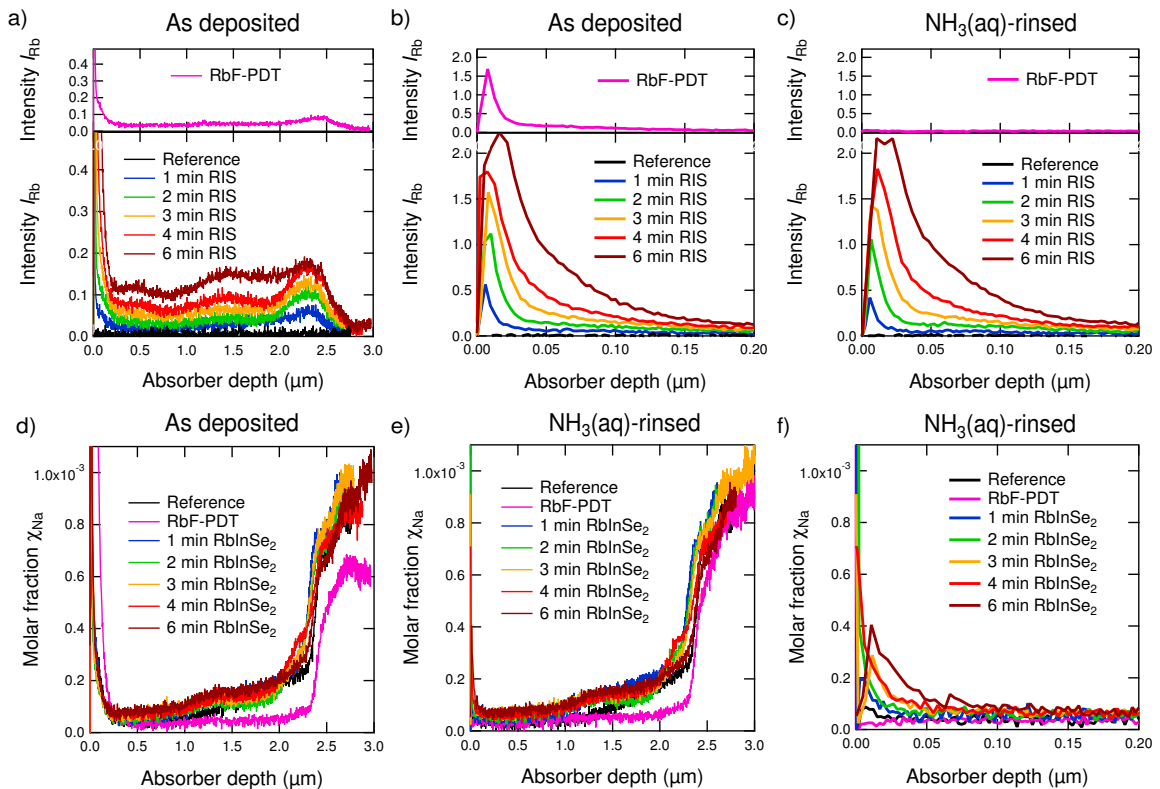
Figure 5.7 shows SEM top view images of the surface of two CIGSe/RIS-samples. It is interesting to note that the direct RIS-deposition does not lead to a nanopatterning of the surface of the CIGSe as the RbF-PDT does. Since it is known that the development of a growth mechanism (Volmer-Weber [231], Frank-van-der-Merwe [242–244], or Stranski-Krastanov [245]) is strongly dependent on the substrate temperature and the growth rate [246], it is likely that these two factors are the reason for the more homogeneous growth of the RIS-layer compared to the RbF-PDT. Both are strongly increased compared to the PDT:  $T_{Sub}^{RIS} = 530\text{ }^{\circ}\text{C} > T_{Sub}^{PDT} = 280\text{ }^{\circ}\text{C}$  as well as  $g_{RIS} \approx 50\text{ } \frac{\text{\AA}}{\text{min}} > g_{PDT} \approx 15\text{ } \frac{\text{\AA}}{\text{min}}$  (cf. Section 3.1). However, the fact that in case of the direct RIS-deposition In is co-evaporated together with RbF and Se might affect the coverage as well.



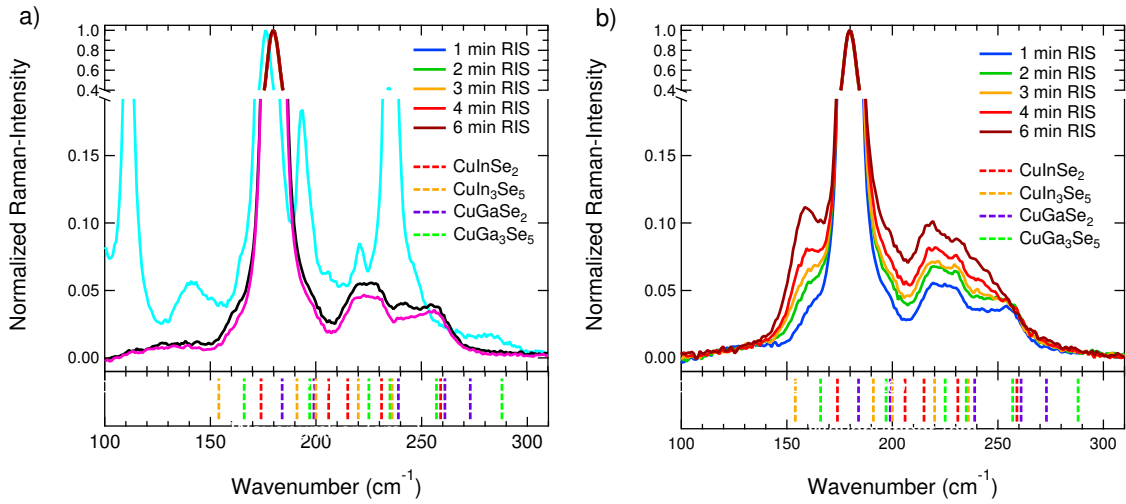
**Figure 5.6:** GD-OES depth profiles of the  $CGI$  (a) and the  $GGI$  (b) of the samples of the CIGSe/RIS sample set. All samples show identical  $CGI$ -profile and the same position of as well as  $GGI$ -amount at the notch.



**Figure 5.7:** SEM top view images of the surface of the absorber layers with a direct RIS-deposition for 1 min (a) and 4 min (b) respectively.



**Figure 5.8:** Alkali metal distributions as measured by GD-OES of the CIGSe/RIS-samples in comparison with an Rb-free reference as well as a sample after RbF-PDT. Zero on the x-axis marks the surface of the CIGSe layer. a) Unquantified Rb-depth profiles measured directly after deposition of the samples of the CIGSe/RIS-set (bottom) and an RbF-treated sample (top); b) The surface region of the same measurements as shown in a; c) The surface region of measurements of the same samples as in a and b, but after rinsing them in NH<sub>3</sub>(aq); d) Quantified Na depth profiles measured directly after deposition; e) Na depth profiles measured after rinsing the samples in NH<sub>3</sub>(aq); f) The surface region of the same measurements as shown in f.



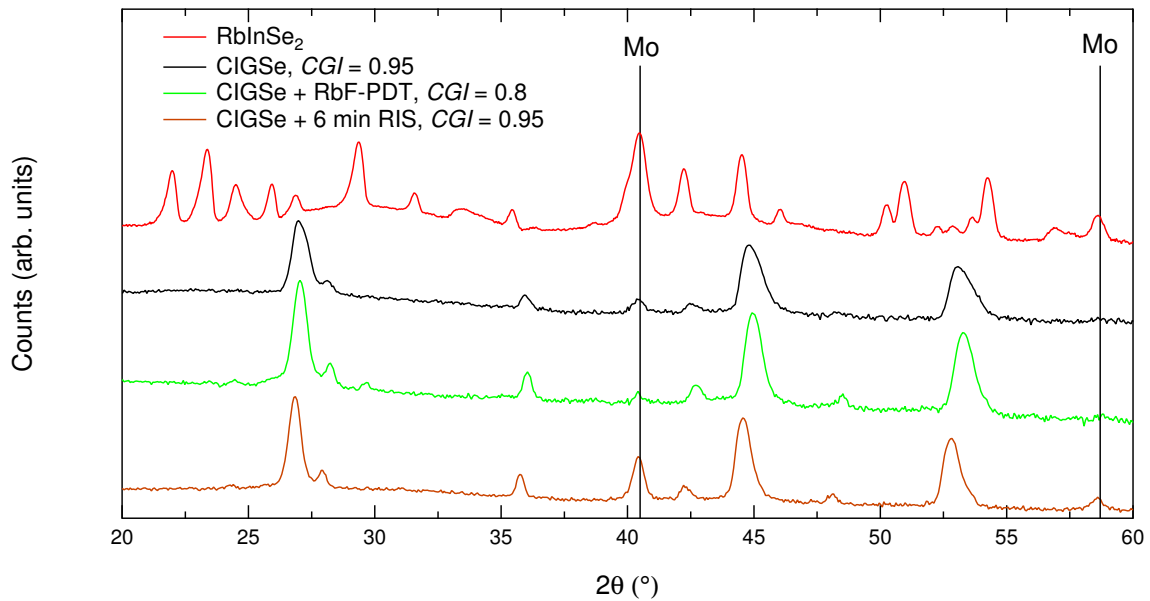
**Figure 5.9:** a) Reference Raman spectra measured on the Rb-free CIGSe sample (black), the RbF-treated CIGSe (pink) and the RIS-reference (light blue). b) Raman spectra of the CIGSe/RIS-sample set in comparison. The bottom part of both graphs indicates the positions of the known modes of CuInSe<sub>2</sub>, CuIn<sub>3</sub>Se<sub>5</sub>, CuGaSe<sub>2</sub>, and CuGa<sub>3</sub>Se<sub>5</sub> taken from References [195, 196]. Note that due to the high number and overlap of the different peak positions as well as the fact that the used material is a mixture of the In- and Ga-compounds, the exact determination of the positions of the peaks related to CIGSe and the ODC is hindered. However, the position of the A<sub>1</sub>-mode of CIGSe and the ODC at wavenumbers of around  $k_{A1}^{CIGSe} = (180 \pm 0.5) \text{ cm}^{-1}$  and  $k_{A1}^{ODC} = (159 \pm 0.5) \text{ cm}^{-1}$ , can be isolated. All spectra were normalized to their respective A<sub>1</sub>-mode. The y-axis is split for convenience.

Figure 5.8 shows the Rb- and Na-distributions in these samples as measured by GD-OES compared to a sample with an RbF-PDT, as it was discussed in Section 4.2, before and after etching them in NH<sub>3</sub>(aq). The Rb-profiles of the RIS-set are almost unchanged by the ammonia etching, while the residual Rb is almost completely removed from the surface of the PDT-sample, as it was already shown in Figure 4.14 for another sample with  $CGI = 0.95$ . Since RIS is stable under ammonia etching (see Section 5.1), it can be assumed that the deposition of RIS on top of the CIGSe was successful.

However, there is again no signature of (poly-)crystalline RIS present in either Raman (see Figure 5.9) or GI-XRD (see Figure 5.10).

The Raman spectra show again that the RbF-PDT is reducing the amount of the ODC. The direct RIS-deposition, on the other, hand leads to a steadily increasing ODC-signal with increasing thickness. It can be assumed that this ODC-contribution is due to an inter-diffusion of Cu and Rb at the high temperatures during the RIS-deposition leading either to the formation of a bi-layer RIS/ODC on top of the CIGSe or the formation of a Rb-deficient (Cu,Rb)InSe<sub>2</sub>-layer with similar phonon-modes as the ODC. Including the GI-XRD-results shown in Figure 5.10, the latter becomes unlikely since all detected peaks can be attributed to CIGSe (including the ODC, which is hardly discernible from the  $\alpha$ -phase CIGSe in such diffractograms [247]). Therefore it can be concluded that the RIS-deposition leads to the formation of a bi-layer of amorphous RIS (just as in case of the RbF-PDT) and ODC.

In agreement with this interpretation, it can be seen that the amount of Rb throughout the bulk of the CIGSe layer (Figure 5.8 a) as well as at its surface (Figure 5.8 b) increases with  $t_{RIS}$ . The amount of Rb incorporated into the bulk after 10 min RbF-PDT is comparable with the amount incorporated after 2 min RIS-deposition. The nominal thickness of the RbF deposited during the RbF-PDT is in the range of 6 nm to 10 nm (RbF deposition rate  $\gtrsim 0.1 \text{ \AA/s} = 6 \text{ nm/10 min}$ ), while the amount of RbF deposited during 1 min of RIS-deposition is about 1.25 nm (cf. Section 3.1.3). This suggests that the elevated process temperature in case of the RIS-deposition (530 °C compared to 280 °C during the RbF-PDT) leads to a stronger in-diffusion of Rb into the bulk of the absorber layer, supposedly in exchange with a Cu-diffusion into the lower region of the RIS-layer.



**Figure 5.10:** Logarithmic plots of the grating incidence (incident angle 0.5°) XRD diffractogram of the RbInSe<sub>2</sub> thin film discussed in the section above in comparison with a CIGSe reference sample, an RbF-treated sample and a sample with RbInSe<sub>2</sub> deposited on top of the CIGSe. While the diffractograms of the three CIGSe samples show only slight peak-shifts that are attributable to the slightly different surface GGI due to the different CGI, no peak correlation with the RbInSe<sub>2</sub> sample can be found.

The elevated temperature during the RIS-deposition is affecting the Rb-Na exchange mechanism discussed in Section 4.1 as well. Two effects can be observed:

1. Na is incorporated into the RIS-layer at the surface as confirmed by Figure 5.8 f. Just as in case of Rb, the amount of Na (measured after rinsing the absorber layers with NH<sub>3</sub>(aq)) increases with longer RIS-deposition, meaning that Na-diffusion occurs during the RIS-deposition and the subsequent cool-down.
2. The RIS-deposition does not lead to an out-diffusion of Na from the bulk of the absorber layer as it was described for the RbF-PDT at  $CGI \geq 0.9$  in the previous chapter. The direct comparison of the Na depth profile of the untreated absorber layer (black curve in Figures 5.8 d and e) with that measured in a sample after RbF-PDT (pink curve in Figures 5.8 d and e) shows again that the amount of Na in the bulk of the CIGSe is strongly reduced during the RbF-PDT. This depletion is pronounced close to the back contact where the molar fraction of Na is about twice as high in the untreated CIGSe as in the RbF-treated one. The molar fraction of Na in the CIGSe samples after RIS-deposition, however, is not decreased but shows the same depth profile as in the untreated layer (neglecting the increased amount of Na at the very surface) with even slightly higher  $\chi_{Na}$  in the bulk of the CIGSe.

The effect of the Rb-incorporation on  $n_{CV}$  is investigated by  $C$ - $V$ -measurements on solar cells that were produced from the complete sample set. The results are displayed in Figure 5.11 a and show no trend of  $n_{CV}$  with  $t_{RIS}$ . The  $n_{CV}$  of all samples lies in the range of  $n_{CV} = 2 \cdot 10^{15} \text{ cm}^{-3}$  to  $n_{CV} = 3 \cdot 10^{15} \text{ cm}^{-3}$  and therefore higher than the reference values of the untreated CIGSe sample and lower than the value of the RbF-PDT sample. Using Equation 2.44 to estimate the reduction of  $\Delta V_{OC}^{CV}$  due to the RIS-deposition leads to a reduction of this Subsequently, loss of up to 19 mV (versus 26 mV in case of this Subsequently, RbF-PDT). The sample with 3 min RIS-deposition is treated as an outlier since it shows slightly lower  $n_{CV}$  than the other samples, which goes along with a lower  $V_{OC}$  measured on this sample (see Figure 5.12).

Figure 5.11 b additionally shows the  $C$ - $V$ -curves that were used to calculate the  $N_{CV}$ -profiles shown in Figure 5.11 a. Neglecting the sample after 3 min, the RIS-samples do not show the

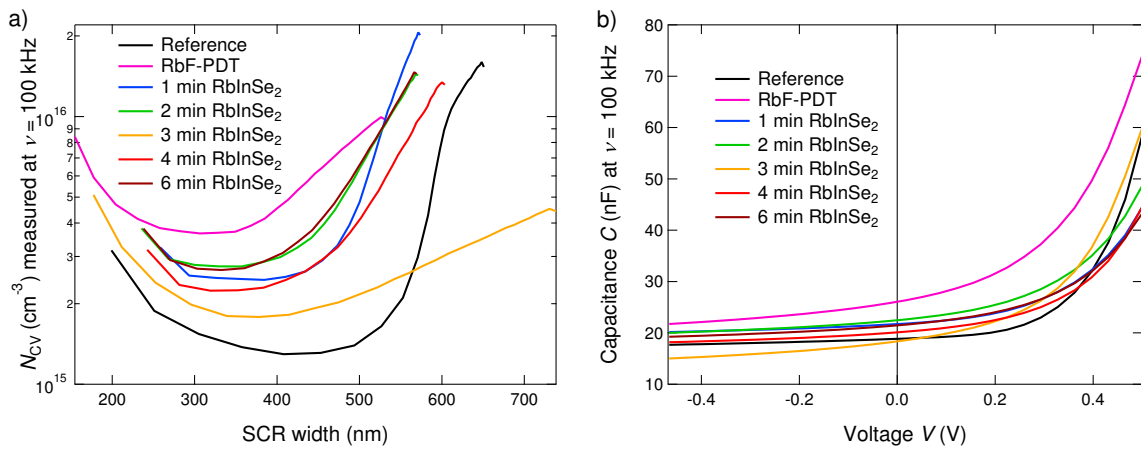


**Figure 5.11:** a) Carrier concentration profiles as measured by C-V of the sample set with an increasingly thick RIS surface layer in comparison to those of an Rb-free reference sample and a sample after RbF-PDT. b) The corresponding C-V-curves.

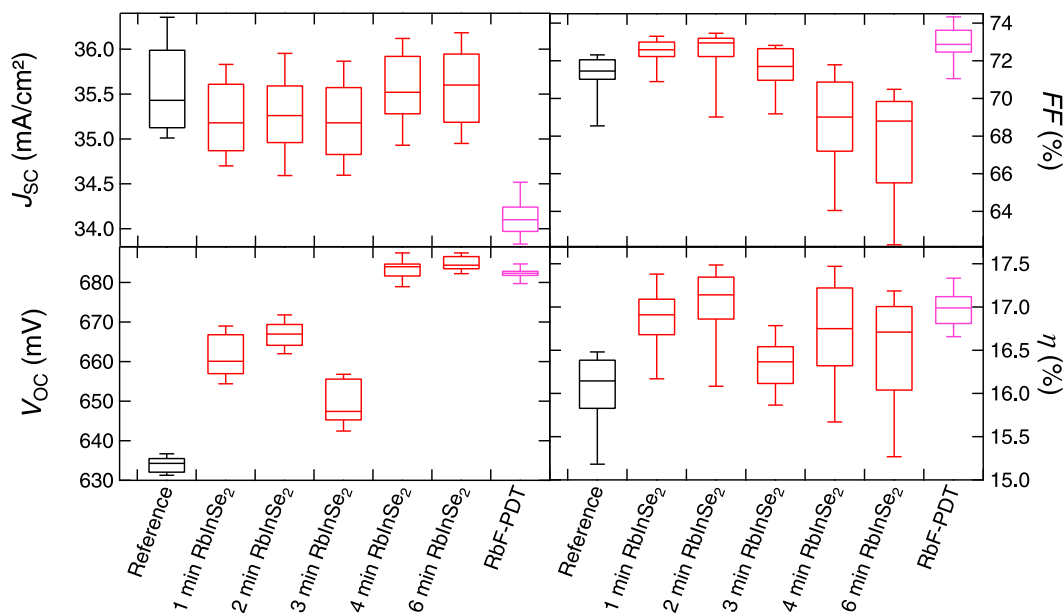


**Figure 5.12:** Boxplots of the PV-parameters of the CIGSe/RIS sample set. The sample with  $CGI = 0.95$  from the experiment described in Section 4.2 was added for comparison. Note that the lower  $j_{SC}$  in case of the RbF-PDT is due to changes in the grid deposition, which were made in between the performance of these two experiments and are not visible in the  $EQE$  (not shown here).

strong contribution to the capacitance at high positive bias voltages that is present in case of the RbF-PDT as it was already discussed in Section 4.1.1. This behavior indicates that the (defect) contribution causing the higher capacitance in samples with an RbF-PDT is not present (or not to the same extent) after the direct RIS-deposition. This behavior will be discussed in the frame of the final device modeling in Chapter 8.

Figure 5.12 shows the PV-parameters as measured on this sample set. The parameters measured on the  $CGI = 0.95$  sample from the experiment described in Section 4.2 were added for comparison. After an initial increase of  $FF$  due to the steadily increasing  $V_{OC}$  (following Equation 2.47), the increasingly thick RIS-layers lead to a steady decrease in  $FF$  and to substantially lower values than the  $FF$  of the RbF-PDT sample. Despite the missing trend of increasing  $n_{CV}$  with  $t_{RIS}$ , the  $V_{OC}$  steadily increases with  $t_{RIS}$  (neglecting the outlier after 3 min RIS-deposition).

The reason for that can be found in a steady reduction of  $\Delta V_{OC}^{rem}$ , i.e. a reduction of the SRH-recombination rate. Figure 5.13a shows four exemplary  $trPL$ -measurements of this set performed using a carrier generation rate of  $\Delta n = 5.65 \cdot 10^{15}$  cm<sup>-3</sup>. The results of the

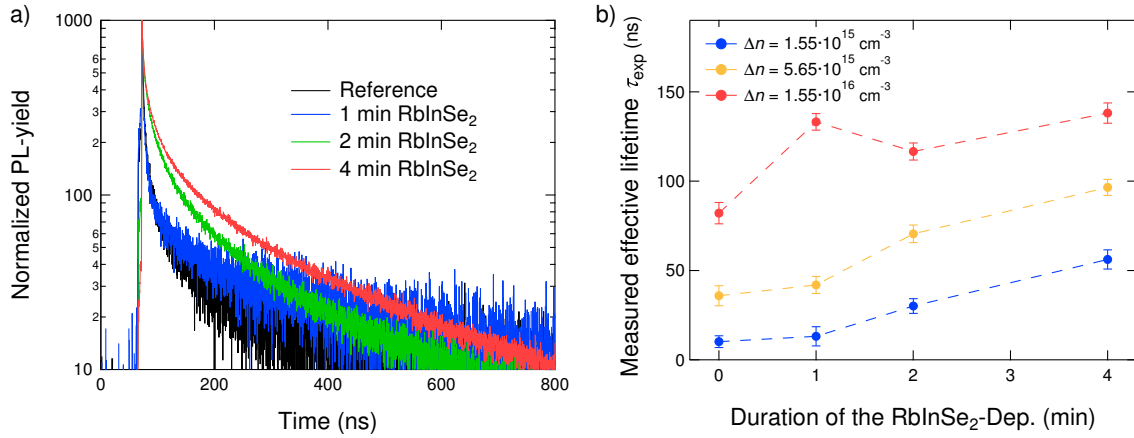


**Figure 5.13:** a) Normalized time resolved measurements of the PL yield of the Rb-free reference sample as well as three samples after differently long RIS-depositions. The measurements were performed at room temperature and  $\Delta n = 5.65 \cdot 10^{15} \text{ cm}^{-3}$ . b) Results of the fits of the trPL-measurements of the samples shown in a) and two additional  $\Delta n$ . Independent of  $\Delta n$  a steadily increasing  $\tau_{\text{exp}}$  with increasing deposition time of the RIS-layer is found, indicating a reduction of the recombination rate in the devices due to the RIS-deposition. The dashed line is meant as guide to the eye only.

bi-exponential fit of these and the corresponding transients at lower and higher  $\Delta n$  are displayed in Figure 5.13 b. Independent of  $\Delta n$  there is a steadily increasing trend of  $\tau_{\text{exp}}$  with  $t_{\text{RIS}}$  visible. It is interesting to note that all lifetimes measured on this sample set are significantly lower than those measured on the sample sets in Chapter 4. This is surprising since the reference sample used in the present section was prepared with the same deposition process as the sample with  $CGI = 0.95$  in Section 4.2 and both devices exhibit similar PV-parameters. Judging from the fact that the PL-decay shows a strongly curved behavior for all samples of the present series, it is assumed that the etching with HCl (which was done on separate days for each sample set) induced a stronger surface modification, i.e. stronger surface recombination, on this sample set compared to the other two. However, as it was already discussed in Section 3.2, the results of the trPL-measurements can be used for a qualitative and comparative analysis of the SRH-recombination. Therefore, when comparing the effect of the RIS-deposition on  $\tau_{\text{exp}}$  with that of the RbF-PDT, one has to take into account the  $\tau_{\text{exp}}$  of the respective reference samples.

Figure 5.14 a shows the extraction of  $E_{\text{U}}$  from the IQE-data measured on this sample set; Figure 5.14 b displays the respective fit-results. Ignoring the sample with 3 min RIS deposition, there is a clear trend of decreasing  $E_{\text{U}}$  with  $t_{\text{RIS}}$ , which seems to level at about  $E_{\text{U}} \approx 15 \text{ meV}$ . Similar as in the case of the RbF-PDT it therefore becomes evident that the incorporation of more Rb steadily passivates defects in the devices. However, due to the rather small reduction of already low  $E_{\text{U}}$  (compared to  $k_{\text{B}}T$  at room temperature), it seems likely that the major effect of the RIS-deposition on  $\Delta V_{\text{OC}}^{\text{rem}}$  is via the passivation of deep defects, which is also similar to the case of the RbF-PDT.

The trade-off of an increasing  $V_{\text{OC}}$  and a decreasing  $FF$  with thicker RIS-layers leads to an optimum  $\eta$  between 2 min and 4 min RIS-deposition, which is – due to the higher  $T_{\text{Sub}}$  – substantially shorter than the RbF-PDT, which takes 15 min.

Another effect of the direct RIS-deposition is shown in Figure 5.15. The RbF-PDT leads to a roll-over at high bias voltages as it was already described in Section 4.1.1. The RIS-deposition on the other hand – independent of its duration – does not lead to such a behavior. This indicates that the  $FF$ -loss and the roll-over in case of the RbF-PDT do not have the same origin since only the  $FF$ -loss appears after a direct RIS-deposition as well.

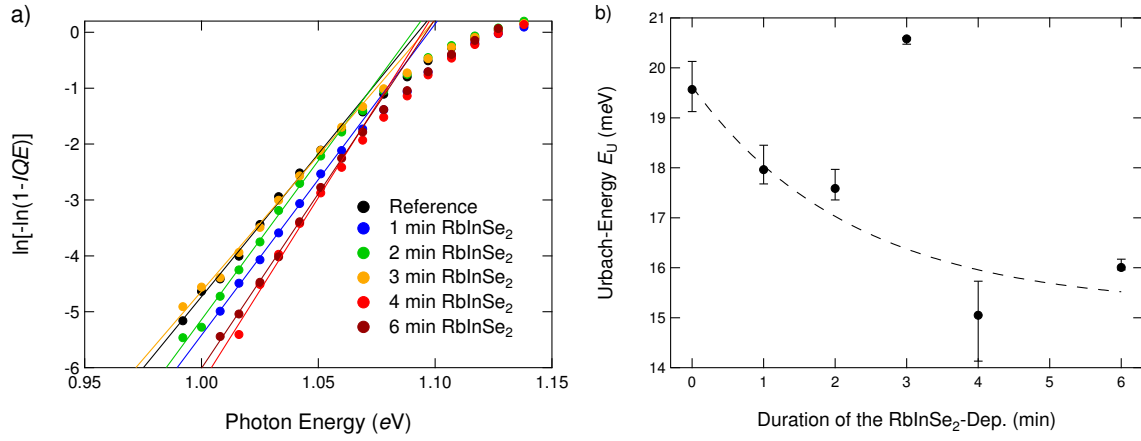


**Figure 5.14:** a) Low-energy slope of the  $\ln[-\ln(1-IQE)]$  versus the photon energy of the incident light. The Urbach-energy is extracted from the linear slope according to Equation 3.10. b) Results of the fits shown in a). The error bars show the deviation by varying the number of measurement points included in the fit. The dashed line shows an exponential fit of the data (excluding the data point at 3 min) as a guide for the eye.

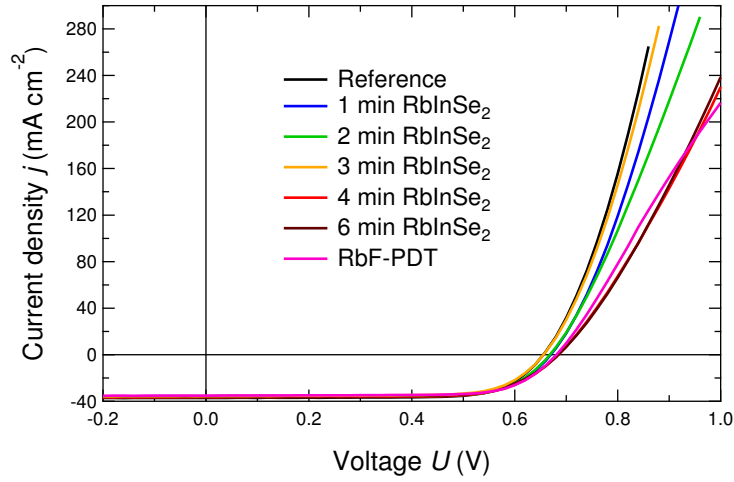


**Figure 5.15:**  $j$ - $V$ -curves of the best cell of each run of the CIGSe/RIS sample set.

## Part II - Combined Discussion

A possible explanation for both, the absence of the roll-over and the independence of  $n_{CV}$  of  $t_{RIS}$  (versus the dependence of  $n_{CV}$  on  $t_{PDT}$ ), can be found in the Na-distribution in the bulk of the CIGSe layer. As it was described above, there is a strong reduction of  $\chi_{Na}$  measured after the RbF-PDT (cf. Figure 5.8), which is not visible after RIS-deposition. This could be due to the fact that the RIS-deposition is done at higher  $T_{Sub}$  than the PDT, which presumably causes more Na to diffuse from the glass into the CIGSe layer during the RIS-deposition than during the PDT. Note that although the samples are at the higher temperature of  $T_{Sub} = 530^\circ\text{C}$  only for a few minutes, additional Na-diffusion can take place during the subsequent cool-down after the RIS-deposition. The Rb-Na exchange mechanism, which was observed for samples with  $CGI > 0.80$  in the previous chapters, is hence not applicable to the RIS-samples. Simply its absence could be the cause for these two effects observed in the RIS-treated devices as it will be discussed in Chapter 7.1 taking into account results of DFT calculations from the literature (Rb-Na exchange mechanism and its effect on  $n_{CV}$ ) and in Chapter 8 respectively (interaction of the Na-depletion and the roll-over effect).

In conclusion, the observed increasing gain in  $V_{OC}$  due to the RIS-deposition is –minus the constant offset of 14 mV to 19 mV, which is due to the reduction of  $\Delta V_{OC}^{CV}$  – due to a steadily growing reduction of  $\Delta V_{OC}^{rem}$ . This reduction, in turn, consists of a reduction of the SRH-recombination rate and the passivation of shallow defects as it is evident by the observed

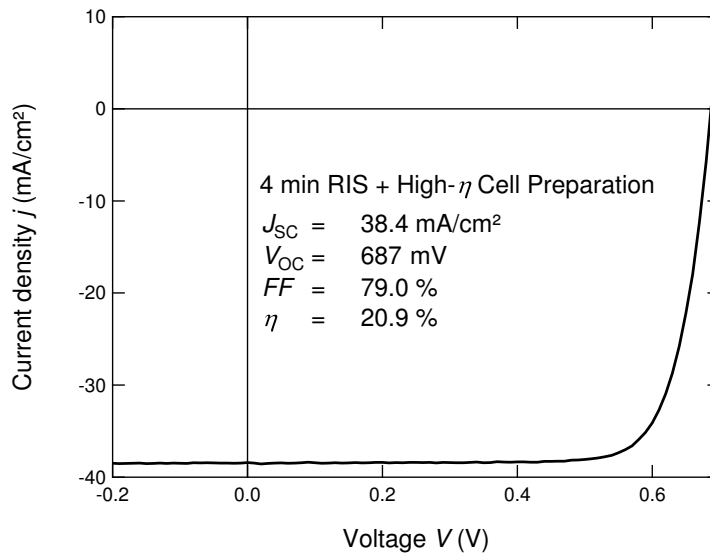


**Figure 5.16:** PV-parameters as well as the  $j$ - $V$ -curve of a device, which was fabricated with  $CGI = 0.95$  and RbF-PDT. The device was finished using HZB's 'high- $\eta$ '-line.

trend of increasing  $\tau_{\text{exp}}$  as well as decreasing  $E_U$  with increasing  $t_{\text{RIS}}$ . Since the change of  $E_U$  is rather small (maximal about 5 meV) it can be further concluded that the major effect of the increased amount of Rb in the absorber layer is the reduction of the SRH-recombination rate, which is leading to the strong trend in  $\tau_{\text{exp}}$  and  $V_{\text{OC}}$ . However, there is no analytical expression available directly quantifying the reduction of  $\Delta V_{\text{OC}}^{\text{rem}}$ -loss due to the reduction of  $E_U$  and the improved  $\tau_{\text{eff}}$ . Therefore device modeling will be used as a numerical instrument for the estimation and subsequent comparison of the impact of the RbF-PDT and the RIS-deposition on  $\Delta V_{\text{OC}}^{\text{rem}}$  in Chapter 8.

The fact that the direct RIS-deposition does not lead to a nanopatterning at the surface of the CIGSe but still shows similar effects on  $\tau_{\text{exp}}$  and  $V_{\text{OC}}$  as the RbF-PDT does, indicates that the effect of the nanopatterning on the device performance is negligible and that surface passivation by point contact formation (if it happens in case of the PDT) is not the main effect on  $\tau_{\text{exp}}$ , as will be discussed in more detail in Section 7.2.3 taking into account thoughts from literature.

In closing this chapter, Figure 5.16 shows the  $j$ - $V$ -curve of a device fabricated with the 'high-efficiency'-line at HZB (photolithographic cell completion + ARC). The efficiency of  $\eta = 20.9\%$  proves that competitive solar cells can be produced with the direct RIS-deposition. Compared to the RbF-treated device presented in Figure 4.23, the efficiency could be even improved mainly due to the higher  $V_{\text{OC}}$ .

## Summary and Conclusions of Chapter 5

In this chapter, it was shown that the co-evaporation of RbF, In, and Se does indeed lead to the formation of RIS, just as it was predicted theoretically [2, 161]. Furthermore, the composition of the surface-phase forming during the PDT is very close to the surface composition of a RIS:Na layer [8]. It is therefore concluded that this PDT-induced surface phase is either RIS:Na or a compound with slightly different composition. Furthermore, the RbInSe<sub>2</sub>-thin films, which were synthesized for the first time in this work, enabled to retrieve some of the optical and structural properties of this RIS-layer. These properties will be used as input parameters in the device simulations in Chapter 8.

In case the RIS-layer is intentionally deposited on a CIGSe absorber layer with  $CGI = 0.95$ , it seems to grow amorphously and does lead to the effects that were expected following the argumentation of Chapter 4. While the RbF-PDT does not lead to a reduction of  $FF$  at this  $CGI$  since the fraction of ODC to  $\alpha$ -phase CIGSe is very low suppressing the intrinsic

formation of RIS,  $FF$  does decrease after intentional, and  $CGI$ -independent RIS deposition. Furthermore, it is shown that the loss in  $FF$  is directly connected with the thickness of the deposited RIS-layer. This supports the direct correlation of the  $FF$ -loss with the thickness of the RIS-layer after the RbF-PDT on samples with  $CGI < 0.95$  as well.

When depositing the RIS layer at high temperatures, Rb quickly diffuses into the bulk of the CIGSe, while at the same time there is a steady Na-supply from the glass substrate. Assumingly due to the high substrate temperature, the indirect Rb-induced doping mechanism is hindered, limiting the reduction of  $\Delta V_{OC}^{CV}$  to about 14 meV to 19 meV compared to the reference. However, due to the steady and strong enrichment of alkali atoms in the absorber layer, the SRH-recombination rate in the device is steadily decreased leading to a subsequently steady increase of  $V_{OC}$ .

## 6 Interaction of an RbF-Conditioned Surface and the Buffer Layer

Following the evaluation of the effects of the RbF-PDT on bulk and surface properties of the absorber layers, in this chapter, the interaction of the RbF-treated surface of the CIGSe and the subsequently deposited CBD-CdS buffer layer is analyzed. Note that the following experiments were performed at the IMN and that the equipment and processes used are therefore different from those described in the other chapters (cf. experimental details in Section 3.1.4). However, preliminary tests showed that the general effects of the RbF-PDT are comparable, also because the procedure was adapted from HZB (cf. Section 3.1.4). This chapter is based on Publication [3].

As it is described in the literature review in Chapter 2.3, heavy alkali-PDTs enable to grow the commonly used CdS layer thinner than on untreated samples without losing performance [95, 126]. Due to the rather narrow energy bandgap of CdS ( $E_g^{\text{CdS}} = 2.4 \text{ eV}$  [248]), a thinner buffer layer leads to reduced absorption losses in the buffer layer and therefore to a gain in  $j_{\text{SC}}$ . In this section, the impact of the RbF-PDT on the CdS growth will be evaluated in detail in order to elucidate why one can grow the CdS thinner on Rb-conditioned CIGSe. To do so, a combinatory approach including Raman scattering and SEM to investigate the PDT-induced changes of the CdS-growth as well as  $j$ - $V$  and  $IQE$ -measurements of respective devices is used. Furthermore, the interplay of the surface-ODC of the absorber layers (with and without RbF-PDT) with the subsequently deposited CdS-buffer layer is examined using Raman scattering.

Two sample sets were prepared consisting of an RbF-treated as well as an untreated CIGSe reference sample each: Set 1 for the growth study and Set 2 for the device study. Therefore in total four CIGSe thin film samples were deposited. The integral composition as measured by XRF exhibits  $CGI \approx 0.8$  and  $GGI \approx 0.35$ . Based on the previous chapters it is expected that the RbF-PDT leads to the growth of a RIS-layer on top of the CIGSe due to the rather low  $CGI$ .

After the deposition of the CIGSe, the samples were removed from the vacuum system, i.e. exposed to air, and on two samples an RbF-PDT was performed as described in Section 3.1.4. The samples of Set 1 were cut in 11 approx.  $1 \times 1 \text{ cm}^2$  sized pieces each, of which ten were dipped into an aqueous chemical bath for the CdS-deposition (for experimental details see Section 3.1.2). Starting after one minute, one sample was taken out of the bath per minute resulting in a variation of the CBD-duration from 0 min to 10 min. To avoid cross contamination the untreated and RbF-treated samples were dipped separately.

The samples of Set 2 were cut in 4 pieces each, which were dipped in a nominally identical CdS bath for 3 min, 4.5 min, 7 min, and 9 min respectively. Afterward, these samples were completed to solar cells as described in Section 3.1.4. Note that no other parameters of the CBD than its duration were varied, but the recipe, which was empirically optimized for CIGSe devices without Rb, was used. It was not investigated if a variation of e.g. the concentration and ratios of the reactants, the temperature or the volume of the bath have a different impact on samples with and without Rb and therefore if the used procedure is optimal for Rb-containing devices as well. A systematic investigation of the effects of the RbF-PDT on the properties of the devices in dependence on all these parameters lies not in the scope of the present work.

## 6.1 Analysis of the ODC-Signature

### Part I: Results

In Figure 6.1 one example fit of the A<sub>1</sub>-region of the Raman spectra of each sample of Set 1 is shown. A detailed description of the utilized fitting procedure is given in Section 3.2.

In order to analyze the impact of the RbF-PDT as well as the CdS-growth on the ODC signature, the area ratio of the ODC-1 contribution over CIGS-1 was calculated for all five measurements of each sample. The average of these five measurements is plotted versus the CdS deposition duration ( $t_{\text{CBD}}$ ) in Figure 6.2.

It is evident that the RbF-PDT leads to a significant reduction of the ODC A<sub>1</sub> mode in these Cu-poor samples, just as it was already shown in Section 4.2. This validates that this behavior is generally valid and not only for samples grown at HZB. Furthermore, there is a steady reduction of the ODC A<sub>1</sub> mode with  $t_{\text{CBD}}$ . To quantify this reduction of ODC-1, a linear fit of both curves was performed. According to the fit results, the RbF-PDT leads to a reduction of the ODC-1 to CIGS-1 ratio at  $t_{\text{CBD}} = 0$  min of  $(16 \pm 5) \%$  compared to the untreated reference. With longer  $t_{\text{CBD}}$  the ODC-contribution is (further) reduced in both cases with indistinguishable rates: the slope of the linear fit is  $(-0.009 \pm 0.001) \text{ min}^{-1}$  for the untreated samples and  $(-0.011 \pm 0.001) \text{ min}^{-1}$  for the RbF treated ones. Note again, that Figure 6.2 shows the *ratio* of the ODC-1 and the CIGS-1 contribution, meaning that this is not an attenuation effect of CdS covering the surface of the CIGSe. Furthermore, it can be excluded that the reduction of the ODC is related to changes of stress or strain in the lattice, because these would always induce a shift of the peak positions [198, 199], which does not occur in the spectra shown in Figure 6.1 (cf. discussion in Section 3.2 for more details). Moreover, this is an indicator for a direct consumption of the ODC phase during the CBD.

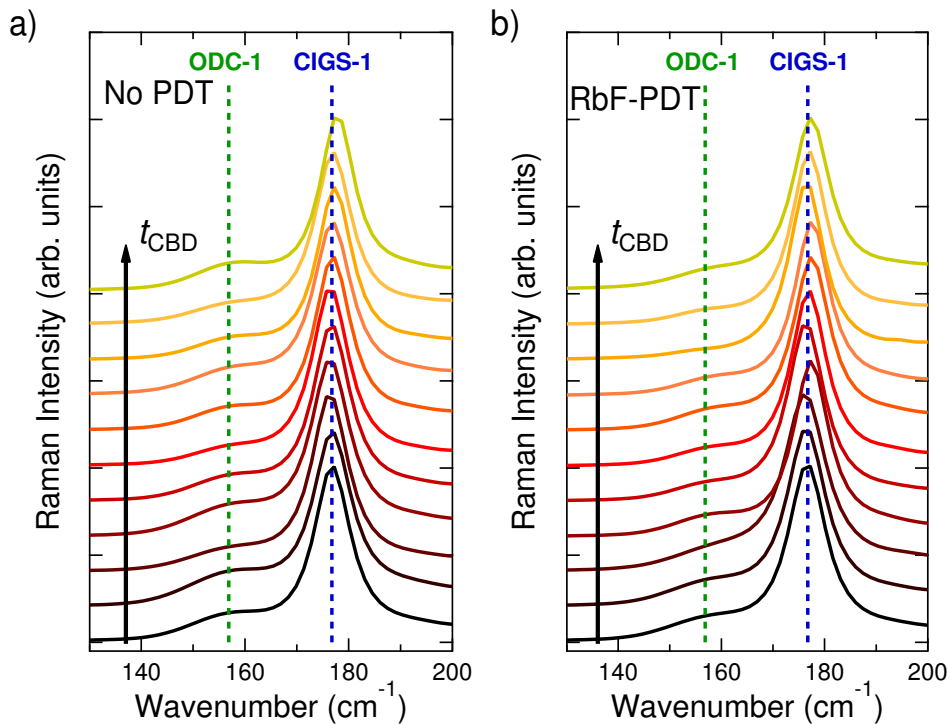


**Figure 6.1:** Examples of how the A<sub>1</sub>-region of the two different sample sets evolves during the CdS deposition in case of untreated CIGSe (a) and RbF-treated CIGSe (b). The deposition time of the CdS is indicated by  $t_{\text{CBD}}$ . The initial reduction of the ODC-feature as well as the steady vanishing of its residuals during the CBD are visible. The fitting procedure of these spectra is shown in Figure 3.5 in Section 3.2.

## Part II: Combined Discussion

The fact that a KF-PDT can lead to a reduction of the ODC-signature in Raman spectra was already published before [128] and for the case of an RbF-PDT for the first time discussed in Section 4.2 above. Following the discussion in Section 4.2, this phenomenon is due to the formation of a RIS-phase at the surface of the Cu-poor absorber layer during the RbF-PDT. The fact that polycrystalline RIS is Raman active (cf. Figure 5.4) but there are no traces visible in the spectra presented here, is another hint that the RIS-layer is growing amorphously since even very thin CdS-layers show distinct features (see following sections).

The further reduction of the ODC signal during the CBD is independent of whether or not a PDT was performed. Therefore this linear reduction has to be attributed to effects, which are valid for samples with and without RbF-PDT. As it is discussed in Section 3.2, the reduction of the ratio of ODC-1 and CIGS-1 most likely means that the fraction of the amount of ODC within the probed volume decreases, i.e. that part of the ODC is consumed during the CdS-growth. The easiest explanation for such a reduction would therefore be the occupation of some of the additional  $V_{Cu}$  in the lattice of the ODC. Since Cu-diffusion seems unlikely due to the low temperature of the deposition and the fact that Cu is already evenly distributed in samples with  $CGI = 0.80$  (see Section 4.2), it appears likely that Cd is diffusing into the ODC during the CBD. However, no direct experimental evidence for the in-diffusion of Cd can be drawn from the presented data. Therefore this interpretation will be discussed taking into account additional depth-dependent hard X-ray photoelectron spectroscopy data from literature in Chapter 7.

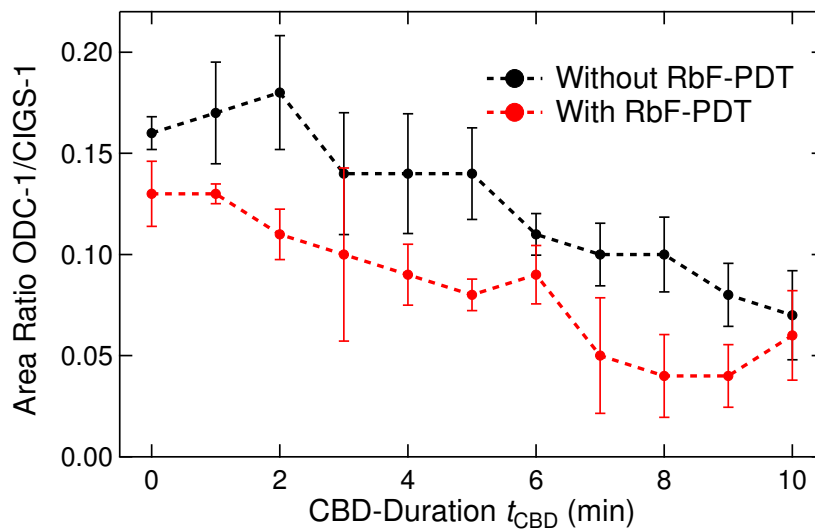


**Figure 6.2:** Evolution of the area ratio of the ODC-1 and the CIGS-1 peak for both sets during the CdS deposition. Dashed lines are shown as guidance for the eye only. The error bars show the standard deviation calculated from the five measurements which were done on each sample.

## 6.2 Impact of the PDTs on the CdS-Growth

### Part I: Results

#### Raman and SEM study (Set 1)

In this section, the impact of the RbF-PDT on the growth morphology (analyzed by SEM) as well as on the growth dynamics (analyzed by Raman scattering) of the CdS is investigated using the samples of Set 1. Starting with the latter, Figure 6.3 shows the Raman spectra in the range of the CdS LO-contributions (one example measurement on each sample). As can be seen there are no traces of CdS-contributions during the first 2 minutes of the CBD.

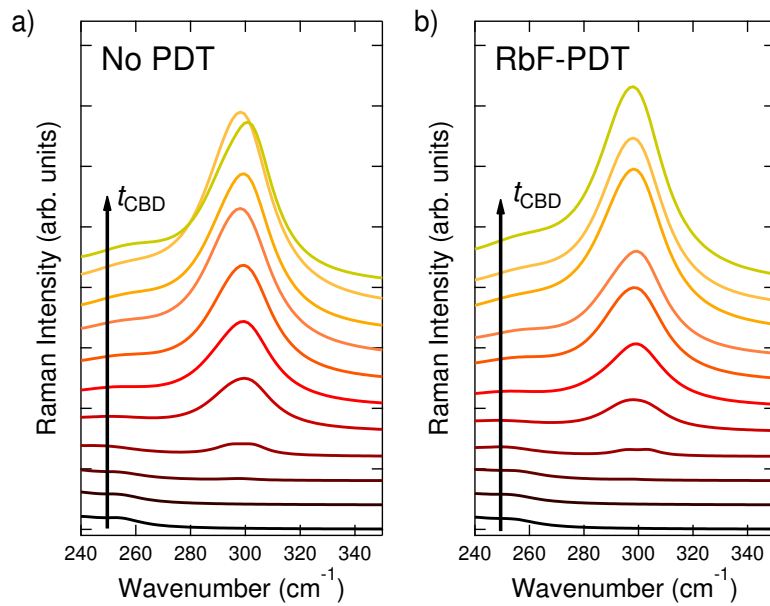


**Figure 6.3:** Raman spectra of one measurement per sample of each set. The plotted region only shows the combined contributions CdS-1 and CdS-2 - still all spectra are normalized to the respective CIGS-1 contribution. a) shows the reference set and b) the RbF-treated set.

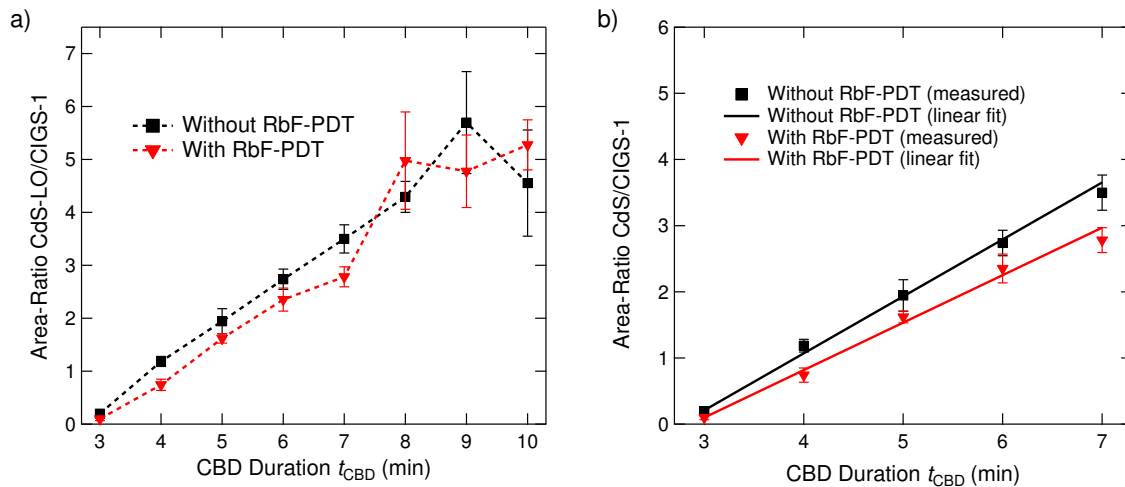


**Figure 6.4:** a) Area ratio of the combined CdS-contributions and the CIGS-1 contribution for both sample sets in dependence of the CBD duration. Each point marks the corresponding middle value of five measurements, the error bars are given by the standard deviation. Dashed lines are guidance for the eye only. b) Region of steady increase of the CdS/CIGSe-area ratios contribution for both sample sets. The solid lines show the result of a linear fit of the correspondingly colored measurement points.

Starting from 3 min, the CdS-signals steadily increase with  $t_{\text{CBD}}$  for both sets. After  $t_{\text{CBD}} > 7$  min, the increase of the CdS-signals is not longer steady but becomes discontinuous. This can also be seen from the area ratio plot in Figure 6.4 a, which includes averaged data from all five measurements per sample: Starting from 8 min the error bars at each point increase and the evolution becomes unsteady. The phase of steady increase can be attributed to the ion-by-ion growth of the CdS layer, while the unsteady behavior is due to the formation of CdS clusters on the surface of the CdS film (see discussion of the CdS-growth in Section 3.1.2 and Reference [185]). Since the measurement spot of the Raman setup used is in the range of the size of these clusters, these can influence the results strongly. The spot is about  $1.25 \mu\text{m}$  in diameter and the clusters range from 100 nm to a few  $\mu\text{m}$  in diameter.

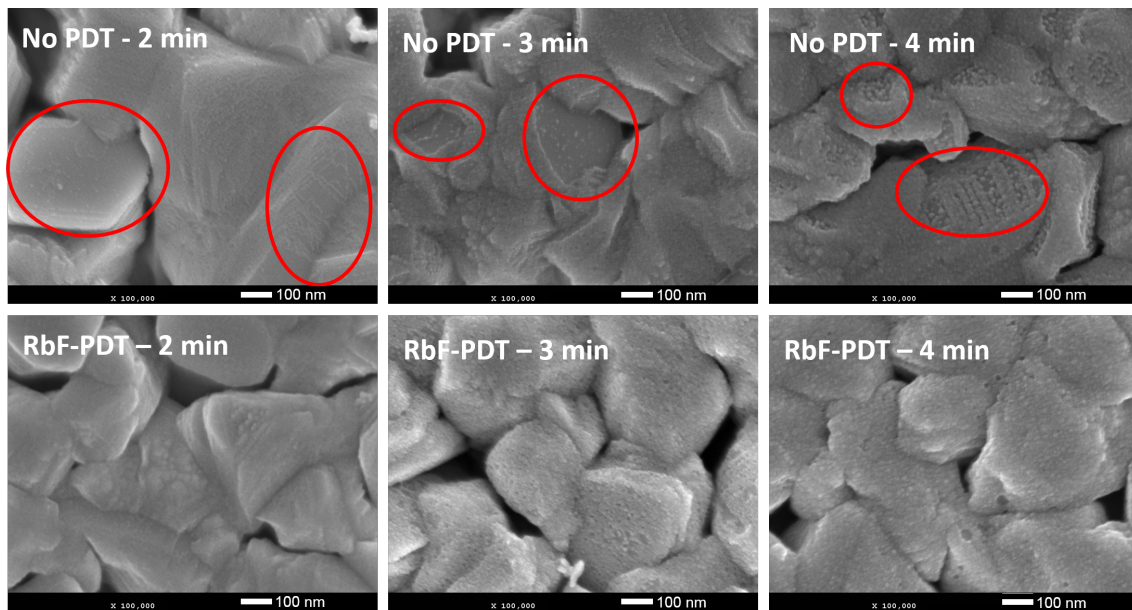


**Figure 6.5:** Top view SEM images of a reference sample (top row) and an RbF treated sample (bottom row) after 2 min, 3 min, and 4 min CBD duration.

To investigate the impact of the RbF-PDT on the ion-by-ion growth phase of the CdS, the steady growth region is separately interpolated using a linear function as shown in Figure 6.4 b. It can be seen from these fits that the growth rate  $r$  of the CdS is slightly, but distinctly lower on surfaces treated with RbF ( $r = (0.72 \pm 0.03) \text{ min}^{-1}$ ) than on untreated surfaces ( $r = (0.86 \pm 0.04) \text{ min}^{-1}$ ). To investigate the nature of these different growth rates, the morphology of the growth at different stages is examined using SEM. In Figure 6.5 top view images of the samples after 2, 3, and 4 minutes of the growth are shown exemplarily. Note that these SEM images were measured on a third sample set, which samples, however, were treated nominally identically as those from Set 1. After two minutes there are only traces of a thin film growing on top of the CIGSe visible on both samples. While the RbF-treated sample is already completely covered by a thin film after three minutes, on the untreated sample only some CIGSe grains seem to be fully covered by a thin layer and others appear to be still completely blank at this point in time (the latter grains are marked with red circles in Figure 6.5). Even after four minutes some grains are still not completely covered by CdS. The fact that there is already a ‘film’ deposited on both samples after 2 min, but no to little CdS detectable via Raman scattering is not contradictory. It was already shown in literature [186, 249] that in the very early stages of the CdS growth there is an ‘induction/coalescence’ mechanism taking place consisting of the adsorption of only  $\text{Cd}(\text{OH})_2$  onto the substrate. Choubrac et al. [186] also reported the beginning of the actual CdS-growth (on  $\text{Cu}(\text{Zn},\text{Sn})\text{Se}_2$ -films) detectable by Raman to start after about 3 min.

### Study of the device parameters (Set 2)

Figure 6.6 shows the combined  $j$ - $V$ -parameters of two representative cells of each sample from Set 2. The solid lines are drawn to provide guidance for the eye only. As one can clearly see, the RbF-PDT results in much higher values for all four parameters after 3 min, meaning it provides a higher junction quality after very short CBD duration, i.e. with a rather thin CdS layer. With longer CBD duration  $V_{\text{OC}}$  of both sample sets increases and stabilizes after 7 to 9 min. This increase is slower for the reference samples compared to the RbF-treated samples. While the latter samples show an overall higher  $FF$ , the reference devices show a stronger increase and reach similar  $FF$  as the RbF-treated samples after 9 min. The  $j_{\text{SC}}$  shows – after a strong increase from 3 to 4.5 min for the reference samples – a slightly decreasing trend for both samples. However, the efficiency mostly follows the trend of the  $V_{\text{OC}}$  and  $FF$ .

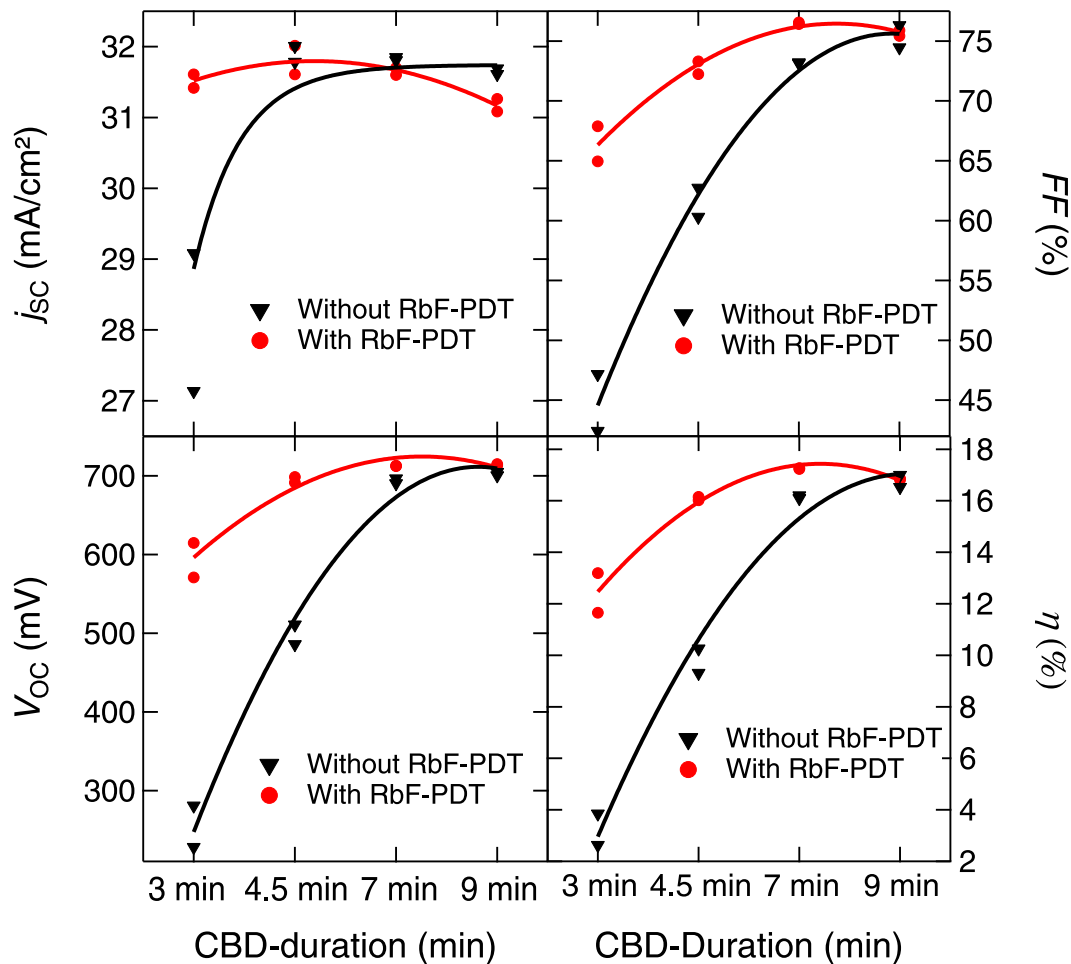


**Figure 6.6:** Electrical parameters of two cells of each sample from Set 2. The solid lines are used as guide to the eye only.

The samples with an RbF-PDT show a higher initial efficiency than the reference samples after short CBDs but due to a less strong gain with  $t_{CBD}$  reach about the same  $\eta$  after longer CBDs. Furthermore, the trend seems to be decreasing for RbF-treated samples but not for the reference samples, indicating that even longer CdS-depositions might be beneficial for the efficiency of the reference samples.

To be able to analyze the behavior of  $j_{sc}$  in more detail, plots of the  $IQE$  are shown in Figure 6.7. In both cases (No PDT and RbF-PDT) one can clearly see how the increased absorption in the CdS layer with longer CBD duration leads to lower quantum efficiencies in the wavelength region between 400 nm and 500 nm. However, it is hard to judge if these  $IQE$ -losses are evolving slower in case of the RbF treated than the untreated samples as it is suggested by the Raman-study.

Furthermore, it can be seen by the comparison of the red-response of the  $IQE$  of the RbF-treated and the untreated samples after 3 min CBD-duration (cf. Figure 6.7 c) that the effective collection length seems to be larger in case of the RbF-PDT. After longer durations of the CBD, it is not clear from the plots of the  $IQE$  whether or not this trend continues. In order to quantify this impression plots of  $-\ln(1 - IQE)$  versus  $\alpha(\lambda)$  are shown in Figures 6.8 a and b, which were derived according to the procedure for the extraction of the collection length that is described in Section 3.2. The linear region of low absorption was fitted in order to obtain  $L_{eff}$  via Equation 3.12 and the results of these fits are shown in Figure 6.8 c. The results of the fit confirm the impression by the  $IQE$  showing a higher  $L_{eff}$  for the RbF-treated samples for all  $t_{CBD}$ . Furthermore, in both cases, the collection length is improving with  $t_{CBD}$  and saturating after long  $t_{CBD}$ .

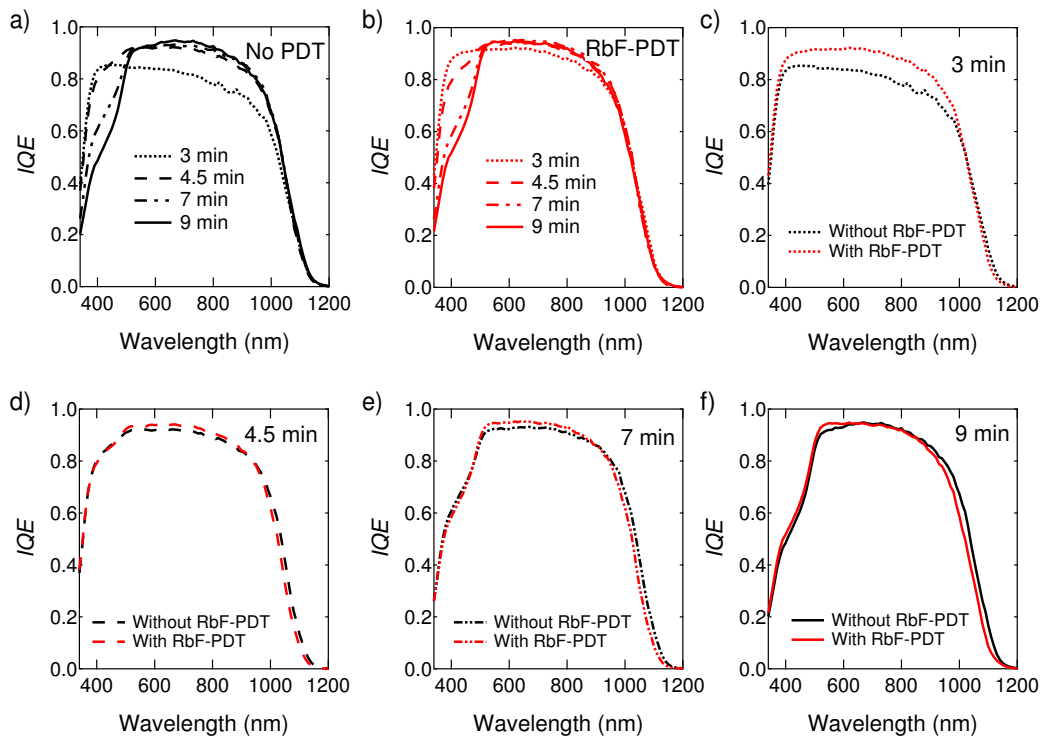


**Figure 6.7:** Internal quantum efficiencies of the best cell of each sample.  $IQE$  was obtained from measuring Reflectance and  $EQE$  on the same cell. The figure shows the results for a) the untreated reference sample, b) the RbF treated sample, as well as combined views of all three curves of the devices with CBD-duration of c) 3 min, d) 4.5 min, e) 7 min, and f) 9 min.

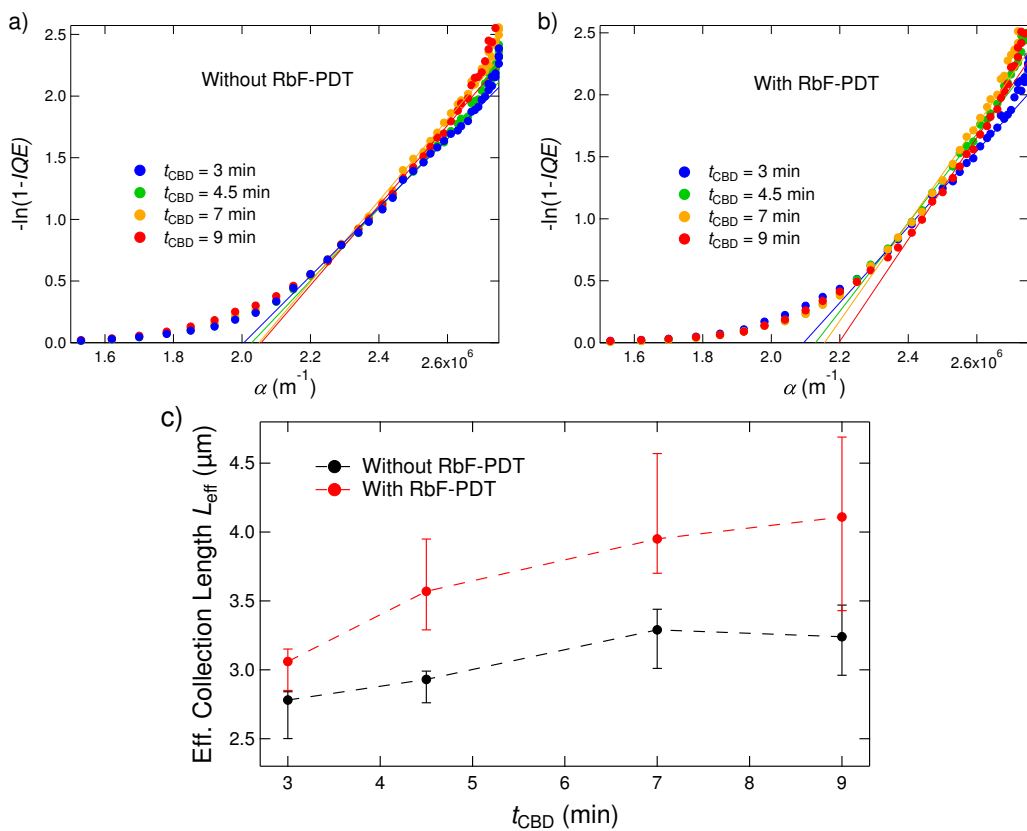


**Figure 6.8:** Extraction of the effective collection length  $L_{\text{eff}}$  from plots of  $-\ln(1 - IQE)$  versus the absorption coefficient  $\alpha$  for the devices of Set 2 without RbF-PDT (a) and with RbF-PDT (b). The values for  $\alpha$  were obtained from fitting the UV-Vis-data of measurements on a CISE-sample. In order to obtain  $L_{\text{eff}}$  from the plots, the linear region was fitted via Equation 3.12. The results of these fits are shown in c). The respective error bars were obtained from varying the range of the linear fits.

## Part II: Combined Discussion

Combining the results of the Raman and the SEM study, there are two effects of the PDT on the subsequent growth of the CdS. The Raman study revealed that the growth rate is decreased by the PDT and the SEM study showed that it leads to a better coverage of the CIGSe by CdS.

It was already shown before that an alkali-PDT can lead to a better coverage as well as a *faster* growth rate of the CdS [156]. However, since the authors of this study did not specify the details of the PDT used, correlation with the present results is impossible. In Publication [3] an accelerated growth of the CdS was reported for a KF-PDT on the same absorber layers as they were used in this chapter, compared to the respective samples without PDT and with RbF-PDT. Accordingly, the interplay of the CdS-growth rate with the surface of the CIGSe seems to depend on the alkali metal used for the PDT.

It nevertheless seems to be a consistent effect of the alkali-PDTs that the coverage of the CdS is enhanced [3, 156], independent of the alkali metal used. The fact that CIGSe without heavy alkali elements incorporated induces an inhomogeneous growth of CBD-buffer layers was observed by other groups as well [250]. However, these studies did not include an investigation of the growth on alkali-conditioned surfaces. In case of RbF-treated surfaces it has to be considered that the CdS is not growing directly on the CIGSe anymore, but on the newly formed RIS-layer, which could therefore alter the growth process. A mechanism for the better coverage of the CdS on Rb-treated CIGSe will be proposed in Chapter 7 taking into account results from Reference [250].

Inclusion of the results of the device study indicates that the CdS-coverage is the deciding factor for establishing a high-quality *p-n*-junction. Despite the lower CdS-growth rate, the RbF-PDT leads to higher  $V_{OC}$ ,  $FF$ , and  $j_{SC}$  compared to the reference at early growth-stages. This interpretation is supported by the fact that a similar trend of the PV-parameters was shown for a KF-PDT in Publication [3] despite the higher CdS-growth rate on these KF-treated surfaces compared to the reference.

Furthermore, the RbF-PDT leads to a higher effective collection length independently of  $t_{CBD}$ , while in both cases (with and without RbF)  $L_{eff}$  further increases and saturates with longer  $t_{CBD}$ . The latter can be explained by the formation of the heterojunction, and the fact that  $L_{eff}$  is generally higher for RbF-treated samples is in good agreement with the result that higher  $\tau_{exp}$  have been shown on similar samples in Chapter 4 and again shows that the recombination rate is lower in Rb-conditioned samples compared to Rb-free samples.

## Summary and Conclusions of Chapter 6

In this chapter, the impact of the RbF-PDT on the growth of the subsequently deposited buffer layer was analyzed. It was shown that independent of the PDT-induced consumption of the ODC, the CBD-CdS further reduces the ODC in both cases with and without an RbF-PDT. This novel result may be a hint for the interaction of  $V_{Cu}$  and Cd during the CBD and will be discussed in a broader context in the next chapter.

Furthermore, it was shown that the RbF-PDT leads to an improved coverage of the absorber layer by the CBD-CdS layer. While some grains of the CIGSe are poorly covered by CdS in early growth stages, the CdS-growth was observed to be homogeneous on RbF-treated CIGSe surfaces. It is proposed that this is due to the fact that the CIGSe is no longer acting as the substrate for the CdS, but the newly formed RIS-layer is.

Additionally, a combination of the results of the Raman and SEM study with the results obtained from the finished devices shows that the quality of the *p-n*-junction at early growth stages of the CdS is mostly determined by the lateral homogeneity of the CdS layer. Although the growth rate on the RbF treated absorber layers is lower than on the untreated ones, RbF-treated samples show much better  $V_{OC}$  and  $FF$  after short CBD-duration. The different growth rates then determine the optimal CBD duration for each sample set.

## 7 Proposed Model of the Structural Effects of Rb in the Frame of Literature

Before a complete device model of the optoelectronic effects of the Rb-conditioning in CIGSe-based solar cells will be derived in Chapter 8, in the following, the experimental results, which were presented in the previous chapters, will be summarized and interpreted alongside with data from the literature.

In Chapter 4, it was shown that the RbF-PDT leads to several effects on the bulk and surface properties of the CIGSe absorber layer, some of which show a strong dependence on the overall  $CGI$  of the CIGSe. While the PDT has a beneficial effect on the carrier lifetime and Urbach-energy regardless of the  $CGI$ , its effect on the carrier concentration is only beneficial on samples with  $CGI \geq 0.8$  – leading to improved  $V_{OC}$  on these samples – but is detrimental on samples with lower  $CGI$ .

The experiments presented in Section 5.2 showed that the Rb-conditioning via a direct deposition of RIS on the CIGSe leads to similar effects on the carrier lifetime and the Urbach-energy, which both are also steadily improved with  $t_{RIS}$ . However, the direct deposition of the RIS did not lead to a steadily increasing  $n_{CV}$  but to a rather constant gain of the carrier concentration compared to an Rb-free reference – independent of  $t_{RIS}$ .

It is interesting to note that in all three experiment series described in Sections 4.1, 4.2, and 5.2 a correlation of  $n_{CV}$  with the distribution of Na in the absorber layer was found. Therefore it is proposed that the Rb-Na exchange mechanism that was discussed in the respective chapters is the driving force for this behavior of  $n_{CV}$ . A model for this exchange mechanism will be proposed combining the results of this thesis with experimentally and theoretically derived data from literature in Section 7.1.

The impact of the Rb-conditioning on  $FF$  was shown to be even more sensitive to changes of the  $CGI$ . Only on samples with  $CGI \approx 0.95$ , the RbF-PDT leads to an increased  $FF$ , while it deteriorates  $FF$  on samples with lower  $CGI$ . This is especially surprising, since according to Equation 2.47 it is expected that  $FF$  follows the trend of the  $V_{OC}$ , i.e. it was expected that the RbF-PDT has a beneficial influence on  $FF$  for all  $CGI \gtrsim 0.80$ . This means that the RbF-PDT induces an additional trend of decreasing  $FF$  with lower  $CGI$  overlying the influence of  $V_{OC}$ .

While no direct connection between the RIS-layer and  $FF$  could be proven, it was shown that its trend with  $CGI$  correlates with the effect of Rb on the structure and composition at the surface of the CIGSe. Generally, the  $\alpha$ - and  $\beta$ -phase (or ODC) of the CIGSe can co-exist over a wide range of the Cu-content [76]. Raman spectra validated this for all samples used in that experiment series and furthermore showed that the fraction of the ODC is reduced with lower Cu-content. Additionally, it was shown that the RbF-PDT leads to a separate reduction of the share of the ODC close to the surface of the CIGSe for all  $CGI$  and that in samples with a very low  $CGI$ , more Rb is incorporated into the surface region of the absorber layer. In combination with the XPS-results presented in Sections 4.1 and 5.2, which showed strong indications for the growth of a RIS-layer on top of the CIGSe during the RbF-PDT, this increased accumulation of Rb in the surface region was attributed to the growth of a thicker RIS-layer with lower  $CGI$ .

The fact that the growth of this layer correlates with the Rb-induced reduction of the ODC, indicates that the ODC is part of the formation mechanism of the RIS-layer. Furthermore, the growth of this thicker RIS-layer might be a possible explanation for the second trend lowering  $FF$  with decreasing  $CGI$ .

The latter hypothesis is strongly supported by the results presented in Section 5.2. There it was shown that while the RbF-PDT does not lead to a reduction of  $FF$  on samples with  $CGI = 0.95$ ,  $FF$  does decrease after an intentional, and  $CGI$ -independent deposition of RIS on such absorber layers. Furthermore, the loss in  $FF$  is directly correlated with the thickness of the deposited RIS-layer. This mechanism will be discussed with regard to the literature in Section 7.1.2.

Additionally, to the effects of the Rb-conditioning on the properties of the absorber layer itself, it was shown in Chapter 6 how it also affects the growth of the subsequently deposited CdS buffer layer. Thereby it was shown that the CdS grows more homogeneously on RbF-treated CIGSe than on an untreated reference sample. This improved coverage of the CdS leads to strongly improved PV-parameters measured on devices with rather short CBDs. It was assumed that the improved coverage on samples with RbF-PDT originates from the fact that the newly formed RIS-layer and not the polycrystalline CIGSe acts as the substrate for the CdS-growth. As it was described above, the existence of this layer was clearly indicated by XPS on several samples, but was neither detected by GI-XRD nor by Raman scattering and hence is assumed to be amorphous. Such an amorphous layer could function as a more homogeneous substrate than the polycrystalline CIGSe. This change of the substrate could also play a role for the origin of the change of the growth rate of the CdS, which was shown to be slower on RbF-treated samples compared to Rb-free references. Furthermore, it was shown that not only the RbF-PDT itself but also the deposition of CdS leads to a reduction of the ODC at the surface of the absorber layer. Both mechanisms will be modeled in Section 7.2.3 taking into account literature data.

## 7.1 Interaction of Rb with Na and Point Defects in the CIGSe

### 7.1.1 The Case of $CGI = 0.90$

The increased carrier concentration, which was measured on samples after long RbF-PDTs in Section 4.1, suggests that a combined incorporation of Na and Rb enhances the existing or gives rise to an additional doping mechanism compared to the incorporation of Na alone. The fact that the steady increase of the amount of Rb in the samples after a direct RIS-deposition did not show a correlation with  $n_{CV}$  of the corresponding devices (cf. Section 5.2), indicates that the Rb-induced doping mechanism works via an interaction with Na.

At first sight, the results of the time-series (Section 4.1) seem to contradict each other: although more Rb is steadily decreasing the measurable amount of Na throughout the bulk of the absorber layer,  $n_{CV}$  constantly recovers after an initial decrease and – after long treatments – reaches higher values than the Rb-free reference. However, when considering recent publications regarding these mechanisms, the results become consistent (cf. schematic view in Figure 7.1). In agreement with the TEM-study shown in Section 4.1, it was proven by Schöppe et al. using nano-XRF measurements and Vilalta-Clemente et al. using APT that in their sample sets Rb was also clearly present at GBs while concentrations in the GI were below the detection limit of the used methods [165, 167].

Furthermore, Vilalta-Clemente et al. found that the presence of Na at the GBs is less likely in samples with RbF, while the concentration of Na in the GI is increased [167]. Based on these findings, the Na-depth profiles as well as their impact on  $n_{CV}$  can be interpreted as follows: Initially, Rb replaces Na at the GBs, which is why Na is partly driven to the surface of the absorber layer and then later washed away by the rinsing step with  $NH_3(aq)$  (see Figures 7.1 x.3 and x.4). After longer PDTs, a part of the Na atoms that was pushed away from the GBs accumulates in the GI, occupies Cu-sites in the CIGSe lattice [162] and therefore forms  $Na_{Cu}$  antisites (see Figures 7.1 x.3).

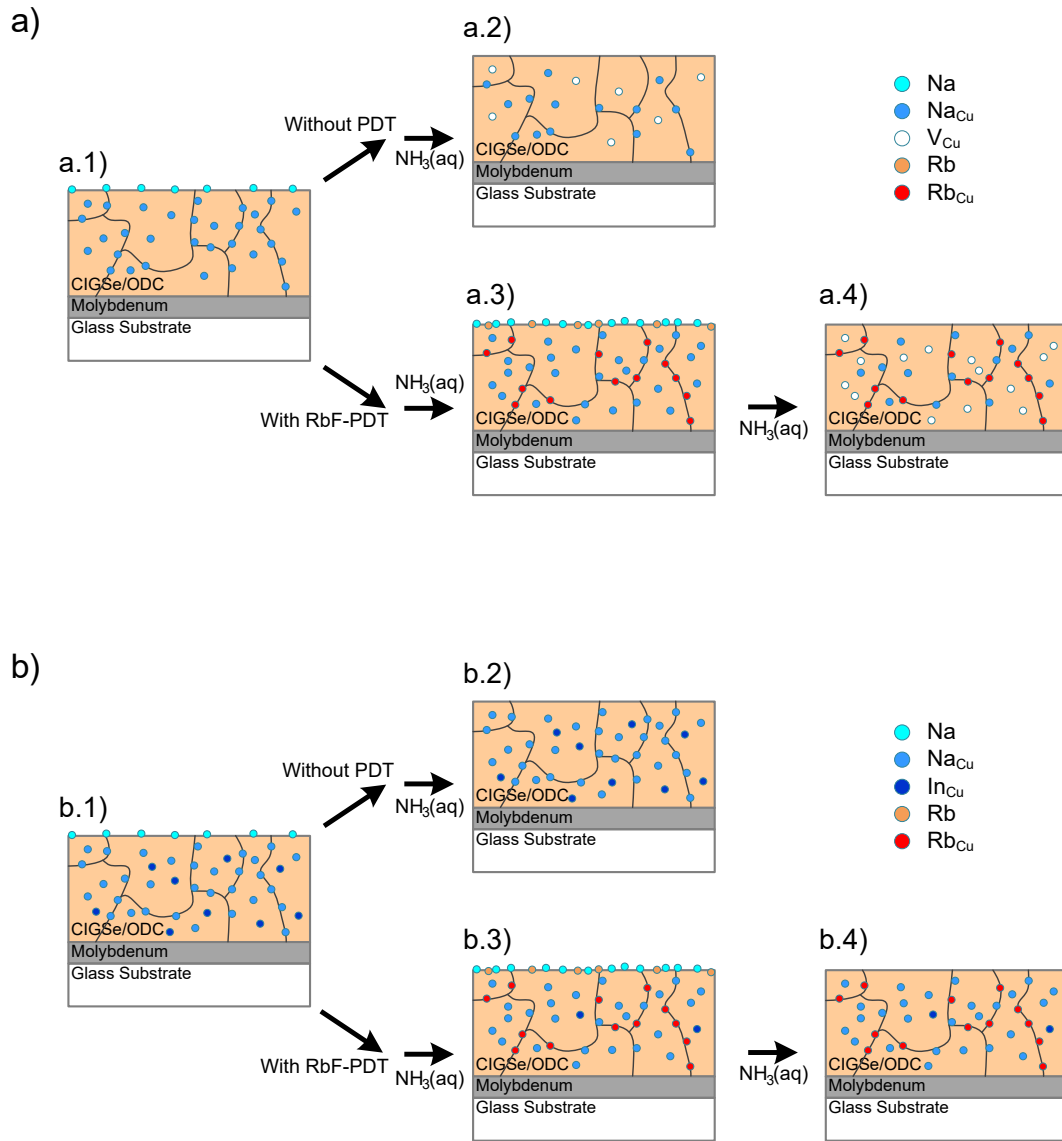


**Figure 7.1:** Schematic representation of the proposed mechanism via which the RbF-PDT might lead to a decreased  $\Delta V_{OC}^{CV}$ . a) shows the mechanism within the model of Yuan et al. [97], while b) shows it within the model proposed by Wei et al. [96].

x.1) ( $x = a, b$ ) show the initial state after finishing the growth. Please note that only those defects are displayed that are necessary for the explanation of the model, while other defects might still be present (e.g. there will be  $In_{Cu}$  in a.1 and  $V_{Cu}$  in b.1 as well). x.2) show the final situation in case without an RbF-PDT (as shown in Figure 2.7). x.3) show the impact of the RbF-PDT: Rb is partly staying at the surface, and partly diffusing along the GBs of the CIGSe replacing Na there. The Na is partly driven to the surface and partly into the GI occupying either more Cu-sites (a) or  $In_{Cu}$ -antisites (b). x.4) During the WCT alkali metal atoms/compounds are removed from the surface and in case of a) also driven out of the GI and GBs increasing the number of  $V_{Cu}$ . In both cases the overall Na-content in the layer is lower in x.4 compared to x.2, while the amount of  $V_{Cu}$  (a) and  $In_{Cu} \rightarrow Na_{Cu}$  (b) is higher than in x.2 leading to the improved  $n_{CV}$ .

Following the Na-model by Yuan et al. [97] (cf. Section 2.3), the solubility of Na in CIGSe decreases during the following cool-down of the samples and therefore the stability of the  $\text{Na}_{\text{Cu}}$  antisite is reduced. During the subsequent washing step in  $\text{NH}_3(\text{aq})$ , which further reduces the chemical stability of Na in the CIGSe grains [97], Na partly diffuses out of the GI leading to an increased number of  $\text{V}_{\text{Cu}}$  in the grains and therefore a higher carrier concentration (see Figure 7.1 a.4).

Following the Na-model by Wei et al. [96] on the other hand, the increased concentration of Na in the GI alone is leading to the improved  $n_{\text{CV}}$  due to the additional formation of  $\text{Na}_{\text{Cu}}$  from  $\text{In}_{\text{Cu}}$ .

In summary, this model proposes that by replacing Na at the GBs, the presence of Rb leads to a migration of Na into the GI and towards the surface as well as to an increased amount of  $\text{Na}_{\text{Cu}}$  and  $\text{V}_{\text{Cu}}$  (within the model of Yuan et al.) or an increased amount of  $\text{In}_{\text{Cu}} \rightarrow \text{Na}_{\text{Cu}}$  (within the model of Wei et al.) in the GI. This interpretation is in good agreement with recently published theoretical predictions, in which it was shown that “the difference of the formation energy of Rb point defects in the bulk and at GBs is larger than the corresponding energy difference in case of Na point defects” [134], meaning that the overall energy of the system is decreased when Rb replaces Na at the GB and pushes it into the GI.

### 7.1.2 Generalization to a CGI-Dependent Model

#### Variation of the Cu-Content

The common correlation of  $\chi_{\text{Na}}$ ,  $n_{\text{CV}}$ , and  $\Delta V_{\text{OC}}$  with the CGI of the absorber layer (cf. Figure 4.18) indicates that the Rb-Na exchange mechanism is strongly dependent on CGI as well. Furthermore, Na, Rb, and the number of available  $\text{V}_{\text{Cu}}$ , which is determined by the ratio of ODC and  $\alpha$ -phase CIGSe, were shown to be part of the surface modification due to the RbF-PDT. In the following, the interaction of Na, Rb and the CGI of the absorber layer will be discussed on the basis of a schematic representation of the proposed mechanisms shown in Figure 7.2.

Recently published Monte-Carlo simulations show that for heavy alkali metals (like Rb) the diffusion via  $\text{V}_{\text{Cu}}$  has much lower energy barriers than diffusion via interstitial positions in the lattice, while in case of Na these barriers are comparable [161, 162]. Therefore it seems likely that Rb occupies preferably Cu-sites in Cu-deficient material, e.g. in the ODC [162], but is rather unlikely to replace Cu in  $\alpha$ -phase CIGSe. In samples with a high share of the ODC, i.e. a high number of available  $\text{V}_{\text{Cu}}$ , part of the Rb may hence not occupy Na-sites at the GBs but directly diffuse into the Cu-poor material. Since the RbF is deposited on top of the CIGSe, this preferably happens at the surface of the CIGSe layer (cf. Figures 4.14 and 4.16 as well as Figure 7.2 a.3). The in-diffusion of Rb into the lattice at the surface of the CIGSe then induces the formation of the RIS-layer.

A similar behavior of the Rb-diffusion, as it was described in Section 4.2, was observed in a recently published study by Wuerz et al. [170]. The authors analyzed the in-diffusion of Rb into CIGSe with rather low CGI ( $0.75 < \text{CGI} < 0.86$ ) and found that part of the Rb is diffusing along the GBs, while a part is in-diffusing into the lattice at the surface of the layer. Additionally, most of the Na, which is still driven away from the GBs by the Rb – as indicated by the results in Figure 4.18 – would also diffuse into the Cu-poor regions of the lattice, e.g. into the newly forming Cu-depleted layer at the surface of the absorber layer. This can indeed be seen by the Na-accumulations in the surface region of samples with low CGI in Figure 4.14.

As a consequence, in samples with low CGI (high amount of  $\text{V}_{\text{Cu}}$ ), the enrichment of Na in the GI of the bulk CIGSe as well as the Rb-induced GB-passivation described above would occur on a much lower potency (Figure 7.2 a.4). This would be a possible reason why the PDT does not increase the  $V_{\text{OC}}$  on samples with  $\text{CGI} < 0.8$  but only on samples with higher CGI (Figure 7.2 b.4).

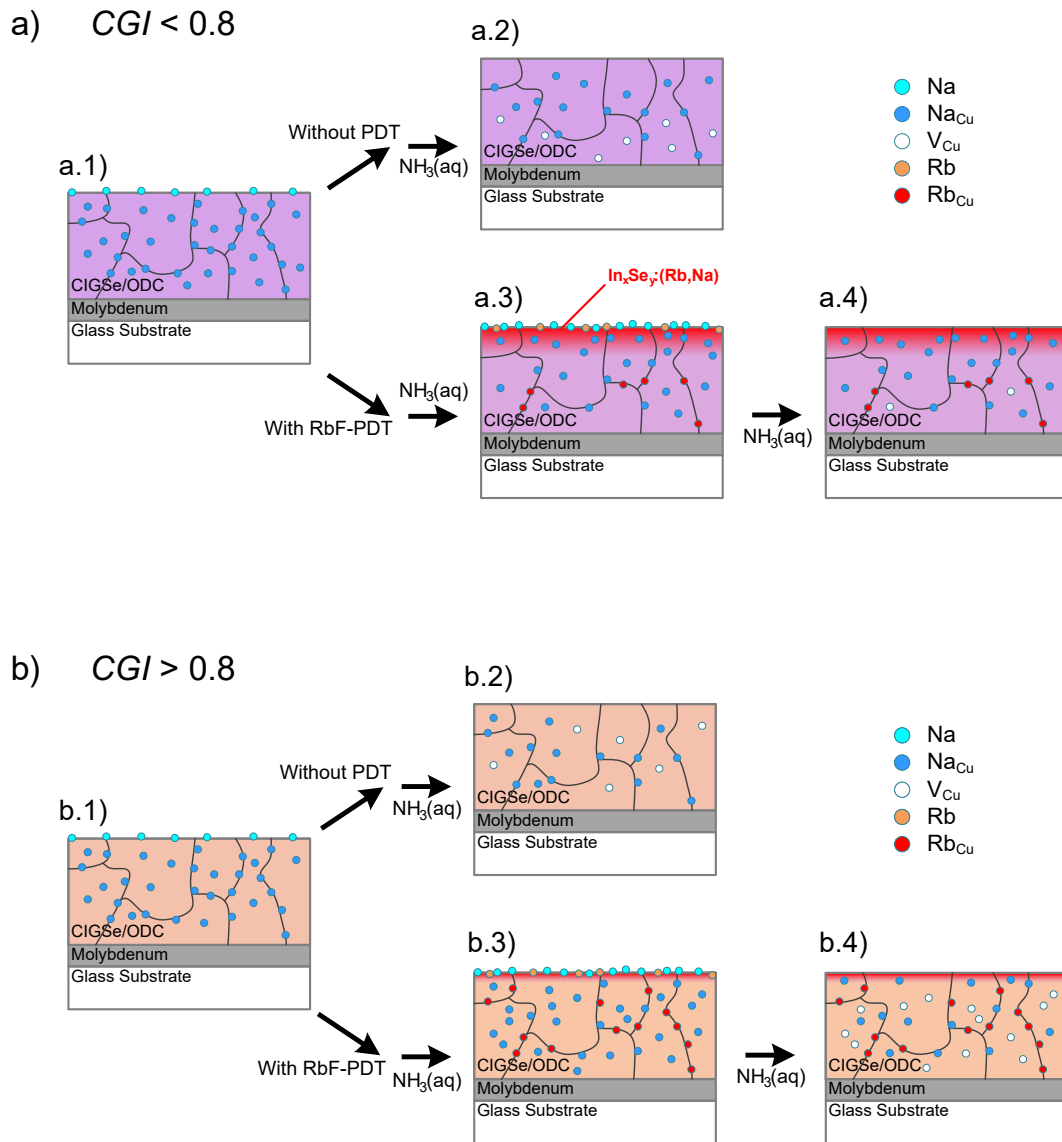


**Figure 7.2:** Schematic representation of the proposed interaction of the RbF-PDT and the  $CGI$  of the absorber layer. a) shows the proposed mechanism for samples with  $CGI \lesssim 0.8$ , while b) shows it for  $CGI \gtrsim 0.8$ . Both representations are made within the model of Yuan et al. [97]. However, the model can be expanded to be in agreement with the Wei-model [96] as well. In the latter case, the interaction of Na and  $V_{Cu}$  would be complemented by the interaction of Na and  $In_{Cu}$  in the very same manner as described in Section 7.1.1.

x.1) ( $x = a, b$ ) show the initial state after finishing the growth. The ratio of  $\alpha$ -phase CIGSe and ODC naturally depends on the  $CGI$  of the layer. x.2) show the final situation in case without an RbF-PDT. x.3) show the impact of the RbF-PDT: in case of a high share of the ODC (a) Rb is partly occupying  $V_{Cu}$  near the surface leading to the growth of a thick RIS-layer and partly replacing Na from the GBs deeper in the bulk. Most of the Na diffuses into the surface layer and leads to an overall low Na-concentration in the GI of the bulk CIGSe. In case of a low share of the ODC (b) only little Rb is staying near the surface forming a thin RIS-layer and most of it is replacing Na at the GBs. Only a small portion of the Na is diffusing into the surface layer, while most of it occupies Cu-sites in the bulk of the CIGSe. x.4) During the WCT alkali atoms/compounds are removed from the surface and part of the Na is also driven out of the GI and GBs creating  $V_{Cu}$ . Due to the fact that in samples with low  $CGI$  only little amounts of Na were accumulating in the GI of the bulk CIGSe the absolute number of  $V_{Cu}$  is lower in a.4 than in a.1, while it is higher in b.4 than in b.1 explaining the different trends in  $n_{CV}$ . In both cases, Rb is still present at the GBs of the bulk CIGSe.

As mentioned in Section 4.2, this proposed model for the growth of the RIS-layer stands in contrast to results published by Lepetit et al. regarding KF-PDTs [128]. Lepetit et al. concluded that in samples grown close to stoichiometry, which contain a limited amount of ODC, i.e. available  $V_{Cu}$ , the in-diffusion of K-atoms leads to the formation of detrimental  $Cu_{2-x}Se$  and therefore strongly reduced performance of the devices [128].

The reason why the RbF-PDT does not lead to such an effect on samples grown close to stoichiometry can be found in the literature: While the formation energy of K- and Rb-related point defects at GBs are comparable, K is predicted to be more likely to diffuse into the GI than Rb [134, 161]. In case of samples grown close to stoichiometry, this means that K can replace Cu in the lattice of the CIGSe. Due to the fact that the amount of available  $V_{Cu}$  is very limited, Cu diffuses to the surface and forms  $Cu_{2-x}Se$ . Rb, on the other hand, is more prone to remain at the GBs by displacing Na, most likely pushing it into the grains improving the  $V_{OC}$  as described above. Residual Rb, however, stays at the surface of the CIGSe and is rinsed off by  $NH_3(aq)$  and does therefore only lead to the formation of a very thin or even no RIS-layer at the surface (Figures 7.2b.3 and b.4). Formation of  $Cu_{2-x}Se$  does not occur.

This proposed mechanism is in good agreement with the fact that samples with  $CGI = 0.95$  do not show any accumulation of the alkali metals at the surface (cf. Figures 4.14 and 4.16). With the absence of a detectable Rb-accumulation at the surface of this sample, i.e. assumingly a very thin RIS-layer,  $FF$  increases with increasing  $V_{OC}$  just as one would expect following equation 2.47.

### Depositing RIS on Absorber Layers with $CGI = 0.95$

This model, however, poses the question for the reason for the independence of  $n_{CV}$  from  $t_{RIS}$  (versus the dependence of  $n_{CV}$  on  $t_{PDT}$ ) that was discussed in Section 5.2. In these samples, the amount of Rb in the absorber layer steadily increases with  $t_{RIS}$ , while  $n_{CV}$  and the amount of Na are slightly enhanced by a very short RIS-deposition but show hardly any further trend with  $t_{RIS}$ . The simultaneous enrichment of Rb and Na was explained by the larger heat transfer to the samples during the RIS-deposition (and the subsequent cool-down) compared to the PDT, which leads to a faster diffusion of Rb along the GBs [170]. For the same reason, there is more Na diffusing from the glass into the bulk during and after the RIS-deposition than in case of the RbF-PDT.

However, in order to explain the missing trend of  $n_{CV}$  with  $t_{RIS}$ , the interaction of Rb and Na with the point defects has to be modeled combining data from this thesis and the literature (cf. Figure 7.3).

In the aforementioned study of the Rb-diffusion in Cu-poor CIGSe, Wuerz et al. found – based on TOF-SIMS measurements – that the amount of Rb in the GI as well as at the GBs of samples with  $CGI = 0.75$  and  $CGI = 0.86$  rises after an RbF-PDT with increasing substrate temperature [170]. On the other hand, it was shown in Section 4.2 that in samples grown with  $CGI = 0.95$  hardly any Rb is incorporated into the lattice of the CIGSe, presumably due to the limited amount of available  $V_{Cu}$ .

This leads to two possible interpretations of the data that were presented in Section 5.2. On the one hand (Mechanism 1 in Figures 5.8b and c) the comparably high temperature during the RIS-deposition and the subsequent cool-down is improving the diffusivity of the Rb even in the GI of absorber layers grown close to stoichiometry in a way that Rb could be replacing Cu-atoms in the lattice. As it was shown experimentally by Wuerz et al. this would hinder the in-diffusion of Na into the GI [170], and therefore suppress the formation of additional  $V_{Cu}$  in the GI within the model of Yuan et al. [97] (Figure 7.3 b), or the additional transformation of  $In_{Cu}$  to  $Na_{Cu}$  within the model of Wei et al. [96] (Figure 7.3 c), and in both cases limit  $n_{CV}$ . The rather high amount of Na measured with GD-OES would be explainable by additional Na at the GBs of the CIGSe due to the increased diffusion of Na from the glass substrate.

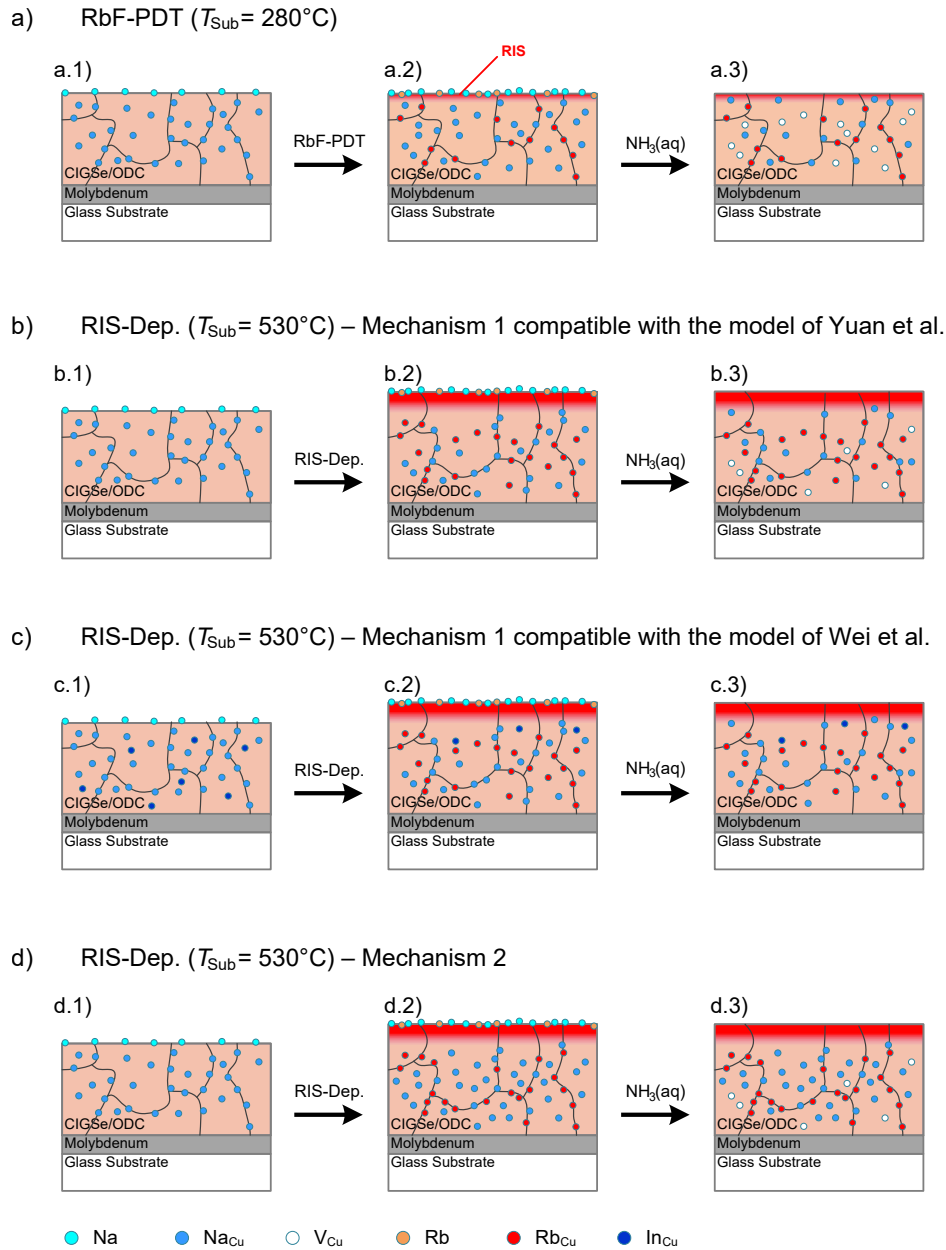


**Figure 7.3:** Comparison of the proposed mechanisms for the  $V_{\text{OC}}$ -gain due to the RbF-PDT (a, same as proposed in Figure 7.2) and the RIS-deposition (b, c, and d) on CIGSe absorber layers with  $\text{CGI} = 0.95$  starting from the bare CIGSe layer (x.1).

Mechanism 1: b.2) due to the higher  $T_{\text{Sub}}$  compared to the PDT, the diffusivity of Rb in the GI of the CIGSe is increased and small amounts of Rb accumulate in the GI additionally to the Rb at the GBs. Simultaneously, additional Na is diffusing from the substrate into the CIGSe (also due to the higher  $T_{\text{Sub}}$ ). However, the presence of Rb in the GI hinders Na to be pushed from the GBs into the GI so that most of the additional Na stays at the GBs. Subsequently (b.3), less additional  $V_{\text{Cu}}$  are formed during the following rinsing step than in case of the PDT (but still some additional  $V_{\text{Cu}}$  compared to the Rb-free case) leading to an  $n_{\text{CV}}$  in between that of the untreated reference and the RbF-treated sample. This version of Mechanism 1 is compatible with the model proposed by Yuan et al. [97].

The same mechanism within the frame of the model of Wei et al. [96] reads as follows: c.2) the presence of Rb in the GI of the CIGSe hinders Na to fully occupy the present  $\text{In}_{\text{Cu}}$  antisites. Therefore the residual  $\text{In}_{\text{Cu}}$ -donors limit the effectiveness of the 'Rb-doping' compared to the case of the PDT (c.3).

Mechanism 2: d.2) Despite the higher  $T_{\text{Sub}}$ , Rb-diffusion into the GI is still hindered but Rb-diffusion along the GBs is increased. Therefore more Rb accumulates there compared to the PDT-case. At the same time, more Na diffuses into the CIGSe due to the higher  $T_{\text{Sub}}$ . The Na preferably accumulates within the GI, since the GBs are 'occupied' by Rb. d.3) During the WCT, most of the Na stays in the GI, because the out-diffusion along the GBs is hindered due to the high concentration of Rb there.

On the other hand (Mechanism 2 in Figure 5.8 d), the observed increase of the Rb-amount with  $t_{\text{RIS}}$  may be linked to a faster diffusion of Rb along the GBs due to the high temperature. Wuerz et al. [170] classify alkali diffusion in the bulk of CIGSe as type C diffusion according to Harrison [251], which means that the Rb-diffusion occurs directly from the surface into the GI of Cu-poor CIGSe and along the GBs deeper into the layer. Diffusion from the GBs into neighboring grains, however, hardly occurs judging from the experiments of Wuerz et al. [170, 251]. Therefore this 'secondary' Rb diffusion into the interior of adjacent grains by leaking from the GBs can be neglected and the increase of the Rb-intensity measured by GD-OES is solely due to the fact that more Rb accumulated at the GBs than in case of the PDT (Figure 7.3 d).

However, at the same time, there is a steady in-diffusion of Na from the glass substrate into the GI as well as along the GBs due to the high temperature. Following the argumentation presented for the Rb-Na exchange mechanism in Section 7.1.1, Rb pushes the additional Na from the GBs into the GI further increasing the number of  $\text{Na}_{\text{Cu}}$ . Due to the fact that the strong, temperature induced Rb-accumulation at the GBs is hindering the out-diffusion of Na [170], the subsequent rinsing of the samples with diluted ammonia is not leading to an as strong out-diffusion of Na from the GI as it happens in case of the RbF-PDT (following the model of Yuan et al. [97]; Figure 7.3 d). Therefore, the additional Na in the GI does only lead to the formation of a limited amount of additional  $\text{V}_{\text{Cu}}$ , which explains the limited effect and independence of  $n_{\text{CV}}$  from  $t_{\text{RIS}}$ .

This second mechanism would also explain why the amount of Na measured by GD-OES in the bulk of the CIGSe is independent of  $t_{\text{RIS}}$  and is not altered by the rinsing step (cf. Figures 5.8 d and e). However, this second interpretation is not in agreement with the Wei-model, since within their model the sheer presence of (more) Na in the GI would reduce the number of  $\text{In}_{\text{Cu}}$  and therefore increase the  $p$ -doping at least up to the level of the PDT sample.

## 7.2 Passivating Effects of Rb

### 7.2.1 Passivation of Deep Defects

In all three experiment series discussed in this thesis the Rb-conditioning (via both RbF-PDT and direct RIS-deposition) lead to a qualitatively increasing carrier lifetime, which – based on the discussion of the trPL-measurements in Section 3.2 – was attributed to the reduction of the SRH-recombination rate. While the origin of this passivating effect is not accessible with the methods utilized in this thesis, a mechanism for it will be proposed in the following combining the findings of this work with results from literature.

As it was shown in Section 4.1 in agreement with several publications [1, 165–167, 169, 219], Rb tends to accumulate at GBs. Therefore it is widely assumed that it passivates deep defects at these GBs [165, 166, 169, 219], which would be an explanation for the observed reduction of the SRH-recombination rate.

This assumption is in very good agreement with theoretical predictions. As already presented in Section 2.3.2 Chugh et al. [134] investigated the effect of Li, Na, and Rb close to symmetrical GBs in  $\text{CuInSe}_2$  and found that Rb – in contrast to Na – is unlikely to diffuse into the GI but segregates at Cu-deficient regions close to the GBs. Furthermore, they found that the density of states within the energy bandgap is reduced by the presence of alkali metals at the GBs in general. In particular, the passivation at some GBs is more effective by Rb than by Na, since it is compensating Se-dangling bonds more effectively than Na due to the fact that it is bigger in size and more electropositive [134].

There are experimental indications for such a GB-passivation as well. Firstly, it was directly shown by deep level optical spectroscopy that an RbF-PDT indeed reduces the defect concentration of a deep defect compared to an Rb-free reference device [252].

Secondly, Nicoara et al. [219] recently showed experimentally that an RbF-PDT can passi-

vate charged defects at the GBs. They observed that the variations of the contact potential difference at the GBs as extracted from Kelvin probe force microscopy are much smaller in RbF-treated samples compared to Rb-free samples, meaning that the potential at the GBs compared to the potential at the grain surfaces is in average lower in RbF-conditioned samples than in Rb-free samples. Furthermore, all investigated GBs of samples with RbF-PDT showed an upward band bending, while some of the GBs of the untreated reference sample showed an upward and some of them a downward band bending. Based on device simulations the authors propose that the latter have a detrimental influence on device performance, while the former are benign [219].

It should be mentioned again though that in another recent publication Abou-Ras et al. [144] did not find any hint for a defect passivation at the GBs of samples with KF-PDT using cathodoluminescence measurements. However, both studies used different methods as well as differently conditioned absorber layers (KF-PDT and RbF-PDT), so that a direct comparison is hindered.

### 7.2.2 Passivation of Shallow Defects

Additionally, to the reduction of the SRH-recombination rate, in all three experiment series, a trend of decreasing  $E_U$  with increasing amount of Rb incorporated into the absorber layer was observed. Since all these changes of  $E_U$  are rather small (maximal about 5 meV) and the Urbach energy of the respective reference samples is already rather low, it is assumed that the major effect of the increased amount of Rb in the absorber layer is the passivation of deep defects, which is leading to the strong trend in  $\tau_{\text{exp}}$  and  $V_{\text{OC}}$ . However, the impact of the passivation of a shallow defect will also be considered during the setup of the final device model in the next chapter.

### 7.2.3 Surface-Passivation

#### Nanopatterning

The nanopatterning, which was shown to appear at the surface of the absorber layer after the RbF-PDT in Section 4.1.2 could be an additional passivation mechanism of the PDT, contributing to the observed  $V_{\text{OC}}$ -boost. A similar effect was observed after a KF-PDT [150] and the authors of that study proposed that the nanostructure leads to a comparable passivation of the interface as the point contact formation in silicon solar cells does [150, 152]. However, in the here presented case of an RbF-PDT, the distribution of these ‘point contacts’ is rather dense and the distance between these contacts is small compared to the diffusion length (which is considered to be in the order of magnitude of  $\sim 1 \mu\text{m}$  [7]). Therefore it will not explicitly be included in the modeling of the presented findings in Chapter 8, which is done by one-dimensional simulations. However, it cannot be excluded that on top of the reduced  $V_{\text{OC}}$ -losses ( $\Delta V_{\text{OC}}^{\text{CV}}$  and  $\Delta V_{\text{OC}}^{\text{rem}}$  as described above) there is an additional reduction of the surface recombination velocity due to this nanopatterning. In fact, there is a theoretical study, suggesting that such a patterning could reduce the surface recombination velocity [253]. However, no such nanopatterning was observed after a direct deposition of RIS on top of the CIGSe, while the effects of the RIS-deposition on the carrier lifetime, i.e. also on the recombination mechanisms, and on  $V_{\text{OC}}$  are similar as in case of the RbF-PDT. This behavior suggests that the nanopatterning does not significantly influence the recombination in the devices, which might either be due to the fact that it is just not a passivating layer, or that even the reference devices do not suffer from significant interface recombination – which is actually generally not assumed for CIGSe-based solar cells [57, 252, 254]. The significance of interface recombination as well as the effect of Rb-conditioning on it will also be analyzed using device simulations in Chapter 8.

### Growth of the Buffer Layer

It was already assumed in Section 6.1 that the linear reduction of the ODC-signal with  $t_{\text{CBD}}$  in the Raman spectra is attributed to Cd-atoms diffusing into the ODC. This consumption of the ODC during the CBD could either take place via the formation of  $\text{Cd}_{\text{Cu}}$  anti-sites from the available  $V_{\text{Cu}}$  or via the formation of a mixed phase like e.g.  $\text{CdIn}_2(\text{S}, \text{Se})_4$  as it was already proposed by Barreau et al. [255] (see proposed growth mechanisms in Figure 7.4).

From the presented Raman data it is not discernible whether the in-diffusion of Cd into the absorber layer is amplified by the PDTs, since the part of the ODC which is consumed during the formation of the RIS and might be further altered during the CBD growth as well, is not visible in the Raman spectra. Therefore, an in-diffusion of Cd into this RIS-layer would not be visible in the Raman spectra, too. Similarly,  $\text{CdIn}_2(\text{S}, \text{Se})_4$ , although Raman active when grown on a glass/Mo-substrate, does not show any Raman modes when deposited on CIGSe [256].

However, it was shown in literature that the overall Cd diffusion into the CIGSe is enhanced by KF- [126, 155] and RbF-PDTs [257]. This enhanced in-diffusion of Cd into the absorber layer together with the fact that the consumption of the ODC with  $t_{\text{CBD}}$  is not altered, is explainable if Cd is not only occupying residual Cu-vacancies in the ODC but additionally either occupies  $\text{Rb}_{\text{Cu}}$  anti-sites in the CIGSe or creates  $\text{Cd}_{\text{Rb}}$  anti-sites in the RIS-layer, i.e. if an ion-exchange between Cd and the alkali-atoms occurs.

At the same time, the RbF-PDT induces a more homogeneous growth of the CdS-layer. Taking into account the calculations done by Rau et al. [66], which were discussed in Section 2.1.3, this more homogeneous growth of the buffer layer could reduce the interface recombination. Rau et al. showed that the  $V_{\text{OC}}$  of the complete devices can be strongly reduced by just a small device volume (e.g. a few grains) or interface area of inferior quality compared to the rest of the device [66]. However, the exact reason for this improved coverage remains unclear so far.

Witte et al. showed that the CdS-growth on Rb-free absorber layers in the early stages is strongly dependent on the orientation of the underlying CIGSe grains [250]. They showed that grains with {112}-orientated surface facets are likely to not be covered in early growth stages and explained this behavior with the lower surface energy of {112}-orientated surfaces [250]. In a subsequent contribution, they showed that the growth of the CdS on these grains can be enhanced by increasing the surface energy by oxidation of the surface [258]. Due to the hydrophilic nature of alkali salts, alkali-PDTs can lead to a stronger oxidation of the surface of the absorber layer too as it was shown in the XPS-study in Section 4.1.2. Therefore the better coverage could be due to an indirect oxidation of the CIGSe between the PDTs and the CBD due to the presence of the alkali elements during the intermediate air exposure.

Another possibility was already discussed in Section 6.1. The growth of the CdS could be altered due to the fact that on Rb-conditioned absorber layers, the CdS does not grow directly on the CIGSe but on the newly formed RIS-layer. In the previous chapters, it was indicated that this RIS-layer grows amorphously. Therefore the surface termination of the underlying CIGSe grains would not play a role for the CdS growth after the PDT since the RIS-layer acts as the substrate.

This is a possible explanation for the altered growth rate of the CdS due to the RbF-PDT as well. It was shown by Lincot et al. [249] that a change of the substrate can lead to significantly altered growth rates of the CdS-layers under otherwise unchanged growth conditions, e.g. CdS growth on RIS could be slower than on CIGSe. Although the presented results agree with the general expectation that a slower growth rate leads to a higher density of nucleation sites and therefore a better coverage [259], in the present case such a correlation does not seem to be the main factor for the improved coverage: In Publication [3] it was shown that both a KF- and an RbF-PDT, improve the coverage of the CdS in a similar manner, while the growth rate of the CdS on KF-conditioned CIGSe is faster and that of CdS on RbF-conditioned CIGSe slower than in the reference case.

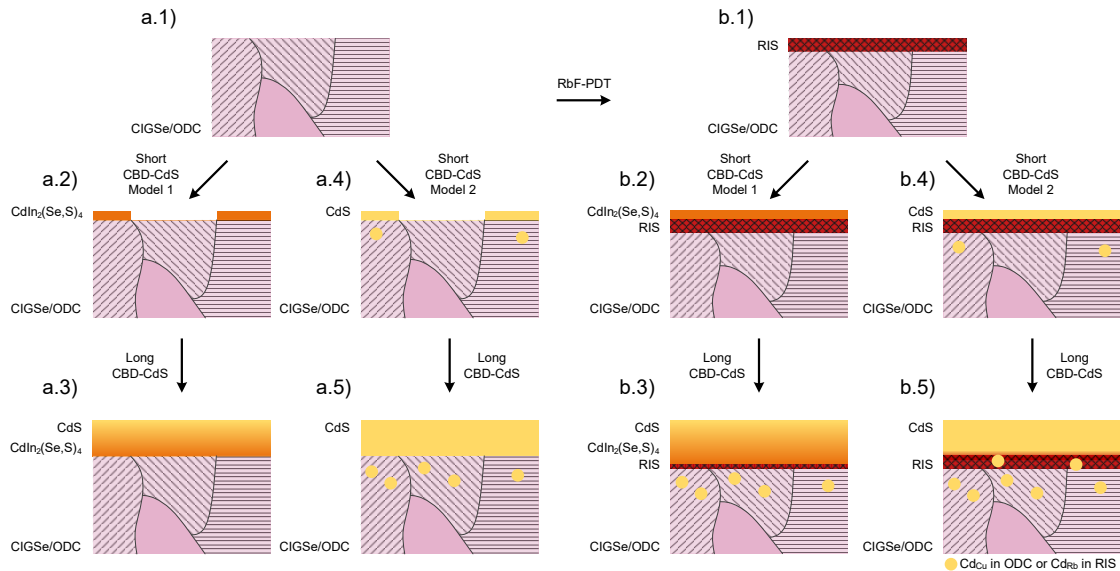


**Figure 7.4:** Schematic representation of the proposed mechanisms for the heterojunction-formation without (a) and with (b) RbF-treated absorber layers. For a detailed description see text.

Figure 7.4 visualizes these proposed growth mechanisms of the CdS. In the Rb-free case, the starting point of the model is the polycrystalline CIGSe-layer, which consists of an intermixed ODC- and  $\alpha$ -phase CIGSe (Figure 7.4 a.1). The differently oriented grains are indicated by the stripe-patterns. Due to the lower surface energy of  $\{112\}$ -orientated surfaces (grain in the middle of the scheme) [250], the CdS hardly grows on these grains in the initial growth phase (Figures 7.4 a.2 and a.4), but covers the whole surface of the absorber layer after long CBDs (Figures 7.4 a.3 and a.5). Note that the CdS is not just growing on top of the CIGSe, but partly consumes the ODC at the surface of the absorber layer during growth as well. Whether this happens via the formation of a mixed phase like  $\text{CdIn}_2(\text{Se},\text{S})_4$  as proposed by Barreau et al. [255] (Figures 7.4 a.2 and a.3) or via the occupation of  $V_{\text{Cu}}$  by Cd-atoms (Figures 7.4 a.4 and a.5) cannot be concluded from the available data.

In case of RbF-treated CIGSe, the ODC at the surface of the absorber layer is partly consumed by the amorphous RIS-surface layer (Figure 7.4 b.1), which acts as the substrate for the CdS-layer. Therefore the orientation of the underlying CIGSe-grains is irrelevant for the nucleation of the CdS leading to a homogeneous growth (Figures 7.4 b.2 and b.4) even after short CBDs.

Again, two possible mechanisms are shown in order to explain the reduction of the ODC and the more pronounced in-diffusion of Cd in Rb-treated samples compared to untreated ones: Figures 7.4 b.2. and b.3 show how Cd diffusing into the absorber layer leads to an ion-exchange with the Rb of the RIS-layer and therefore a partial transformation of the RIS-layer to a mixed phase as e.g.  $\text{CdIn}_2(\text{Se},\text{S})_4$ . Additionally, there is Cd diffusing into the underlying ODC explaining the overall lower ODC-amount after long CBDs. Within this model the more pronounced in-diffusion of Cd (compared to the Rb-free case) is explained by the combination of the formation of an (or a thicker) additional Cd-containing layer and (more)  $\text{Cd}_{\text{Cu}}$ -antisites compared to the Rb-free reference case. Within the Model 2 (Figures 7.4 b.4 and b.5) the stronger Cd in-diffusion is explained by the formation of additional  $\text{Cd}_{\text{Rb}}$  antisites in the RIS without the formation of a mixed phase. However, combinations of these mechanisms would be plausible too.

### 7.3 Summary and Conclusions of Chapter 7

In summary, the amount of available  $V_{Cu}$  in the CIGSe is the key factor deciding the effectiveness of the RbF-PDT. The presented models propose that in samples with very low  $CGI$  there are plenty of  $V_{Cu}$  available to be occupied by the Rb so that the interaction of Na and Rb is weak. This leads to a pronounced growth of the secondary RIS-layer at the surface, which is proposed to be the reason for the lowered  $FF$ . In samples with high  $CGI$ , however, the amount of available  $V_{Cu}$  is lower, leading to a thinner RIS-phase at the absorber surface and therefore better  $FF$ . Furthermore, more Rb-atoms occupy  $Na_{Cu}$ -sites at the GBs leading to two additional effects: Some of the Na-atoms are driven into the GI and increase the carrier concentration, while at the same time Rb is passivating the GBs, e.g. by reducing the density of states within the energy bandgap or passivating charged defects. The accumulation of Rb at the GBs presumably is independent of the  $CGI$ , since a reduced SRH-recombination rate was observed for all Rb-conditioned samples discussed in this thesis.

The formation of a RIS-layer also has a beneficial influence on device performance. Possibly due to its assumed amorphous structure, it acts as a more homogeneous substrate for the growth of the absorber layer and therefore improves the homogeneity of the CBD-CdS. This, in turn, can reduce the  $V_{OC}$ -losses due to partially reduced quality of the heterojunction as described by Rau et al. [66] and furthermore enables to grow the buffer layer thinner and therefore induce a gain in  $j_{SC}$ .

# 8 Modeling the Mechanisms of the Rb-Conditioning by Device Simulations

In this final chapter, one-dimensional electrical solar cell device simulations using the software code SCAPS-1D (cf. Section 3.2) are used in order to combine all results of the experimental findings that were presented and discussed in Chapters 4 through 6 and interpreted into a complete device model in Chapter 7. This model is able to represent both the Rb-free reference and Rb-conditioned solar cells. The device simulations are oriented towards high efficiency solar cells and therefore concentrate on devices based on absorber layers grown with  $CGI \geq 0.9$ . However, a generalization of the model to cases with lower  $CGI$  appears to be possible as well.

The goal of this chapter is to build up a one-dimensional model that is compatible with all the experimental data presented above and is able to accurately fit the  $j$ - $V$ - and  $C$ - $V$ -curves of selected devices as well as to provide possibilities to trace the trends of the PV-parameters in the different experimental series of this thesis. To the best of the author's knowledge, no such device model was published in literature yet.

## 8.1 Setting up the Device Model

### 8.1.1 The Reference Case

In order to be able to model the effects of the Rb-conditioning (by the RbF-PDT and by the direct RIS-deposition) on the optoelectronic properties of a complete solar cell, a model for the Rb-free reference has to be set up. For this, the reference device with  $CGI = 0.9$ , of which the  $j$ - $V$ -curve is shown in Figure 4.7, is used as a starting point.

Ideally, a device model does not only provide an accurate fit of the experimentally derived  $j$ - $V$ -curves but also reproduces the corresponding  $C$ - $V$ -curves in order to ensure the accuracy of the model. Various device setups can produce similar  $j$ - $V$ -curves, but if a model is able to fit experimental  $j$ - $V$ - and  $C$ - $V$ -curves, it is likely that the major defect distributions in the device are chosen accurately (cf. Section 3.2). However, since a SCAPS-model does not consider two- or three-dimensional effects, some deviations from the measured data are expected. Furthermore, simplifications of the defect distributions have to be made in order to ensure stable fitting conditions. Therefore especially a fit of the  $C$ - $V$ -profile can not always represent all features of a measured curve. The reference device model, which will be discussed below, was chosen because it is able to reproduce all trends observed in the measured  $C$ - $V$ -curves, while providing accurate fits of the  $j$ - $V$ -curves. It is therefore assumed to be a well-suited basis to interpret the experimental data regarding the major effects of the Rb-conditioning. Note, that this model is chosen because it accurately represents the experimental data. However, it might not be the only possible explanation for the observed effects.

Several (defect) contributions are implemented into the model (cf. Table 3.1 in Section 3.2.3 for a full description of the reference model).

- There is a neutral, mid-gap defect in the bulk of each layer in order to be able to modify the SRH-recombination rate in the bulk while maintaining a simple device model. More complex defect distributions in the absorber layer, as e.g. the combination of a donor-acceptor-pair or a  $GGI$ -dependent defect density [260] have been tested. These

provided similarly accurate results for the reference model but lead to computing-difficulties in case of Rb-conditioned devices. It is assumed that the change of the carrier lifetime after Rb-conditioning, which is the major effect of the bulk defect in the absorber layer, can be accurately described using a neutral, deep defect.

- Furthermore, the model consists of an acceptor-like defect at the heterointerface in order to be able to account for the increase of the capacitance under forward bias and for interface recombination. The presence of an acceptor defect at the heterointerface was discussed in literature before [212]. Furthermore, Hölscher et al. [261] proposed the formation of an interface defect (unspecified if acceptor or donor) at the heterointerface due to air- and light-exposure of the absorber layer based on voltage-dependent admittance spectroscopy [261]. This could be a possible explanation for the origin of this acceptor defect since all absorbers were exposed to air and daylight for a few minutes during the transfer from the PVD-B to the CdS-deposition (cf. Section 3.1). Other groups, however, proposed the presence of near interface-defects acceptor defects in the surface region of the absorber layer [262, 263], which would have a similar effect as the interface-defects chosen in this work.
- Additionally, there is a hole barrier at the back contact. The presence of such a barrier at the back contact was proposed to be present in similarly prepared CIGSe-based devices by several groups [126, 209, 264, 265].

Figure 8.1 a) shows the energy band diagram of this simulated reference device, which is described in more detail in Section 3.2.3. Figures 8.1 b) and 8.1 c) display the respective  $j$ - $V$ - and  $C$ - $V$ -curves together with the measured data. Both curves are accurately described by the chosen model.

The fact that the  $FF$  of the simulated device is slightly higher than that of the real device (see Figure 8.1 b), and Table 8.1) can be explained by  $FF$ -losses due to the mechanical cell area definition in case of the real device, which cannot be reproduced in the one-dimensional model. These losses become apparent by the fact that the  $FF$  of photolithographically scribed devices is improved by several percent compared to the device with standard mechanical scribing (cf. Figures 4.23 and 5.16).

The increase of the capacitance under forward bias appears due to the fact that under these voltages the interface acceptor is located energetically close to  $E_{F,p}$  meaning that its charge state can be altered by the applied AC-voltage during the  $C$ - $V$ -measurement due to the asymmetrically chosen capture cross sections ( $\sigma_p \gg \sigma_n$ ) as will be discussed in the sections below. A similar interpretation of such an increase of the capacitance under forward bias due to an acceptor state at the interface is given in Reference [212]. However, no clear validation of the presence of these acceptor states was given.

A method to test the presence of charged interface states was proposed in Reference [42]. Following Equation 3.14, it holds

$$C \propto \frac{1}{\sqrt{V_{bi} - V}}. \quad (8.1)$$

When determining  $V_{bi}$  from the Mott-Schottky-relation, i.e. from the extrapolation of  $1/C^2$  to  $1/C^2 = 0$  (see Equation 3.15), an interface charge leads to an additional contribution to  $1/C^2$  and therefore alters the value derived for  $V_{bi}$  [42]. Thereby a negative interface charge leads to a higher extrapolated voltage than the actual  $V_{bi}$  and vice versa. In turn, this means that in case of a device with charged interface defects, the shape of  $(V_{bi} - V)^{-1/2}$  plotted versus  $V$  should deviate from the actually measured  $C$ - $V$ -curve [42] due to the over- or underestimated value for  $V_{bi}$ . Therefore, this approach can be used in order to test the presence of a charged acceptor defect at the heterointerface. The rather good agreement of  $(V_{bi} - V)^{-1/2}$  and  $C$  in Figure 8.1 d) is therefore an argument against the presence of a charged acceptor state at the hetero-interface. However, the severity of the deviation the extrapolated voltage value from  $V_{bi}$  depends on the density of the interface defect and various

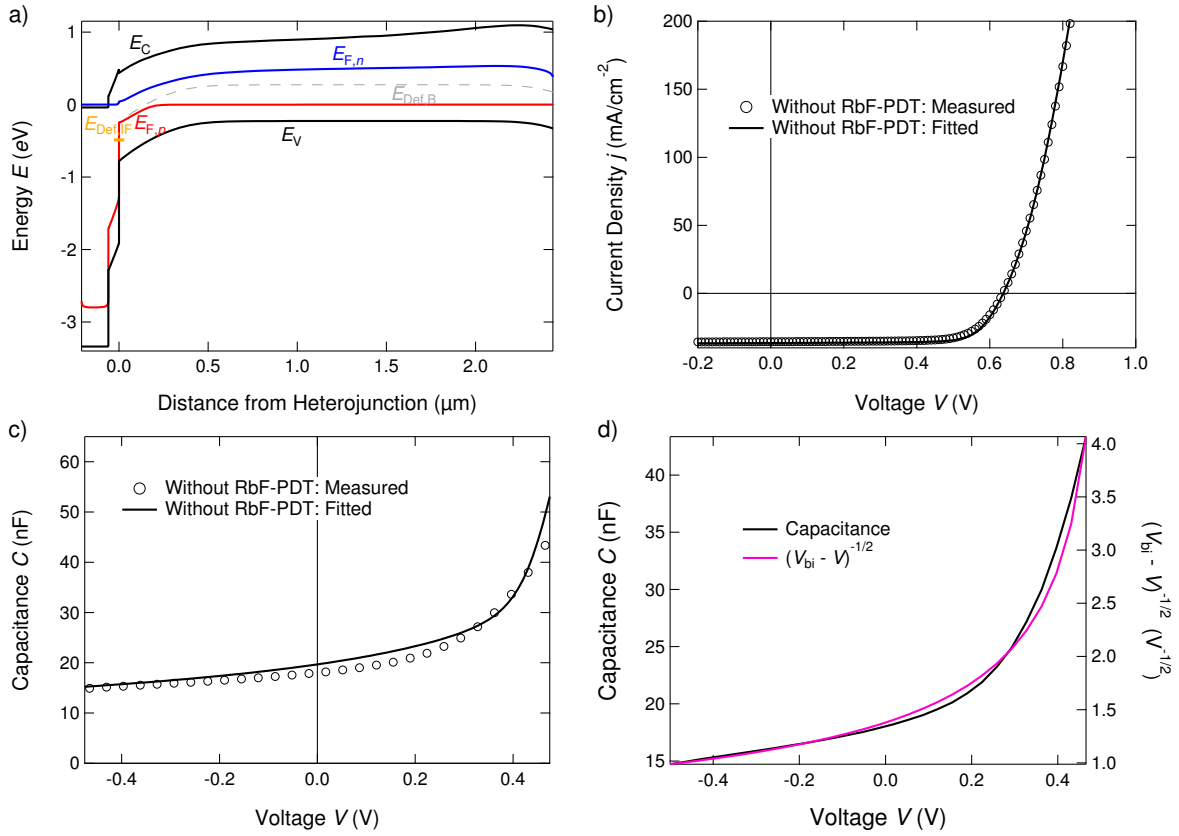


**Figure 8.1:** a) Simulated energy band diagram of the Rb-free reference device described in Table 3.1 under illumination without applied bias voltage, which was already shown in Figure 3.7. For the sake of simplicity, the defects in the window layer are not marked. b) Measured  $j$ - $V$ -curve of the Rb-free reference device discussed in Section 4.1 (open circles) and the fitted  $j$ - $V$ -curve corresponding to the device shown in a) (solid line). c) Measured  $C$ - $V$ -curve of the Rb-free reference device discussed in Section 4.1 (open circles) and the fitted  $C$ - $V$ -curve corresponding to the device shown in a) (solid line). d) Measured capacitance (black line) as well as  $\sqrt{V_{\text{bi}} - V}$  as derived from the Mott-Schottky-relation following Equation 3.15 (pink line) versus  $V$ .

properties of the buffer layer [42] and is furthermore also affected by deep defects in the bulk of the absorber layer as well as the carrier density in the absorber layer [266]. Therefore, the fact that  $(V_{\text{bi}} - V)^{-1/2}$  only slightly deviates from  $C$  is an argument against the proposed presence of an interface defect but cannot exclude this possibility.

Due to the fact that the model containing acceptor defects at the hetero-interface is the only model that was found explaining the experimentally derived  $j$ - $V$ -curves while providing the observed increase of  $C$  under forward bias (especially for the Rb-conditioned samples, as will be discussed below), it will nevertheless be used in the further process of this chapter. Note, however, that there might be more complex scenarios explaining the increasing capacitance under forward bias. This issue will be discussed again below.

Over the course of this chapter, the energetic position and density of interface defects will be chosen in a way that its effect on the  $j$ - $V$ -curve of the simulated devices is minimized, while it mostly accounts for the large capacitance under forward bias.

In the following, this model will accordingly be extended in order to be able to describe the experimentally observed effects of the Rb-conditioning. Therefore Sections 8.1.2 through 8.1.6 use parameter variations to elucidate the impact of several components of the model on the simulated device parameters in order to isolate the parameters which will be included in the fitting of the experimentally derived  $j$ - $V$ - and  $C$ - $V$ -curves in Section 8.2.

Since these parameter variations appear to be complex, the main differences of each input parameter set to the default values, which are depicted in Table 3.1, will be given in an individual table in Appendix A.3.

### 8.1.2 Bulk Effects of Rb: Defects and Carrier Density

Summarizing the experimental results presented in the chapters above, the RbF-PDT reduces the  $V_{OC}$ -losses due to a reduction of  $\Delta V_{OC}^{CV}$ ,  $\Delta V_{OC}^{rem}$ , and by establishing better growth conditions for the buffer layer. Thereby the main effect on  $\Delta V_{OC}^{rem}$  is the improved  $\tau_{exp}$  due to Rb-incorporation, which is assumed to be caused by the passivation of deep defects that might be located at the GBs. Additionally, the Rb-incorporation leads to a slight reduction of the density of tail states, e.g. to a lower  $E_U$ .

Since no analytical expression for  $V_{OC}$  in dependence of  $\tau_{eff}$  and/or  $E_U$  is available, the correlation of  $\Delta V_{OC}^{rem}$  and  $\tau_{exp}$  of deep defects and tail states is done using device modeling. Thereby it is assumed that  $E_U$  is only influenced by shallow defects, based on a study by Sutter-Fella, in which even strong variations of the density of deep defects were reported to not impact the value of  $E_U$  determined from the quantum efficiency [218].

Generally, it seems obvious from the considerations regarding the efficiency of SRH-recombination in dependence on the energetic level of the defect, which were discussed in Section 2.1.2, that a deep defect leads to a higher recombination rate than a shallow defect. However, since the exact influence of the defects depend on the carrier density of the absorber layer [42], in the following the impact of a shallow and a deep defect on  $\Delta V_{OC}^{rem}$  will be analyzed for the special case of the reference model that was proposed in the section above.

In order to be able to estimate this impact of the reduction of  $E_U$  on  $\Delta V_{OC}^{rem}$ , therefore a neutral, shallow defect level ( $E_{Def,B} = 0.05$  eV above the VBM) is (additionally) introduced into the absorber layer of the device structure. In order to compare the effect of such a shallow defect with that of a deep defect (as it is already present in the model), Figure 8.2 a shows the individual dependence of  $V_{OC}$  of this device on the defect density  $N_{Def,B}$  of the shallow defect level or the deep defect level. Here, the case of the respective defect being the only defect in the bulk of the absorber layer is shown, while Figure 8.2 b shows the case in which both defects are present in the CIGSe simultaneously. In the latter case the defect density of one defect is varied, while the other one is present at a fixed  $N_{Def,B} = 10^{14}$  cm $^{-3}$ . An overview of these parameter variations is shown in Table A.2 in the appendix.

As expected the impact of the deep defect on  $\Delta V_{OC}^{rem}$  and therefore on  $V_{OC}$  is – within the chosen range of  $N_{Def,B}$  – about one order of magnitude larger than the impact of the shallow defect. In the (more realistic) case of both defects being present in the absorber layer at the same time, the impact of the shallow defect (within the chosen range for  $N_{Def,B}$ ) is even two orders of magnitude lower than that of the deep defect. Considering the fact that the

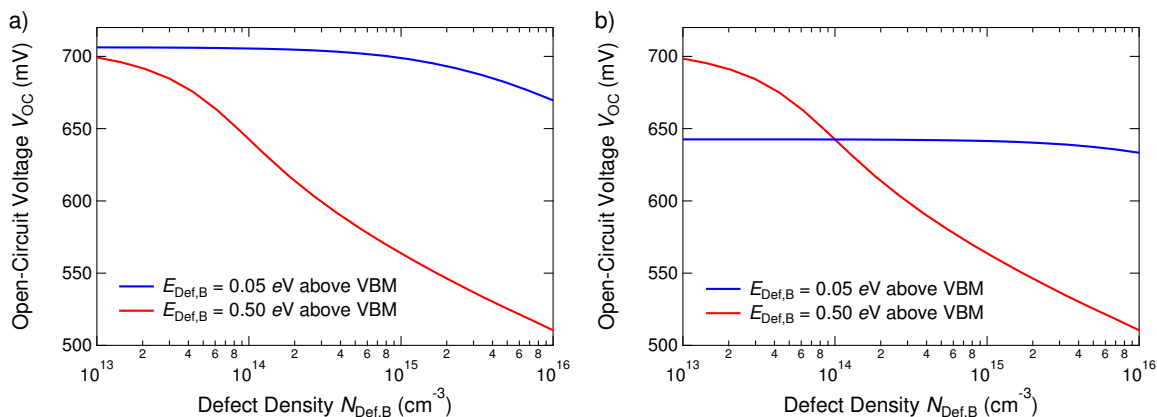


**Figure 8.2:** Influence of the defect density  $N_{Def,B}$  of a shallow (defect level  $E_{Def,B} = 0.05$  eV) and a deep defect (defect level  $E_{Def,B} = 0.50$  eV) on the  $V_{OC}$  of the simulated device. a) shows the case in which the respective defect is present alone in the absorber layer, while b) shows the case in which the respective other defect is present at a fixed defect density of  $N_{Def,B} = 10^{14}$  cm $^{-3}$ . In order to clarify the utilized parameter sets, the input parameters for both defects for all four simulations are given in Table A.2. The input parameters for all properties not mentioned in this table are unchanged to the reference case in Table 3.1. Note that there is no RIS-layer in this reference device (and accordingly only one interface defect at the CdS/CIGSe-interface).

reduction of  $E_U$  due to the RbF-PDT was shown to be in the order of magnitude of 1 meV (cf. Figures 4.6, 4.20, and 5.14) its impact on  $\Delta V_{OC}^{rem}$  will be neglected and the effect of the Rb-conditioning on  $\tau_{exp}$  will be solely represented by the defect density of the deep bulk defect.

The bulk effects of the Rb-conditioning on the respective  $V_{OC}$ -losses will therefore be represented by  $\tau_{eff}$  (via the defect density of the bulk defect,  $N_{Def,B}$ ) as well as the doping density of the absorber layer,  $N_D^{CIGSe}$ . These two parameters will be used as free fit parameters in the simulations of the Rb-conditioned devices in Section 8.2.

### 8.1.3 Surface Effects of Rb: The RIS-Layer

Since a one-dimensional model was chosen for the device simulations, the improved coverage of the surface of the absorber layer by the CdS layer due to the presence of the RIS-layer, and the subsequently improved lateral homogeneity of the CdS/CIGSe hetero-interface are not considered. However, the RIS-layer itself can be included into the one-dimensional layer stack. An example of the energy band diagram close to the hetero-junction of such a modified stack is shown in Figure 8.3 b.

Some physical properties of the RIS-layer have been determined in Section 5.1 but still most of its properties are not known. Its impact on  $V_{OC}$  and  $FF$  in dependence on these properties is therefore investigated systematically by simulations as well.

## Part I: Results

### RIS-Layer: Impact on $V_{OC}$

The impact of the properties of the RIS-layer on  $V_{OC}$  via its thickness  $d_{RIS}$  as derived from these device simulations is shown in Figure 8.4. These properties include the following:

- The bandgap energy  $E_g$  (see Figure 8.4 a to c).  
 $E_g^{RIS:Na}$  was shown to be 2.8 eV in case of single-phase RIS:Na. However, as it was discussed in the previous chapters, it is possible that the RIS-layer is partly Rb-deficient and/or transforming into a mixed phase during the CdS-deposition. Therefore the cases of  $E_g^{CdIn_2(S,Se)_4} = 2.7$  eV [255] and  $E_g^{In_2Se_3:(Rb,Na)} = 2.0$  eV are included.  
 As can be seen from Figures 8.4 a to c, for a cliff configuration the  $V_{OC}$  is reduced with increasing  $E_g$  by up to  $V_{OC}^{2.0 eV} - V_{OC}^{2.8 eV} \approx 1.2$  mV (see Figure 8.4 c). This slight depen-

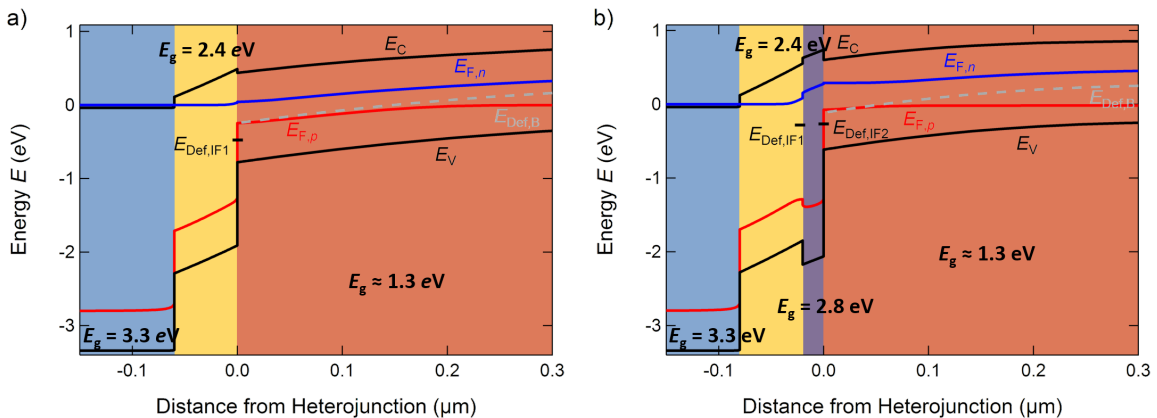


**Figure 8.3:** Zoom in into the heterojunction region of the energy band diagram of the reference device (a) and of the modified layer stack including the RIS-surface layer (b). The blue marked region is the i-ZnO, the yellow one the CdS buffer, the brown one the CIGSe, and the purple one the RIS-layer. Note that this is an example with  $\Delta E_C = 75$  meV,  $E_g^{RIS:Na} = 2.8$  eV,  $N_D^{RIS} = 10^{14}$  cm $^{-3}$ , no defects in the RIS-layer but with the additional defect at the CdS/RIS-interface. These parameters and the presence of the interface defects vary in the simulations that are discussed in this chapter (see text). For each set of parameter variations, i.e. each following figure, there will be a table given listing the used parameters and features of this device model.

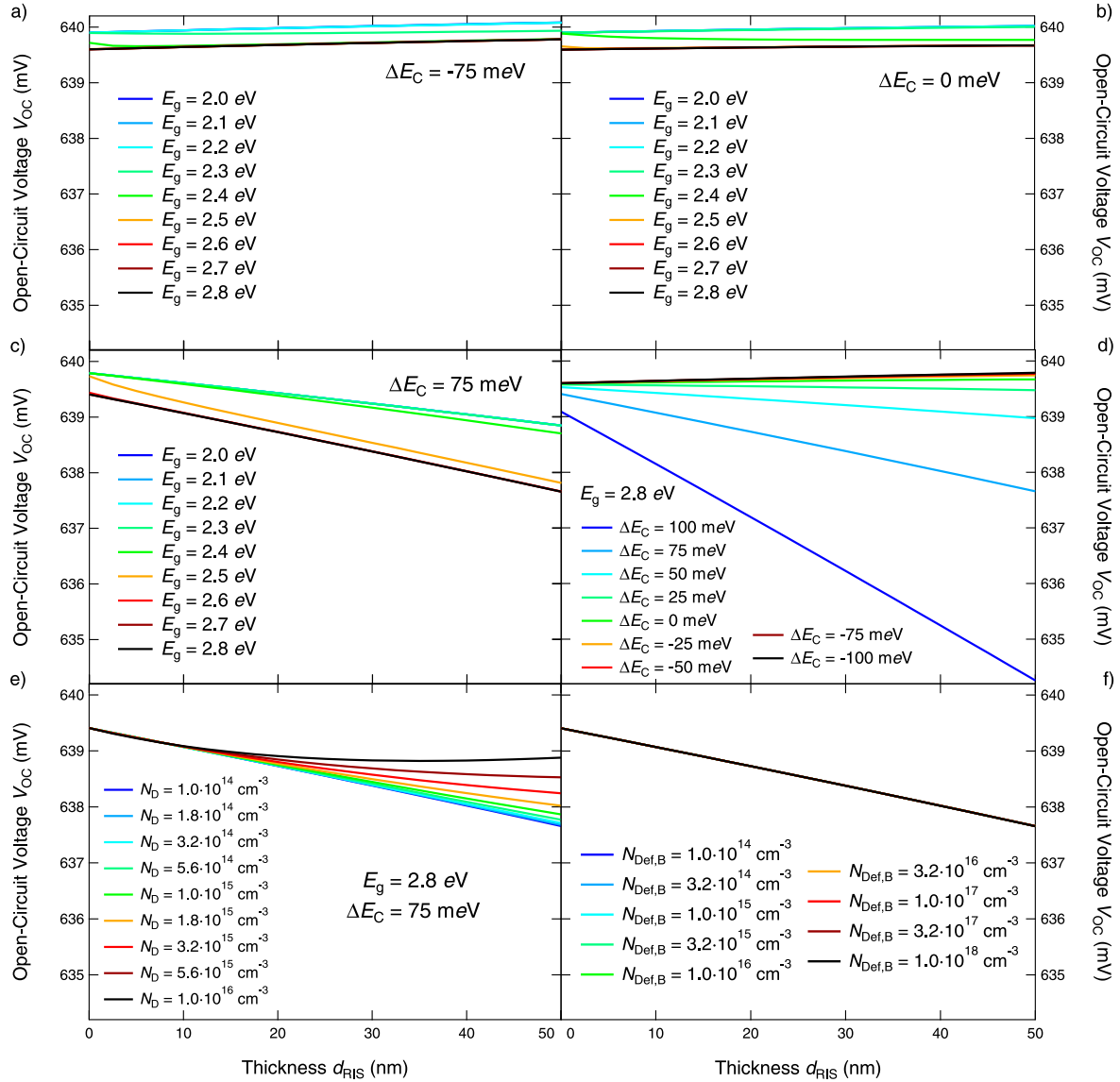


**Figure 8.4:** Simulated trend of the  $V_{OC}$  in dependence of  $d_{RIS}$  (cf. Figure 8.3) for different parameter sets: a) Variation of  $E_g^{RIS}$  at  $\Delta E_C = -75$  meV (spike), b) Variation of  $E_g^{RIS}$  at  $\Delta E_C = 0$  meV (flat bands), c) Variation of  $E_g^{RIS}$  at  $\Delta E_C = 75$  meV (cliff), d) Variation of  $\Delta E_C$ , e) Variation of the carrier concentration  $N_D$ , f) Variation of the defect density  $N_{Def,B}$ . If not mentioned otherwise the following parameters were used for the RIS-layer:  $E_g^{RIS} = 2.8$  eV,  $\Delta E_C = 75$  meV,  $N_D = 10^{14}$  cm $^{-3}$ ,  $N_{Def,B} = 0$  cm $^{-3}$  (see Table A.3). In order to clarify which variations were performed in Figures a) to d), the corresponding energy band diagrams are shown in Figure 8.5. More complete parameter-variations can be found in Figures A.3 to A.5 in the appendix.

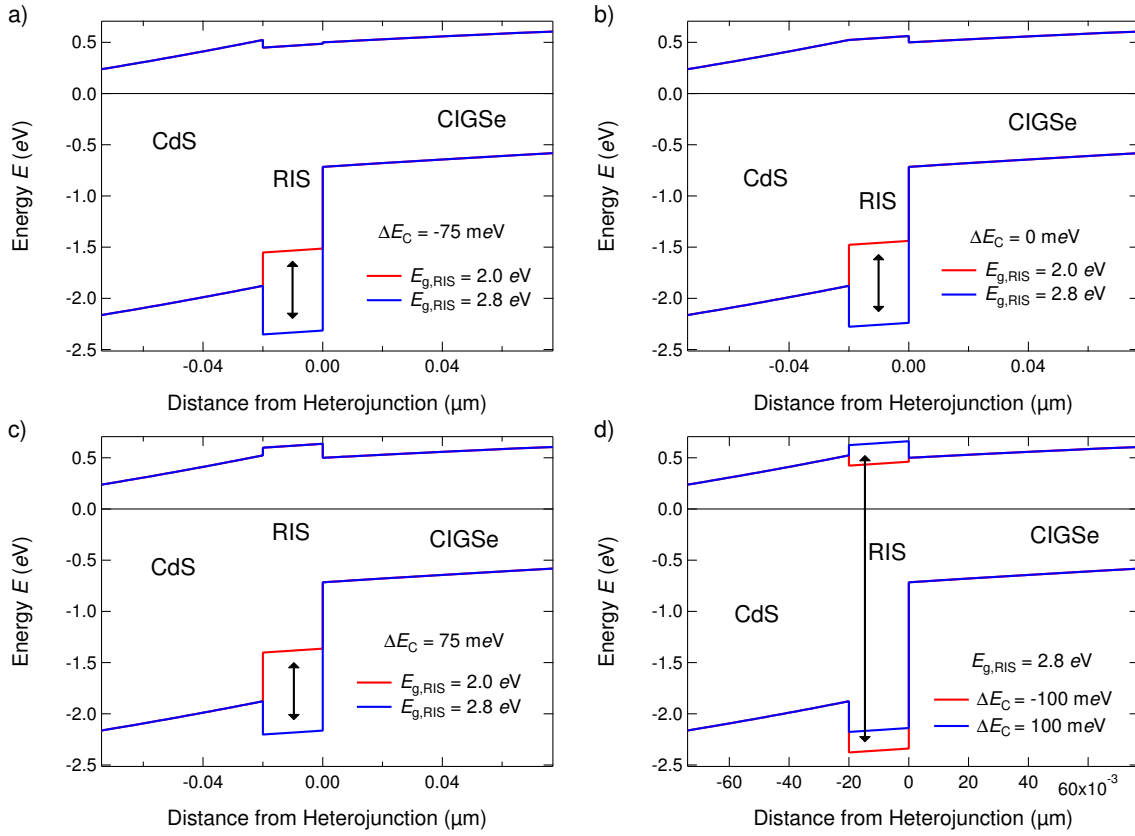


**Figure 8.5:** Energy band diagrams of corresponding to the parameter variations leading to the trends in  $V_{OC}$  and  $FF$  that are shown in Figures 8.4 and 8.6. The black arrows indicate the respective parameter variation. a) shows the situation for Figures 8.4 a and 8.6 a, b) the situation corresponding to Figures 8.4 b and 8.6 b, c) the situation corresponding to Figures 8.4 c and 8.6 c, and d) the situation corresponding to Figures 8.4 d and 8.6 d.

dence of the  $V_{OC}$  on  $E_g$  is due to a slightly increased interface recombination current via the defect at the CdS/RIS-interface in case the energy bandgap of the RIS-layer is large enough to induce a hole barrier in the VBM at the CdS/RIS-interface (see Figures 8.5 a to c). However, the overall impact of  $E_g$  on  $V_{OC}$  is negligible (less than 1.5 mV). Therefore in the following simulations, only the case of  $E_g^{RIS:Na} = 2.8 \text{ eV}$  is shown. Additional plots of the following parameter variations for the case of  $E_g^{In_2Se_3:(Rb,Na)} = 2.0 \text{ eV}$  are shown in Figures A.3 to A.5 in the appendix.

- The electron affinity  $EA$  (see Figure 8.4 d).

In order to analyze the impact of the RIS-layer for the cases of a perfect band line-up with the CdS buffer layer (as shown in Figure 8.5 b), a spike (Figure 8.5 a), or a cliff towards the buffer (Figure 8.5 c),  $EA$  is varied from  $EA = 4.2 \text{ eV}$  to  $EA = 4.4 \text{ eV}$  corresponding to a CBM-offset with the CdS-layer of  $\Delta E_C = EA_{CdS} - EA_{RIS} = -0.1 \text{ eV}$  (spike) to  $\Delta E_C = 0.1 \text{ eV}$  (cliff). Note that the limits for  $\Delta E_C$  were chosen within a range that results in not too strong performance losses (cf. also Figure 8.6 d), even though stronger cliff-configurations were proposed in case of a KF-PDT based on inverse photoelectron spectroscopy (IPES) [145]. To the best of the author's knowledge, no IPES-study is available on comparably RbF-conditioned absorber layers.

While  $V_{OC}$  slightly increases with  $d_{RIS}$  in case of a neutral and a spike-configuration ( $\Delta E_C \leq 0$ ), a cliff ( $\Delta E_C > 0$ ) leads to a comparably severe reduction of  $V_{OC}$  with increasing thickness of the RIS-layer.

These trends can be attributed to two overlying effects: As already mentioned in the bullet point above, there is a small hole barrier forming under moderate forward biases at the CdS/RIS-interface due to the high energy bandgap of the RIS-layer (see Figures 8.5 a to c) inducing interface recombination via the defect at this interface.

However, with increasing  $d_{\text{RIS}}$  the distance from this interface defect to the electrons at the surface of the absorber layer is increased, which leads to a small reduction of this recombination current, and – in case of the neutral- or spike-configuration – an improving  $V_{\text{OC}}$ . In case of a cliff-configuration there is an additional barrier forming for the photo-generated electrons at the RIS/CIGSe-interface (see Figure 8.5 c), slightly increasing the bulk recombination rate in the surface area of the absorber layer and therefore decreasing the  $V_{\text{OC}}$ . This effect is amplified by an increasing  $d_{\text{RIS}}$  as well.

In the following simulations only the case of a cliff with  $\Delta E_c = 75$  meV is shown since variations of  $N_{\text{D}}$  and  $N_{\text{Def}}$  for a spike-configuration and  $\Delta E_c = 0$  meV hardly affect  $V_{\text{OC}}$  (see additional simulations for  $\Delta E_c = 0$  and  $\Delta E_c = -75$  meV in Figures A.4 and A.5 in the appendix).

- The donor density  $N_{\text{D}}$  of the RIS-layer (see Figure 8.4 e).

The donor density in the surface layer is assumed to be rather low due to the fact that the conductivity of the RbInSe<sub>2</sub> thin film, which is discussed in Section 5.1, is below the detection limit of a standard four-probe measurement. In the simulations  $N_{\text{D}}$  was varied from  $10^{14} \text{ cm}^{-3} < N_{\text{D}} < 10^{16} \text{ cm}^{-3}$  (see Figure 8.4 e).

While rather high  $N_{\text{D}}$  lead to a stabilizing trend for  $V_{\text{OC}}$  after an initial decrease, cases of  $N_{\text{D}} \lesssim 3 \cdot 10^{15} \text{ cm}^{-3}$  lead to a steady loss of  $V_{\text{OC}}$  for the selected thicknesses.

The stabilizing trend at high  $N_{\text{D}}$  is due to a third effect of the RIS-layer in a cliff-scenario, overlying with the general trends at a cliff-configuration. For these rather high doping densities, the barrier effects described above (which lead to the initial reduction of  $V_{\text{OC}}$  with  $d_{\text{RIS}}$ ) are accompanied by an enhanced type-inversion in the surface region of the absorber layer [267] leading to a reduction of the recombination rate in the surface region of the absorber layer. This effect gets stronger for thicker RIS-layers. A similar effect was discussed in context with highly doped  $n$ -type buffer layers in Reference [267], which is similar to the case described here.

For the following simulations, the case of  $N_{\text{D}} = 10^{14} \text{ cm}^{-3}$  is assumed.

- Bulk-defects in the RIS-layer (see Figure 8.4 f).

Although the formation of manifold intrinsic defects is possible [2], only the most severe case of a mid-gap defect level is exemplarily analyzed here. Its defect density is varied in the range of  $10^{14} \text{ cm}^{-3} < N_{\text{Def,B}} < 10^{18} \text{ cm}^{-3}$ , which translates to a variation of the bulk carrier lifetime of  $0.01 \text{ ns} < \tau < 100 \text{ ns}$  or of the diffusion length of  $0.051 \mu\text{m} < \tau < 5.1 \mu\text{m}$  for the given cross sections of the defect (cf. Table A.3).

However, there is hardly any influence of the presence of such a defect on  $V_{\text{OC}}$  observed, which is why all other simulations were carried out without a defect in the bulk of the RIS-layer.

It is expected that a defect level in a layer with such a high energy bandgap does not significantly contribute to the net recombination rate, since under forward bias  $R \propto n_i^2 \propto \exp\left(-\frac{E_g}{k_{\text{B}}T}\right)$  [42], i.e. the major part of the SRH-recombination takes place in the layer with the lowest  $E_g$ . That is the absorber layer.

### RIS-Layer: Impact on $FF$

In Sections 4.2 and 5.2 it was shown that the formation of the RIS-layer induces a current blocking barrier that lowers  $FF$ . From these experiments it is expected that  $FF$  of the devices decreases with increasing  $d_{\text{RIS}}$ , which can originate either from a variation of the duration of the PDT, (see Section 4.1), a variation of the ratio of the ODC- to  $\alpha$ -phase CIGSe prior to the RbF-PDT (due to a lower  $CGI$  of the absorber layer, Section 4.2), or due to the direct deposition of a thicker RIS-phase (Section 5.2).

In order to test this hypothesis the dependence of  $FF$  on the thickness of the RIS-layer, considering all the variations of its parameters as mentioned in case of the  $V_{\text{OC}}$ -simulations above, is simulated and the results are shown in Figure 8.6.

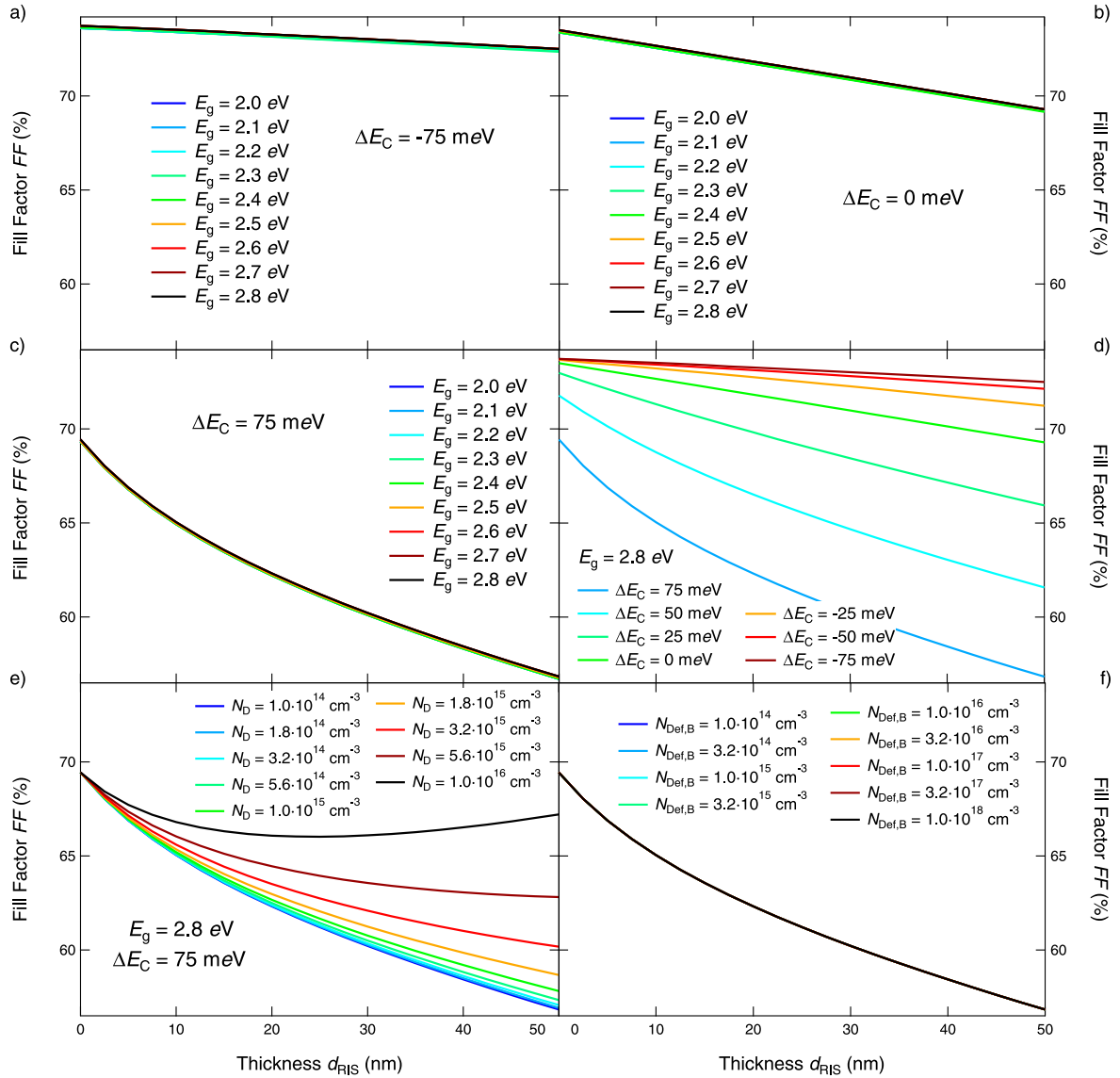


**Figure 8.6:** Simulated trend of the  $FF$  in dependence of the thickness of the RIS-layer (cf. Figure 8.3) for different parameter sets: a) Variation of  $E_g^{\text{RIS}}$  at  $\Delta E_C = -75$  meV, b) Variation of  $E_g^{\text{RIS}}$  at  $\Delta E_C = 0$  meV, c) Variation of  $E_g^{\text{RIS}}$  at  $\Delta E_C = 75$  meV, d) Variation of  $\Delta E_C$ , e) Variation of the carrier concentration  $n$ , f) Variation of the defect density  $N_{\text{Def,B}}$ . If not mentioned otherwise the following parameters were used for the RIS-layer:  $E_g^{\text{RIS}} = 2.8$  eV,  $\Delta E_C = 75$  meV,  $N_D = 10^{14}$  cm $^{-3}$ ,  $N_{\text{Def,B}} = 0$  cm $^{-3}$ . The energy band diagram corresponding to the variations done in a) to d) are shown in Figure 8.5, an overview of the input parameters of these simulations is given in Table A.3. More complete parameter-variations can be found in Figures A.6 to A.8 in the appendix.

Generally, the  $FF$  decreases with increasing RIS-thickness for all chosen parameter combinations (that is without significant recombination at the hetero-interface) and therefore supports the hypothesis stated based on the experimental results. The effect of  $E_g$  ( $\Delta FF < 0.2\%$  absolute, cf. Figures 8.6 a to c) and the presence of a neutral, deep defect in the bulk of the RIS-layer ( $\Delta FF = 0.0\%$  absolute, cf. Figure 8.6 f) on  $FF$  are negligible.

In fact,  $FF$  is dominated by the band line-up with the buffer layer ( $\Delta E_C$ , see Figure 8.6 d) and by the donor density ( $N_D$ , see Figure 8.6 e). Here, a pronounced cliff-configuration and a low donor density induce the strongest effect on  $FF$ , because these configurations lead to stronger barriers for the photo-generated carriers as can be seen from the energy band diagrams in Figure 8.5 and as it was already discussed in case of the  $V_{OC}$ .

## Part II: Combined Discussion

Generally, the one-dimensional influence of the RIS-layer on  $V_{OC}$  is negligible in most cases. After an initial gain of about 3 mV compared to the RIS-free reference ( $V_{OC}^{Ref} = 636.9$  mV),  $V_{OC}$  is rather stable in case of a neutral or spike-like line-up of the CBM, while it slightly drops for almost all parameter combinations with increasing  $d_{RIS}$  in case of a cliff-configuration.

The initial increase of the  $V_{OC}$  occurs even for the introduction of an infinitesimal thin RIS-layer (in SCAPS nominally  $d_{RIS} = 0.01$  nm). This gain in  $V_{OC}$  can be attributed to a reduction of the interface recombination, which occurs due to the fact that the RIS-layer is placed in between the CdS and the CIGSe layers but no additional defects at the RIS/CIGSe-interface were introduced. Due to the fact that the bandgap energy of the RIS-layer is larger than the bandgap energy of the CIGSe, the charge carriers at the interface are shifted farther away from the interface defect at  $E_{Def,IF1}$  (CdS/RIS-interface) reducing the recombination via this defect.

The fact that the RIS-layer hardly affects  $V_{OC}$  is generally no surprising result since the reference device is limited by recombination in the bulk and not at the interfaces as will be shown in Section 8.2 (cf. Figure 8.15 a), which is generally in good agreement with experimental results [57, 252, 254]. Therefore the introduction of an additional, high energy bandgap layer at the interface does not lead to any significant changes in the saturation current density, i.e. the net recombination in the device.

However, the fact that the high energy bandgap of the RIS-layer induces barriers for the photo-current (holes or electrons depending on  $\Delta E_C$  and  $E_g$ ), leads to a strong dependence of  $FF$  on  $d_{RIS}$ . Hereby the scenario of a cliff-configuration ( $\Delta E_C \approx 75$  meV) with a rather low doping density in the RIS-layer ( $N_D^{RIS} \approx 10^{14}$  cm $^{-3}$ ) appears to be accurate to model the experimentally observed effects since it induces a pronounced and steady  $FF$ -loss with  $d_{RIS}$ . This scenario will therefore be used for the modeling of the Rb-conditioned devices. The properties  $d_{RIS}$ ,  $\Delta E_C$ , and  $N_D =: N_D^{RIS}$  are used as free fit parameters in the device simulations in Section 8.2. Furthermore,  $E_g = E_g^{RIS:Na} = 2.8$  eV and no defects in the RIS-layer are chosen for simplicity.

### 8.1.4 Defining the Interface Defects

#### Part I: Results

As it was stated above, the introduction of the RIS-layer separates the CdS from the CIGSe-layer and therefore creates two new interfaces. The 'new' hetero-interface, i.e. the RIS/CIGSe-interface (IF 2), and the CdS/RIS-interface (IF1). Due to this new layer stack, the defect at the absorber layer/buffer layer interface is shifted from the CdS/CIGSe to the CdS/RIS-interface. However, in order to be able to accurately fit the strong increase of the capacitance at positive bias voltages in case of samples with an RbF-PDT (cf. Figure 4.4), an interface-defect at the hetero-junction is necessary (at least no other feature was found accurately describing this contribution to the capacitance, see discussion below). As shown

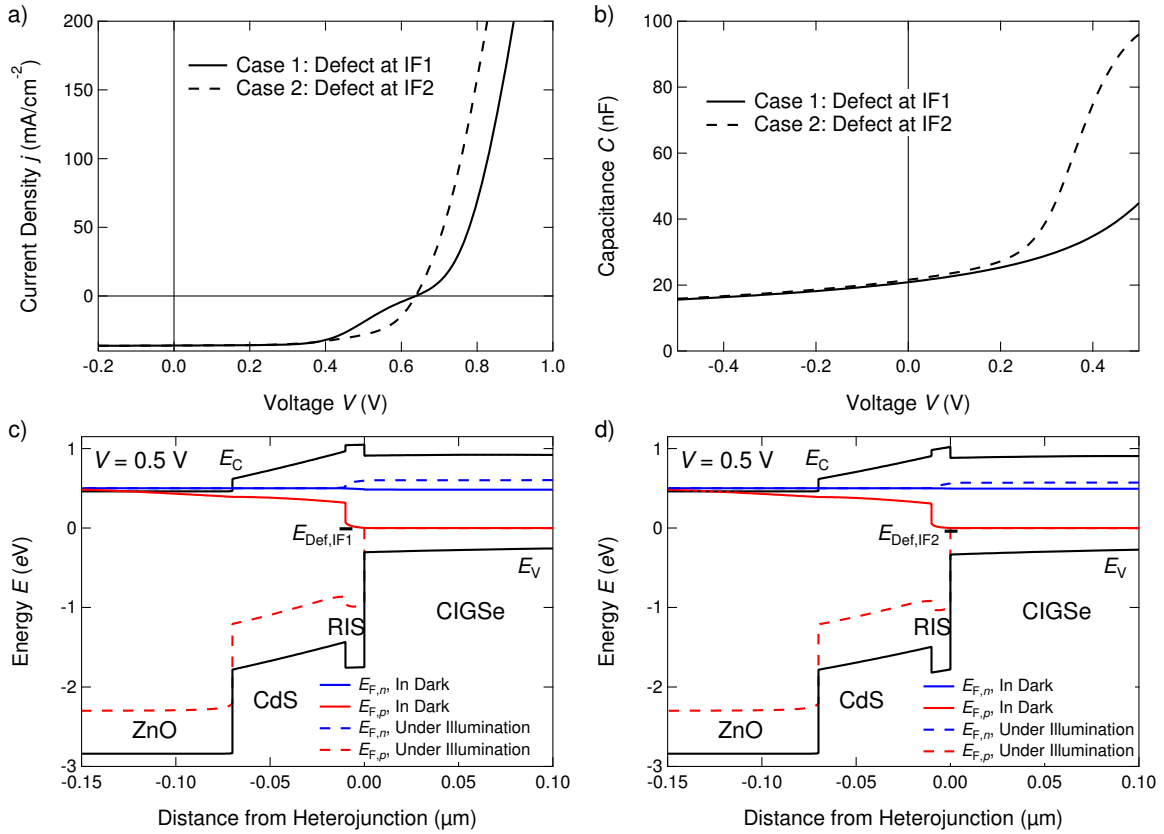


**Figure 8.7:** Simulated  $j$ - $V$ - (a) and  $C$ - $V$ -curves (b) of the two cases with an interface defect at only one interface each. Case 1 is the case with a defect at the CdS/RIS-interface (IF1), and Case 2 the case with a defect at the RIS/CIGSe-interface (IF2). The respective energy band diagrams are shown in c (Case 1) and d (Case 2). Both energy band diagrams show the respective situation under forward bias  $V = 0.5$  V, i.e. the distributions of the carriers are described by qFLs. The input parameters for these simulations are given in Table A.4.

in Figure 8.7, an acceptor-like defect at the CdS/RIS-interface can not sufficiently represent the experimental data, because it leads to a strong kink in the  $j$ - $V$ -curve (cf. 8.7 a) at defect densities, which are not high enough to strongly contribute to the capacitance under forward bias (Figure 8.7 b).

A defect at the 'new' hetero-interface, the RIS/CIGSe-interface, on the other hand, does not lead to a pronounced kink at the chosen defect densities, but strongly contributes to the capacitance under forward bias.

## Part II: Discussion

In the following, the differently severe effect of these two interface defects on the  $j$ - $V$ - and  $C$ - $V$ -curves is discussed. Generally, a kink in the  $j$ - $V$ -curve is attributed to a barrier for the photo-current [42]. This barrier forms due to the spike at the RIS/CIGSe-interface, which is in both cases amplified by the (partly occupied) interface defects and the resulting interface charges. Due to this barrier, electrons tend to accumulate in the surface area of the absorber layer under forward bias. In Case 1 the interface recombination velocity at the hetero-interface is low, because no defect is present there (see Figure 8.7 c). Therefore a rather strong accumulation of electrons takes place, leading to an upward bending of  $E_{F,n}$  in the surface region of the absorber layer and a flow of electrons back into the absorber where they recombine leading to a reduced photo-current, i.e. the kink [42]. In Case 2 the interface recombination at the hetero-interface is higher due to the defect there (see Figure 8.7 d). Accordingly, fewer electrons accumulate at the interface (since some of them recombine via  $E_{Def,IF2}$ ) and the current flow across the junction is less influenced even under forward bias. At the same time the defect level  $E_{Def,IF1}$  is located too far below  $E_{F,p}^{CdS}$  in the dark to interact

with it during the  $C$ - $V$ -measurement. Therefore it is only interacting with  $E_{F,p}^{\text{RIS}}$  inhibiting a stronger contribution to the capacitance since its charge state cannot be altered as much by the applied AC-voltage (cf. Section 3.2).

The defect at the RIS/CIGSe-IF, on the other hand, is located close to both  $E_{F,p}^{\text{RIS}}$  and  $E_{F,p}^{\text{CIGSe}}$ , in dark. Therefore its charge state is more likely to be altered by the AC-voltage during the  $C$ - $V$ -measurement in dark and therefore strongly contributes to the capacitance under forward bias. Furthermore, the energetic distance of  $E_{\text{Def,IF2}}$  to the closest VBM and CBM is smaller than that of  $E_{\text{Def,IF1}}$  due to the high  $E_g$  of the RIS-layer. Therefore the emission rates of the defect at IF1 are smaller than the ones at IF2 amplifying the described effect.

Note that due to the asymmetrically chosen capture cross sections ( $\sigma_p \gg \sigma_n$ ) in principle both defects strongly interact with  $E_{F,p}$ .

Consequently in the following the acceptor-defect at the newly formed hetero-interface, the RIS/CIGSe-interface is used (if not mentioned otherwise) additionally to the acceptor-like defect at the CdS/RIS-interface (see Figure 8.3 b). Note that the defect density of the latter defect,  $N_{\text{Def,IF1}}$ , is reduced in presence of the RIS-layer and the second interface defect, in order to prevent the kink-formation. This appears reasonable due to the improved growth of the CdS-layer on top of the RIS-layer (cf. Section 6.1).

It should be noted that no direct experimental indication for this additional interface defect has so far been identified. It is merely suggested by the simulations done here, because no other model was found to accurately describe the measured  $j$ - $V$ - and  $C$ - $V$ -curves for both the RbF-PDT and the direct RIS-sample, in common. In principle, a more complicated assumption of e.g. metastable effects could also be attributed to the strong increase of the capacitance under high forward bias. However, this would raise the question of why these metastable effects appear only in samples with RbF-PDT and not in the direct RIS-samples even though the measurement procedure (storing the samples in dark before the  $C$ - $V$ -measurement) was identical for all samples.

The formation of an additional acceptor defect at the alkali-rich RIS/CIGSe-interface, for which the complete device model describes all the samples, hence seems to be more likely than other scenarios. The presence of this defect will have to be further analyzed theoretically by defect calculations and experimentally e.g. by voltage-dependent admittance spectroscopy.

However, as it was pointed out above, the main role of this acceptor within the proposed model is to account for the strong increase of the capacitance under forward bias, while having as little influence on the  $j$ - $V$ -curve as possible. Therefore the main statements of this model regarding the effects of the Rb-conditioning on the  $j$ - $V$ -characteristics of the devices are only weakly affected by the proposal of the acceptor defect. Accordingly, in the next section, the properties of the acceptor defect will be chosen in a way to minimize its influence on the  $j$ - $V$ -characteristics.

## 8.1.5 Interaction of the RIS-Layer and the Interface Defects

### Part I: Results

Figure 8.8 shows the dependence of  $V_{\text{OC}}$ , and Figure 8.9 the dependence of  $FF$  on the properties of the interface defect at IF2 in combination with  $\Delta E_C$  and  $d_{\text{RIS}}$ . Furthermore, Figure 8.10 exemplarily shows the  $C$ - $V$ -curves of two parameter-variations. Please note that for these calculations the defect at IF1 was removed in order to be able to isolate the effect of only the defect at the RIS/CIGSe-interface (cf. Table A.5 and Figure 8.11 b).

In general  $V_{\text{OC}}$  is rather weakly dependent on  $N_{\text{Def,IF2}}$  but stronger on  $E_{\text{Def,IF2}}$  and – in parallel to what is already discussed above – the CBM-offset towards the CdS buffer layer. The  $FF$  on the other hand strongly depends on both the energetic position and the density of the interface defect. Furthermore, this interface defect can dominate the capacitance measured at positive bias voltages (cf. Figure 8.10) if it is located in a range of roughly  $200 \text{ meV} < E_{\text{Def,IF2}} < 450 \text{ meV}$  from the VBM of the absorber layer.

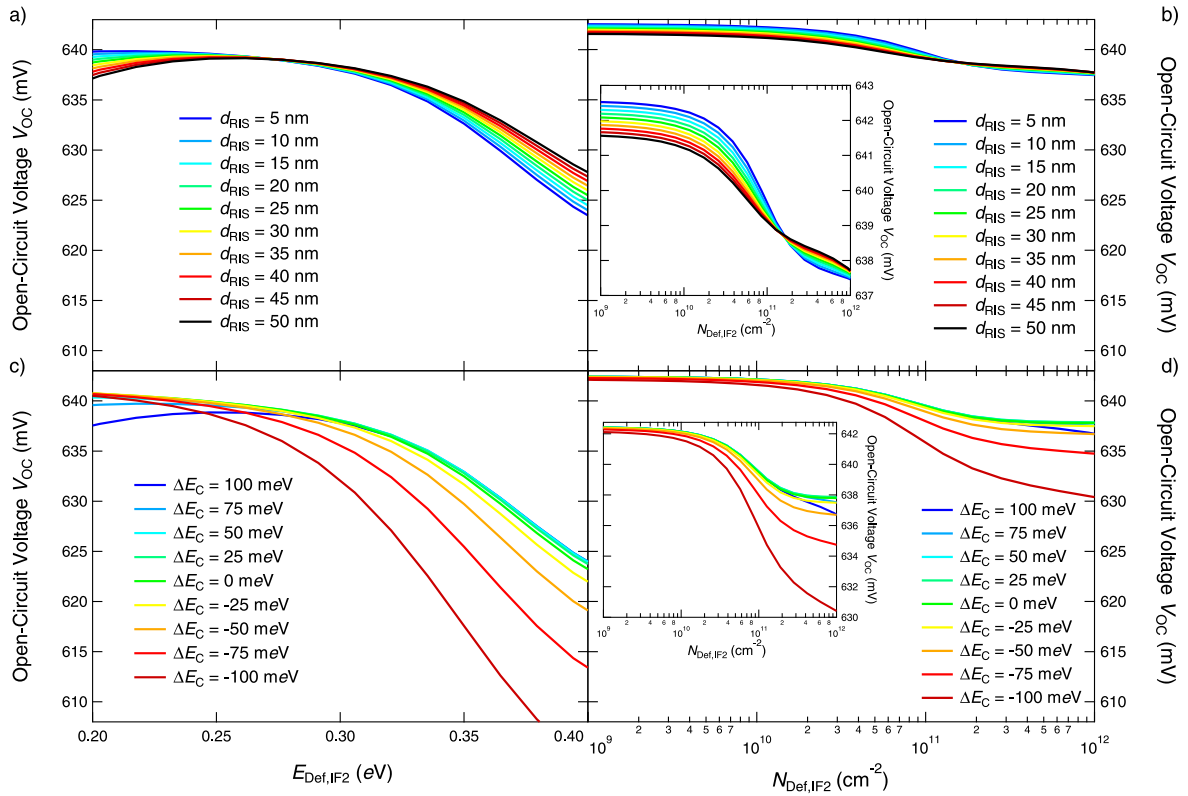


**Figure 8.8:** Dependence of  $V_{OC}$  on the interplay of the properties of the acceptor-like point defect at the RIS/CIGSe-interface and of the RIS-layer. a) Effect of  $d_{RIS}$  and the energetic position of the interface defect  $E_{Def,IF2}$ , b) effect of  $d_{RIS}$  and the defect density  $N_{Def,IF2}$ , c) effect of the electron affinity of the RIS-layer and the energetic position of the interface defect  $E_{Def,IF2}$ , d) effect of the electron affinity of the RIS-layer and the defect density. The insets in b) and d) show the same data with a differently scaled  $y$ -axis. If not varied, the following applies:  $d_{RIS} = 10$  nm and  $\Delta E_C = 75$  meV,  $N_{Def,IF2} = 3 \cdot 10^{11}$  cm $^{-2}$ , and  $E_{Def,IF2} = 300$  meV (cf. also Table A.5).

Additionally, several interesting effects can be noted:

- First, it is interesting to note that – next to the expected loss of  $FF$  and  $V_{OC}$  for high defect densities – in case of the variation of  $E_{Def,IF2}$ ,  $V_{OC}$ , and  $FF$  show opposing trends:  $V_{OC}$  decreases and  $FF$  increases with increasing  $E_{Def,IF2}$ . The trend of  $FF$  with  $E_{Def,IF2}$  can be explained by the occurrence of a kink in the  $j$ - $V$ -curve for low  $E_{Def,IF2}$  (see Figure 8.11 a) analogously to the discussion regarding the defect at the CdS/RIS-interface in the previous section. As can be seen from the comparison of the energy band diagram of two different  $E_{Def,IF2}$  under illumination and forward bias in Figure 8.11 b, an interface defect closer to the VBM does indeed lead to a stronger electron barrier, because it is located closer to the VBM, making it a less effective recombination center. With increasing  $d_{RIS}$  this barrier becomes wider, further decreasing  $FF$ .
- The opposing trend of  $V_{OC}$  at low  $E_{Def,IF2}$ , i.e. a decreasing  $V_{OC}$  with higher  $d_{RIS}$  (see Figure 8.11 a), is accompanied by a second effect: The trends of  $V_{OC}$  with increasing  $d_{RIS}$  and  $\Delta E_C$  invert at about  $E_{Def,IF2} \approx 280$  meV and also at defect densities of about  $N_{Def,IF2} \approx 2 \cdot 10^{11}$  cm $^{-2}$  (see Figure 8.8). At higher  $E_{Def,IF2}$  or  $N_{Def,IF2}$  respectively,  $V_{OC}$  increases with higher  $d_{RIS}$ . An analysis of the recombination currents shows that an increasing  $d_{RIS}$  in presence of this interface defect leads to a higher recombination rate in the bulk of the absorber layer as well as to a decreased recombination velocity at the interfaces (not shown). At low  $E_{Def,IF2}$  and/or low  $N_{Def,IF2}$  the effect of  $d_{RIS}$  on the bulk recombination is dominant and therefore decreasing  $V_{OC}$ , while at high  $E_{Def,IF2}$  and/or  $N_{Def,IF2}$  the reduction of the interface recombination velocity with  $d_{RIS}$  is dominant, increasing  $V_{OC}$ .

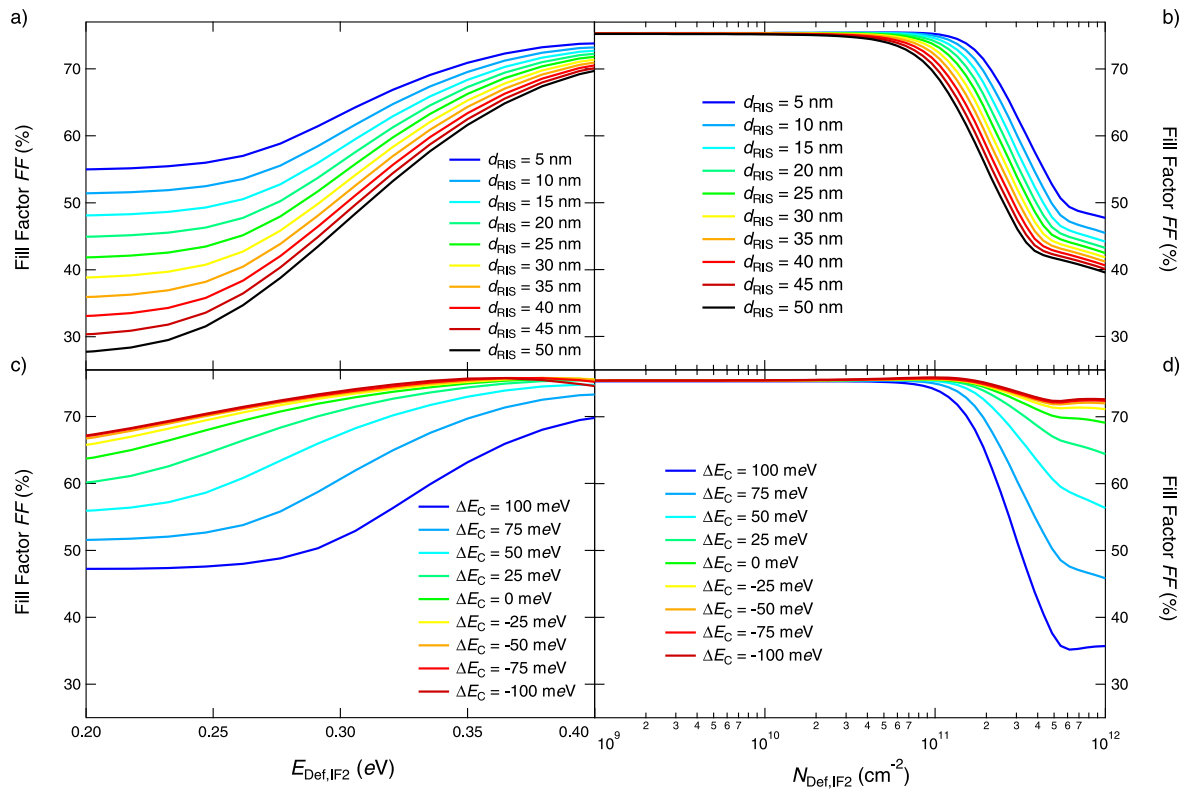


**Figure 8.9:** Dependence of  $FF$  on the interplay of the properties of the acceptor-like point defect at the RIS/CIGSe-interface and the RIS-layer. a) effect of  $d_{RIS}$  and  $E_{Def,IF2}$ , b) effect of  $d_{RIS}$  and  $N_{Def,IF2}$ , c) effect of  $\Delta E_C$  and  $E_{Def,IF2}$ , d) effect of  $\Delta E_C$  and  $N_{Def,IF2}$ . If not varied, the following applies:  $d_{RIS} = 10$  nm and  $\Delta E_C = 75$  meV,  $N_{Def,IF2} = 3 \cdot 10^{11}$  cm $^{-2}$ , and  $E_{Def,IF2} = 300$  meV (cf. also Table A.5).

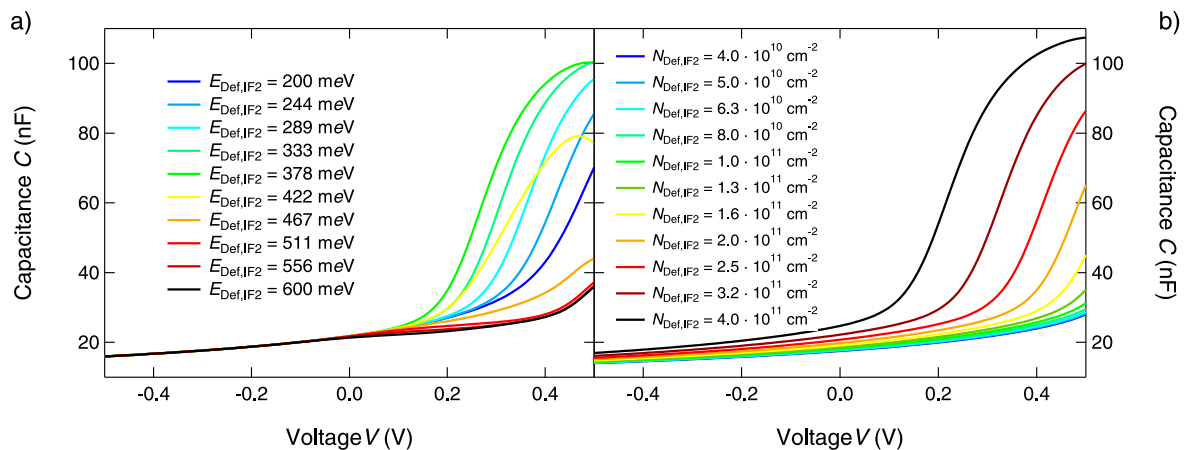


**Figure 8.10:** Examples of simulated  $C$ - $V$ -curves for a) different energetic positions of the interface defect for a defect density of  $N_{Def,IF2} = 3 \cdot 10^{11}$  cm $^{-2}$  and b) different defect densities for an energetic position of the defect of  $E_{Def,IF2} = 300$  meV. In both cases  $d_{RIS} = 10$  nm and  $\Delta E_C = 75$  meV was chosen (cf. Table A.5).

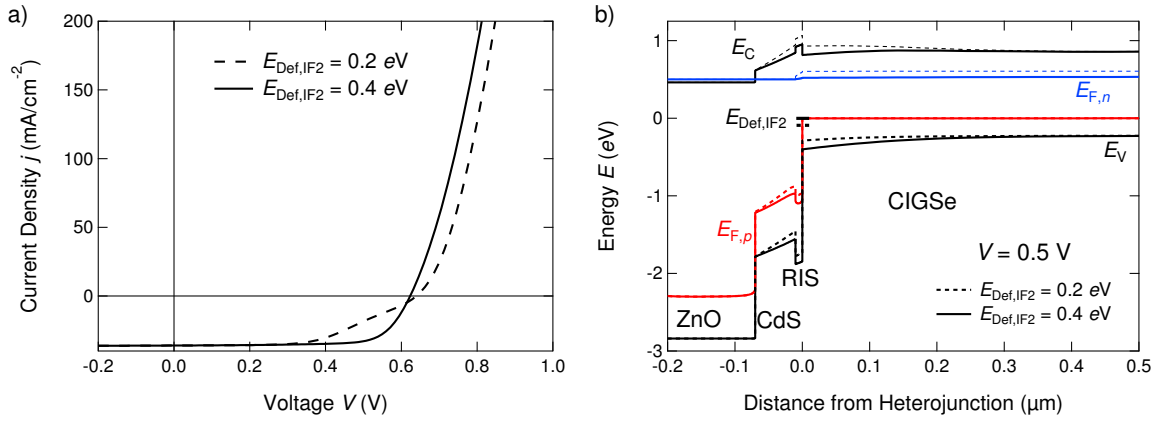


**Figure 8.11:** Example of how a variation of  $E_{\text{Def,IF2}}$  induces a pronounced kink of the  $j$ - $V$ -curve (a) due to the amplification of an electron barrier at the hetero-interface. b) shows the respective energy band diagram under illumination and forward bias. The input parameters for these simulations are given in Table A.6.

It is proposed that these effects of the interface defect on the recombination are due to these two opposing trends with increasing  $d_{\text{RIS}}$ :

On the one hand, an increasing  $d_{\text{RIS}}$  slightly reduces the width of the SCR in the absorber layer following Equation 2.7, because of the low carrier concentration in the RIS-layer compared to the CdS and the window layer (in the chosen parameter set). Due to the decreasing width of the SCR, the effective collection length  $L_{\text{eff}}$  is decreased leading to a slightly increased recombination current in the QNR (cf. Equation 2.20).

On the other hand, a thicker RIS-layer reduces the probability of recombination via the defect at the RIS/CIGSe-interface across the interface (e.g. of holes in the VBM of the absorber layer and electrons in the CBM of the RIS or the CdS) leading to the observed decrease of the interface recombination current.

The proportions of these two effects are determined by the severity of the interface recombination. This means that the latter effect is more dominant at higher  $E_{\text{Def,IF2}}$ ,  $N_{\text{Def,IF2}}$ , and/or in case of negative  $\Delta E_C$ , while the effect of  $d_{\text{RIS}}$  on the width of the SCR is more dominant at lower  $E_{\text{Def,IF2}}$ ,  $N_{\text{Def,IF2}}$ , and/or in case of positive  $\Delta E_C$ , which explains the observed trends in Figure 8.8.

- The third interesting effect appears in the evolution of the capacitance with increasing  $E_{\text{Def,IF2}}$  (Figure 8.10 a). While the effect of  $N_{\text{Def,IF2}}$  on the capacitance is straightforward,  $C$  increases for  $E_{\text{Def,IF2}} \lesssim 350$  meV and decreases for higher  $E_{\text{Def,IF2}}$ . This is due to the fact that when changing the energetic position of the interface defect, it is displaced relative to  $E_{F,p}$  in the dark as can be seen in Figure 8.7 d. The farther below or above  $E_{F,p}$  the defect is located, the smaller its overlap with the Fermi-distribution of the holes and therefore its response to the AC-voltage, i.e. if the defect is too far from  $E_{F,p}$  its charge state is not altered by the AC-voltage anymore.

## Part II: Combined Discussion

As it was already discussed in Sections 4.1.1 and 5.2 the device model has to be able to fit the phenomenon of an increasing capacitance together with a higher carrier lifetime and an improved  $V_{\text{OC}}$  after the RbF-PDT. As it appears from these simulations, an interface acceptor at a position of  $E_{\text{Def,IF2}} = 300$  meV with a density in the order of magnitude of  $10^{11}$  cm<sup>-2</sup> would show a similar capacitance response as the measured one, while having only limited effect on  $V_{\text{OC}}$ . Such a defect could be the origin of the observed trend in the  $C$ - $V$ -curves and would not significantly reduce the gain in  $V_{\text{OC}}$ , which can be obtained e.g. by adapting the carrier lifetime in the bulk or the carrier density in the CIGSe to the experimental values. At the same time, such an interface defect amplifies the effect of the RIS-layer on  $FF$ , which has to be kept in mind when analyzing the results of this device model.

For the fits of the experimentally derived  $j$ - $V$  and  $C$ - $V$ -curves of the Rb-conditioned devices in Section 8.2, this interface defect will therefore be used with its energetic position fixed to  $E_{\text{Def,IF2}} = 300 \text{ meV}$  and the defect density of this interface defect,  $N_{\text{Def,IF2}}$ , as a free fit parameter.

In summary, the presented simulations support the experimental results that the beneficial effects of the Rb-conditioning of CIGSe absorbers with  $\text{CGI} = 0.9$  on  $V_{\text{OC}}$  are likely to be caused by effects in the bulk. The surface-modification due to the RbF-induced compositional changes, on the other hand, do not seem to play a significant role for the  $V_{\text{OC}}$ -gain but are mainly affecting  $FF$  – at least in the chosen, one-dimensional model. However, the modeling of the Rb-conditioned devices in Section 8.2 will be used for further discussion of these individual contributions.

### 8.1.6 Interface Effects of the Rb: Roll-Over

The last important feature to be modeled is the roll-over effect of the  $j$ - $V$ -curve at high bias voltages (cf. Figure 4.7), which is present after an RbF-PDT but not visible after a direct RIS-deposition. Generally, a roll-over is associated with either an electron blocking barrier at the buffer/window-interface, a hole blocking barrier at the back contact, or with the formation of acceptor-like point defects at the CdS/ZnO-interface [42].

In principle, the latter case can indeed fit the experimental data of an RbF-treated device as it was shown in Publication [1], and the assumption of the formation of acceptor states in ZnO due to Rb point defects is theoretically and experimentally proven [268–270], which might justify the proposal of acceptor states at the CdS/ZnO-interface as well. However, this scenario cannot explain the absence of the roll-over effect in case of the direct RIS-deposition. As it was shown in Section 5.2, the accumulation of Rb at the surface of the absorber layer (e.g. the RIS-layer) after the direct RIS-deposition is comparable to that after an RbF-PDT and should therefore lead to a similar diffusion towards the ZnO-layer, the subsequent formation of acceptor states, and their expression as a roll-over as well. As this is not observed, the origin of the roll-over is assumed to be found in a barrier forming at one of the interfaces of the absorber layer.

In agreement with the theoretical predictions stated in the beginning of this section, it was already shown in Section 5.2 that the RIS-layer itself is not the origin for the roll-over either since even rather thick, directly deposited RIS-layers do not lead to a roll-over. It was therefore proposed that the roll-over originates from an additional barrier forming at the back-contact due to the accumulation of Rb at the CIGSe/MoSe<sub>2</sub>-interface [165, 166] and the corresponding Na-depletion there, which takes place after a PDT but not after the direct RIS-deposition (cf. Figures 4.2 and 5.8).

In order to test this interpretation of the experimental data, Figure 8.12 shows the simulated influence of the barrier height  $\Phi_{\text{BC}}$  of the back contact barrier on the shape of the  $j$ - $V$ -curves. Note that the impact of the RIS-layer (with and without IF-defect) on the shape of the  $j$ - $V$ -curve will be analyzed as well in order to be able to analyze the interaction of the RIS-layer and the barrier at the back contact. The impact of the RIS-layer on the shape of the  $j$ - $V$ -curve, which results in the decreased  $FF$ , is shown in Figure 8.12 a, the impact of  $\Phi_{\text{BC}}$  in absence of a RIS-layer in Figure 8.12 b, and the combinatory influence of RIS-layer and a variation of  $\Phi_{\text{BC}}$  in Figures 8.12 c and d. A higher back contact barrier leads – as expected – to a stronger roll-over of the  $j$ - $V$ -curves, while the RIS-induced  $FF$ -loss is due to a stronger voltage-dependence of the current collection in the fourth quadrant due to its barrier-behavior for the photo-generated electrons (cf. Section 8.1.3). The fact that a barrier height of more than  $\Phi_{\text{BC}} \approx 290 \text{ meV}$  leads to a rather strong, kink-like reduction of  $FF$ , indicates that  $\Phi_{\text{BC}}$  of the real device is lower than  $290 \text{ meV}$  since the  $FF$ -reduction in case of the real device is not accompanied by such a strong kink-like development of the  $j$ - $V$ -curve (cf. Figure 4.7).

Even if combined with the back contact barrier, the simple presence of the RIS-layer does

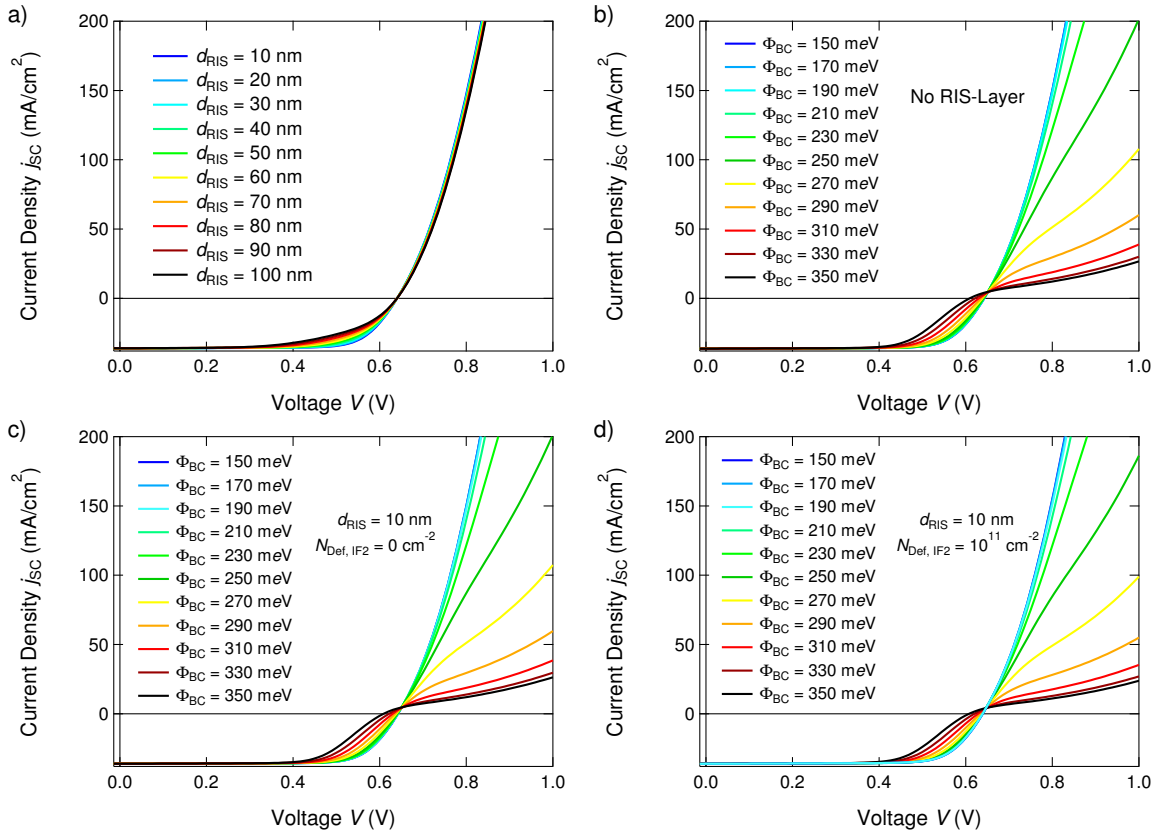


**Figure 8.12:** a) Simulated influence of the RIS-thickness on the shape of the  $j$ - $V$ -curves of a device without any barrier at the back contact. The  $FF$ -loss originates from a stronger voltage-dependence of the collection in the fourth quadrant and does not lead to a roll-over. b)-d) Influence of the barrier height of the back contact barrier on the shape of the  $j$ - $V$ -curve in absence of a RIS-layer (b), together with a 10 nm thick RIS-layer (c) and together with a 10 nm thick RIS-layer and the interface defect at  $E_{\text{Def,IF2}} = 300$  meV (d). The input parameter sets are given in Table A.7.

not influence the severity of the roll-over effect (Figure 8.12c). Adding a defect to the RIS/CIGSe-interface, however, leads to a stronger manifestation of the roll-over if present in a device with a high back contact barrier in comparison to the same device without the RIS-layer (compare Figures 8.12 b and d).

The interplay of the back contact barrier with the defect density is therefore analyzed in more detail in Figures 8.13 a, c, and e. Additionally, the interplay of the back contact barrier and the absorber doping are shown in Figures 8.13 b, d, and f.

The variation of both the density of the interface defect and the doping of the absorber layer, does not influence the occurrence/severity of the roll-over effect in case of a moderate barrier height at the back contact. Once the barrier is more pronounced, both do have an impact on the roll-over though.

In case of the higher  $N_{\text{Def,IF2}}$ , a second barrier is forming at this IF due to the additional charge in the defect (once the voltage is high enough that  $E_{\text{Def,IF2}} > E_{F,p}$  and the defect is fully occupied) and its interaction with the band bending due to the SCR at the back contact, leading to a decreased hole current (see Figure 8.13 e). Since this effect is not easily visible in Figure 8.13 e, the energy band diagrams of a scenario with a very high  $N_{\text{Def,IF2}}$  for two different  $\Phi_{\text{BC}}$  is shown in Figures 8.13 g and h. Hereby both figures show the same scenario, but in Figure 8.13 h the energy bands of both diagrams are intentionally shifted so that the  $E_{F,p}$  are at the same position in the SCR. Here it becomes more obvious that the barriers at the front interface and the back contact influence each other and that the band bending due to the back contact barrier affects the relative positions of  $E_{\text{Def,IF2}}$  and  $E_{F,p}$  which leads to a second, hole blocking barrier at the front interface amplifying the roll-over.

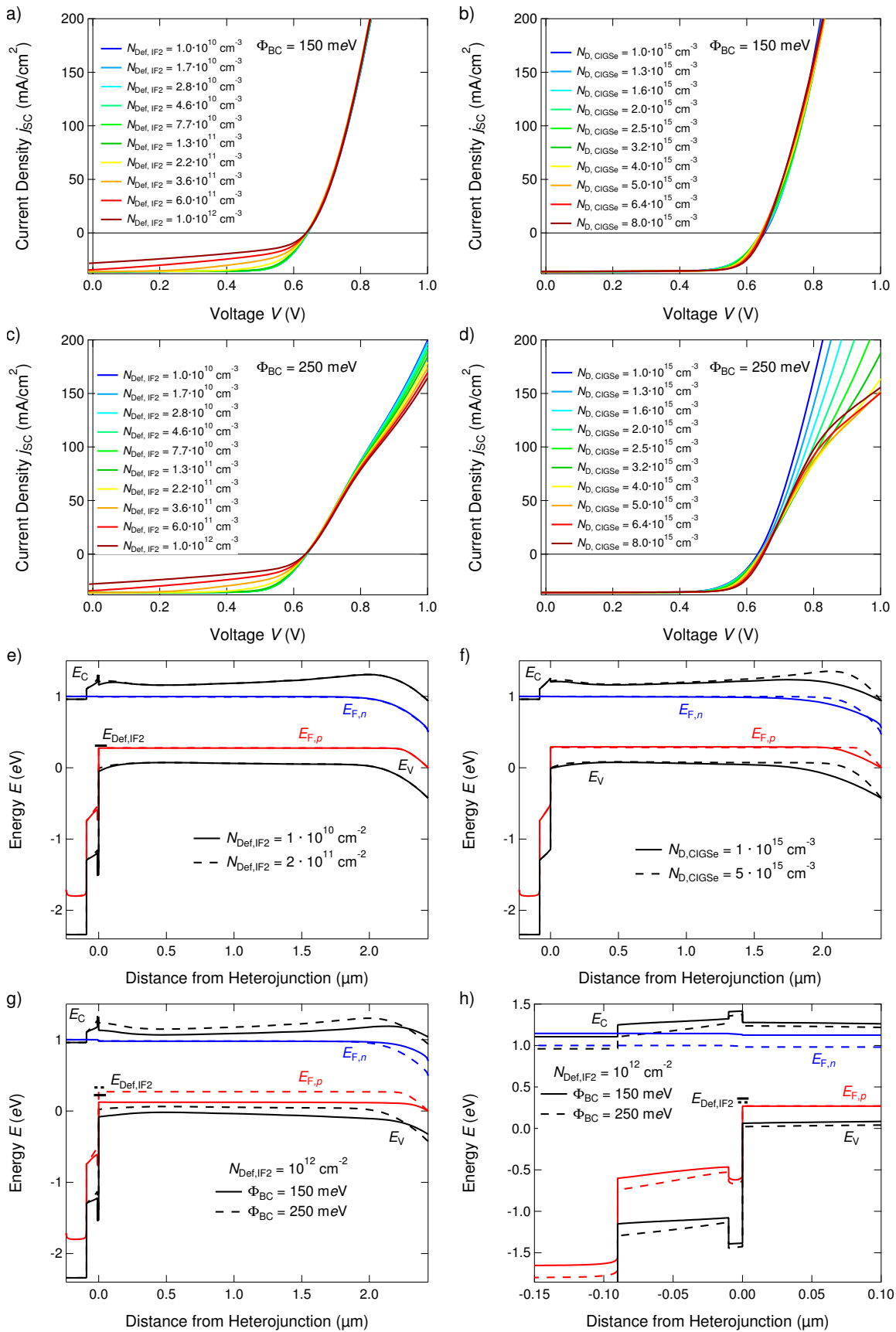


**Figure 8.13:** Dependence of the simulated  $j$ - $V$ -curves on the density of the defect at the RIS/CIGSe-interface (a and b) as well as  $N_{\text{D,CIGSe}}$  (c and d) for configurations with two different  $\Phi_{\text{BC}}$ . e) and f) show the energy band diagrams with  $\Phi_{\text{BC}} = 250 \text{ meV}$  at a bias voltage of 1 V for two exemplary situations (see legends), while g) and h) show it for a fixed  $N_{\text{Def,IF2}}$  for two different barrier heights. Note that h) just shows a close-up of the region of the hetero-junction of the same energy band diagram as shown in g). However, in h) all energy bands were shifted so that the  $E_{\text{F,p}}$  in the SCR of both scenarios are at the same level in order to demonstrate the effect of the back contact barrier. The corresponding parameter sets are shown in Table A.8.

In case of high  $N_D^{\text{CIGSe}}$  the amplification of the roll-over is not due to a direct amplification of the hole barrier at the back contact, but due to the formation of an additional electron barrier under high forward bias. A similar barrier for the electrons as for the holes forms in the absorber layer close to the back contact. Even for small increases of  $N_{D,\text{CIGSe}}$ , the width of the second SCR (at the back contact) is noticeably narrower (cf. Equation 2.5 and Figure 8.13 f). Together with the increasing bandgap energy towards the back contact and the strong band bending in the SCR due to the back contact barrier, the VBM is shifted upwards leading to a similar gradient of  $E_{F,n}$  blocking the electron current.

In summary, the roll-over effect after an RbF-PDT can be explained by an increased height of the back contact barrier, just as it was assumed in the experimental part of this work. The manifestation of this barrier in the  $j$ - $V$ -curve is not only dependent on the barrier height itself, which will be included as an additional fit-parameter into the device modeling, but multiple parameters can have further influence, once  $\Phi_{\text{BC}}$  is in the range of about 200 meV.

Generally, the impact of the input parameters on  $V_{\text{OC}}$ ,  $FF$  as well as the shape of the  $j$ - $V$ - and the  $C$ - $V$ -curves are obviously manifold and interdependent. Therefore, a full decoupling of the effects of the individual parameters is hardly possible and the interaction of all parameters has to be kept in mind during the fitting of the experimental data. For the final device modeling, which is presented in the next section, the following parameters were used as free fit parameters:  $N_{\text{Def,B}}$ ,  $N_D^{\text{CIGSe}}$ ,  $d_{\text{RIS}}$ ,  $\Delta E_C$ ,  $N_D^{\text{RIS}}$ ,  $N_{\text{Def,IF2}}$ , and  $\Phi_{\text{BC}}$ . The fitting procedure is described in Section 3.2.3.

## 8.2 Modeling the Rb-Conditioned Devices

### Part I: Results

In this section the reference model that was described in Section 8.1 is extended to include all the Rb-induced effects described above:

- the reduction of  $\Delta V_{\text{OC}}^{\text{CV}}$  by an increased  $N_D^{\text{CIGSe}}$ ,
- the reduction of  $\Delta V_{\text{OC}}^{\text{rem}}$  by the passivation of the deep defect in the bulk of the CIGSe,
- the reduction of  $\Delta V_{\text{OC}}^{\text{rem}}$  by the passivation of the interface defect at the CdS/CIGSe-interface (via the introduction of the RIS-layer),
- an additional contribution to the capacitance under forward bias as well as a small contribution to  $\Delta V_{\text{OC}}^{\text{rem}}$  due to the newly introduced defect at the RIS/CIGSe-interface,
- the  $FF$ -loss due to the formation of the RIS-layer, which is amplified by the additional interface defect at the RIS/CIGSe-interface,
- the occurrence of a roll-over effect caused by the increased  $\Phi_{\text{BC}}$ ,

as well as the interaction of all these properties.

Using the measured  $j$ - $V$ - and  $C$ - $V$ -curves of an RbF-treated device with  $\text{CGI} = 0.9$  (the device with  $t_{\text{PDT}} = 10$  min that was discussed in Section 4.1) as well as a device with  $\text{CGI} = 0.95$  and a directly deposited RIS-layer (the device with  $t_{\text{RIS}} = 4$  min that was discussed in Section 5.2) were fitted. Figure 8.14 a shows the resulting energy band diagram of the RbF-treated device and Figure 8.14 b that of the 'RIS-deposition'-device in comparison to that of the Rb-free reference. The resulting fits together with the experimental  $j$ - $V$ -curves are displayed in Figure 8.14 e; Figure 8.14 f shows the results of the measured and simulated  $C$ - $V$ -curves. A comparison of the experimentally derived parameters with the simulated parameters is shown in Table 8.1.

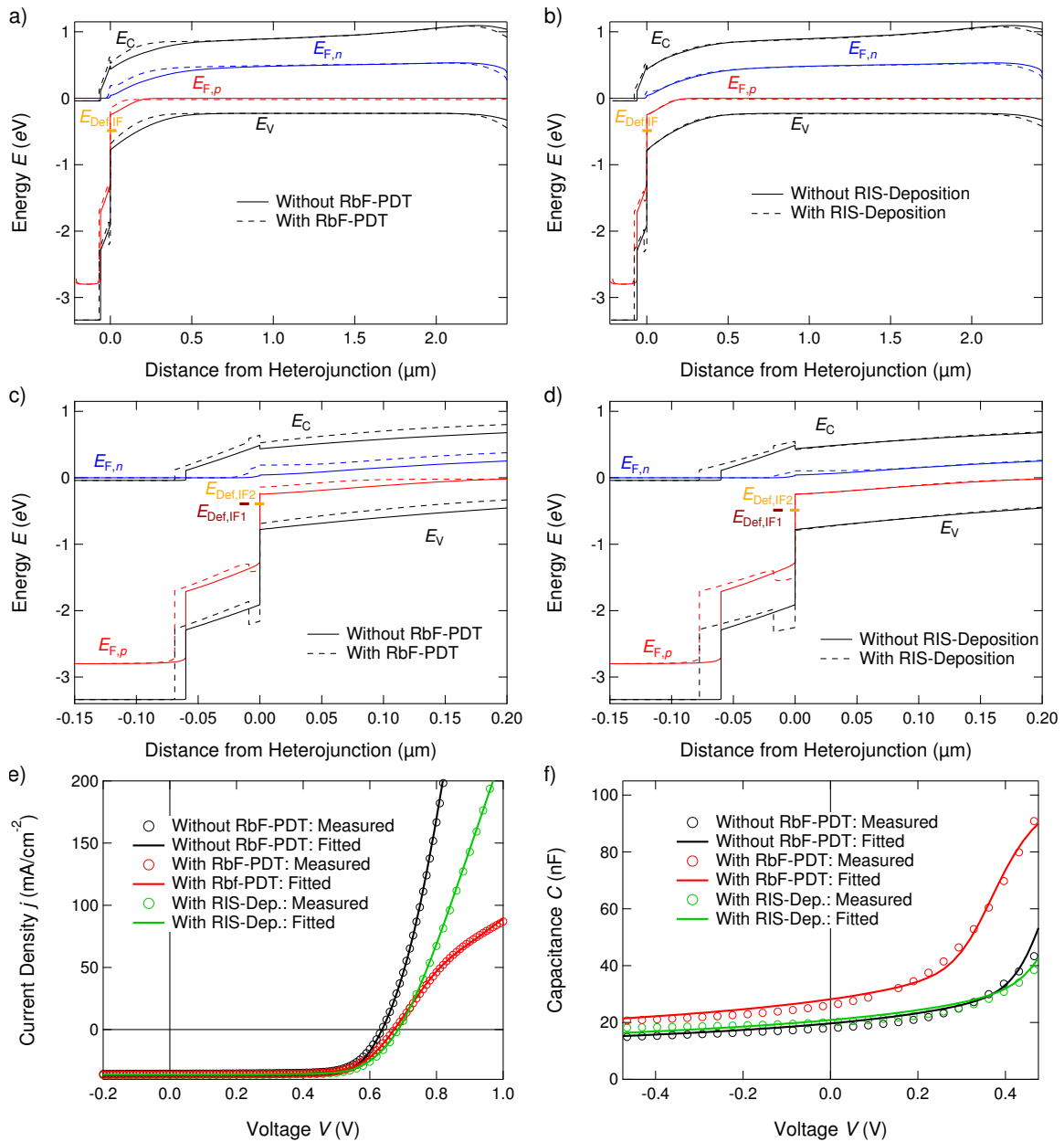


**Figure 8.14:** a) Energy band diagram of the layer stack used to fit the  $j$ - $V$ - and  $C$ - $V$ -curves of the reference device (solid lines) and the RbF-treated device (dashed lines). b) Band diagram of the same reference device (solid lines) in comparison to that used to fit the data of the device based on the absorber layer with 4 min RIS-deposition (dashed lines). c) and d) show the same energy band diagrams, but scaled to a close-up view of the heterojunction. The interface defects shown in c) and d) represent the case of the respective Rb-conditioned device model. For the reference model without the RIS-layer, there is only one interface defect at the position of  $E_{\text{Def,IF1}}$ , which is at the CdS/CIGSe-interface in that case. Results of the corresponding fits in comparison with the experimentally derived  $j$ - $V$ -curves are shown in e) and the respective  $C$ - $V$ -curves in f).

Table 8.1: The PV-parameters and key properties of the simulated and the real devices that correspond to the  $j$ - $V$  and  $C$ - $V$ -curves shown in Figure 8.14.  $S_{it}/h_{it}$  depicts the recombination velocity at the heterointerface, that is the CdS/CIGSe-interface in case of the reference sample and the RIS/CIGSe-interface for the other two cases.

\*Note that  $\tau_{exp}^{low}$  of the Rb-free reference of the respective experiment is about 10 ns. The origin for this deviation of this experiment is discussed in Section 3.2.

	Reference		RbF-PDT (CGI = 0.9)		RbF-PDT (CGI = 0.9)		4 min RIS		4 min RIS	
	Measured	Simulated	Measured	Simulated	Measured	Simulated	Measured	Simulated	Measured	Simulated
$E_{Def,B}$ (eV above VBM)	-	0.5	-	0.5	-	0.5	-	0.5	-	0.5
$N_{Def,B}$ (cm <sup>-3</sup> )	-	$1.1 \cdot 10^{14}$	-	$4.9 \cdot 10^{13}$	-	$4.9 \cdot 10^{13}$	-	$3.4 \cdot 10^{13}$	-	$3.4 \cdot 10^{13}$
$\sigma_{e,B}$ (cm <sup>2</sup> )	-	$1.8 \cdot 10^{-14}$	-	$1.8 \cdot 10^{-14}$	-	$1.8 \cdot 10^{-14}$	-	$1.8 \cdot 10^{-14}$	-	$1.8 \cdot 10^{-14}$
$\sigma_{h,B}$ (cm <sup>2</sup> )	-	$1.0 \cdot 10^{-15}$	-	$1.0 \cdot 10^{-15}$	-	$1.0 \cdot 10^{-15}$	-	$1.0 \cdot 10^{-15}$	-	$1.0 \cdot 10^{-15}$
$\tau_{eff}$ (ns)	-	48	-	110	-	110	-	160	-	160
$\tau_{exp}^{low}$ (ns)	34	-	180	-	56*	-	-	-	56*	-
$n_{CV}^{CIGSe} / N_D^{CIGSe}$ (cm <sup>-3</sup> )	$1.5 \cdot 10^{15}$	$2.9 \cdot 10^{15}$	$2.9 \cdot 10^{15}$	$5.5 \cdot 10^{15}$	$2.9 \cdot 10^{15}$	$5.5 \cdot 10^{15}$	$2.2 \cdot 10^{15}$	$3.5 \cdot 10^{15}$	$2.2 \cdot 10^{15}$	$3.5 \cdot 10^{15}$
$E_{Def,IF1}$ (eV)	-	0.3 above $E_V^{CIGSe}$	-	0.96 eV below $E_C^{CdS}$						
$N_{Def,IF1}$ (cm <sup>-2</sup> )	-	$2.3 \cdot 10^{11}$	-	$6.0 \cdot 10^{10}$						
$\sigma_{e,IF1}$ (cm <sup>2</sup> )	-	$1.8 \cdot 10^{-16}$	-	$1.8 \cdot 10^{-16}$	-	$1.8 \cdot 10^{-16}$	-	$1.8 \cdot 10^{-16}$	-	$1.8 \cdot 10^{-16}$
$\sigma_{h,IF1}$ (cm <sup>2</sup> )	-	$1.2 \cdot 10^{-14}$	-	$1.2 \cdot 10^{-14}$	-	$1.2 \cdot 10^{-14}$	-	$1.2 \cdot 10^{-14}$	-	$1.2 \cdot 10^{-14}$
$S_{it,IF1}$ (cm/s)	-	$4.1 \cdot 10^2$	-	$1.1 \cdot 10^2$	-	$1.1 \cdot 10^2$	-	$1.1 \cdot 10^2$	-	$1.1 \cdot 10^2$
$S_{it,IF1}$ (cm/s)	-	$2.6 \cdot 10^4$	-	$7.2 \cdot 10^3$						
$E_{Def,IF2}$ (eV)	-	-	-	0.3 above $E_V^{CIGSe}$						
$N_{Def,IF2}$ (cm <sup>-2</sup> )	-	-	-	$2.2 \cdot 10^{11}$	-	$2.2 \cdot 10^{11}$	-	$1.1 \cdot 10^{11}$	-	$1.1 \cdot 10^{11}$
$\sigma_{e,IF2}$ (cm <sup>2</sup> )	-	-	-	$1.8 \cdot 10^{-16}$						
$\sigma_{h,IF2}$ (cm <sup>2</sup> )	-	-	-	$1.2 \cdot 10^{-14}$						
$S_{it,IF2}$ (cm/s)	-	-	-	$3.9 \cdot 10^2$	-	$3.9 \cdot 10^2$	-	$2.0 \cdot 10^2$	-	$2.0 \cdot 10^2$
$S_{it,IF2}$ (cm/s)	-	-	-	$2.6 \cdot 10^4$	-	$2.6 \cdot 10^4$	-	$1.3 \cdot 10^4$	-	$1.3 \cdot 10^4$
$\Phi_{BC}$ (meV)	-	152	-	272	-	272	-	248	-	248
$d_{RIS}$ (nm)	-	-	-	9	-	9	-	18	-	18
$\Delta E_C$ (meV)	-	-	-	53	-	53	-	61	-	61
$N_D^{RIS}$ (cm <sup>-3</sup> )	-	-	-	$1.0 \cdot 10^{14}$						
$j_{sc}$ (mA/cm <sup>2</sup> )	35.5	36.4	36.1	36.0	36.1	36.0	36.5	36.1	36.5	36.1
$V_{OC}$ (mV)	636	637	673	673	673	673	685	685	685	685
$\Delta V_{OC,Ref}^{CV} - \Delta V_{OC}^{CV}$ (mV)	-	-	8 (A = 1) to 17 (A = 2)	5 to 8	5 (A = 1) to 10 (A = 2)	5 to 8	5 (A = 1) to 10 (A = 2)	1 to 3	5 (A = 1) to 10 (A = 2)	1 to 3
$\Delta V_{OC,Ref}^{rem,B} - \Delta V_{OC}^{rem,B}$ (mV)	-	-	-	25 to 35	-	25 to 35	-	37 to 46	-	37 to 46
$\Delta V_{OC,Ref}^{rem,IF} - \Delta V_{OC}^{rem,IF}$ (mV)	-	-	-	-3 to 3	-	-3 to 3	-	0 to 7	-	0 to 7
FF (%)	72.4	74.7	69.5	69.5	69.5	69.5	71.2	71.2	71.2	71.2
$\eta$ (%)	16.3	17.3	16.9	16.9	16.9	16.9	17.8	17.6	17.8	17.6

## Part II: Discussion

The used model accurately describes the behavior of the  $j$ - $V$ -curves, provides the correct trends of the  $C$ - $V$ -curves, and calculates reasonably well fitting PV-parameters in all three cases (Reference, RbF-PDT, and RIS-deposition). However, some remarks have to be made with respect to the values given in Table 8.1:

- As it was already discussed in Section 3.2, the experimentally derived carrier lifetimes  $\tau_{\text{exp}}$  of different experiment series are not quantitatively reliable and therefore not directly comparable. For example, all samples discussed in Section 5.2 showed lower lifetimes than comparable samples in Chapter 4. Therefore one has to keep in mind the measured lifetimes of the respective reference samples when judging the accuracy of the simulations. The reference- and the RbF-PDT-sample used in the simulation both belong to the same experiment series (see Section 4.1). Accordingly, the change in the simulated  $\tau_{\text{eff}}$  ( $\tau_{\text{eff}}^{\text{Ref}} = 48$  ns and  $\tau_{\text{eff}}^{\text{RbF}} = 110$  ns) is in good agreement with the experimentally observed trend ( $\tau_{\text{exp}}^{\text{Ref}} = 34$  ns and  $\tau_{\text{exp}}^{\text{RbF}} = 180$  ns at  $\Delta n = 5.65 \cdot 10^{15} \text{ cm}^{-3}$ ). The fact that the simulated lifetime of the RIS-deposition sample ( $\tau_{\text{eff}} = 160$  ns) is even higher than that of the RbF-PDT sample is not in contrast to the experiment either, considering that the measured lifetime of the corresponding sample is even stronger improved compared to that of the respective reference in Section 5.2 ( $\tau_{\text{exp}}^{\text{Ref}} = 10$  ns and  $\tau_{\text{exp}}^{\text{RIS}} = 56$  ns at  $\Delta n = 5.65 \cdot 10^{15} \text{ cm}^{-3}$ ).
- In all cases, the simulated carrier density of the absorber layer ( $N_{\text{D}}^{\text{CIGSe}}$ ) is rather low compared to some values reported in literature [126, 159]. However, these simulated values are even higher than the experimental  $n_{\text{CV}}$ . It is known that the minimum of the  $N_{\text{CV}}$ -profiles underestimates the real carrier density [210]. Furthermore,  $N_{\text{D}}^{\text{CIGSe}}$  of the simulated devices leads to a good agreement of the simulated  $C$ - $V$ -curves with the experimental ones. Therefore it is concluded that the simulated carrier densities are close to those of the real devices.
- In order to estimate the individual contributions of the reduction due to the Rb-conditioning in  $\Delta V_{\text{OC}}^{\text{CV}}$  as well as of the  $V_{\text{OC}}$ -losses due to SRH-recombination in the bulk ( $\Delta V_{\text{OC}}^{\text{rem,B}}$ ) and at the interfaces ( $\Delta V_{\text{OC}}^{\text{rem,IF}}$ ), the simulations were carried out consecutively adapting only isolated parameters in each run – starting from both the reference and the Rb-conditioned device. That means, in order to estimate the impact of  $\Delta V_{\text{OC}}^{\text{CV}}$  after the RbF-PDT,  $V_{\text{OC}}$  was first calculated using all parameters of the reference device except  $N_{\text{D,CIGSe}} = 5.5 \cdot 10^{15} \text{ cm}^{-3}$  of the RbF-PDT-device and compared to the  $V_{\text{OC}}$  of the reference device (showing a difference of 5 mV). Then  $V_{\text{OC}}$  was calculated using all parameters of the device after RbF-PDT except  $N_{\text{D,CIGSe}} = 2.9 \cdot 10^{15} \text{ cm}^{-3}$  of the reference device and compared to the  $V_{\text{OC}}$  of the RbF-PDT-device (showing a difference of 8 mV).

Due to the described interdependence of all parameters, these values differ from each other – especially in case of  $\Delta V_{\text{OC}}^{\text{rem,IF}}$  due to the complex interface-structure of the model. However, they still provide valuable estimates of the impact of the RbF-conditioning on each loss-mechanism, *within* the proposed device model.

In addition to these estimates Figure 8.15 a shows the simulated recombination currents of the reference device, and Figure 8.15 b the differences of the recombination currents after Rb-conditioning. It can be seen that in all three devices, bulk recombination is the dominant recombination path. This is in good agreement with the general assumption that the dominant recombination path in highly efficient CIGSe-based solar cells is recombination in the bulk of the absorber layer [57, 252, 254]. This observation seems to still be valid for the devices analyzed in this thesis (with and without Rb-conditioning) as well [215].

Consequently the main benefit after RbF-PDT and the direct RIS-deposition according to this model, is a reduction of the bulk recombination. The interface recombination

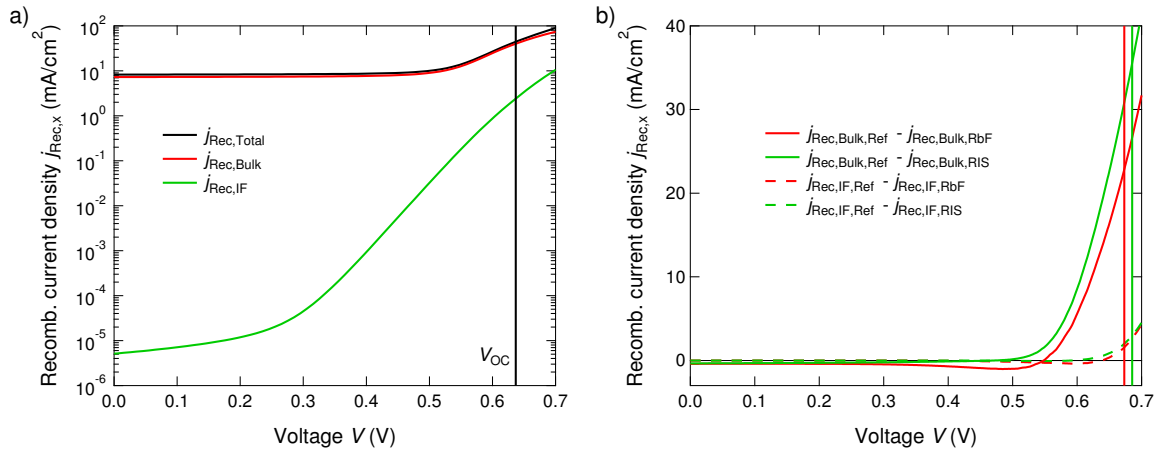


**Figure 8.15:** a) Recombination currents of the simulated reference device. b) Difference between the respective recombination currents for bulk- and interface-recombination of the Rb-conditioned devices and the reference device. The straight lines mark the respective  $V_{\text{OC}}$  (red for the RbF-PDT-device, green for the RIS-device).

current for the simulated device,  $j_{\text{Rec,IF}}$ , is even increased after the RbF-PDT, which is in agreement with the lower boundary of the estimation in Table 8.1.

The direct RIS-deposition, on the other hand, reduces both the bulk- and the interface-recombination. However, considering two- or three-dimensional effects of the formation of the RIS-layer, which were discussed in Section 6.1, a combination of a passivation of interface and bulk defects due to the RbF-PDT seems possible as well.

- In case of the RIS-deposition, the gain in  $V_{\text{OC}}$  due to the Rb-incorporation is predicted by the model to be almost solely due to the reduction of  $\Delta V_{\text{OC}}^{\text{rem,B}}$ , while the share of the reduction of  $\Delta V_{\text{OC}}^{\text{CV}}$  is bigger in case of the RbF-PDT. This is in good agreement with the experimental results.
- As it was already discussed above, the fact that the  $FF$  of the simulated reference device is higher than that of the real device can be explained by  $FF$ -losses due to the mechanical cell scribing of the real device, which is not reproduced in the one-dimensional model. This effect would be expected to occur in case of the RbF- and RIS-devices as well. However, since there are more fit parameters available regulating  $FF$  ( $d_{\text{RIS}}$ ,  $N_{\text{D}}^{\text{RIS}}$ , and  $\Delta E_{\text{C}}$ ), a better fitting of the PV-parameters is possible. In turn, this means that it is likely that the real thickness of the RIS-layer is slightly thinner (and/or its defect density lower and/or  $\Delta E_{\text{C}}$  smaller) and the actual  $FF$  – as it is limited by one-dimensional effects – slightly higher than the results of these simulations indicate.
- The reduction of  $FF$  due to the introduction of the RIS-layer (with its assumed properties) into the device stack and the variation of  $\Phi_{\text{BC}}$  of the back contact barrier can accurately describe the trend of the decreasing  $FF$  after both the RbF-PDT and the direct RIS-deposition, as well as the shape of the respective  $j$ - $V$ -curves in both cases.

Note again that the acceptor like defects at the interfaces were mostly introduced into the model in order to be able to account for the strong increase of the capacitance under forward bias, especially after Rb-conditioning. The properties of the defects were chosen in a way that its effects on the PV-parameters are rather low. The main statements of the model regarding the effects of the Rb-conditioning as stated above and further discussed below are hardly affected by these defects. Even though there are hints for the presence of such defects in literature [212, 261], there is no direct experimental indication for them given in this work. However, several different approaches were tested and none was able to represent the experimentally observed  $C$ - $V$ -curves without inducing strong deviations of the simulated from the measured  $j$ - $V$ -curve.

However, the proposed model may still be but one possibility to reproduce the experimental data, although no similarly accurate fit of them could be obtained with other models, i.e. using other combinations of interface and bulk defects, barriers, etc. To the best of the author's knowledge, there is no model published yet providing similarly accurate fits of experimental  $j$ - $V$ - and  $C$ - $V$ -curves as well as accordance with the experimentally observed trends of  $t_{\text{PDT}}$ ,  $t_{\text{RIS}}$ , and  $CGI$ . In particular, the results of the presented device simulations are in good agreement with all main hypotheses stated in the experimental part of this work:

Regarding  $V_{\text{OC}}$ :

The gain in  $V_{\text{OC}}$  due to Rb-incorporation can be completely described by a reduction of  $\Delta V_{\text{OC}}^{\text{CV}}$  and  $\Delta V_{\text{OC}}^{\text{rem}}$  (the latter mainly due to the passivation of a deep bulk defect). While the RbF-PDT is – according to the presented model – leading to a mixture of beneficial (reduction of  $\Delta V_{\text{OC}}^{\text{CV}}$  and  $\Delta V_{\text{OC}}^{\text{rem,B}}$ ) and detrimental effects (increase of  $\Delta V_{\text{OC}}^{\text{rem,IF}}$ ), the direct RIS-deposition reduces  $\Delta V_{\text{OC}}^{\text{rem,B}}$  even further and additionally passivates the interface defect.

An additional two-dimensional contribution of the RIS:Na-layer, e.g. by improving the homogeneity of the buffer layer, seems possible for both cases, though. This interpretation of the device simulations and the experimental data leads to the conclusion that the direct RIS-deposition, assumingly due to the higher  $T_{\text{Sub}}$ , can be a faster alternative to the traditionally used RbF-PDT.

Even though the used model is able to describe all major trends in the  $C$ - $V$ -curves, more complex defect distributions than the presence of just one deep bulk defect are likely and more sophisticated characterization i.e. by low- $T$  PL and/or deep level optical/transient spectroscopy is needed to identify the exact defect levels. This may affect the extracted values for  $\Delta V_{\text{OC}}^{\text{CV}}$  and  $\Delta V_{\text{OC}}^{\text{rem}}$  slightly. Furthermore, the presence and origin of the postulated acceptor defect at the RIS/CIGSe-interface have to be investigated. The fact that its defect density seems to be higher in case of the RbF-PDT than in case of the direct RIS-deposition might indicate that it is a structural defect, which does not occur at high substrate temperatures or that it is linked to the Na-diffusion, which is different in both cases (see discussion in Section 5.2).

Regarding  $FF$  and the roll-over:

The simulations show that the formation of an increasingly thick (increasing with either  $t_{\text{RbF}}$ ,  $d_{\text{ODC}}$ , or  $t_{\text{RIS}}$ ) RIS-surface layer (or a similar Rb-deficient mixed phase containing Cd, and/or S) can lead to the observed, steady loss in  $FF$ . While the exact thickness of this layer is dependent on the input parameters for its various properties, the general trend of lower  $FF$  with  $d_{\text{RIS}}$  is valid for all tested, realistic parameter combinations.

The formation of the roll-over of the  $j$ - $V$ -curve, on the other hand, is not attributed to this barrier at the heterointerface, which is in good agreement with the experimental results as well.

In fact, the roll-over can be explained by an increase of the back contact barrier height  $\Phi_{\text{BC}}$  due to the Rb-incorporation. Experimentally it seems likely that this increase is due to the strong Rb-accumulation at the CIGSe/MoSe<sub>2</sub>-interface. Following the proposed model, its impact on the  $j$ - $V$ -curve is more pronounced in case of the RbF-PDT compared to the direct RIS-deposition, because of the slightly bigger barrier height (which might be due to the Na-depletion at the back contact) and because of the higher absorber doping and interface defect density  $N_{\text{Def,IF2}}$  in case of the PDT.

However, additional investigations are needed in order to identify the exact origin of the back contact barrier even in the Rb-free reference case and its interaction with Na and Rb.

### 8.3 Evaluating the Device Model in Regard to Literature

The model proposed in this thesis is – to the best of the author’s knowledge – the first device model providing an accurate fit of the  $j$ - $V$ - and  $C$ - $V$ -curves of Rb-free and Rb-conditioned devices and is therefore a clear improvement towards the model that was presented in Publication [7]. The latter does not yet provide an accurate description of the defect distributions (e.g. a fit of the experimental  $C$ - $V$ -curves) nor gives an explanation on the effect of the RbF-PDT on  $FF$ .

The model established in this thesis, however, is able to reproduce and explain both the experimentally derived  $j$ - $V$ - and  $C$ - $V$ -curves, and can furthermore elucidate the effect of both the RbF-PDT as well as the direct RIS-deposition on the optoelectronic properties of the CIGSe-based devices. The main assumption of this model is that the beneficial effect of the Rb-conditioning is almost solely attributable to the bulk of the absorber layer, while its detrimental effects – if present – are attributed to the interfaces. The central elements of the model and the respective (main) influence of the Rb-conditioning on them are:

- The deep defect in the bulk, which defect density is reduced by both the RbF-PDT and the RIS-deposition, mainly improving  $\tau_{\text{eff}}$  and  $V_{\text{OC}}$ .
- The back contact barrier, which barrier height is increased by both the RbF-PDT and the direct RIS-deposition, and therefore leads to a roll-over of the  $j$ - $V$ -curve in case of the RbF-PDT (see next bullet point).
- The carrier density of the absorber layer, which is strongly enhanced by the PDT and less significantly by the direct RIS-deposition. In both cases, this gain has a beneficial influence on  $V_{\text{OC}}$  but in case of the RbF-PDT, it induces the roll-over effect together with the back contact barrier.
- The introduction of the RIS-layer after Rb-conditioning, which has a slightly beneficial effect on  $V_{\text{OC}}$  (see last bullet point) and reduces the  $FF$  in dependence on its thickness.
- The acceptor-like defect at the CdS/CIGSe-interface, which was shifted to the CdS/RIS-interface by the Rb-conditioning and therefore has a reduced influence on the interface-recombination at the heterointerface.
- The introduction of an acceptor defect at the newly formed RIS/CIGSe-interface, which slightly reduces  $V_{\text{OC}}$  and amplifies the effect of the RIS-layer on  $FF$ , leads to the strong capacitance signal at high voltages, and enhances the roll-over effect.

While most studies assume that the RbF-PDT passivates deep defects in the bulk of the CIGSe [7, 159, 160, 164–166, 219] and increases  $n_{\text{CV}}$  [1, 158, 159, 164], they often assign a positive role to the Rb-induced surface modifications as well. So far it was widely assumed that the formation of a wide-bandgap layer at the surface of the CIGSe during the RbF-PDT is reducing the interface recombination velocity and therefore improving  $V_{\text{OC}}$  [128, 146, 147, 157, 168]. There has only been one other study so far (next to Publication [4]), suspecting that this interface layer could – depending on the amount of incorporated Rb – actually be detrimental for device performance [41]. However, in that publication, it was not investigated under which circumstances the effect of the surface modification would be detrimental and beneficial. Therefore the role, which is attributed to the RIS-layer in this thesis, shines new light on the mechanism of the RbF-PDT.

Furthermore, the proposed model is able to resolve a fundamental discrepancy between effects described in different publications. While most studies report an improved  $V_{\text{OC}}$  due to the PDT [1, 40, 157–160], some were reporting a gain in  $FF$  [4, 40, 157, 158, 164], while others showed  $FF$ -losses due to the RbF-PDT [1, 41, 159]. In agreement with the experimental findings presented in this thesis, the proposed device model gives an explanation for this behavior in a broader context. On the one hand, the RbF-PDT has a beneficial influence on

$FF$  just due to the improved  $V_{OC}$  (cf. Equation 2.47), while on the other hand, the RIS-layer is lowering  $FF$ . The latter effect is strengthened by the introduction of the acceptor-like defect at the RIS/CIGSe-interface but is dependent on the exact properties of the RIS-layer anyway. Due to the dependence of  $FF$  on  $d_{RIS}$ , the ratio of the beneficial and detrimental effect of the PDT on  $FF$  according to this model depends on the amount of Rb incorporated into the surface of the absorber layer.

In the experimental part of this thesis, it was shown that the latter is not only influenced by the deposition parameters of the PDT, but also by the integral  $CGI$  of the absorber layer. Since the 'standard'  $CGI$  of the CIGSe is different in different laboratories, this could explain the contradictory results published regarding the PDT's effect on  $FF$ . However, a detailed analysis of these literature data is impeded since not all publications mention the  $CGI$ . Furthermore, even in cases the  $CGI$  is given, a comparison of samples from different laboratories is difficult since an accurate determination of the composition is challenging and often different results are obtained depending on the used method (compare e.g. the differences between SEM-EDX and GD-OES in Section 4.2).

In conclusion, the proposed device model is not only able to reproduce all effects of the RbF-PDT and the RIS-deposition as well as the trends of the variation of  $t_{RbF}$ ,  $CGI$ , and  $t_{RIS}$  in the three presented experiment series, but is compatible with the data published in literature and able to potentially resolve discrepancies between results of different labs and therefore provides a more general understanding of the Rb-conditioning. In order to further support the latter statement, a critical evaluation of the model in a comprehensive comparison of devices from different labs is desired.

## 9 Summary and Conclusions

The primary goal of this work is to understand the mechanism behind the Rb-conditioning of CIGSe absorber layers on both the level of material properties of the thin film as well as on the level of the optoelectronic properties of the complete device. It is desired to elucidate under which circumstances the Rb-conditioning enables to improve the power conversion efficiency of the devices in order to be able to optimize the Rb-supply and to adapt it to future developments. Using a combination of several characterization methods as well as one-dimensional device simulations, a comprehensive model explaining both the beneficial and detrimental effects of the RbF-PDT under various process conditions is proposed for the first time. Furthermore, this model enables to resolve apparent contradictions regarding the effect of the PDT that were published in the literature. Finally, the application of this model allows for an adaptation of the procedure for a further improvement of the Rb-incorporation.

The most established way of conditioning a CIGSe absorber layer with Rb is the RbF-PDT. The main effect of the PDT hereby is a gain in  $V_{OC}$ , which the present work could attribute to a combination of several effects.

First, the RbF-PDT induces a Na-Rb exchange, which leads to an increased carrier density of the CIGSe absorber layer for an optimized PDT. Together with results from literature, it is proposed that this Rb-Na exchange mechanism works via the accumulation of Rb at the GBs leading to an in-diffusion of additional Na into the GI. The additional Na in the GI might be the reason for the improved carrier density – e.g. by the creation of additional  $V_{Cu}$  or by passivating a higher number of  $In_{Cu}$ .

Secondly, it is shown that the RbF-PDT leads to a higher carrier lifetime and a slight reduction of the Urbach-energy – presumably due to the passivation of a deep defect in the bulk and tail states in the energy bandgap. Since the latter effect is rather small, while the carrier lifetime is strongly improved by the RbF-PDT, a passivation of a deep point defect is assumed to be the main factor improving the  $V_{OC}$ . Although the accumulation of Rb at the GBs (e.g. shown in this work by TEM) suggests a passivating effect there, future work is needed in order to determine the exact position – in the GI or at the GBs – and in the latter case, the properties of such Rb-passivated GBs and their vicinity.

Furthermore, the RbF-PDT induces the growth of a nanopatterned, secondary  $In_xSe_y:(Rb,Na)$ -film on top of the absorber layer, which in the literature is assumed to additionally reduce the interface recombination velocity. Since one-dimensional device simulations were used to model the effects of the RbF-PDT within this work, the exact influence of the nanopatterning on the interface-recombination was not investigated. However, the aforementioned device model predicts the one-dimensional influence of the  $In_xSe_y:(Rb,Na)$ -layer on  $V_{OC}$  to be insignificant compared to that of the bulk effects.

For the first time, this work revealed that the effectiveness of the PDT strongly depends on the composition of the underlying CIGSe – i.e. on the Cu-content of the absorber layer. Only within the high efficiency regime of the composition of the CIGSe ( $0.8 < CGI < 0.95$ ) the described effects of the RbF-PDT improve the  $V_{OC}$  of the devices. On samples with lower Cu-content, the PDT deteriorates  $V_{OC}$  due to a reduction of the carrier density, whereas a reduced SRH-recombination rate due to Rb seems to occur for all  $CGI$ .

Taking into account theoretical predictions from literature, the  $CGI$ -dependence of the Rb-induced gain of  $n_{CV}$  is proposed to originate from an interaction of Rb, Na, and  $V_{Cu}$ . At  $CGI < 0.80$ , the absorber layer naturally exhibits a higher number of Cu-vacancies. Therefore the diffusivity of Rb into the lattice of the CIGSe increases and Rb is proposed to not only accumulate at the GB but also to occupy part of these  $V_{Cu}$  within the lattice of the CIGSe.

This, in turn, is proposed to reduce the amount of Na in the GI and therefore the probability of the formation of  $\text{Na}_{\text{Cu}}$  anti-sites in the lattice, resulting in a lower carrier density and a loss in  $V_{\text{OC}}$  compared to the Rb-free case.

Similar to its effect on  $V_{\text{OC}}$ , the influence of the RbF-PDT on  $FF$  strongly depends on the  $CGI$  of the CIGSe layer; the process window for a beneficial PDT is even narrower in case of  $FF$ . The RbF-PDT only has a beneficial effect on samples with  $CGI = 0.95$ , for when  $CGI \leq 0.9$ , it reduces  $FF$ . The already mentioned model enables to explain the reduction of  $FF$  by the formation of the  $\text{In}_x\text{Se}_y:(\text{Rb},\text{Na})$ -layer at the surface of the absorber layer. In order to determine the exact phase content and composition of the newly formed  $\text{In}_x\text{Se}_y:(\text{Rb},\text{Na})$ -layer,  $\text{RbInSe}_2:\text{Na}$  and  $\text{In}_2\text{Se}_3:(\text{Rb},\text{Na})$  reference thin films were synthesized for the first time and compared to the surface of the RbF-treated CIGSe using XPS, Raman scattering and GI-XRD. This evaluation indicates that the surface layer is an amorphous  $\text{RbInSe}_2:\text{Na}$  or a slightly off-stoichiometric compound of this kind. Subsequently, the optical and electrical properties of this reference layer are investigated in order to be able to use them as input parameters for the device simulations.

Furthermore, it could be shown that the Cu-deficient ODC, which is detected at the surface of the CIGSe by Raman scattering, is consumed during the growth of this RIS-layer. This leads to the incorporation of more Rb into the surface of absorber layers with lower  $CGI$  and it is proposed that this incorporation of more Rb into the absorber layer is the result of the formation of a thicker RIS-layer. Therefore, the presence of this RIS-layer is proposed to be the reason for the detrimental effect of the RbF-PDT on  $FF$  of samples with  $CGI < 0.95$ . The device simulations support the hypothesis that this layer induces an electron barrier and therefore leads to a steady reduction of the  $FF$  with increasing layer thickness. Following this model, the formation of this detrimental surface-layer can be minimized on samples grown close to stoichiometry, while maintaining the beneficial effects of Rb. As a result, highly efficient CIGSe devices ( $\eta = 20.0\%$ ) with  $CGI = 0.95$  and RbF-PDT could be prepared.

In addition, the RIS-model is tested experimentally by directly depositing RIS-layers on CIGSe-layers with a composition grown close to stoichiometry ( $CGI = 0.95$ ). While the RbF-PDT on such layers does not lead to a reduction of  $FF$ , the  $CGI$ -independent deposition of RIS does steadily reduce  $FF$  with increasing RIS-thickness, providing further support for the proposed model.

Comparing the buffer layer growth of chemical bath deposited CdS on samples with and without RbF-PDT, it is shown that the RbF-PDT leads to a more homogeneous growth of the chemical bath deposited CdS. On the one hand, this enables the use of thinner buffer layers without degrading the quality of the heterojunction. On the other hand, it also leads to an improved coverage of the surface of the absorber layer by the CdS and therefore improves the lateral homogeneity of the hetero-interface and subsequently reduces the respective  $V_{\text{OC}}$ -losses. It is suggested that the amorphous nature of the RIS is responsible for the improved growth of the buffer layer. This ambivalent effect of the RIS-layer leads to the conclusion that a very thin RIS-layer together with the beneficial bulk effects allows for an optimal effect of the Rb-incorporation.

Along with the assumption – based on device simulations – that the direct RIS-deposition at  $530^\circ\text{C}$  suppresses the Rb-Na exchange mechanism and the subsequent amplification of the back contact barrier, this knowledge enables to fabricate highly efficient devices using the direct RIS-deposition. An optimized RIS-deposition is not only significantly faster than the RbF-PDT (2-4 min versus about 15 min) but was shown in this work to be able to lead to even higher efficiencies of up to  $\eta = 20.9\%$ . According to the proposed device model, the main benefit of this newly developed Rb-conditioning by the direct RIS-deposition in comparison to the established RbF-PDT is that due to the higher  $T_{\text{Sub}}$ , the formation of an interface defect that is proposed at the RIS/CIGSe-interface after Rb-conditioning is suppressed, leading to an additional reduction of the interface recombination velocity. Furthermore, it is also more

---

effectively reducing the bulk recombination rate presumably due to the fact that more Rb is incorporated into the bulk of the absorber layer.

A future challenge will be the optimization of the Rb-conditioning for the implementation into a fully dry deposited device without the availability of a rinsing step after the PDT. Further modifications of the surface of the device appear to be necessary to allow for such a device preparation. A possible way would be the incorporation of sulfur into the surface of the absorber layer in combination with heat-light-soaking treatments, which showed promising results in other groups [271].

Additionally, one would need to analyze the impact of fluorides (e.g.  $\text{GaF}_3$ ) on the performance of CIGSe devices in more detail since these compounds formed during the PDT would not be rinsed off of the surface anymore. Depending on the results of such a study, the substitution of RbF by other Rb-sources such as metallic Rb, RbCl [6], or RbS might be useful in order to hinder the formation of these additional F-compounds.

All in all this thesis provides a new and improved understanding of the physical effects of Rb-incorporation on the structural and optoelectronic properties of CIGSe-based solar cells. For the first time, a full device model is proposed that is able to reproduce the interaction of the procedure parameters of the Rb-incorporation and the properties of the underlying CIGSe absorber material.



# A Appendix

## A.1 Electrostatic Potential Fluctuations - Data taken from Publication [10]

Please note that the data, which are presented and analyzed in the following, are taken from the yet unpublished work of Nikolaeva et al. [12]. The data were obtained from the very same samples that are discussed in Section 4.1; the reference sample, the sample with  $t_{\text{PDT}} = 1$  min, and the sample with  $t_{\text{PDT}} = 10$  min. All measurements presented in this section were done by and are shown with kind permission of Aleksandra Nikolaeva.

In order to estimate the electrostatic potential fluctuations of these samples, electron beam induced current (EBIC) measurements were performed on cross sectional specimens prepared from the samples mentioned above. Details of the measurements, taken from Publication [12]: “The cross-sectional specimen were prepared by gluing two stripes of the solar cells face-to-face together, in a way that one stripe was shorter than the other, which provided areas to contact the back and front contacts of one cell for the EBIC measurements. Flat cross-sectional surfaces were obtained by mechanical polishing. On top of the cross-section, a 4-5 nm thick carbon layer was evaporated in order to protect the surface and reduce charging of specimens during irradiation by the electron beam. EBIC data were acquired using a Zeiss UltraPlus SEM, equipped with a beam blaker, an EBIC amplifier by point electronic GmbH and an Oxford Instruments XMax80 X-ray detector. EBIC measurements were performed at low beam current in order to avoid high injection conditions and varying beam energies from  $E_b = 5$  kV to  $E_b = 15$  kV. The frequency of the beam blaker was 5 kHz.”

Figure A.1 shows EBIC images of all three samples taken at  $E_b = 7$  kV. It can be seen that for the cases of the reference sample and the sample with  $t_{\text{PDT}} = 10$  min, the width of the SCR does not exhibit any substantial fluctuations, whereas the sample with  $t_{\text{PDT}} = 1$  min shows strong lateral variations of  $d_{\text{SCR}}$  (cf. also range of  $d_{\text{SCR}}$  shown in Table A.1).

In order to estimate the electrostatic potential fluctuations from these measurements, current profiles were extracted from these images perpendicular to the heterojunction. Following the procedures described in References [272, 273],  $d_{\text{SCR}}$  and  $L_D$  were extracted from the profiles. Performing these evaluations at measurements taken with different  $E_b$  enables to correct for the influence of surface recombination on  $L_D$  [274]. Using furthermore the models derived in References [42, 274–276], the variations of the charge density at the heterointerface,  $\Delta N_{\text{IF}}$ , as well as of the net-doping densities of the  $p$ - and the  $n$ -side of the heterojunction ( $\Delta N_A$  and  $\Delta N_D$ ) were estimated. Subsequently, the average amplitude of the electrostatic potential fluctuations  $\bar{\varphi}_{\text{el}}$  and finally the standard deviation of the electrostatic potential fluctuations,  $\sigma_{\text{el}}$  were derived. The results of these estimations are given in Table A.1 together with the estimated width of the SCR.

The average amplitude of the electrostatic potential fluctuations as well as the standard

Table A.1: Summarized values for  $d_{\text{SCR}}$  and  $\sigma_{\text{el}}$  as estimated in Publication [12] and the corresponding loss in  $V_{\text{OC}}$  according to Equation 2.41.

Sample	$d_{\text{SCR}}$ (nm)	$\bar{\varphi}_{\text{el}}$ (meV)	$\sigma_{\text{el}}$ (meV)	$\Delta V_{\text{OC}}^{\text{el}}$ (mV)
Reference	100-230	28	8	1.2
$t_{\text{PDT}} = 1$ min	100-500	50	35	23.8
$t_{\text{PDT}} = 10$ min	150-270	30	10	1.9

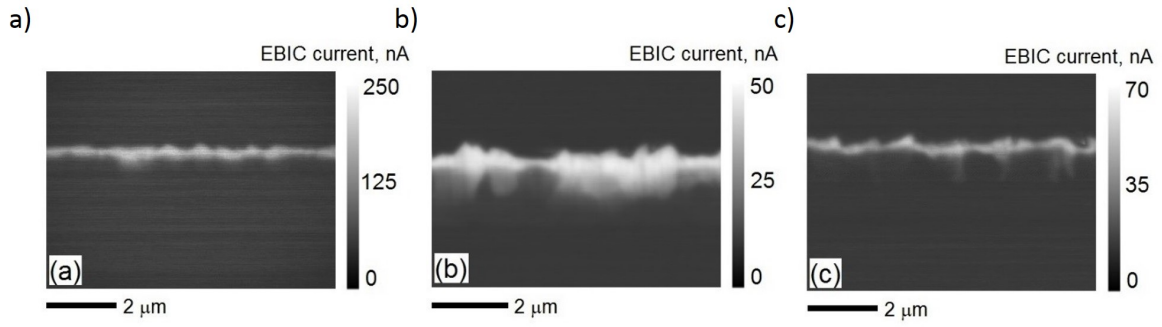


**Figure A.1:** EBIC images obtained at  $E_b = 7$  kV for CIGSe solar cells with CdS/i-ZnO buffer system: a) Rb-free reference cell ; b) 1 min RbF treatment (sample No. 8); c) 10 min RbF treatment (samples No. 9).

deviation of the electrostatic potential fluctuations are almost unchanged by the RbF-PDT with  $t_{\text{PDT}} = 10$  min compared to the reference sample. However, for the very short RbF-PDT ( $t_{\text{PDT}} = 1$  min), both are significantly increased. Using Equation 2.41 to calculate  $\Delta V_{\text{OC}}^{\text{el}}$  reveals that the observed loss in  $V_{\text{OC}}$  after a very short PDT (cf. Section 4.1) can be explained by the strongly increased electrostatic potential fluctuations. The optimized RbF-PDT ( $t_{\text{PDT}} = 10$  min) however, does not influence  $\Delta V_{\text{OC}}^{\text{el}}$  noticeably.

## A.2 Additional XRD-Diffractograms to Section 5.1

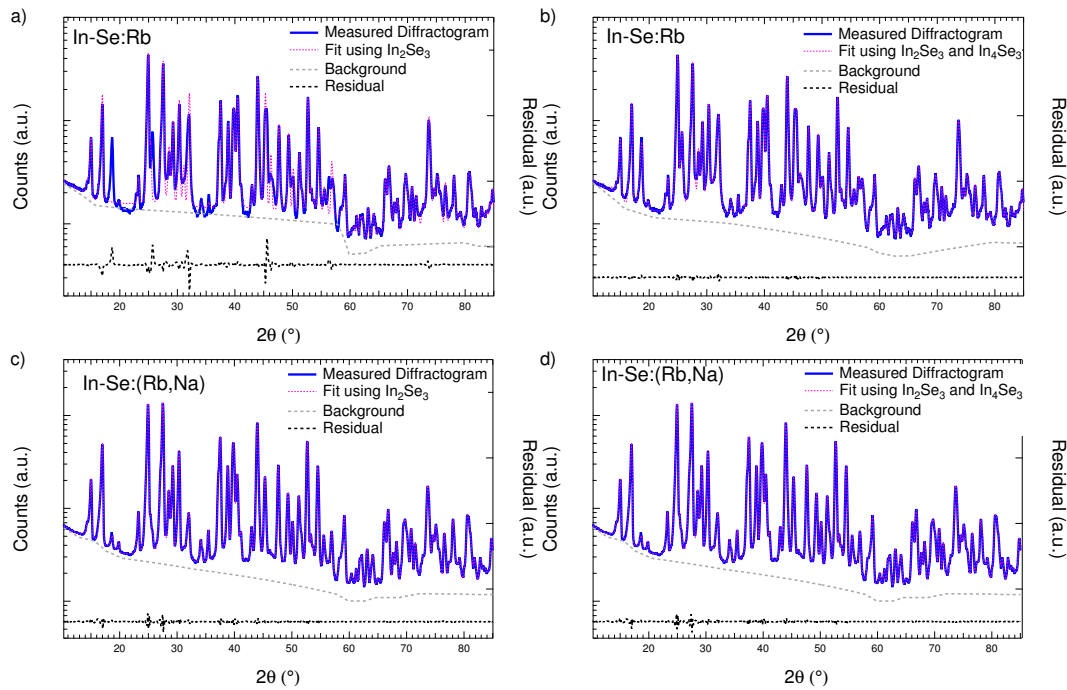


**Figure A.2:** XRD-diffractograms as well as the results of the corresponding Le Bail analyses [200] of a) the In-Se:Rb-sample fitted only with  $\text{In}_2\text{Se}_3$  contributions, b) the In-Se:Rb-sample fitted with both  $\text{In}_2\text{Se}_3$  and  $\text{In}_4\text{Se}_3$  contributions, c) the In-Se:(Rb,Na)-sample fitted only with  $\text{In}_2\text{Se}_3$  contributions, and d) the In-Se:(Rb,Na)-sample fitted with both  $\text{In}_2\text{Se}_3$  and  $\text{In}_4\text{Se}_3$  contributions. The fits were performed using the following data from literature: Reference [233] for  $\text{In}_2\text{Se}_3$ , Reference [234] for  $\text{In}_4\text{Se}_3$ , Reference [235] for  $\text{RbInSe}_2$ , and Reference [236] for Mo. As one can see from the residuals (axis are scaled the same in all images), the diffractogram of the In-Se:(Rb,Na) sample can be well fitted with only contributions of  $\text{In}_2\text{Se}_3$ , while the sample In-Se:Rb shows at least five features, which are significantly better matched with a combination of  $\text{In}_2\text{Se}_3$  and  $\text{In}_4\text{Se}_3$ . Note that the counts are plotted on a logarithmic scale, while the residuals are plotted on a linear one.

## A.3 Input-Parameter Sets for the Simulations in Chapter 8

Table A.2: Input parameters for the simulations leading to the plots shown in Figure 8.2. All parameters not mentioned in this table, are unchanged compared to the ones in Table 3.1, except for the RIS-layer and the respective interface defects, which are not present in this variation.

Neutral Defect States									
		CIGSe: Shallow Defect				CIGSe: Deep Defect			
		Figure 8.2 a		Figure 8.2 b		Figure 8.2 a		Figure 8.2 b	
Symbol	Unit	Case 1	Case 2	Case 1	Case 2	Case 1	Case 2	Case 1	Case 2
$N_{\text{Def,B}}$	$\text{cm}^{-3}$	-	varied	$1 \cdot 10^{14}$	varied	varied	-	varied	$1 \cdot 10^{14}$
$\sigma_{\text{D}}$	$e\text{V}$	-	Single	Single	Single	Single	-	Single	Single
$E_{\text{Def,B}}$	$e\text{V}$ above VB	-	0.05	0.05	0.05	0.5	-	0.5	0.5
$\sigma_n$	$\text{cm}^2$	-	$1.8 \cdot 10^{-14}$	$1.8 \cdot 10^{-14}$	$1.8 \cdot 10^{-14}$	$1.8 \cdot 10^{-14}$	-	$1.8 \cdot 10^{-14}$	$1.8 \cdot 10^{-14}$
$\sigma_p$	$\text{cm}^2$	-	$1 \cdot 10^{-15}$	$1 \cdot 10^{-15}$	$1 \cdot 10^{-15}$	$1 \cdot 10^{-15}$	-	$1 \cdot 10^{-15}$	$1 \cdot 10^{-15}$

Table A.3: Input parameters for the simulations leading to the plots shown in Figures 8.4 and 8.6. All parameters not mentioned in this table, are unchanged compared to the ones in Table 3.1, except for the interface defect at the CdS/CIGSe interface, which is obviously not present in this device model.

Symbol	Parameter	Unit	CIGSe	CdS	RbInSe <sub>2</sub>	ZnO
$E_g$	Bandgap Energy	$e\text{V}$	from GD-OES	2.4	2.8 / varied	3.3
$EA$	Electron Affinity	$e\text{V}$	from GD-OES	4.3	4.225 / varied	4.45
$d$	Thickness	nm	from GD-OES	60	varied	150
$N_{\text{D}}/N_{\text{A}}$	Min. Carrier Concentr.	$\text{cm}^{-3}$	$p = 2.9 \cdot 10^{15}$	$n = 1 \cdot 10^{16}$	$n = 1 \cdot 10^{14}$ / varied	$n = 1 \cdot 10^{19}$
Neutral (Gaussian) Defect States						
$N_{\text{Def,B}}$	Defect Density	$\text{cm}^{-3}$	$1.1 \cdot 10^{14}$	$1.8 \cdot 10^{18}$	- / varied	$1.8 \cdot 10^{16}$
$\sigma_{\text{D}}$	Distribution Width	$e\text{V}$	Single Defect	0.1	- / Single Defect	0.1
$E_{\text{Def,B}}$	Energetic Position	$e\text{V}$	0.5 above VB	Mid-gap	- / Mid-gap	Mid-gap
$\sigma_n$	Capture Cross Section	$\text{cm}^2$	$1.8 \cdot 10^{-14}$	$1 \cdot 10^{-13}$	- / $1 \cdot 10^{-14}$	$1 \cdot 10^{-12}$
$\sigma_p$	Capture Cross Section	$\text{cm}^2$	$1 \cdot 10^{-15}$	$1 \cdot 10^{-13}$	- / $1 \cdot 10^{-14}$	$1 \cdot 10^{-12}$
Single Acceptor Interface Defect States						
			RIS/CIGSe		CdS/RIS	
$N_{\text{Def,IF}}$	Defect Density	$\text{cm}^{-3}$	-	-	$1.8 \cdot 10^{11}$	-
$\sigma_{\text{D}}$	Distribution Width	$e\text{V}$	-	-	Single Defect	-
$E_{\text{Def,IF}}$	Energetic Position	$e\text{V}$	-	-	0.96 $e\text{V}$ below $E_{\text{C}}^{\text{CdS}}$	-
$\sigma_n$	Capture Cross Section	$\text{cm}^2$	-	-	$1.8 \cdot 10^{-16}$	-
$\sigma_p$	Capture Cross Section	$\text{cm}^2$	-	-	$1.2 \cdot 10^{-14}$	-

Table A.4: Input parameters for the simulations leading to the plots shown in Figure 8.7. All parameters not mentioned in this table, are unchanged compared to the ones in Table 3.1. The parameters of the RIS-layer were chosen to:  $E_{\text{g,RIS}} = 2.8 e\text{V}$ ,  $d_{\text{RIS}} = 10 \text{ nm}$ ,  $EA_{\text{RIS}} = 4.225 e\text{V}$ , and  $N_{\text{D,RIS}} = 10^{14} \text{ cm}^{-3}$ .

Single Acceptor Interface Defect States					
		Case 1 - Figure 8.7 c		Case 2 - Figure 8.7 d	
Symbol	Unit	CdS/RIS-Interface	RIS/CIGSe-Interface	CdS/RIS-Interface	RIS/CIGSe-Interface
$N_{\text{Def,B}}$	$\text{cm}^{-3}$	$3 \cdot 10^{11} \text{ cm}^{-2}$	-	-	$3 \cdot 10^{11} \text{ cm}^{-2}$
$\sigma_{\text{D}}$	$e\text{V}$	Single	-	-	Single
$E_{\text{Def,B}}$	$e\text{V}$	0.96 $e\text{V}$ below $E_{\text{C}}^{\text{CdS}}$	-	-	0.3 above $E_{\text{V}}^{\text{CIGSe}}$
$\sigma_n$	$\text{cm}^2$	$1 \cdot 10^{-16}$	-	-	$1 \cdot 10^{-16}$
$\sigma_p$	$\text{cm}^2$	$1 \cdot 10^{-14}$	-	-	$1 \cdot 10^{-14}$

Table A.5: Input parameters for the simulations leading to the plots shown in Figure 8.8. All parameters not mentioned in this table, are unchanged compared to the ones in Table 3.1, except for the interface defect at the CdS/CIGSe interface, which is obviously not present in this device model.

Symbol	Parameter	Unit	CIGSe	CdS	RbInSe <sub>2</sub>	ZnO
$E_g$	Bandgap Energy	eV	from GD-OES	2.4	2.8	3.3
$EA$	Electron Affinity	eV	from GD-OES	4.3	varied / 4.225	4.45
$d$	Thickness	nm	from GD-OES	60	varied / 10	150
$N_D/N_A$	Min. Carrier Concentr.	cm <sup>-3</sup>	$p = 2.9 \cdot 10^{15}$	$n = 1 \cdot 10^{16}$	$n = 1 \cdot 10^{14}$	$n = 1 \cdot 10^{19}$
Single Acceptor Interface Defect States						
	Interfaces with RIS		RIS/CIGSe		CdS/RIS	
$N_{Def,IF}$	Defect Density	cm <sup>-3</sup>	varied / $3 \cdot 10^{11}$		-	
$\sigma_D$	Distribution Width	eV	Single Defect		-	
$E_{Def,IF}$	Energetic Position	eV	varied / 0.3 eV above $E_V^{CIGSe}$		-	
$\sigma_n$	Capture Cross Section	cm <sup>2</sup>	$1.0 \cdot 10^{-16}$		-	
$\sigma_p$	Capture Cross Section	cm <sup>2</sup>	$1.0 \cdot 10^{-14}$		-	

Table A.6: Input parameters for the simulations leading to the plots shown in Figure 8.11. All parameters not mentioned in this table, are unchanged compared to the ones in Table 3.1, except for the interface defect at the CdS/CIGSe interface, which is obviously not present in this device model.

Symbol	Parameter	Unit	CIGSe	CdS	RbInSe <sub>2</sub>	ZnO
$E_g$	Bandgap Energy	eV	from GD-OES	2.4	2.8	3.3
$EA$	Electron Affinity	eV	from GD-OES	4.3	4.225	4.45
$d$	Thickness	nm	from GD-OES	60	10	150
$N_D/N_A$	Min. Carrier Concentr.	cm <sup>-3</sup>	$p = 2.9 \cdot 10^{15}$	$n = 1 \cdot 10^{16}$	$n = 1 \cdot 10^{14}$	$n = 1 \cdot 10^{19}$
Single Acceptor Interface Defect States						
	Interfaces with RIS		RIS/CIGSe		CdS/RIS	
$N_{Def,IF}$	Defect Density	cm <sup>-3</sup>	$3 \cdot 10^{11}$		-	
$\sigma_D$	Distribution Width	eV	Single Defect		-	
$E_{Def,IF}$	Energetic Position	eV	0.3 eV above $E_V^{CIGSe}$		-	
$\sigma_n$	Capture Cross Section	cm <sup>2</sup>	$1 \cdot 10^{-16}$		-	
$\sigma_p$	Capture Cross Section	cm <sup>2</sup>	$1 \cdot 10^{-14}$		-	

Table A.7: Input parameters for the simulations leading to the plots shown in Figure 8.12. All parameters not mentioned in this table, are unchanged compared to the ones in Table 3.1.

Symbol	Parameter	Unit	CIGSe	CdS	RbInSe <sub>2</sub>	ZnO
$E_g$	Bandgap Energy	eV	from GD-OES	2.4	- / 2.8	3.3
$EA$	Electron Affinity	eV	from GD-OES	4.3	- / 4.225	4.45
$d$	Thickness	nm	from GD-OES	60	- / 10 / varied	150
$N_D/N_A$	Min. Carrier Concentr.	cm <sup>-3</sup>	$p = 2.9 \cdot 10^{15}$	$n = 1 \cdot 10^{16}$	- / $n = 1 \cdot 10^{14}$	$n = 1 \cdot 10^{19}$
Single Acceptor Interface Defect States						
	Interface without RIS		CdS/CIGSe			
	Interfaces with RIS (if present)				RIS/CIGSe	CdS/RIS
$N_{Def,IF}$	Defect Density	cm <sup>-3</sup>	$1.8 \cdot 10^{11}$		- / $1 \cdot 10^{11}$	-
$\sigma_D$	Distribution Width	eV	Single Defect		- / Single Defect	-
$E_{Def,IF}$	Energetic Position	eV	0.3 eV above $E_V^{CIGSe}$		- / 0.3 eV above $E_V^{CIGSe}$	-
$\sigma_n$	Capture Cross Section	cm <sup>2</sup>	$1.8 \cdot 10^{-16}$		- / $1.0 \cdot 10^{-16}$	-
$\sigma_p$	Capture Cross Section	cm <sup>2</sup>	$1.2 \cdot 10^{-14}$		- / $1.0 \cdot 10^{-14}$	-

Table A.8: Input parameters for the simulations leading to the plots shown in Figure 8.13. All parameters not mentioned in this table, are unchanged compared to the ones shown in Table 3.1.

Symbol	Parameter	Unit	CIGSe	CdS	RbInSe <sub>2</sub>	ZnO
$E_g$	Bandgap Energy	eV	from GD-OES	2.4	2.8 / -	3.3
$EA$	Electron Affinity	eV	from GD-OES	4.3	4.225 / -	4.45
$d$	Thickness	nm	from GD-OES	60	10 / -	150
$N_D/N_A$	Min. Carrier Concentr.	cm <sup>-3</sup>	$p = 2.9 \cdot 10^{15}$ / varied	$n = 1 \cdot 10^{16}$	$n = 1 \cdot 10^{14}$ / -	$n = 1 \cdot 10^{19}$
Single Acceptor Interface Defect States						
	Interface without RIS		CdS/CIGSe		RIS/CIGSe	CdS/RIS
	Interfaces with RIS (if present)					
$N_{Def,IF}$	Defect Density	cm <sup>-3</sup>	$1.8 \cdot 10^{11}$	varied		$1.8 \cdot 10^{11}$
$\sigma_D$	Distribution Width	eV	Single Defect	Single Defect		Single Defect
$E_{Def,IF}$	Energetic Position	eV	0.3 eV above $E_V^{CIGSe}$	0.3 eV above $E_V^{CIGSe}$		0.96 eV below $E_C^{CdS}$
$\sigma_n$	Capture Cross Section	cm <sup>2</sup>	$1.8 \cdot 10^{-16}$	$1.0 \cdot 10^{-16}$		$1.8 \cdot 10^{-16}$
$\sigma_p$	Capture Cross Section	cm <sup>2</sup>	$1.2 \cdot 10^{-14}$	$1.0 \cdot 10^{-14}$		$1.2 \cdot 10^{-14}$

## A.4 Additional Simulations to Chapter 8

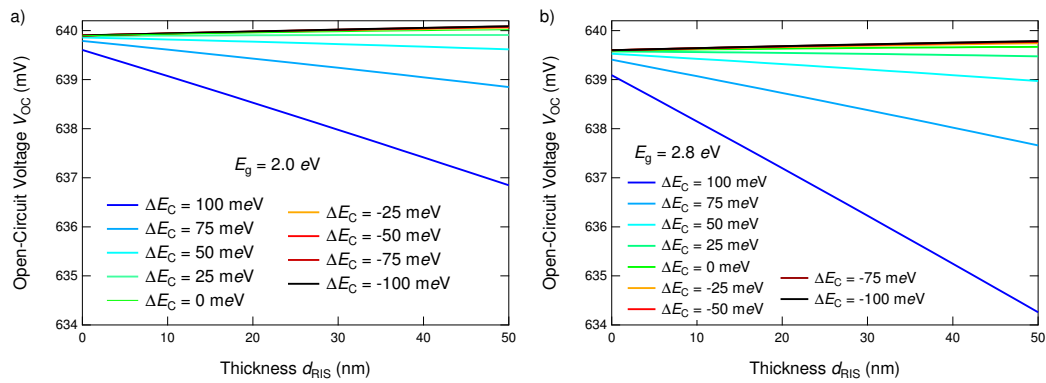


**Figure A.3:** Dependence of  $V_{OC}$  on the CBM-Offset  $\Delta E_C$  and the thickness of the RIS-layer for a)  $E_g^{\text{RIS:Na}} = 2.0$  eV and b)  $E_g^{\text{RIS:Na}} = 2.8$  eV.

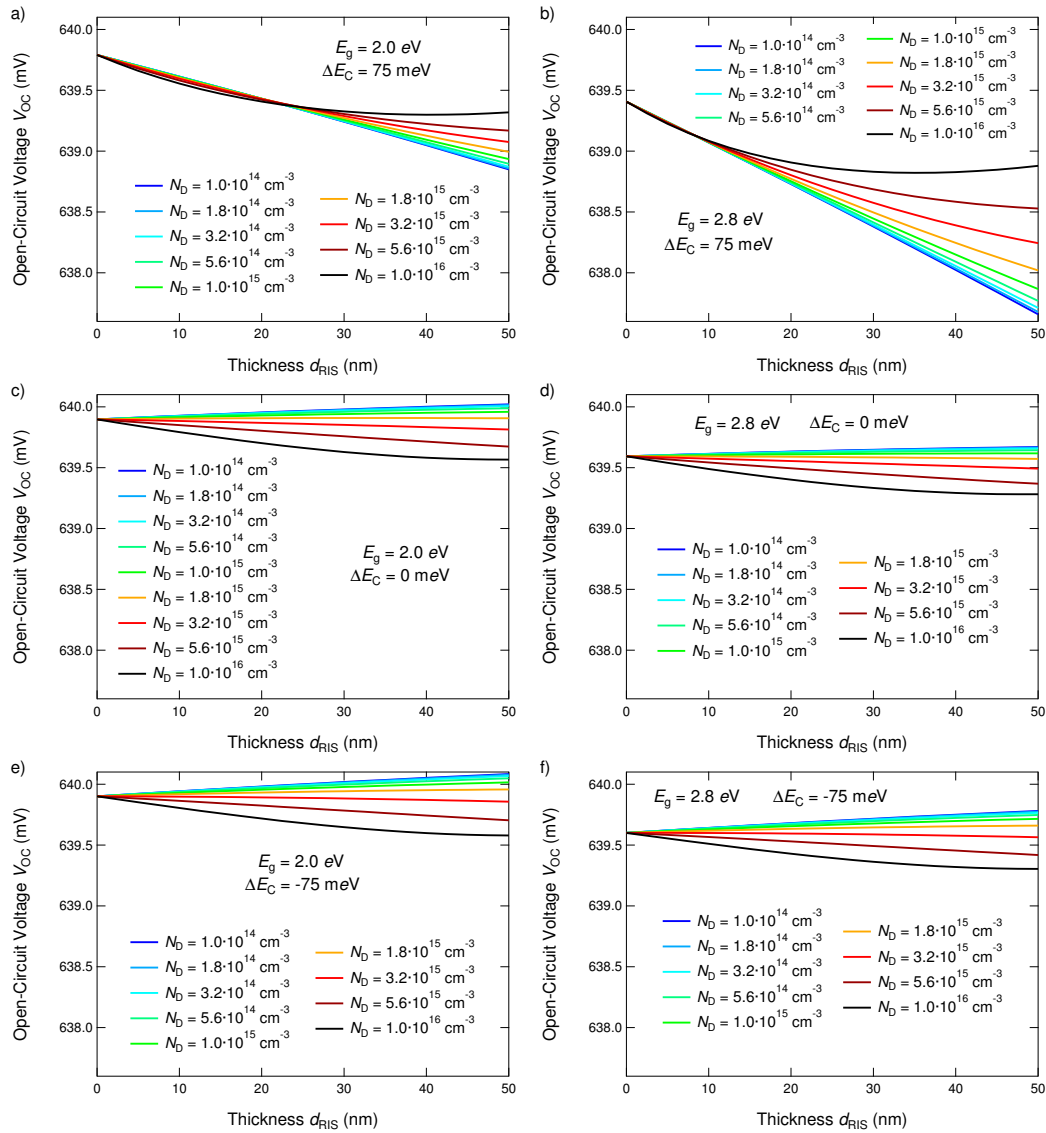


**Figure A.4:** Dependence of  $V_{OC}$  on the donor density  $N_D$  and the thickness of the RIS-layer for different combinations of  $E_g^{\text{RIS}}$  and  $\Delta E_C$ .

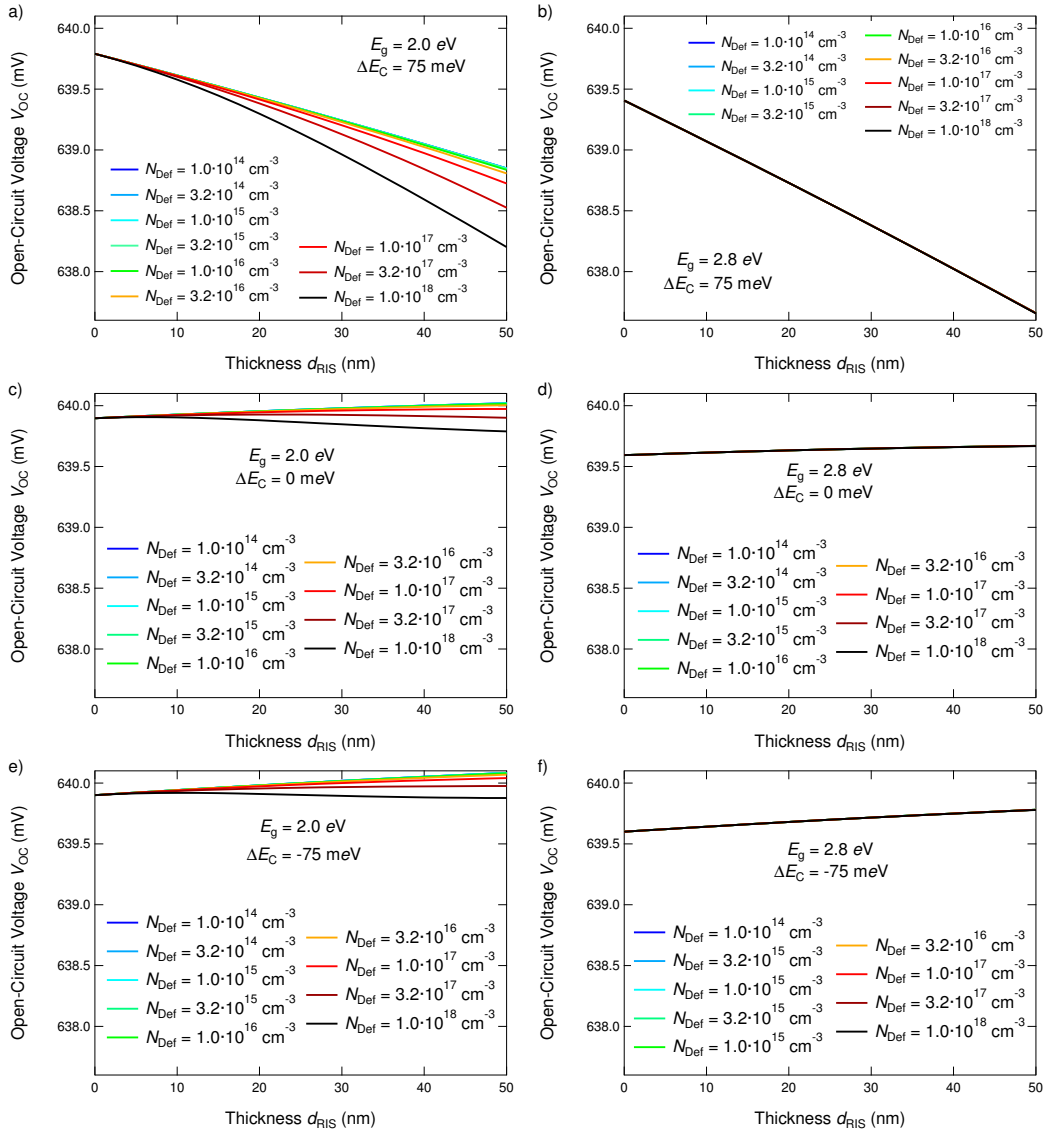


**Figure A.5:** Dependence of  $V_{OC}$  on the defect density of  $N_{Def}$  and the thickness of the RIS-layer for different combinations of  $E_g^{RIS}$  and  $\Delta E_C$ .

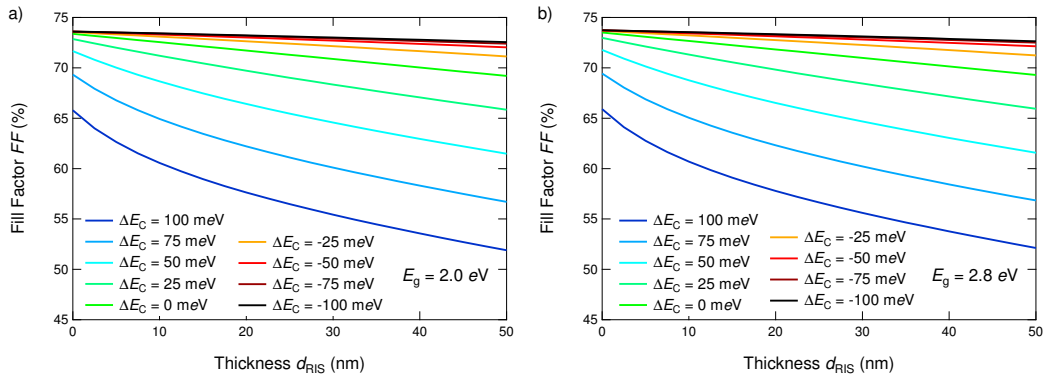


**Figure A.6:** Dependence of  $FF$  on the CBM-Offset  $\Delta E_C$  and the thickness of the RIS-layer for a)  $E_g^{RIS:Na} = 2.0$  eV and b)  $E_g^{RIS:Na} = 2.8$  eV.

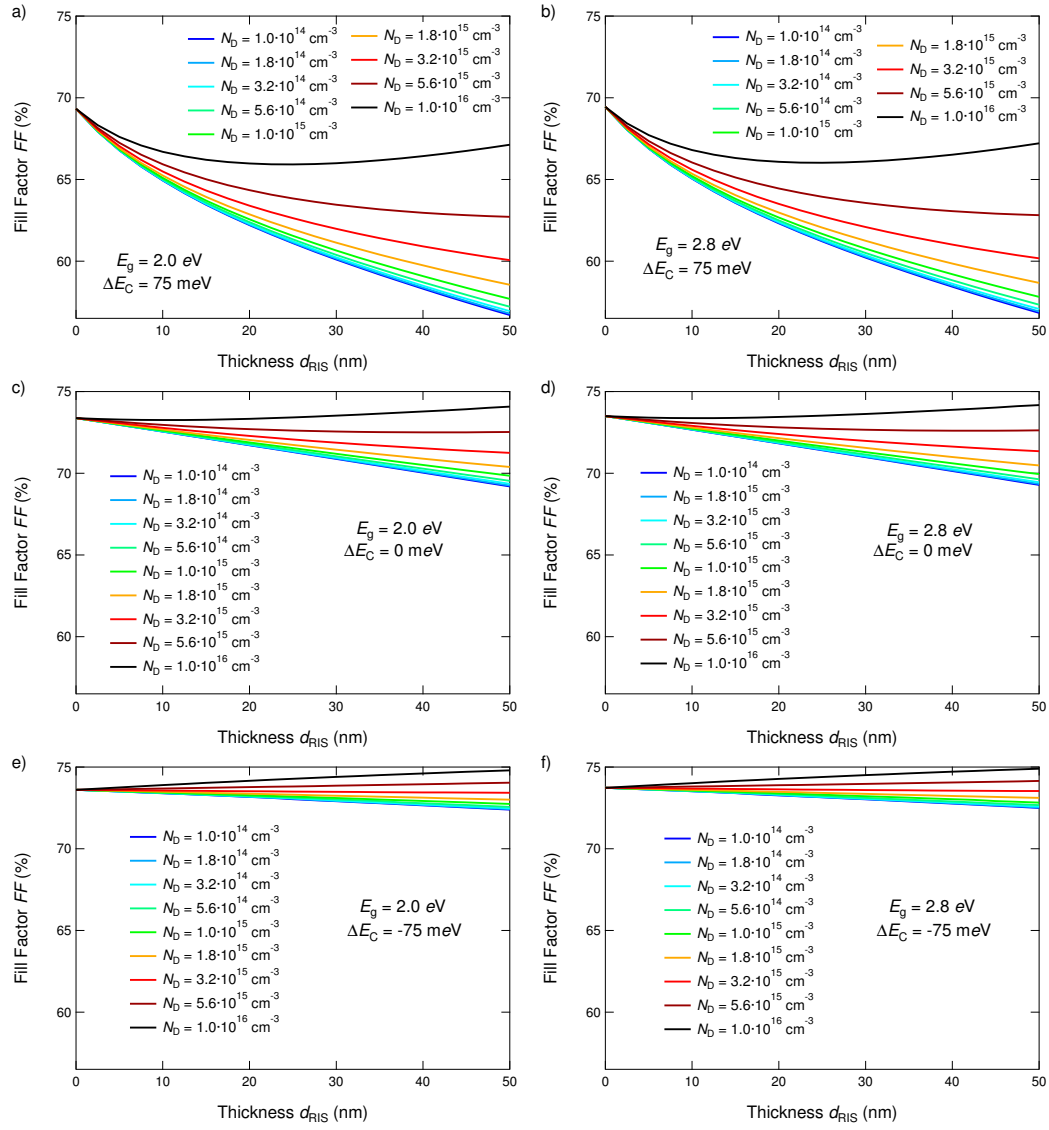


**Figure A.7:** Dependence of FF on the donor density  $N_D$  and the thickness of the RIS-layer for different combinations of  $E_g^{\text{RIS}}$  and  $\Delta E_C$ .

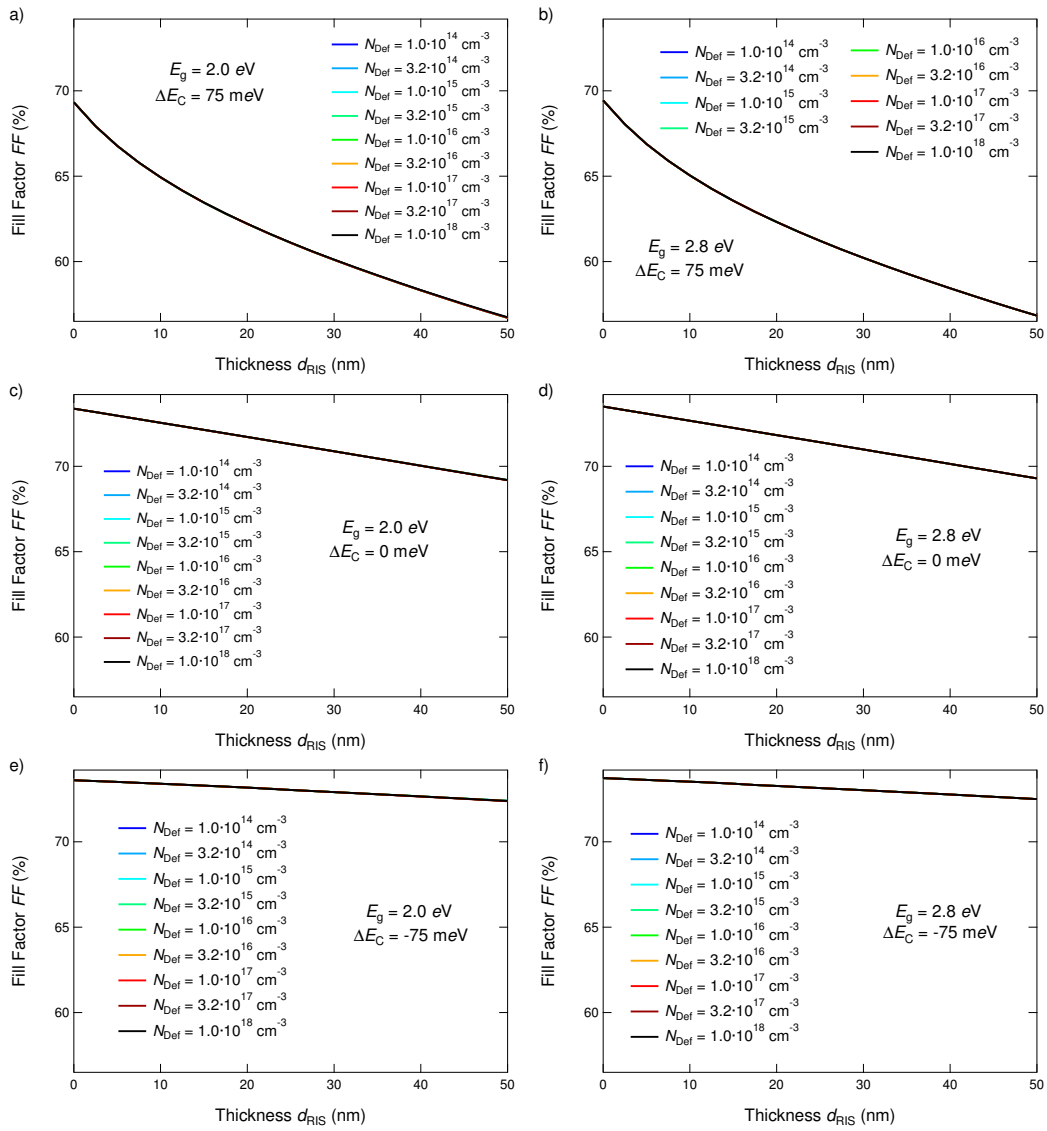


**Figure A.8:** Dependence of FF on the defect density of  $N_{\text{Def}}$  and the thickness of the RIS-layer for different combinations of  $E_g^{\text{RIS}}$  and  $\Delta E_C$ .



## Bibliography

- [1] T. Kodalle, M. D. Heinemann, D. Greiner, H. A. Yetkin, M. Klupsch, C. Li, P. A. van Aken, I. Lauer mann, R. Schlatmann, C. A. Kaufmann. Elucidating the Mechanism of an RbF Post Deposition Treatment in CIGS Thin Film Solar Cells. *Solar RRL*, 2(9): 1800156, 2018.
- [2] T. Kodalle, R. Kormath Madam Ragupathy, T. Bertram, N. Maticiuc, H. A. Yetkin, R. Gunder, R. Schlatmann, T. D. Kühne, C. A. Kaufmann, H. Mirhosseini. Properties of Co-Evaporated RbInSe<sub>2</sub> Thin Films. *physica status solidi (RRL)-Rapid Research Letters*, 13:1800564, 2019.
- [3] T. Kodalle, L. Choubrac, L. Arzel, R. Schlatmann, N. Barreau, C. A. Kaufmann. Effects of KF and RbF Post Deposition Treatments on the Growth of the CdS Buffer Layer on CIGS Thin Films - a Comparative Study. *Solar Energy Materials and Solar Cells*, 200: 109997, 2019.
- [4] T. Kodalle, T. Bertram, R. Schlatmann, C. A. Kaufmann. Effectiveness of an RbF Post Deposition Treatment of CIGS Solar Cells in Dependence on the Cu-Content of the Absorber Layer. *IEEE Journal of Photovoltaics*, 9(6):1839–1845, 2019.
- [5] T. Kodalle, D. Greiner, V. Brackmann, K. Prietzel, A. Scheu, T. Bertram, P. Reyes-Figueroa, T. Unold, D. Abou-Ras, R. Schlatmann, C. A. Kaufmann, V. Hoffmann. Glow Discharge Optical Emission Spectrometry for Quantitative Depth Profiling of CIGS Thin-Films. *Journal of Analytical Atomic Spectrometry*, 34:1233–1241, 2019.
- [6] T. Kodalle, C. A. Hsu, T. Bertram, N. Maticiuc, J. Lauche, I. Kafedjiska, I. Lauer mann, R. Schlatmann, C. S. Ferekides, C. A. Kaufmann. Reducing Air- and Moisture-Induced Degradation of Cu(In,Ga)Se<sub>2</sub> Absorber Layers for Thin Film Solar Cells by RbCl Treatment. In *Proceedings of the 46th IEEE Photovoltaic Specialists Conference*, pages 159–164, 2019.
- [7] M. D. Heinemann, T. Kodalle, C. Hages, M. Klupsch, D. Greiner, L. Korte, S. Levenco, T. Unold, R. Schlatmann, C. A. Kaufmann. Evaluation of Recombination Losses in Thin Film Solar Cells Using an LED Sun Simulator - the Effect of RbF Post-Deposition on CIGS Solar Cells. *EPJ Photovoltaics*, 9(9):1–6, 2018.
- [8] N. Maticiuc, T. Kodalle, J. Lauche, R. Wenisch, T. Bertram, C. A. Kaufmann, I. Lauer mann. In Vacuo XPS Investigation of Cu(In,Ga)Se<sub>2</sub> Surface after RbF Post-Deposition Treatment. *Thin Solid Films*, 665:143–147, 2018.
- [9] T. Bertram, J. Lauche, T. Kodalle, H. A. Yetkin, M. D. Heinemann, R. Schlatmann, C. A. Kaufmann. RbF-PDT Induced Sodium Displacement in Cu(In,Ga)Se<sub>2</sub> Absorbers Grown Under High Substrate Temperatures. In *Proceedings of the IEEE 7th World Conference on Photovoltaic Energy Conversion*, pages 109–113, 2018.
- [10] M. Guc, T. Kodalle, R. Kormath Madam Ragupathy, H. Mirhosseini, T. D. Kühne, I. Becerril-Romero, A. Perez-Rodriguez, C. A. Kaufmann, V. Izquierdo-Roca. Vibrational Properties of RbInSe<sub>2</sub>: Raman Scattering Spectroscopy and First Principle Calculations. *The Journal of Physical Chemistry C*, 124(2):1285–1291, 2019.

- [11] A. Vilanueva-Tovar, T. Kodalle, C. A. Kaufmann, R. Schlatmann, R. Klenk. Limitation of Current Transport across the Heterojunction in Cu(In,Ga)Se<sub>2</sub> Solar Cells Prepared with Alkali Fluoride Postdeposition Treatment. *Solar RRL*, Early View - DOI: 10.1002/solr.201900560:1900560, 2020.
- [12] A. Nikolaeva, M. Krause, N. Schäfer, W. Witte, D. Hariskos, T. Kodalle, C. A. Kaufmann, N. Barreau, J. A. Marquez Prieto, S. Levenco, T. Unold, D. Abou-Ras. Electrostatic Potential Fluctuations and Light-Soaking Effects in Cu(In,Ga)Se<sub>2</sub> Solar Cells. *Submitted to Progress in Photovoltaics: Research and Applications*, 2019.
- [13] AP News. Climate Change is Hot Topic in the European Parliament Vote. Online, Retrieved 25.07.2019. URL <https://www.apnews.com/d872c718e1a1483b86931ffdac0ab50d>.
- [14] BBC. EU Leaders Face Pressure to Deliver on Climate Change. Online, Retrieved 25.07.2019. URL <https://www.bbc.com/news/world-europe-48621860>.
- [15] The Telegraph. The 'Green' Wave Will Make It Impossible for the European Parliament to Ignore Climate Change. Online, Retrieved 25.07.2019. URL <https://www.telegraph.co.uk/news/2019/05/27/green-wave-will-make-impossible-european-parliament-ignore-climate/>.
- [16] The Guardian. School Climate Strikes: 1.4 Million People Took Part, Say Campaigners. Online, Retrieved 25.07.2019. URL <https://www.theguardian.com/environment/2019/mar/19/school-climate-strikes-more-than-1-million-took-part-say-campaigners-greta-thunberg>.
- [17] The Independent. Germany's Far-Right AfD Takes Aim at Greta Thunberg as it Denies Climate Emergency. Online, Retrieved 25.07.2019. URL <https://www.independent.co.uk/news/world/europe/germany-afd-greta-thunberg-climate-change-denial-far-right-a8914721.html>.
- [18] Greenpeace. German Far Right Targets Greta Thunberg in Anti-Climate Push. Online, Retrieved 25.07.2019. URL <https://unearthed.greenpeace.org/2019/05/14/germany-climate-denial-populist-eike-afd/>.
- [19] Time Magazine. President Trump Renews Climate Change Denial Days After Defense Department Releases Daunting Report on Its Effects. Online, Retrieved 25.07.2019. URL <https://time.com/5508259/trump-climate-change-defense-department/>.
- [20] New York Times. Trump Administration Hardens Its Attack on Climate Science. Online, Retrieved 25.07.2019. URL <https://www.nytimes.com/2019/05/27/us/politics/trump-climate-science.html>.
- [21] Scientists for Future. Online, Retrieved 25.07.2019. URL <https://www.scientists4future.org/>.
- [22] S. Kurtz, N. Haegel, R. Sinton, R. Margolis. The Future of Photonics. *Nature Photonics*, 11:3–5, 2017.
- [23] C. Breyer, D. Bogdanov, A. Gulagi, A. Aghahosseini, L. S. N. S. Barbosa, O. Koskinen, M. Barasa, U. Caldera, S. Afanasyeva, M. Child, J. Farfan, P. Vainikka. On the Role of Solar Photovoltaics in Global Energy Transition Scenarios. *Progress in Photovoltaics: Research and Applications*, 25:727–745, 2017.
- [24] D. Bogdanov, J. Farfan, K. Sadovskaia, M. Fasihi, M. Child, C. Breyer. Arising Role of Photovoltaic and Wind Energy in the Power Sector and Beyond: Changing the Northeast Asian Power Landscape. *Japanese Journal of Applied Physics*, 57:08RJ01, 2018.

- [25] S. Chu, A. Majumdar. Opportunities and Challenges for a Sustainable Energy Future. *Nature*, 488:294–303, 2012.
- [26] Shell International B.V. Skyscenario. Online, Retrieved 04.09.2019. URL <https://www.shell.com/energy-and-innovation/the-energy-future/scenarios/shell-scenario-sky.html>.
- [27] A. Jäger-Waldau. Snapshot of Photovoltaics - February 2019. *Energies*, 12(5):769–776, 2019.
- [28] European Technology and Innovation Platform for Photovoltaics. Photovoltaic Solar Energy Big and Beyond. *ETIP PV*, 2019.
- [29] Renewables 2018. Global Status Report. Online, Retrieved 04.09.2019. URL <http://www.ren21.net/gsr-2018/>.
- [30] J. Jean, P. R. Brown, R. L. Jaffe, T. Buonassisi, V. Bulovic. Pathways for Solar Photovoltaics. *Energy & Environmental Science*, 8:1200–1219, 2015.
- [31] N. M. Haegel, H. Atwater Jr., T. Barnes, C. Breyer, A. Burrell, Y.-M. Chiang, S. De Wolf, B. Dimmler, D. Feldman, S. Glunz, J. C. Goldschmidt, D. Hochschild, R. Inzunza, I. Kaizuka, B. Kroposki, S. Kurtz, S. Leu, R. Margolis, K. Matsubara, A. Metz, W. K. Metzger, M. Morjaria, S. Niki, S. Nowak, I. Marius Peters, S. Philipps, T. Reindl, A. Richter, D. Rose, K. Sakurai, R. Schlatmann, M. Shikano, W. Sinke, R. Sinton, B. J. Stanbery, M. Topic, W. Tumas, Y. Ueda, J. van de Lagemaat, P. Verlinden, M. Vetter, E. Warren, M. Werner, M. Yamaguchi, and A. W. Bett. Terawatt-Scale Photovoltaics: Transform Global Energy. *Science*, 364(6443):836–838, 2019.
- [32] C. Kost, S. Shammugam, V. Jülich, H.-T. Nguyen, T. Schlegl. Levelized Cost of Electricity Renewable Energy Technologies. *Study of the Fraunhofer Institute for Solar Energy System ISE*, 2018.
- [33] A. Blakers, B. Lu, M. Stocks. 100% Renewable Electricity in Australia. *Energy*, 133:471–482, 2017.
- [34] C. Heske, D. Lincot, M. Powalla, P. Salome, R. Schlatmann, A. N. Tiwari, H. Linden, K. Melkonyan, V. Petrova-Koch, A. Wade, T. Dalibor, B. Dimmler, O. Lundberg, S. Petroncini, D. Poplavskyy, U. Rühle, H. Schneider, M. Fischer, E. Jaremalm, and H. Reinhardt. CIGS White Paper 2019. 2019. URL <https://cigs-pv.net/cigs-white-paper-initiative/>.
- [35] M. A. Green, Y. Hishikawa, E. D. Dunlop, D. H. Levi, J. Hohl-Ebinger, A. W. Y. Ho-Baillie. Solar Cell Efficiency Tables (Version 52). *Progress in Photovoltaics: Research and Applications*, 26:427–436, 2018.
- [36] M. Nakamura, K. Yamaguchi, Y. Kimoto, Y. Yasaki, T. Kato, H. Sugimo. Cd-Free Cu(In,Ga)(Se,S)<sub>2</sub> Thin-Film Solar Cell With Record Efficiency of 23.35%. *IEEE Journal of Photovoltaics*, 9(6):1863–1867, 2019.
- [37] W. Shockley, H. J. Queisser. Detailed Balance Limit of Efficiency of *p-n* Junction Solar Cells. *Journal of Applied Physics*, 32:510–519, 1961.
- [38] J.-F. Guillemoles, T. Kirchartz, D. Cahen, U. Rau. Solar Energy Conversion and the Shockley-Queisser Model, a Guide for the Perplexed. *Nature Photonics*, 13(8):501–505, 2019.
- [39] P. Jackson, D. Hariskos, E. Lotter, S. Paetel, R. Wuerz, R. Menner, W. Wischmann, M. Powalla. New World Record Efficiency for Cu(In,Ga)Se<sub>2</sub> Thin-Film Solar Cells Beyond 20%. *Progress in Photovoltaics: Research and Applications*, 19:894–896, 2011.

- [40] P. Jackson, R. Wuerz, D. Hariskos, E. Lotter, W. Witte, M. Powalla. Effects of Heavy Alkali Elements in Cu(In,Ga)Se<sub>2</sub> Solar Cells with Efficiencies up to 22.6%. *physica status solidi-Rapid Research Letters*, 10(8):583–586, 2016.
- [41] T. P. Weiss, S. Nishiwaki, B. Bissig, R. Carron, E. Avancini, J. Löckinger, S. Buecheler, A. N. Tiwari. Injection Current Barrier Formation for RbF Postdeposition-Treated Cu(In,Ga)Se<sub>2</sub>-Based Solar Cells. *Advanced Materials Interfaces*, 5:1701007, 2018.
- [42] R. Scheer, H.-W. Schock. *Chalcogenide Photovoltaics*. WILEY-VCH, 2011.
- [43] T. Kawashima, S. Adachi, H. Miyake, K. Sugiyam. Optical Constants of CuGaSe<sub>2</sub> and CuInSe<sub>2</sub>. *Journal of Applied Physics*, 84:5202–5209, 1998.
- [44] P. Würfel. *Physik der Solarzellen*, volume 2. Spektrum Akademischer Verlag, Heidelberg - Berlin, 2000.
- [45] M. Gloeckler, A. L. Fahrenbruch, J. R. Sites. Numerical Modeling of CIGS and CdTe Solar Cells: Setting the Baseline. *Proceedings of 3rd World Conference on Photovoltaic Energy Conversion*, 1:491–494, 2003.
- [46] W. Shockley. The Theory of *p-n* Junctions in Semiconductors and *p-n* Junction Transistors. *Bell System Technical Journal*, 28:435–489, 1949.
- [47] M. A. Green. Limits of the Open-Circuit Voltage and Efficiency of Silicon Solar Cells Imposed by Intrinsic Auger Processes. *IEEE Transactions on Electron Devices*, ED-31(5): 671–678, 1984.
- [48] A. Richter, S. W. Glunz, F. Werner, J. Schmidt, A. Cueva. Improved Quantitative Description of Auger Recombination in Crystalline Silicon. *Physical Review B*, 86:165202, 2012.
- [49] T. Kirchartz, U. Rau. What Makes a Good Solar Cell? *Advanced Energy Materials*, 8: 1703385, 2018.
- [50] P. Asbeck. Self-Absorption Effects on the Radiative Lifetime in GaAs-GaAlAs Double Heterostructures. *Journal of Applied Physics*, 48:820–822, 1977.
- [51] W. Shockley, W. T. Read. Statistics of the Recombination of Holes and Electrons. *Physical Review*, 87(5):835–842, 1952.
- [52] R. N. Hall. Electron Hole Recombination in Germanium. *Physical Review Journals Archive*, 87(2):387, 1952.
- [53] U. Rau, B. Blank, T. C. M. Müller, T. Kirchartz. Efficiency Potential of Photovoltaic Materials and Devices Unveiled by Detailed-Balance Analysis. *Physical Review Applied*, 7:044016, 2017.
- [54] P. W. Bridgman. Note on the Principle of Detailed Balancing. *Physical Review Journals Archive*, 31:101, 1928.
- [55] L. C. Hirst, N. J. Ekins-Daukes. Fundamental Losses in Solar Cells. *Progress in Photovoltaics: Research and Applications*, 19:286–293, 2011.
- [56] J. H. Werner, J. Mattheis, U. Rau. Efficiency Limitations of Polycrystalline Thin Film Solar Cells: Case of Cu(In,Ga)Se<sub>2</sub>. *Thin Solid Films*, 480-481:399–409, 2005.
- [57] U. Rau, H.-W. Schock. Electronic Properties of Cu(In,Ga)Se<sub>2</sub> Heterojunction Solar Cells - Recent Achievements, Current Understanding, and Future Challenges. *Applied Physics A*, 69:131–147, 1999.

- [58] S. Siebentritt. What Limits the Efficiency of Chalcopyrite Solar Cells? *Solar Energy Materials and Solar Cells*, 95:1471–1476, 2010.
- [59] D. Abou-Ras, N. Schäfer, C. J. Hages, S. Levencenco, J. Marquez, T. Unold. Inhomogeneities in Cu(In,Ga)Se<sub>2</sub> Thin Film Solar Cells: Band-Gap Versus Potential Fluctuations. *Solar RRL*, 2(1):1700199, 2018.
- [60] U. Rau, J. H. Werner. Radiative Efficiency Limits of Solar Cells with Lateral Band-Gap Fluctuations. *Applied Physics Letters*, 84:3735–3737, 2004.
- [61] S. Siebentritt, S. Sadewasser, M. Wimmer, C. Leendertz, T. Eisenbarth, M. C. Lux-Steiner. Evidence for a Neutral Grain-Boundary Barrier in Chalcopyrites. *Physical Review Letters*, 97(14):146601, 2006.
- [62] M. Hafemeister, S. Siebentritt, J. Albert, M. C. Lux-Steiner, S. Sadewasser. Large Neutral Barrier at Grain Boundaries in Chalcopyrite Thin Films. *Physical Review Letters*, 104(19):196602, 2010.
- [63] S. Sadewasser, D. Abou-Ras, D. Azulay, R. Baier, I. Balberg, D. Cahen, S. Cohen, K. Gartsman, K. Ganesan, J. Kavalakkatt, W. Li, O. Millo, T. Rissom, Y. Rosenwaks, H.-W. Schock, A. Schwarzman, T. Unold. Nanometer-Scale Electronic and Microstructural Properties of Grain Boundaries in Cu(In,Ga)Se<sub>2</sub>. *Thin Solid Films*, 519(21):7341–7346, 2011.
- [64] L. Gütay, G. H. Bauer. Lateral Variations of Optoelectronic Quality of Cu(In<sub>1-x</sub>Ga<sub>x</sub>)Se<sub>2</sub> in the Submicron-Scale. *Thin Solid Films*, 487:8–13, 2005.
- [65] L. Gütay, G. H. Bauer. Local Fluctuations of Absorber Properties of Cu(In,Ga)Se<sub>2</sub> by Sub-Micron Resolved PL Towards Real Life Conditions. *Thin Solid Films*, 517:2222–2225, 2009.
- [66] U. Rau, M. Schmidt. Electronic Properties of ZnO/CdS/Cu(In,Ga)Se<sub>2</sub> Solar Cells - Aspects of Heterojunction Formation. *Thin Solid Films*, 387:141–146, 2001.
- [67] S. M. Wasim, C. Rincon, G. Marin, P. Bocaranda, E. Hernandez, I. Bonalde, E. Medina. Effect of Structural Disorder on the Urbach Energy in Cu Ternaries. *Physical Review B*, 64:195101, 2001.
- [68] J. I. Pankove. Absorption Edge of Impure Gallium Arsenide. *Physical Review*, 140(6A):2059–2065, 1965.
- [69] T. Walter, R. Herberholz, C. Müller, H.-W. Schock. Determination of Defect Distributions from Admittance Measurements and Application to Cu(In,Ga)Se<sub>2</sub> Based Heterojunctions. *Journal of Applied Physics*, 80:4411, 1996.
- [70] T. Tiedje. Band Tail Recombination Limit to the Output Voltage of Amorphous Silicon Solar Cells. *Applied Physics Letters*, 40:627–629, 1998.
- [71] S. De Wolf, J. Holovsky, S.-J. Moon, P. Löper, B. Niesen, M. Ledinsky, F.-J. Haug, J.-H. Yum, C. Ballif. Organometallic Halide Perovskites: Sharp Optical Absorption Edge and Its Relation to Photovoltaic Performance. *The Journal of Physical Chemistry Letters*, 5:1035–1039, 2014.
- [72] M. Solomon, A. Johnson. New Research in Solar Cells: Urbach Tails and Open Circuit Voltage. *Elements*, 11(1):45–52, 2015.
- [73] S. Bourdais, C. Chone, B. Delatouche, A. Jacob, G. Larramona, C. Moisan, A. Lafond, F. Donatini, G. Rey, S. Siebentritt, A. Walsh, G. Dennler. Is the Cu/Zn Disorder the Main Culprit for the Voltage Deficit in Kesterite Solar Cells? *Advanced Energy Materials*, 6(12):1502276, 2016.

- [74] J. Jean, T. S. Mahony, D. Bozyigit, M. Sponseller, J. Holovsky, M. G. Bawendi, V. Bulovic. Radiative Efficiency Limit with Band Tailing Exceeds 30% for Quantum Dot Solar Cells. *ACS Energy Letters*, 2:2616–2624, 2017.
- [75] M. A. Green. Solar Cell Fill Factors: General Graph and Empirical Expressions. *Solid State Electronics*, 24(8):788–789, 1981.
- [76] T. Haalboom, T. Gödecke, F. Ernst, M. Rühle, R. Herberholz, H.-W. Schock, C. Beilharz, K. W. Benz. Phase Relations and Microstructure in Bulk Materials and Thin Films of the Ternary System Cu-In-Se. In *Proceedings of the 11th Conference on Ternary and Multiternary Compounds*, volume 152, pages 249–252, 1997.
- [77] H. G. Grimm, A. Sommerfeld. Über den Zusammenhang des Abschlusses der Elektronengruppen im Atom mit den Chemischen Valenzzahlen. *Zeitschrift für Physik*, 36(1):36–59, 1926.
- [78] J. L. Shay, B. Tell, H. M. Kasper, L. M. Schiavone.  $p$ - $d$ -Hybridization of the Valence Band of I-III-VI<sub>2</sub> Compounds. *Physical Review B: Condensed Matter and Materials Physics*, 5(12):5003–5005, 1972.
- [79] J. E. Jaffe, A. Zunger. Electronic Structure of the Ternary Chalcopyrite Semiconductors CuAlS<sub>2</sub>, CuGaS<sub>2</sub>, CuInS<sub>2</sub>, CuAlSe<sub>2</sub>, CuGaSe<sub>2</sub> and CuInSe<sub>2</sub>. *Physical Review B: Condensed Matter and Materials Physics*, 28(10):5822–5847, 1983.
- [80] S. Ishizuka, K. Sakurai, A. Yamada, H. Shibata, K. Matsubara, M. Yonemura, S. Nakamura, H. Nakanishi, T. Kojima, S. Niki. Progress in the Efficiency of Wide-Gap Cu(In<sub>1-x</sub>Ga<sub>x</sub>)Se<sub>2</sub> Solar Cells Using CIGSe Layers Grown in Water Vapor. *Japanese Journal of Applied Physics*, 44(22):679–682, 2005.
- [81] A. Stokes, M. Al-Jassim, A. Norman, D. Diercks, B. Gorman. Nanoscale Insight into the  $p$ - $n$  Junction of Alkali-Incorporated Cu(In,Ga)Se<sub>2</sub> Solar Cells. *Progress in Photovoltaics: Research and Applications*, 25(9):764–772, 2017.
- [82] S. B. Zhang, S.-H. Wei, A. Zunger, H. Katayama-Yoshida. Defect Physics of the CuInSe<sub>2</sub> Chalcopyrite Semiconductor. *Physical Review B*, 57(16):9642–9656, 1998.
- [83] H. Neumann. Vacancy Formation Enthalpies in A<sup>I</sup>B<sup>III</sup>C<sub>2</sub><sup>VI</sup> Chalcopyrite Semiconductors. *Crystal Research and Technology*, 18(7):901–906, 1983.
- [84] S. Fiechter, Y. Tomm, K. Diesner, T. Weiss. Homogeneity Ranges, Defect Phases and Defect Formation Energies in A<sup>I</sup>B<sup>III</sup>C<sub>2</sub><sup>VI</sup> Chalcopyrites (A = Cu; B = Ga, In; C = S, Se). *Journal of Applied Physics*, 39(1):123–126, 2000.
- [85] D. Schmid, M. Ruckh, F. Grunwald, H.-W. Schock. Chalcopyrite/Defect Chalcopyrite Heterojunctions on the Basis of CuInSe<sub>2</sub>. *Journal of Applied Physics*, 73(6):2902–2909, 1993.
- [86] R. Caballero, C. A. Kaufmann, V. Efimova, T. Rissom, V. Hoffmann, H.-W. Schock. Investigation of Cu(In,Ga)Se<sub>2</sub> Thin-Film Formation During the Multi-Stage Co-Evaporation Process. *Progress in Photovoltaics: Research and Applications*, 21:30–46, 2013.
- [87] T. Nishimura, H. Sugiura, K. Nakada, A. Yamada. Accurate Control and Characterization of Cu Depletion Layer for Highly Efficient Cu(In,Ga)Se<sub>2</sub> Solar Cells. *Progress in Photovoltaics: Research and Applications*, 27(2):171–178, 2018.
- [88] B. Ümsür, W. Calvet, B. Höpfner, A. Steigert, I. Lauermaun, M. Gorgoi, K. Prietzel, H. A. Navirian, C. A. Kaufmann, T. Unold, M. C. Lux-Steiner. Investigation of Cu-Poor and Cu-Rich Cu(In,Ga)Se<sub>2</sub>/CdS Interfaces Using Hard X-Ray Photoelectron Spectroscopy. *Thin Solid Films*, 582:366–370, 2015.

- [89] C. Persson, Y.-J. Zhao, S. Lany, A. Zunger. *n*-type Doping of CuInSe<sub>2</sub> and CuGaSe<sub>2</sub>. *Physical Review B*, 72:035211, 2005.
- [90] S. Shirakata, T. Nakada. Photoluminescence and Time-Resolved Photoluminescence in Cu(In,Ga)Se<sub>2</sub> Thin Films and Solar Cells. *Physica Status Solidi C: Current Topics in Solid State Physics*, 6(5):1059–1062, 2009.
- [91] J. Hedström, H. Ohlsen, M. Bodegard, A. Kylner, L. Stolt, D. Hariskos, M. Ruckh, H.-W. Schock. ZnO/CdS/Cu(In,Ga)Se<sub>2</sub> Thin Film Solar Cells with Improved Performance. In *Conference Record of the 23rd IEEE Photovoltaic Specialists Conference*, pages 364–371, 1993.
- [92] M. Bodegard, L. Stolt, J. Hedström. The Influence of Sodium on the Grain Boundary of CuInSe<sub>2</sub> Films for Photovoltaic Application. In *Proceedings of the 12th European Photovoltaic Solar Energy Conference*, pages 1743–1746, 1994.
- [93] H.-W. Schock, M. Burgelman, M. Carter, L. Stolt, J. Vedel. High Efficiency Chalcopyrite Based Thin Film Solar Cells - Results of the Eurocis-Collaboration. In *Proceedings of the 11th European Photovoltaic Solar Energy Conference*, pages 116–119, 1992.
- [94] M. A. Contreras, B. Egaas, P. Dippo, J. Webb, J. Granata, K. Ramanathan, S. Asher, A. Swartzlander, and R. Noufi. On the Role of Na and Modifications to Cu(In,Ga)Se<sub>2</sub> Absorber Materials Using Thin-MF (M=Na, K, Cs) Precursor Layers. In *The Conference Record of the 26th IEEE Photovoltaic Specialists Conference*, page 359, 1997.
- [95] A. Chirilă, P. Reinhard, F. Pianezzi, P. Bloesch, A. R. Uhl, C. Fella, L. Kranz, D. Keller, C. Gretener, H. Hagendorfer, D. Jaeger, R. Erni, S. Nishiwaki, S. Buecheler, A. N. Tiwari. Potassium-Induced Surface Modification of Cu(In,Ga)Se<sub>2</sub> Thin Films for High-Efficiency Solar Cells. *Nature Materials*, 12(12):1107–1111, 2013.
- [96] S.-H. Wei, S. B. Zhang, A. Zunger. Effects of Na on the Electrical and Structural Properties of CuInSe<sub>2</sub>. *Journal of Applied Physics*, 85(10):7214–7218, 1999.
- [97] Z.-K. Yuan, S. Chen, Y. Xie, J.-S. Park, H. Xiang, X.-G. Gong, S.-H. Wei. Na-Diffusion Enhanced *p*-Type Conductivity in Cu(In,Ga)Se<sub>2</sub>: A New Mechanism for Efficient Doping in Semiconductors. *Advanced Energy Materials*, 6(24):1601191, 2016.
- [98] D. Rudmann. *Effects of Sodium on Growth and Properties of Cu(In,Ga)Se<sub>2</sub> Thin Films and Solar Cells*. Dissertation, ETH Zuerich, 2004.
- [99] J. E. Granata, J. R. Sites, S. Asher, R. J. Matson. Quantitative Incorporation of Sodium in CuInSe<sub>2</sub> and Cu(In,Ga)Se<sub>2</sub> Photovoltaic Devices. In *Conference Record of the 26th IEEE Photovoltaic Specialists Conference*, 1997.
- [100] M. A. Contreras, B. Egaas, D. King, A. Swartzlander, T. Dullweber. Texture Manipulation of CuInSe<sub>2</sub> Thin Films. *Thin Solid Films*, 361-362:167–171, 2000.
- [101] B. M. Keyes, F. Hasoon, P. Dippo, A. Balcioglu, F. Abulfotuh. Influence of Na on the Electro-Optical Properties of Cu(In,Ga)Se<sub>2</sub>. In *Record of the 26th IEEE Photovoltaic Specialists Conference*, pages 479–482, 1997.
- [102] M. Ruckh, D. Schmid, M. Kaiser, R. Schaffler, T. Walter, H.-W. Schock. Influence of Substrates on the Electrical Properties of Cu(In,Ga)Se<sub>2</sub> Thin Films. In *Conference Records of the 24th IEEE Photovoltaic Specialists Conference*, pages 156–159, 1994.
- [103] K. Granath, M. Bodegard, L. Stolt. The Effect of NaF on Cu(In, Ga)Se<sub>2</sub> Thin Film Solar Cells. *Solar Energy Materials and Solar Cells*, 60:279–293, 2000.

- [104] D. Rudmann, A. F. da Cunha, M. Kaelin, F. Kurdesau, H. Zogg, A. N. Tiwari, G. Bilger. Efficiency Enhancement of Cu(In,Ga)Se<sub>2</sub> Solar Cells due to Post-Deposition Na Incorporation. *Applied Physics Letters*, 84:1129–1131, 2004.
- [105] A. Rockett, J. S. Britt, T. Gillespie, C. Marshall, M. M. Al Jassim, F. Hasoon, R. Matson, B. Basol. Na in Selenized Cu(In,Ga)Se<sub>2</sub> on Na-Containing and Na-Free Glasses: Distribution, Grain Structure, and Device Performances. *Thin Solid Films*, 372:212–217, 2000.
- [106] D. W. Niles, K. Ramanathan, F. Hasoon, R. Noufi, B. J. Tielsch, J. E. Fulghum. Na Impurity Chemistry in Photovoltaic CIGS Thin Films: Investigation with X-Ray Photoelectron Spectroscopy. *Journal of Vacuum Science & Technology A: Vacuum, Surfaces, and Films*, 15(6):3044–3049, 1997.
- [107] D. Rudmann, G. Bilger, M. Kaelin, F.-J. Haug, H. Zogg, A. N. Tiwari. Effects of NaF Coevaporation on Structural Properties of Cu(In,Ga)Se<sub>2</sub> Thin Films. *Thin Solid Films*, 431-432:37–40, 2003.
- [108] D. Rudmann, D. Bremaud, A. F. da Cunha, G. Bilger, A. Strohm, M. Kaelin, H. Zogg, A. N. Tiwari. Sodium Incorporation Strategies for CIGS Growth at Different Temperatures. *Thin Solid Films*, 480-481:55–60, 2005.
- [109] D. W. Niles, M. Al-Jassim, K. Ramanathan. Direct Observation of Na and O Impurities at Grain Surfaces of CuInSe<sub>2</sub> Thin Films. *Journal of Vacuum Science & Technology A: Vacuum, Surfaces, and Films*, 17(291):291–296, 1999.
- [110] D. Braunger, D. Hariskos, G. Bilger, U. Rau, H.-W. Schock. Influence of Sodium on the Growth of Polycrystalline Cu(In,Ga)Se<sub>2</sub> Thin Films. *Thin Solid Films*, 361-362:161–166, 2000.
- [111] E. Cadel, N. Barreau, J. Kessler, P. Pareige. Atom Probe Study of Sodium Distribution in Polycrystalline Cu(In,Ga)Se<sub>2</sub> Thin Film. *Acta Materialia*, 58:2634–2637, 2010.
- [112] F. Couzinie-Devy, E. Cadel, N. Barreau, L. Arzel, P. Pareige. Atom Probe Study of Cu-Poor to Cu-Rich Transition During Cu(In,Ga)Se<sub>2</sub> Growth. *Applied Physics Letters*, 99:232108, 2011.
- [113] A. Laemmle, R. Wuerz, T. Schwarz, O. Cojocar-Miredin, P.-P. Choi, M. Powalla. Investigation of the Diffusion Behavior of Sodium in Cu(In,Ga)Se<sub>2</sub> Layers. *Journal of Applied Physics*, 115:154501, 2014.
- [114] F. Couzinie-Devy, E. Cadel, N. Barreau, L. Arzel, P. Pareige. Na Distribution in Cu(In,Ga)Se<sub>2</sub> Thin Films: Investigation by Atom Probe Tomography. *Scripta Materialia*, 104:83–86, 2015.
- [115] H. P. Wang, I. Shih, C. H. Champness. Characteristics of CuInSe<sub>2</sub> Bridgman Ingots Grown with Sodium. In *Records of the 28th IEEE Photovoltaic Specialists Conference*, pages 642–645, 2000.
- [116] B. J. Stanbery, E. S. Lambers, T. J. Anderson. XPS Studies of Sodium Compound Formation and Surface Segregation in CIGS Thin Films. In *Record of the 26th IEEE Photovoltaic Specialists Conference*, pages 499–502, 1997.
- [117] R. Herberholz, H.-W. Schock, U. Rau, J. H. Werner, T. Haalboom, T. Gadecke, F. Ernst, C. Beilharz, K. W. Benz, D. Cahen. New Aspects of Phase Segregation and Junction Formation in CuInSe<sub>2</sub>. *Record of the 26th IEEE Photovoltaic Specialists Conference*, pages 323–326, 1997.

- [118] L. Kronik, D. Cahen, H.-W. Schock. Effects of Sodium on Polycrystalline Cu(In,Ga)Se<sub>2</sub> and Its Solar Cell Performance. *Advanced Materials*, 10(1):31–36, 1998.
- [119] L. E. Oikkonen, M. G. Ganchenkova, A. P. Seitsonen, R. M. Nieminen. Effect of Sodium Incorporation into CuInSe<sub>2</sub> from First Principles. *Journal of Applied Physics*, 114:083503, 2013.
- [120] E. Ghorbani, J. Kiss, H. Mirhosseini, G. Roma, M. Schmidt, J. Windeln, T. D. Kühne, C. Felser. Hybrid-Functional Calculations on the Incorporation of Na and K Impurities into the CuInSe<sub>2</sub> and CuIn<sub>5</sub>Se<sub>8</sub> Solar-Cell Materials. *The Journal of Physical Chemistry C*, 119:25197–25203, 2015.
- [121] D. J. Schroeder, A. A. Rockett. Electronic Effects of Sodium in Epitaxial CuIn<sub>1-x</sub>Ga<sub>x</sub>Se<sub>2</sub>. *Journal of Applied Physics*, 82:4982–4985, 1997.
- [122] R. Wuerz, A. Eicke, F. Kessler, S. Paetel, S. Efimenko, C. Schlegel. CIGS Thin-Film Solar Cells and Modules on Enamelled Steel Substrates. *Solar Energy Materials and Solar Cells*, 100:132–137, 2012.
- [123] A. Laemmle, R. Wuerz, M. Powalla. Investigation of the Effect of Potassium on Cu(In,Ga)Se<sub>2</sub> Layers and Solar Cells. *Thin Solid Films*, 582:27–30, 2015.
- [124] T. Lepetit, S. Harel, L. Arzel, G. Ouvrard, N. Barreau. Coevaporated KInSe<sub>2</sub>: A Fast Alternative to KF Postdeposition Treatment in High-Efficiency Cu(In,Ga)Se<sub>2</sub> Thin Film Solar Cells. *IEEE Journal of Photovoltaics*, 6(5):1316–1320, 2016.
- [125] C. P. Muzzillo, L. M. Mansfield, K. Ramanathan, T. J. Anderson. Properties of Cu<sub>1-x</sub>K<sub>x</sub>InSe<sub>2</sub> Alloys. *Journal of Materials Science*, 51(14):6812–6823, 2016.
- [126] F. Pianezzi, P. Reinhard, A. Chirilă, B. Bissig, S. Nishiwaki, S. Buecheler, A. N. Tiwari. Unveiling the Effects of Post-Deposition Treatment with Different Alkaline Elements on the Electronic Properties of CIGS Thin Film Solar Cells. *Physical Chemistry Chemical Physics*, 16(19):8843–8851, 2014.
- [127] A. Laemmle, R. Wuerz, M. Powalla. Efficiency Enhancement of Cu(In,Ga)Se<sub>2</sub> Thin-Film Solar Cells by a Post-Deposition Treatment with Potassium Fluoride. *Physica Status Solidi Rapid Research Letters*, 7(9):631–634, 2013.
- [128] T. Lepetit, G. Ouvrard, N. Barreau. KF Post Deposition Treatment in Co-Evaporated Cu(In,Ga)Se<sub>2</sub> Thin Film Solar Cells: Beneficial or Detrimental Effect Induced by the Absorber Characteristics. *Progress in Photovoltaics: Research and Applications*, 25:1068–1076, 2017.
- [129] J. M. Raguse, C. P. Muzzillo, J. R. Sites, L. Mansfield. Effects of Sodium and Potassium on the Photovoltaic Performance of CIGS Solar Cells. *IEEE Journal of Photovoltaics*, 7(1):303–307, 2017.
- [130] I. Khatrin, H. Fukai, H. Yamaguchi, M. Sugiyama, T. Nakada. Effect of Potassium Fluoride Post-Deposition Treatment on Cu(In,Ga)Se<sub>2</sub> Thin Films and Solar Cells Fabricated onto Sodalime Glass Substrates. *Solar Energy Materials and Solar Cells*, 155: 280–287, 2016.
- [131] S. A. Jensen, S. Glynn, A. Kanevce, P. Dippo, J. V. Li, D. H. Levi, D. Kuciauskas. Beneficial Effect of Post-Deposition Treatment in High-Efficiency Cu(In,Ga)Se<sub>2</sub> Solar Cells Through Reduced Potential Fluctuations. *Journal of Applied Physics*, 120(6):063106, 2016.

- [132] P. Pistor, D. Greiner, C. A. Kaufmann, S. Brunken, M. Gorgoi, A. Steigert, W. Calvet, I. Lauermann, R. Klenk, T. Unold, M. C. Lux-Steiner. Experimental Indication for Band Gap Widening of Chalcopyrite Solar Cell Absorbers After Potassium Fluoride Treatment. *Applied Physics Letters*, 105(6):63901, 2014.
- [133] C. P. Muzzillo. Review of Grain Interior, Grain Boundary, and Interface Effects of K in CIGS Solar Cells: Mechanisms for Performance Enhancement. *Solar Energy Materials and Solar Cells*, 172:18–24, 2017.
- [134] M. Chugh, T. D. Kühne, H. Mirhosseini. Diffusion of Alkali Metals in Polycrystalline CuInSe<sub>2</sub> and Their Role in the Passivation of Grain Boundaries. *ACS Applied Materials & Interfaces*, 11(16):14821–14829, 2019.
- [135] D. Shin, J. Kim, T. Gershon, R. Mankad, M. Hopstaken, S. Guha, B. T. Ahn, B. Shin. Effects of the Incorporation of Alkali Elements on Cu(In,Ga)Se<sub>2</sub> Thin Film Solar Cells. *Solar Energy Materials and Solar Cells*, 157:695–702, 2016.
- [136] T. Maeda, A. Kawabata, T. Wada. First-Principles Study on Alkali-Metal Effect of Li, Na, and K in CuInSe<sub>2</sub> and CuGaSe<sub>2</sub>. *Japanese Journal of Applied Physics*, 54:08KC20, 2015.
- [137] S. Karki, P. K. Paul, G. Rajan, T. Ashrafee, K. Aryal, P. Pradhan, R. W. Collins, A. Rockett, T. J. Grassman, S. A. Ringel, A. R. Arehart, S. Marsillac. In Situ and Ex Situ Investigations of KF Postdeposition Treatment Effects on CIGS Solar Cells. *IEEE Journal of Photovoltaics*, 7(2):665–669, 2017.
- [138] Thomas Lepetit. *Influence of KF Post Deposition Treatment on the Polycrystalline Cu(In,Ga)Se<sub>2</sub>/CdS Hetero-Junction Formation for Photovoltaic Application*. PhD thesis, Universite de Nantes, 2015.
- [139] I. Khatri, K. Shudo, J. Matsuura, M. Sugiyama, T. Nakada. Impact of Heat-Light Soaking on Potassium Fluoride Treated CIGS Solar Cells with CdS Buffer Layer. *Progress in Photovoltaics: Research and Applications*, 26(3):1–8, 2017.
- [140] J. Nishinaga, T. Koida, S. Ishizuka, Y. Kamikawa, H. Takahashi, M. Iioka, H. Higuchi, Y. Ueno, H. Shibata, S. Niki. Effects of Long-Term Heat-Light Soaking on Cu(In,Ga)Se<sub>2</sub> Solar Cells with KF Postdeposition Treatment. *Applied Physics Express*, 10:092301, 2017.
- [141] A. Stokes, M. Al-Jassim, D. Diercks, B. Gorman. Alkali Segregation and Matrix Concentrations in Thin Film Cu(In,Ga)Se<sub>2</sub> at Targeted Interfaces Characterized in 3-D at the Nanoscale. *Proceedings of the IEEE 42nd Photovoltaic Specialists Conference*, 2015.
- [142] A. Stokes, M. Al-Jassim, B. Gorman. Semi-Statistical Atom Probe Tomography Analysis of Thin Film Grain Boundaries. *Microscopy and Microanalysis*, 22:644–645, 2016.
- [143] F. Pianezzi, P. Reinhard, A. Chirilă, S. Nishiwaki, B. Bissig, S. Buecheler, A. N. Tiwari. Defect Formation in Cu(In,Ga)Se<sub>2</sub> Thin Films due to the Presence of Potassium During Growth by Low Temperature Co-Evaporation Process. *Journal of Applied Physics*, 114:194508, 2013.
- [144] D. Abou-Ras, A. Nikolaeva, S. C. Davila, M. Krause, H. Guthrey, M. Al-Jassim, M. Morawski, R. Scheer. No Evidence for Passivation Effects of Na and K at Grain Boundaries in Polycrystalline Cu(In,Ga)Se<sub>2</sub> Thin Films for Solar Cells. *Solar RRL*, 3(8):1900095, 2019.
- [145] E. Handick, P. Reinhard, J. H. Alsmeier, L. Köhler, F. Pianezzi, S. Krause, M. Gorgoi, E. Ikenaga, N. Koch, R. G. Wilks, S. Buecheler, A. N. Tiwari, M. Bär. Potassium Post-deposition Treatment-Induced Band Gap Widening at Cu(In,Ga)Se<sub>2</sub> Surfaces - Reason for Performance Leap? *ACS Applied Materials and Interfaces*, 7(49):27414–27420, 2015.

- [146] E. Handick, P. Reinhard, R. G. Wilks, F. Pianezzi, T. Kunze, D. Kreikemeyer-Lorenzo, L. Weinhardt, M. Blum, W. Yang, M. Gorgoi, E. Ikenaga, D. Gerlach, S. Ueda, Y. Yamashita, T. Chikyow, C. Heske, S. Buecheler, A. N. Tiwari, M. Bär. Formation of a K-In-Se Surface Species by NaF/KF Post-Deposition Treatment of Cu(In,Ga)Se<sub>2</sub> Thin-Film Solar Cell Absorbers. *ACS Applied Materials & Interfaces*, 2:3581–3589, 2017.
- [147] P. Reinhard, B. Bissig, F. Pianezzi, E. Avancini, H. Hagendorfer, D. Keller, P. Fuchs, M. Dobeli, C. Vigo, P. Crivelli, S. Nishiwaki, S. Buecheler, A. N. Tiwari. Features of KF and NaF Postdeposition Treatments of Cu(In,Ga)Se<sub>2</sub> Absorbers for High Efficiency Thin Film Solar Cells. *Chemistry of Materials*, 27:5755–5764, 2015.
- [148] H. Elanzeery, F. Babbe, M. Melchiorre, A. Zelenina, S. Siebentritt. Potassium Fluoride Ex Situ Treatment on Both Cu-Rich and Cu-Poor CuInSe<sub>2</sub> Thin Film Solar Cells. *IEEE Journal of Photovoltaics*, 7(2):684–689, 2017.
- [149] F. Babbe, H. Elzaneery, M. Melchiorre, A. Zelenina, S. Siebentritt. Potassium Fluoride Postdeposition Treatment with Etching Step on Both Cu-Rich and Cu-Poor CuInSe<sub>2</sub> Thin Film Solar Cells. *Physical Review Materials*, 2:105405, 2018.
- [150] P. Reinhard, B. Bissig, F. Pianezzi, H. Hagendorfer, G. Sozzi, R. Menozzi, C. Gretener, S. Nishiwaki, S. Buecheler, A. N. Tiwari. Alkali-Templated Surface Nanopatterning of Chalcogenide Thin Films: A Novel Approach Toward Solar Cells with Enhanced Efficiency. *Nano Letters*, 15(5):3334–3340, 2015.
- [151] E. Handick, P. Reinhard, R. G. Wilks, F. Pianezzi, R. Félix, M. Gorgoi, T. Kunze, S. Buecheler, A. N. Tiwari, M. Bär. NaF / KF Post-Deposition Treatments and their Influence on the Structure of Cu(In,Ga)Se<sub>2</sub> Absorber Surfaces. *Proceedings of the IEEE 43rd Photovoltaic Specialists Conference*, 43:17–21, 2016.
- [152] J. Zhao, A. Wang, M. A. Green. 24.5% Efficiency Silicon PERT Cells on MCZ Substrates and 24.7% Efficiency PERL Cells on FZ Substrates. *Progress in Photovoltaics: Research and Applications*, 7(6):471–474, 1999.
- [153] N. Nicoara, T. Lepetit, L. Arzel, S. Harel, N. Barreau, S. Sadewasser. Effect of the KF Post-Deposition Treatment on Grain Boundary Properties in Cu(In,Ga)Se<sub>2</sub> Thin Films. *Scientific Reports*, 7:41361, 2017.
- [154] J. A. Aguiar, A. Stokes, C.-S. Jiang, T. Aoki, P. G. Kotula, M. K. Patel, B. Gorman, M. Al-Jassim. Revealing Surface Modifications of Potassium-Fluoride-Treated Cu(In,Ga)Se<sub>2</sub>: A Study of Material Structure, Chemistry, and Photovoltaic Performance. *Advanced Materials Interfaces*, 3(17):1600013, 2016.
- [155] B. Ümsür, W. Calvet, A. Steigert, I. Lauermann, M. Gorgoi, K. Prietzel, D. Greiner, C. A. Kaufmann, T. Unold, M. C. Lux-Steiner. Investigation of the Potassium Fluoride Postdeposition Treatment on the CIGSe/CdS Interface Using Hard X-Ray Photoemission Spectroscopy - a Comparative Study. *Physical Chemistry Chemical Physics*, 18: 14129–14138, 2016.
- [156] T. M. Friedlmeier, P. Jackson, D. Kreikemeyer-Lorenzo, D. Hauschild, O. Kiowski, D. Hariskos, L. Weinhardt, C. Heske, M. Powalla. A Closer Look at Initial CdS Growth on High-Efficiency Cu(In,Ga)Se<sub>2</sub> Absorbers Using Surface-Sensitive Methods. *Proceedings of the 43rd IEEE Photovoltaic Specialists Conference*, pages 457–461, 2016.
- [157] E. Avancini, R. Carron, T. P. Weiss, C. Andres, M. Bürki, R. Figi, Y. E. Romanyuk, S. Buecheler, A. N. Tiwari. Effects of Rubidium Fluoride and Potassium Fluoride Post Deposition Treatments on Cu(In,Ga)Se<sub>2</sub> Thin Films and Solar Cell Performance. *Chemistry of Materials*, 29(22):9695–9704, 2017.

- [158] S. Ishizuka, N. Taguchi, J. Nishinaga, Y. Kamikawa, S. Tanaka, H. Shibita. Group III Elemental Composition Dependence of RbF Postdeposition Treatment Effects on Cu(In,Ga)<sub>2</sub> Thin Films and Solar Cells. *The Journal of Physical Chemistry C*, 122(7): 3809–3817, 2018.
- [159] S. Karki, P. Paul, G. Rajan, B. Belfore, D. Poudel, A. Rockett, E. Danilov, F. Castellano, A. Arehart, S. Marsillac. Analysis of Recombination Mechanisms in RbF-Treated CIGS Solar Cells. *IEEE Journal of Photovoltaics*, 9(1):313–318, 2019.
- [160] M. H. Wolter, B. Bissig, E. Avancini, R. Carron, S. Buecheler, P. Jackson, S. Siebentritt. Influence of Sodium and Rubidium Postdeposition Treatment on the Quasi-Fermi Level Splitting of Cu(In,Ga)Se<sub>2</sub> Thin Films. *IEEE Journal of Photovoltaics*, 8(5): 1320–1325, 2018.
- [161] M. Malitckaya, H.-P. Komsa, V. Havu, M. J. Puska. Effect of Alkali Metal Atom Doping on the CuInSe<sub>2</sub>-Based Solar Cell Absorber. *The Journal of Physical Chemistry C*, 121(29): 15516–15528, 2017.
- [162] R. Kormath Madam Raghupathy, T. D. Kühne, G. Henkelman, H. Mirhosseini. Alkali Atoms Diffusion Mechanism in CuInSe<sub>2</sub> Explained by Kinetic Monte Carlo Simulations. *Advanced Theory and Simulations*, 2(6):1900036, 2019.
- [163] G. Kresse, J. Furthmüller. Efficient Iterative Schemes for Ab-Initio Total-Energy Calculations Using a Planar Wave Basis Set. *Physical Review B*, 54:11169–11186, 1996.
- [164] S. Ishizuka, H. Shibata, J. Nishinaga, Y. Kamikawa, P. J. Fons. Effects of RbF Postdeposition Treatment and Heat-Light Soaking on the Metastable Acceptor Activation of CuInSe<sub>2</sub> Thin Film Photovoltaic Devices. *Applied Physics Letters*, 113:063901, 2018.
- [165] P. Schöppe, S. Schönherr, R. Wuerz, W. Wisniewski, G. Martínez-Criado, M. Ritzer, K. Ritter, C. Ronning, C. S. Schnohr. Rubidium Segregation at Random Grain Boundaries in Cu(In,Ga)Se<sub>2</sub> Absorbers. *Nano Energy*, 42:307–313, 2017.
- [166] P. Schöppe, S. Schönherr, P. Jackson, R. Wuerz, W. Wisniewski, M. Ritzer, M. Zapf, A. Johannes, C. S. Schnohr, C. Ronning. Overall Distribution of Rubidium in Highly Efficient Cu(In,Ga)Se<sub>2</sub> Solar Cells. *ACS Applied Materials & Interfaces*, 10:40592–40598, 2018.
- [167] A. Vilalta-Clemente, M. Raghuwanshi, S. Duguay, C. Castro, E. Cadel, P. Pareige, P. Jackson, R. Wuerz, D. Hariskos, W. Witte. Rubidium Distribution at Atomic Scale in High Efficient Cu(In,Ga)Se<sub>2</sub> Thin-Film Solar Cells. *Applied Physics Letters*, 112(10): 103105, 2018.
- [168] N. Taguchi, S. Tanaka, S. Ishizuka. Direct Insights into RbInSe<sub>2</sub> Formation at Cu(In,Ga)Se<sub>2</sub> Thin Film Surface with RbF Postdeposition Treatment. *Applied Physics Letters*, 113:113903, 2018.
- [169] M. Raghuwanshi, A. Vilalta-Clemente, C. Castro, S. Duguay, E. Cadel, P. Jackson, D. Hariskos, W. Witte, P. Pareige. Influence of RbF Post Deposition Treatment on Heterojunction and Grain Boundaries in High Efficient (21.1%) Cu(In,Ga)Se<sub>2</sub> Solar Cells. *Nano Energy*, 60:103–110, 2019.
- [170] R. Wuerz, W. Hempel, P. Jackson. Diffusion of Rb in Polycrystalline Cu(In,Ga)Se<sub>2</sub> Layers and Effect of Rb on Solar Cell Parameters of Cu(In,Ga)Se<sub>2</sub> Thin-Film Solar Cells. *Journal of Applied Physics*, 124:165305, 2018.
- [171] R. Carron, S. Nishiwaki, T. Feurer, R. Hertwig, E. Avancini, J. Löckinger, S.-C. Yang, S. Buecheler, A. N. Tiwari. Advanced Alkali Treatments for High-Efficiency

- Cu(In,Ga)Se<sub>2</sub> Solar Cells on Flexible Substrates. *Advanced Energy Materials*, 9(24): 1900408, 2019.
- [172] S. Zahedi-Azad, M. Maiberg, R. Clausing, R. Scheer. Influence of Heavy Alkali Post Deposition Treatment on Wide Gap Cu(In,Ga)Se<sub>2</sub>. *Thin Solid Films*, 669:629–632, 2019.
- [173] A. Jain, S. P. Ong, G. Hautier, W. Chen, W. D. Richards, S. Dacek, S. Cholia, D. Gunter, D. Skinner, G. Ceder, K. A. Persson. Commentary: The Materials Project: A Materials Genome Approach to Accelerating Materials Innovation. *Applied Physics Letters Materials*, 1:011002, 2013.
- [174] D. Greiner. PVD-B Manual. HZB internal, 2014.
- [175] J. Kessler, J. Schöldström, L. Stolt. Rapid Cu(In,Ga)Se<sub>2</sub> Growth Using End Point Detection. *Record of the 28th IEEE Photovoltaic Specialists Conference*, 1:509–512, 2000.
- [176] R. Scheer, A. Neisser, K. Sakurai, P. Fons, S. Niki. Cu(In<sub>1-x</sub>,Ga<sub>x</sub>)Se<sub>2</sub> Growth Studies by In Situ Spectroscopic Light Scattering. *Applied Physics Letters*, 82:2091–2093, 2003.
- [177] R. Scheer, A. Perez-Rodriguez, W. K. Metzger. Advanced Diagnostic and Control Methods of Processes and Layers in CIGS Solar Cells and Modules. *Progress in Photovoltaics: Research and Applications*, 18:467–480, 2010.
- [178] M. A. Contreras, J. Tuttle, A. Gabor, A. Tennant, K. Ramanathan, S. Asher, A. Franz, J. Keane, L. Wang, J. Scofield, R. Noufi. High Efficiency Cu(In,Ga)Se<sub>2</sub>-Based Solar Cells: Processing of Novel Absorber Structures. *Conference Record of the 24th IEEE Photovoltaic Specialists Conference*, 1:5572–5577, 1994.
- [179] I. Repins, M. A. Contreras, B. Egaas, C. DeHart, J. Scharf, C. L. Perkins, B. To, R. Noufi. 19.9%-Efficient ZnO/CdS/CuInGaSe<sub>2</sub> Solar Cell with 81.2% Fill Factor. *Progress in Photovoltaics: Research and Applications*, 16:235–239, 2008.
- [180] N. Barreau, T. Painchaud, F. Couzinie-Devy, L. Arzel, J. Kessler. Recrystallization of CIGSe Layers Grown by Three-Step Processes: A Model Based on Grain Boundary Migration. *Acta Materialia*, 58:5572–5577, 2010.
- [181] L. Gütay, D. Regesch, J. K. Larsen, Y. Aida, V. Depredurand, S. Siebentritt. Influence of Copper Excess on the Absorber Quality of CuInSe<sub>2</sub>. *Applied Physics Letters*, 99:151912, 2011.
- [182] T. Rissom, R. Mainz, C. A. Kaufmann, R. Caballero, V. Efimova, V. Hoffmann, H.-W. Schock. Examination of Growth Kinetics of Copper Rich Cu(In,Ga)Se<sub>2</sub>-Films Using Synchrotron Energy Dispersive X-Ray Diffractometry. *Solar Energy Materials and Solar Cells*, 95:250–253, 2011.
- [183] R. Mainz, H. Rodriguez-Alvarez, M. Klaus, D. Thomas, J. Lauche, A. Weber, M. D. Heinemann, S. Brunken, D. Greiner, C. A. Kaufmann, T. Unold, H.-W. Schock, C. Genzel. Sudden Stress Relaxation in Compound Semiconductor Thin Films Triggered by Secondary Phase Segregation. *Physical Review B*, 93:159902, 2016.
- [184] R. Ortega-Borges, D. Lincot. Mechanism of Chemical Bath Deposition of Cadmium Sulfide Thin Films in the Ammonia-Thiourea System. *Journal of the Electrochemical Society*, 140(12):3464–3474, 1993.
- [185] D. Lincot, M. Froment, H. Cachet. *Advances in Electrochemical Science and Engineering*, volume 6. Wiley-VCH, Weinheim, 1999. Pages 165-235.
- [186] L. Choubrac, G. Brammertz, N. Barreau, L. Arzel, S. Harel, M. Meuris, B. Vermang. 7.6 % CZGSe Solar Cells Thanks to Optimized CdS Chemical Bath Deposition. *Physica Status Solidi A: Applications and Materials Science*, 215:1800043, 2018.

- [187] D. Abou-Ras, T. Kirchartz, U. Rau. *Advanced Characterization Techniques for Thin Film Solar Cells*, volume 1. Wiley-VCH, 2. edition, 2016.
- [188] W. H. Bragg, W. L. Bragg. The Reflection of X-Rays by Crystals. *Proceedings of the Royal Society of London Series A Containing Papers of a Mathematical and Physical Character*, 88 (605):428–438, 1913.
- [189] *GDA 650 HR - User's Manual*. Spectruma GmbH, Hof.
- [190] A. Bengtson, T. Nelis. The Concept of Constant Emission Yield in GDOES. *Analytical Bioanalytical Chemistry*, 385:568–585, 2006.
- [191] I. Lauermann, A. Steigert. CISSY: A Station for Preparation and Surface/Interface Analysis of Thin Film Materials and Devices. *Journal of Large-Scale Research Facilities*, 2 (A67), 2016.
- [192] J. Lehmann, S. Lehmann, I. Lauermann, T. Rissom, C. A. Kaufmann, M. C. Lux-Steiner, M. Bär, S. Sadewasser. Reliable Wet-Chemical Cleaning of Natively Oxidized High-Efficiency Cu(In,Ga)Se<sub>2</sub> Thin-Film Solar Cell Absorbers. *Journal of Applied Physics*, 116: 233502, 2014.
- [193] M. Wojdyr. Fityk: a General-Purpose Peak Fitting Program. *Journal of Applied Crystallography*, 43:1126–1128, 2010.
- [194] D. Papadimitriou, N. Esser, C. Xue. Structural Properties of Chalcopyrite Thin Films Studied by Raman Spectroscopy. *Physica Status Solidi B: Basic Solid State Physics*, 242 (13):2633–2643, 2005.
- [195] C. Rincon, F. J. Ramirez. Lattice Vibrations of CuInSe<sub>2</sub> and CuGaSe<sub>2</sub> by Raman Microspectrometry. *Journal of Applied Physics*, 72:4321–4324, 1992.
- [196] C. Rincon, S. M. Wasim, G. Marin, J. M. Delgado, J. R. Huntzinger, A. Zwick, J. Galibert. Raman Spectra of the Ordered Defect Compounds CuIn<sub>3</sub>Se<sub>5</sub> and CuGa<sub>3</sub>Se<sub>5</sub>. *Applied Physics Letters*, 73(4):441–443, 1998.
- [197] S. Mishra, A. Ingale, U. N. Roy, A. Gupta. Study of Annealing-Induced Changes in CdS Thin Films Using X-Ray Diffraction and Raman Spectroscopy. *Thin Solid Films*, 516:91–98, 2007.
- [198] I. De Wolf. Micro-Raman Spectroscopy to Study Local Mechanical Stress in Silicon Integrated Circuits. *Semiconductor Science and Technology*, 11:139–154, 1996.
- [199] S. Binetti, P. Garattini, R. Mereu, A. Le Donne, S. Marchionna, A. Gasparotto, M. Meschia, I. Pinus, M. Acciarri. Fabricating Cu(In,Ga)Se<sub>2</sub> Solar Cells on Flexible Substrates by a New Roll-to-Roll Deposition System Suitable for Industrial Applications. *Semiconductor Science and Technology*, 30:105006, 2015.
- [200] A. Le Bail, H. Duroy, J. L. Fourquet. Ab Initio Structure Determination of LiSbWO<sub>6</sub> by X-Ray Powder Diffraction. *Materials Research Bulletin*, 23:447–452, 1988.
- [201] D. K. Schroder. *Semiconductor Material and Device Characterization*. John Wiley & Sons, Inc., New Jersey, 3. edition, 1990.
- [202] M. Maiberg, R. Scheer. Theoretical Study of Time-Resolved Luminescence in Semiconductors. II. Pulsed Excitation. *Journal of Applied Physics*, 116:123711, 2014.
- [203] M. Maiberg, T. Hölscher, S. Zahedi-Azad, R. Scheer. Theoretical Study of Time-Resolved Luminescence in Semiconductors. III. Trap States in the Band Gap. *Journal of Applied Physics*, 118:105701, 2015.

- [204] C. J. Hages, A. Redinger, S. Levchenko, H. Hempel, M. J. Koeper, R. Agrawal, D. Greiner, C. A. Kaufmann, T. Unold. Identifying the Real Minority Carrier Lifetime in Nonideal Semiconductors: A Case Study of Kesterite Materials. *Advanced Energy Materials*, 7(18):1700167, 2017.
- [205] A. Redinger, S. Levchenko, C. J. Hages, D. Greiner, C. A. Kaufmann, T. Unold. Time Resolved Photoluminescence on Cu(In,Ga)Se<sub>2</sub> Absorbers: Distinguishing Degradation and Trap States. *Applied Physics Letters*, 110:122104, 2017.
- [206] T. Hänel. Spannungs- und Intensitätsabhängige Spektrale Empfindlichkeit von Poly-Si Dünnschicht-Solarzellen. Diploma Thesis, HTW Berlin, 2008.
- [207] M. Troviano, K. Taretto. Analysis of Internal Quantum Efficiency in Double-Graded Bandgap Solar Cells Including Sub-Bandgap Absorption. *Solar Energy Materials and Solar Cells*, 95:821–828, 2011.
- [208] R. Klenk. *Polykristalline CuGaSe<sub>2</sub>-Dünnschichten Für die Photovoltaik - Herstellung und Charakterisierung von Absorbern und Heteroübergängen*. PhD Thesis, University of Stuttgart, 1993.
- [209] T. Eisenbarth. *Identifikation von Defekten und Metastabilitäten in Cu(In,Ga)Se<sub>2</sub>-Dünnschicht-Solarzellen*. PhD Thesis, Freie Universität Berlin, 2010.
- [210] G. Sozzi, M. Lazzarini, R. Menozzi, R. Carron, E. Avancini, B. Bissig, S. Buecheler, A. N. Tiwari. A Numerical Study of the Use of C-V Characteristics to Extract the Doping Density of CIGS Absorbers. *Proceedings of the 43rd IEEE Photovoltaic Specialists Conference*, 1:2283–2288, 2016.
- [211] J. Hilibrand, R. D. Gold. Determination of Impurity Distribution in Junction Diodes from Capacitance-Voltage Measurements. *RCA Review*, 21:245–252, 1960.
- [212] M. D. Heinemann. *CIGSe Superstrate Solar Cells: Growth and Characterization of CIGSe Thin Films on Transparent Conductive Oxides*. PhD Thesis, Technical University Berlin, 2015.
- [213] M. Burgelman, P. Nollet, S. Degraeve. Modelling Polycrystalline Semiconductor Solar Cells. *Thin Solid Films*, 361:527–532, 2000.
- [214] H. A. Yetkin. *Modifikation der CIGSe-Absorberoberfläche mittels RbF-Nachbehandlung zur Anwendung in Solarzellen*. Master Thesis, Technical University Berlin, 2016.
- [215] A. Vilanueva-Tovar. *Analysis of Transport Mechanisms in Advanced Chalcopyrite Thin Film Solar Cells*. PhD Thesis, Freie Universität Berlin, In Preparation.
- [216] C. Godet, Y. Bouizem, L. Chahed, I. El Zawawi, M. L. Theye, M. Meaudre, R. Meaudre, S. Basrouf, J. C. Bruyere. Band Tails and Deep-Defect Density of States in Hydrogenated Amorphous Germanium. *Physical Review B*, 44(11):5506–5509, 1991.
- [217] N. Wyrsh, F. Finger, T. J. McMahon, M. Vanecek. How to Reach More Precise Interpretation of Subgap Absorption Spectra in Terms of Deep Defect Density in a-Si:H. *Journal of Non-Crystalline Solids*, 137-138:347–350, 1991.
- [218] C. M. Sutter-Fella, D. W. Miller, Q. P. Ngo, E. T. Roe, F. M. Toma, I. D. Sharp, M. C. Lonergan, A. Javey. Band Tailing and Deep Defect States in CH<sub>3</sub>NH<sub>3</sub>Pb(I<sub>1-x</sub>Br<sub>x</sub>)<sub>3</sub> Perovskites As Revealed by Sub-Bandgap Photocurrent. *ACS Energy Letters*, 2:709–715, 2017.

- [219] N. Nicoara, R. Manaligod, P. Jackson, D. Hariskos, W. Witte, G. Sozzi, R. Menozzi, S. Sadewasser. Direct Evidence for Grain Boundary Passivation in Cu(In,Ga)Se<sub>2</sub> Solar Cells through Alkali-Fluoride Post-Deposition Treatments. *Nature Communications*, 10: 3980, 2019.
- [220] A. Kylner. The Chemical Bath Deposited CdS/Cu(In,Ga)Se<sub>2</sub> Interface as Revealed by X-Ray Photoelectron Spectroscopy. *Journal of The Electrochemical Society*, 146(5):1816, 1999.
- [221] K. Otte, G. Lippold, D. Hirsch, A. Schindler, F. Bigl. XPS and Raman Investigations of Nitrogen Ion Etching for Depth Profiling of CuInSe<sub>2</sub> and CuGaSe<sub>2</sub>. *Thin Solid Films*, 361-362:498–503, 2000.
- [222] J. F. Moulder, W. F. Stickle, P. E. Sobol, K. D. Bomben. *Handbook of X-Ray Photoelectron Spectroscopy*. Perkin-Elmer Corporation, 1992.
- [223] C. Heske, R. Fink, E. Umbach, W. Riedl, F. Karg. Na-Induced Effects on the Electronic Structure and Composition of Cu(In,Ga)Se<sub>2</sub> Thin-Film Surfaces. *Applied Physics Letters*, 68(24):3431, 1996.
- [224] A. Barrie, F. J. Street. An Auger and X-Ray Photoelectron Spectroscopic Study of Sodium Metal and Sodium Oxide. *Journal of Electron Spectroscopy and Related Phenomena*, 7(1):1–31, 1975.
- [225] H. Seyama, M. Soma. X-Ray Photoelectron Spectroscopic Study of the Effect of Heating on Montmorillonite Containing Sodium and Potassium Cations. *Clays and Clay Minerals*, 34(6):672–676, 1986.
- [226] W. E. Morgan, J. R. Van Wazer, W. J. Stec. Inner-Orbital Photoelectron Spectroscopy of the Alkali Metal Halides, Perchlorates, Phosphates, and Pyrophosphates. *Journal of the American Chemical Society*, 95(3):751–755, 1973.
- [227] B. Canava, J. Vigneron, A. Etcheberry, J. F. Guillemoles, D. Lincot. High Resolution XPS Studies of Se Chemistry of a Cu(In,Ga)Se<sub>2</sub> Surface. *Applied Surface Science*, 202 (1-2):8–14, 2002.
- [228] A. J. Nelson, S. Gebhard, L. L. Kazmerski, E. Colavita, M. Engelhardt, H. Höchst. Characterization of the Native Oxide of CuInSe<sub>2</sub> Using Synchrotron Radiation Photoemission. *Applied Physics Letters*, 57:1428–1430, 1990.
- [229] I. Miyake, T. Tanpo, C. Tatsuyama. Related Content XPS Study on the Oxidation of InSe. *Japanese Journal of Applied Physics*, 23(2):172–178, 1984.
- [230] R. Klauser, M. Oshima, H. Sugihara. RbF as Reactive and Dipole Interlayers Between the Ge/GaAs Interface. *Physical Review B*, 43(6):4879–4884, 1991.
- [231] M. Volmer, A. Weber. Keimbildung in Übersättigten Gebilden. *Zeitschrift für physikalische Chemie*, 1926.
- [232] H. Rodriguez-Alvarez, R. Mainz, S. Sadewasser. A One-Dimensional Fickian Model to Predict the Ga Depth Profiles in Three-Stage Cu(In,Ga)Se<sub>2</sub>. *Journal of Applied Physics*, 115:204913, 2014.
- [233] A. Pfizner, H. D. Lutz. Redetermination of the Crystal Structure of  $\gamma$ -In<sub>2</sub>Se<sub>3</sub> by Twin Crystal X-Ray Method. *Journal of Solid State Chemistry*, 124:305–308, 1996.
- [234] J. H. C. Hogg, H. H. Sutherland, D. J. Williams. The Crystal Structure of Tetraindium Triselenide. *Acta Crystallographica, Section B: Structural Crystallography and Crystal Chemistry*, 29:1590–1593, 1973.

- [235] F. Q. Huang, B. Deng, D. E. Ellis, J. A. Ibers. Preparation, Structures, and Band Gaps of  $\text{RbInSe}_2$  and  $\text{RbInSe}_2$ . *Journal of Solid State Chemistry*, 178:2128–2132, 2005.
- [236] C. Bernuy-Lopez, M. Allix, C. A. Bridges, J. B. Claridge, M. J. Rosseinsky.  $\text{Sr}_2\text{MgMoO}_{6-d}$ : Structure, Phase Stability, and Cation Site Order Control of Reduction. *Chemistry of Materials*, 19(5):1035–1043, 2007.
- [237] C. Julien, A. Chevy, D. Siapkak. Optical Properties of  $\text{In}_2\text{Se}_3$  Phases. *Physica Status Solidi A: Applications and Materials Science*, 118:553–559, 1990.
- [238] J. P. Perdew, W. Yang, K. Burke, Z. Yang, E. K. U. Gross, M. Scheffler, G. E. Scuseria, T. M. Henderson, I. Y. Zhang, A. Ruzsinszky, H. Peng, J. Sun, E. Trushin, A. Görling. Understanding Band Gaps of Solids in Generalized Kohn-Sham Theory. *Proceedings of the National Academy of Sciences*, 114:2801–2806, 2017.
- [239] K. Bindu, C. Sudha Kartha, K. P. Vijayakumar, T. Abe, Y. Kashiwaba. Structural, Optical and Electrical Properties of  $\text{In}_2\text{Se}_3$  Thin Films Formed by Annealing Chemically Deposited Se and Vacuum Evaporated In Stack Layers. *Applied Surface Science*, 191:138–147, 2002.
- [240] S. Marsillac, A. M. Combot-Marie, J. C. Bernede, A. Conan. Experimental Evidence of the Low-Temperature Formation of  $\gamma\text{-In}_2\text{Se}_3$  Thin Films Obtained by a Solid-State Reaction. *Thin Solid Films*, 288:14–20, 1996.
- [241] D. Y. Lyu, T. Y. Lin, T. W. Chang, S. M. Lan, T. N. Yang, C. C. Chiang, C. L. Chen, H. P. Chiang. Structural and Optical Characterization of Single-Phase  $\gamma\text{-In}_2\text{Se}_3$  Films with Room-Temperature Photoluminescence. *Journal of Alloys and Compounds*, 499:104–107, 2010.
- [242] F. C. Frank, J. H. van der Merwe. One-Dimensional Dislocations. I. Static Theory. *Proceedings of the Royal Society of London. Series A, Mathematical and Physical Sciences*, 198(1053):205–216, 1949.
- [243] F. C. Frank, J. H. van der Merwe. One-Dimensional Dislocations. II. Misfitting Monolayers and Oriented Overgrowth. *Proceedings of the Royal Society of London. Series A, Mathematical and Physical Sciences*, 198(1053):216–225, 1949.
- [244] F. C. Frank, J. H. van der Merwe. One-Dimensional Dislocations. III. Influence of the Second Harmonic Term in the Potential Representation, on the Properties of the Model. *Proceedings of the Royal Society of London. Series A, Mathematical and Physical Sciences*, 200(1060):125–134, 1949.
- [245] I. N. Stranski, L. Krastanow. Zur Theorie der Orientierten Ausscheidung von Ionenkristallen Aufeinander. *Monatshefte fuer Chemie*, 71(1):351–364, 1937.
- [246] R. W. Vook. Nucleation and Growth of Thin Films. *Optical Engineering*, 23(3):343–348, 1984.
- [247] T. Maeda, W. Gong, T. Wada. Crystallographic and Optical Properties and Band Structures of  $\text{CuInSe}_2$ ,  $\text{CuIn}_3\text{Se}_5$ , and  $\text{CuIn}_5\text{Se}_8$  Phases in Cu-Poor  $\text{Cu}_2\text{Se-In}_2\text{Se}_3$  Pseudo-Binary System. *Japanese Journal of Applied Physics*, 55:04ES15, 2016.
- [248] A. I. Oliva, O. Solis-Canto, R. Castro-Rodriguez, P. Quintana. Formation of the Band Gap Energy on  $\text{CdS}$  Thin Films Growth by Two Different Techniques. *Thin Solid Films*, 391:28–35, 2001.
- [249] D. Lincot, R. O. Borges. Chemical Bath Deposition of Cadmium Sulfide Thin Films. In Situ Growth and Structural Studies by Combined Quartz Crystal Microbalance and Electrochemical Impedance Techniques. *Journal of the Electrochemical Society*, 139:1880–1889, 1992.

- [250] W. Witte, D. Abou-Ras, D. Hariskos. Chemical Bath Deposition of Zn(O,S) and CdS Buffers: Influence of Cu(In,Ga)Se<sub>2</sub> Grain Orientation. *Applied Physics Letters*, 102 (051607):1–4, 2013.
- [251] L. G. Harrison. Influence of Dislocations on Diffusion Kinetic in Solids with Particular Reference to the Alkali Halides. *Transactions of the Faraday Society*, 57:1191–1199, 1961.
- [252] S. Karki. *Effect of Alkali on the Efficiency and Reliability of Cu(In,Ga)Se<sub>2</sub> Solar Cells*. PhD Thesis, Old Dominion University, 2019.
- [253] A. Bercegol, B. Chacko, R. Klenk, I. Lauermann, M. C. Lux-Steiner, M. Liero. Point Contacts at the Copper-Indium-Gallium-Selenide Interface - a Theoretical Outlook. *Journal of Applied Physics*, 119:155304, 2016.
- [254] T. Walter, R. Herberholz, H. W. Schock. Distribution of Defects in Polycrystalline Chalcopyrite Thin Films. *Solid State Phenomena*, 51-52:309–316, 1996.
- [255] N. Barreau, A. Frelon, T. Lepetit, E. Gautron, N. Gautier, R. Ribeiro-Andrade, N. Nicoara, S. Sadewasser, P. Zabierowski, L. Arzel, L. Choubrac, S. Harel, C. Deudon, C. Latouche, S. Jobic, M. Caldes, L. Assmann, P. Tsoulka, E. V. Pean, J. Lorthioir, F. Geschier, I. Braems, M. Moret, O. Briot, and G. Ouyard. High Efficiency Solar Cell Based on Full PVD Processed Cu(In,Ga)Se<sub>2</sub>/CdIn<sub>2</sub>S<sub>4</sub> Heterojunction. *Solar RRL*, 1700140:1–7, 2017.
- [256] N. Barreau. Personal Communication, 2019.
- [257] B. Ümsür, T. Kodalle, N. Maticiuc, I. Majumdar, Y. Wang, R. Wenisch, H. A. Yetkin, T. Bertram, R. Felix, C. A. Kaufmann, R. Schlattmann, I. Lauermann. Effects of Rubidium Fluoride Post Deposition Treatment on Cu(In,Ga)Se<sub>2</sub>/XS (X: Cd, Zn) Interfaces Studied by Hard X-Ray Photoemission Spectroscopy. *In Preparation*, 2019.
- [258] W. Witte, D. Abou-Ras, D. Hariskos. Improved Growth of Solution-Deposited Thin Films on Polycrystalline Cu(In,Ga)Se<sub>2</sub>. *physica status solidi: Rapid Research Letters*, 10: 300–304, 2016.
- [259] T. Schwarz-Selinger, Y. L. Foo, D. G. Cahill, J. E. Greene. Surface Mass Transport and Island Nucleation During Growth of Ge on Laser Textured Si(001). *Physical Review B*, 65:125317, 2002.
- [260] G. Hanna, A. Jasenek, U. Rau, H.-W. Schock. Influence of the Ga-Content on the Bulk Defect Densities of Cu(In,Ga)Se<sub>2</sub>. *Thin Solid Films*, 387:71–73, 2001.
- [261] T. Hölscher, T. Schneider, M. Maiberg, R. Scheer. Impact of Air-Light Exposure on the Electrical Properties of Cu(In,Ga)Se<sub>2</sub> Solar Cells. *Progress in Photovoltaics: Research and Applications*, 26:934–941, 2018.
- [262] S. Lany, A. Zunger. Light- and Bias-Induced Metastabilities in Cu(In,Ga)Se<sub>2</sub>-Based Solar Cells Caused by the (V<sub>Se</sub>-V<sub>Cu</sub>) Vacancy Complex. *Journal of Applied Physics*, 100: 113725, 2006.
- [263] M. Igalson, P. Zabierowski, D. Przado, A. Urbaniak, M. Edoff, W. N. Shafarman. Understanding Defect-Related Issues Limiting Efficiency of CIGS Solar Cells. *Solar Energy Materials and Solar Cells*, 93:1290–1295, 2009.
- [264] T. Ott, T. Walter, T. Unold. Phototransistor Effects in Cu(In,Ga)Se<sub>2</sub> Solar Cells. *Thin Solid Films*, 535:275–278, 2013.
- [265] D. Ledinek, O. Donzel-Gargand, M. Sköld, J. Keller, M. Edoff. Effect of Different Na Supply Methods on Thin Cu(In,Ga)Se<sub>2</sub> Solar Cells With Al<sub>2</sub>O<sub>3</sub> Rear Passivation Layers. *Solar Energy Materials and Solar Cells*, 187:160–169, 2018.

- [266] T. P. Weiss. *Electrical Characterization of Kesterite Thin Film Absorbers and Solar Cells*. PhD Thesis, University of Luxembourg, 2015.
- [267] C. A. Kaufmann. *Chemical Bath Deposition of Thin Semiconductor Films for Use as Buffer Layers in CuInS<sub>2</sub> Thin Film Solar Cells*. PhD Thesis, University of Oxford, 2002.
- [268] C. H. Park, S. B. Zhang, S.-H. Wei. Origin of *p*-Type Doping Difficulty in ZnO: The Impurity Perspective. *Physical Review B*, 66(7):073202, 2002.
- [269] D. Zwingel. Trapping and Recombination Processes in the Thermoluminescence of Li-Doped ZnO Single Crystals. *Journal of Luminescence*, 5(6):385–405, 1972.
- [270] B. K. Meyer, J. Stehr, A. Hofstaetter, N. Volbers, A. Zeuner, J. Sann. On the Role of Group I Elements in ZnO. *Applied Physics A*, 88:119–123, 2007.
- [271] J. Chantana, T. Kato, H. Sugimoto, T. Minemoto. 20% Efficient Zn<sub>0.9</sub>Mg<sub>0.1</sub>O:Al/Zn<sub>0.8</sub>Mg<sub>0.2</sub>O/Cu(In,Ga)(S,Se)<sub>2</sub> Solar Cell Prepared by All-Dry Process through a Combination of Heat-Light-Soaking and Light-Soaking Processes. *ACS Applied Materials & Interfaces*, 10(13):11361–11368, 2018.
- [272] M. Nichterwitz, D. Abou-Ras, K. Sakurai, J. Bundesmann, T. Unold, R. Scheer, H.-W. Schock. Influence of Grain Boundaries on Current Collection in Cu(In,Ga)Se<sub>2</sub> Thin-Film Solar Cells. *Thin Solid Films*, 517(7):2554–2557, 2009.
- [273] R. Kniese, M. Powalla, U. Rau. Evaluation of Electron Beam Induced Current Profiles of Cu(In,Ga)Se<sub>2</sub> Solar Cells with Different Ga-Contents. *Thin Solid Films*, 517(7):2357–2359, 2009.
- [274] M. Nichterwitz. *Charge Carrier Transport in Cu(In,Ga)Se<sub>2</sub> Thin-Film Solar-Cells Studied by Electron Beam Induced Current and Temperature and Illumination Dependent Current Voltage Analyses*. PhD Thesis, Technical University Berlin, 2012.
- [275] C. Donolato. Evaluation of Diffusion Lengths and Surface Recombination Velocities from Electron Beam Induced Current Scans. *Applied Physics Letters*, 43(1):120–122, 1983.
- [276] D. Abou-Ras, N. Schäfer, N. Baldaz, S. Brunken, C. Boit. Electron-Beam-Induced Current Measurements with Applied Bias Provide Insight to Locally Resolved Acceptor Concentrations at *p-n*-Junctions. *AIP Advances*, 5:077191, 2015.



# Acknowledgments

First of all, I'd like to thank Christian Kaufmann for his patience, the guidance and the freedom he gave me when choosing the direction of this work and his support during the last three years. Furthermore, thanks to Rutger Schlatmann and Roland Scheer for their support, the opportunities they provided for me, and for reviewing this thesis.

At PVcomB I want to thank Iver Lauermann, Reiner Klenk, Dieter Greiner, Marc Heine-  
mann, Sebastian Schmidt, Tobias Bertram, Natalia Maticiuc, and Robert Wenisch for many fruitful discussions and for sharing their experience in sample preparation, characterization, modeling, and writing with me. For their technical support I want to thank Jakob Lauche, Tobias Hänel, Tim Münchenberg, Bianka Bunn, Iris Dorbandt, Stefanie Stutzke, Manuel Hartig, Katja Mayer-Stillrich, Karolina Mack, Michael Kirsch, Sonja Cinque, Erik Waack, Carola Klimm, Michael Klupsch, Silvio Knoop, and Jerome Deumer as well as Jan Lucassen and Kadiatou Coulibaly for their engagement during their internships. Alexandros Cruz, Darja Erfurt, Hasan Yetkin, Stefan Körner, Alejandra Vilanueva, Guillermo Farias, and Fuxi Bao, thanks for their company and the good times in the PhD-office at PVcomB and at the Stammtisch.

At HZB in Wannsee, I want to thank Thomas Unold, Sergej Levenco, Marin Rusu, Pepe Marquez, Pascal Becker and Charles Hages for their help regarding PL, trPL, and other measurements; Daniel Abou-Ras, Aleksandra Nikolaeva, and Norbert Schäfer for their help with all questions around micro-scale characterization, René Gunder for his expertise regarding XRD, and Marcus Bär, Jakob Bombsch, Roberto Felix, and Evelyn Handick for the collaboration regarding HAXPES-measurements.

At the University of Halle, I want to thank Setareh Zahedi-Azad for the collaboration regarding GD-OES and Matthias Maiberg for the fits of the trPL-data. Also for their expertise in GD-OES and the fruitful collaboration I want to thank Volker Hoffmann and Varvara Brackmann. Other fruitful collaborations I'm very thankful for are that with Nikolaus Weinberger and his colleagues from the University of Innsbruck and Suplugged, that with Hossein Mirhosseini, Ramya Kormath Madam Ragupathy, and Thomas Kühne from the University of Paderborn, that with Chen Li and Peter van Aken from the Max-Planck Institute in Stuttgart, that with Maxim Guc, Victor Izquierdo, and Alejandro Perez Roudriguez from IREC in Barcelona, and that with Amala Elizabeth and Harry Mönig at the University of Münster.

Furthermore, I want to thank Nicolas Barreau and Chris Ferekides for hosting me in their groups and for supporting my ideas. An additional thanks to Nicolas for providing various samples throughout the past years. Additionally, I want to thank all the coworkers and friends I made during these stays in Nantes and in Tampa: Pablo Reyes, Léo Choubrac, Xenia Tsoulka, Justine Lorthioir, Adrien Rivalland, Ludovic Arzel, Sylvie Harel, Thomas Lepetit, Lionel Assmann, Chih An Hsu, Zahangir Alom, Sheik Elahi, and Don Morel.

A special thanks for proof-reading this thesis goes to my friends Tobi, Pablo, Darja, Vanessa, Elisabeth, and Sören.

Finally, I want to thank my beloved Abigail, also for proof-reading, but mainly for her patience and encouragement during the most stressful time of this thesis, my siblings, Martin, Nina, and especially Fabian for their help in the last months and years and of course my parents, Petra and Axel, for their lifelong support and their trust in me.



# Curriculum Vitae

## Personal Details

Title: Master of Science  
Name: Tim Kodalle  
Date of Birth: 17.08.1990  
Place of Birth: Troisdorf  
Sex: Male  
Nationality: German  
Present Address: Karl-Marx-Allee 67, 10243 Berlin, Germany  
Email: tim.kodalle@freenet.de

## Education

10/2016 - 09/2019     Doctoral Researcher at Helmholtz-Zentrum Berlin & Martin-Luther University Halle-Wittenberg

Topic:                     Unraveling the Structural and Optoelectronic Effects of Rb on Chalcopyrite Solar Cells

Supervisors:             Prof. Dr. R. Scheer, Prof. Dr. R. Schlatmann

10/2013 - 04/2016     Master of Physics at the Humboldt-University Berlin

Specialization:         Solid State Physics

Thesis:                     Sulfurization after Selenization of Sequentially Processed Cu(In,Ga)Se<sub>2</sub> -Thin Film Solar Cells

Final Grade:             1.1

Supervisors:             Dr. M. Mulazzi, Dr. S. S. Schmidt

10/2010 - 09/2013     Bachelor of Physics at the Westfälische Wilhelms-University Münster

Thesis:                     Interferometric Measurement of Mirror Movements at an Autocorrelator for the European XFEL

Final Grade:             1.3

Supervisors:             Prof. Dr. H. Zacharias, Dr. M. Bartsch



# Eidesstattliche Erklärung

Hiermit erkläre ich, Tim Kodalle, dass ich die vorliegende Arbeit mit dem Titel: “Unraveling the Structural and Optoelectronic Effects of Rb on Chalcopyrite Solar Cells” selbstständig und ohne fremde Hilfe verfasst und dabei keine anderen als die angegebene Quellen und Hilfsmittel benutzt habe. Alle wörtlich oder inhaltlich übernommenen Textstellen anderer Werke sowie die Beiträge Dritter habe ich als solche kenntlich gemacht.

Des Weiteren erkläre ich weder bereits vergebliche Promotionsversuche unternommen zu haben, noch die vorliegende oder eine andere Arbeit als Dissertation bei einer anderen Fakultät eingereicht zu haben.

Ich bin weder vorbestraft, noch wurde ein Ermittlungsverfahren gegen mich eingeleitet.

Berlin, den 27.09.2019

---

Tim Kodalle